Atmospheric aerosol optical property retrieval with scanning polarimeters

Kirk D. Knobelspiesse

Submitted in partial fulfillment of the

requirements for the degree

of Doctor of Philosophy

in the Graduate School of Arts and Sciences

COLUMBIA UNIVERSITY

2011

©2010

Kirk D. Knobelspiesse

All Rights Reserved

ABSTRACT

Atmospheric aerosol optical property retrieval with scanning polarimeters

Kirk D. Knobelspiesse

The radiative energy balance of the Earth is controlled by aerosols, clouds and gases, which scatter and absorb incident solar radiation and emitted infra-red radiation. Climate models simulate this process, along with the dynamical energy redistribution of the atmosphere and oceans. In the last decade, climate models have become increasingly accurate as they include complex processes in a more physical manner. However, the climatic effect of one component, atmospheric aerosols, continues to remain highly uncertain. Aerosols are short lived airborne particulate matter of both natural and anthropogenic (human) origin that have complex interactions with atmospheric radiation, clouds, and chemistry. A complete understanding of aerosols is limited by the inability of satellite remote sensing instruments to consistently measure all of the aerosol optical parameters that are required to define their radiative effects. This is mainly because the retrieval of these parameters is often underdetermined, and because the aerosol optical signal is difficult to separate from other signals, such as surface reflection. However, a new class of instruments, called scanning polarimeters, have the potential to vastly improve orbital retrieval of aerosol optical properties. These instruments use multiple angles, spectral bands and polarization states, to provide measurements with maximized information content that can differentiate aerosols from other scatterers.

This research is an investigation of the aerosol retrieving potential of scanning polarimeters that uses data collected by the Research Scanning Polarimeter (RSP) during several field campaigns. The RSP is the airborne prototype of the Aerosol Polarimetry

Sensor (APS), soon to be launched into orbit as part of the NASA Glory orbital mission. Field campaign data have already been used to verify the capability of RSP (and APS) to retrieve aerosol properties in cloudless areas over the ocean and land surfaces. Here I have continued that work, and investigate the potential for aerosol property retrieval in more complicated scenes, such as aerosols lofted above clouds or extremely large aerosol loads near forest fires. As part of this, I constructed an automated aerosol and cloud retrieval technique that combines a first-principles based atmospheric radiative transfer model with the Levenberg-Marquardt nonlinear optimization approach. This method retrieves optical parameters and quantifies their uncertainties, which provide an assessment of optimization success. The software is very flexible, and was also used to determine the sensitivity of the RSP measurements to various parameters that determine atmospheric radiative transfer.

The retrieval software is applied to investigate two scenarios. The first analysis is of data collected near an extremely optically thick and weakly absorbing forest fire smoke (aerosol) plume in northern Canada. This well characterized plume is used to test the importance of assumptions about aerosol vertical distribution during retrieval. It also allows for an evaluation of simple approaches to merging aerosol vertical profile data from remote sensing instruments. A second study is performed for aerosols suspended above clouds, evaluating the theoretical feasibility of these observations, and then applying the method to data from a particular field campaign. This scene involved aerosols originating in central Mexico suspended over low altitude marine stratocumulus clouds in the Gulf of Mexico. These studies will guide both operational APS algorithms and the design of future aerosol remote sensing instruments.

An additional component of this thesis is an examination of the capability of RSP and APS instruments to estimate the surface bidirectional reflectance distribution function (BRDF) across the solar spectrum, and therefore constrain the surface radiation balance. The retrieved BRDF can also be used to validate similar products from other instruments that will have higher spatial resolution and global coverage than APS, but poorer angular sampling, such as the NASA Moderate Resolution Imaging Spectroradiometer (MODIS)

instrument. The BRDF and broadband albedo are estimated using RSP data collected in central Oklahoma, and a good agreement is found with both direct surface measurements and MODIS remote sensing observations.

Table of Contents

1 Introduction **1**

1.1 Aerosols and Climate 5

1.1.1 Types of Aerosols 5

1.1.2 Aerosol climate impacts 10

1.1.3 Aerosol climate modeling 14

1.2 Aerosol Observation 16

1.2.1 Orbital instrument history 17

1.2.2 The advantages of polarization for aerosol remote sensing 19

1.2.3 RSP and APS 21

2 Background **24**

2.1 Polarization 25

2.2 Observation units 27

2.3 Atmospheric single scattering 28

2.3.1 Rayleigh Scattering 30

2.3.2 Lorenz-Mie scattering 32

2.4 Surface reflectance 35

2.5 Multiple Scattering 39

2.6 Optimal estimation 40

2.7 Error characterization and information content analysis 46

3 **Combined retrievals of boreal forest fire aerosol properties with a Polarimeter and Lidar** **51**

3.1 Introduction 52

3.2 Method 54

3.2.1 RSP instrument specifics 54

3.2.2 ARCTAS and data selection 56

3.2.3 Optimization Approach 58

3.2.4 Validation data 71

3.3 Results 75

3.4 Discussion 79

3.5 Conclusion 86

3.6 Appendix 88

4 **Simultaneous retrieval of aerosol and cloud properties during the MILAGRO field campaign** **99**

4.1 Introduction 100

4.2 Method 104

4.2.1 AAC scene 107

4.2.2 Aerosol sources 108

4.2.3 Determination of initial cloud size distribution 110

4.2.4 Optimization 111

4.3 Simulated aerosol above cloud 113

4.4 Results 117

4.4.1 Cloud properties 117

4.4.2 Aerosol and cloud simultaneous retrieval 117

4.4.3 Comparison with other observations 120

4.4.4 Model uncertainty 121

4.5 Discussion 124

4.6 Conclusions 127

4.7 Appendix: Correlation in simulations 128

5 Surface BRDF estimation from an aircraft compared to MODIS and ground estimates at the Southern Great Plains site 138

5.1 Abstract 138

5.2 Introduction 139

5.3 Background 143

5.3.1 Albedo, BRDF, and other definitions 143

5.3.2 Ross-Li BRDF kernel models 145

5.3.3 Instrument description 147

5.4 Method 152

5.4.1 RSP data preparation 152

5.4.2 MODIS data preparation 164

5.4.3 BEFLUX data preparation 166

5.4.4 Albedo parameterizations 167

5.5 Results 168

5.5.1 RSP model fitting results 168

5.5.2 BHR (white-sky albedo) 170

5.5.3 DHR (black-sky albedo) 170

5.5.4 Remote sensing, ground radiometer and parameterization comparison 174

5.5.5 Azimuth angle independence 175

5.6 Discussion 178

5.7 Conclusion 181

5.8 Appendix 182

5.8.1 Correction for gas absorption 182

5.8.2 Vegetation Indicies 184

6 Conclusion **185**

6.1 Future work 188

7 Symbols and Acronyms **194**

List of Figures

1.1 Aerosol climate effects 11

2.1 Doubling / Adding geometry 41

3.1 Data location 56
3.2 Example optimization 70
3.3 RSP results compared to in situ observations 93
3.4 Aerosol optical thickness comparison 94
3.5 'Successful' and 'unsuccessful' minimization comparison 95
3.6 Size distribution comparison 96
3.7 'Successful' and 'unsuccessful' minimization phase function comparison . 97

4.1 Multi-angle polarization sensitivity to clouds and aerosols 130
4.2 Aerosol above cloud scene 131
4.3 Descending spiral vertical profile 132
4.4 Emission sensitivity footprint 133
4.5 Simulated AAC retrieval error 134
4.6 Cloud droplet size determination 135
4.7 Optimization results for AAC scene 135
4.8 Spectral aerosol optical thickness and single scattering albedo 136

5.1 ARVI Histogram 155
5.2 Imagery and classification results 157

5.3 Average degree of diagonal dominance of iteration matrix for multiple surface-atmosphere scattering 162
5.4 MODIS reflectances from September 16th, 2005 165
5.5 RSP and MODIS BRDF approximation 169
5.6 Bihemispherical reflectance (white-sky albedo) 171
5.7 MODIS and RSP DHR 173
5.8 MODIS and RSP normalized DHR 174
5.9 DHR comparison 176
5.10 Relative Azimuth angle comparison 177
5.11 BEFLUX fit comparison 180

List of Tables

1.1 Orbital aerosol observing instruments 18

3.1 Retrieved aerosol parameters and the initial values used in optimization . . 89
3.2 Derived aerosol parameters 90
3.3 Directly retrieved aerosol parameters 90
3.4 Derived aerosol parameters 91
3.5 Retrieved aerosol results for validation data 92
3.6 Error Components 94
3.7 Percent error for the segment 170 retrieval with HSRL data 95
3.8 Retrieval segment location, time, and solar and instrument geometry 96

4.1 Retrieved aerosol parameters and the a priori values used in optimization . . 107
4.2 Geometry and other parameters associated with the AAC scene 109
4.3 Retrieved aerosol and cloud parameters 119
4.4 Retrieval sensitivity to model perturbations 121
4.5 Simulated scene correlation matrix for all angle retrievals 128
4.6 Simulated scene correlation matrix for side scattering angle retrievals . . . 129

5.1 Low altitude ALIVE flight segments used for surface characterization . . . 153
5.2 Lucht et al. [2000b] DHR parameters 164
5.3 Wang et al. [2007] albedo parameters 168
5.4 BHR from RSP, MODIS and the Wang et al. [2007] parameterizations . . 172
5.5 Gas absorption parameters 183

Acknowledgments

I have been fortunate to be associated so many wonderful people throughout graduate school. First, I am deeply indebted to my thesis advisor, Brian Cairns. I am grateful for his patience with me as I found my way, and lucky to work with somebody who knows something about almost everything. I am also thankful to Barbara Carlson, Lorenzo Polvani and Adam Sobel, who had faith in me from the beginning. I sincerely appreciate the efforts of Faye McNeill and Knut Stamnes, who served on my thesis committee, and David Keyes and Michael Mauel for participating on other examination committees. Thanks to my colleges Mikhail Alexandrov, Jacek Chowdhary, Will Martin, Matteo Ottaviani and Fabien Waquet, who beyond our scientific discussions helped me maintain a realistic perspective and have fun. To my friends and fellow students, Allegra, Avi, Braxton, Chad, Christy, Jen, Jeremy, Jing, Joy, Kirstie, Michael, Matt, Melinda, Pratap, and Sonali, you have made it worthwhile and I am both sad and proud to see us scatter to the ends of the earth. Thanks to Giulietta Fargion, Chuck McClain and Bryan Franz who pushed me to return to graduate school and encouraged me when I was worried I would not make it. Of course, I would not have been able to take the first steps of this without the continual love and support of my parents, Ernie and Mary, and my brother, Eric, his wife, Deanna, and their children, Nathan and Connor.

Deployment of scientific instrumentation in the field involves many people, whom I hope to properly acknowledge here. I would like to thank Andy Korb, Edgar Russell and Larry Weaver, the RSP and APS instrument engineers. The B-200 aircraft was flown as part of the ARCTAS field campaign, and I am grateful to the efforts of the B-200 pilot, Les Kagey, aircraft crew chief Dale Bowser and the rest of the B-200 support team. The J-31 aircraft was flown during the ALIVE and MILAGRO field campaigns, and I would like to thank the pilot, Ben Hovelman, and Rose Dominguez, who provided navigational data. NASA was a source of funding for all three field campaigns, and personally through the NASA Glory project for most of my graduate studies. I was also a grateful recipient of an

IGERT fellowship from the National Science Foundation. Finally, I acknowledge sources of other data, such as the NASA GSFC Rapid Response System and the Atmospheric Radiation Measurement (ARM) Program of the Department of Energy.

E, naturalmente, Barbara. Non so come ringraziarti per tutto quello che hai fatto per me.

in memory of Alison

Chapter 1

Introduction

Anthropogenic changes to the global climate system can be described in terms of radiative forcing (RF), which is the energy balance of incoming and outgoing radiation. Aerosols are particulate matter in the atmosphere that have a highly uncertain RF, especially when compared to that of greenhouse gases. The Fourth Assessment Report of the Intergovernmental Panel on Climate Change (IPCC) finds anthropogenic aerosol RF to be between -0.4 and -2.7 w/m^2, with a 'low' to 'medium-low' level of scientific understanding. RF is defined as a globally averaged flux change due to modification of a component of the atmosphere. In contrast to aerosols, the RF for long-lived greenhouse gases (LLGHG) is between 2.07 and 2.53 w/m^2, with a 'high' level of scientific understanding (IPCC [2007]). There are several reasons for the low level of scientific understanding of aerosols. Aerosols are heterogeneous, and have a wide range of physical and chemical compositions, optical properties, sources and sinks. They interact radiatively with the climate directly (by scattering and/or absorbing radiation) and indirectly (by influencing atmospheric chemistry and clouds, which scatter and absorb radiation). They tend to persist in the atmosphere for much shorter periods than LLGHG's, and so have strong regional, rather than global, influence. The sole exception are volcanic aerosols (due primarily to sulfur dioxide) that are injected into the stratosphere, where they persist for years and therefore have significant global climate effects (Hansen et al. [1998], Hansen et al. [2002], Hansen et al. [2005]).

To predict the climate, we require global models that can simulate the entire system to

determine the effects of various anthropogenic forcings. Because of this global scale, orbital remote sensing instruments are needed to properly inform and verify climate models. However, the current set of remote sensing instruments are unable to consistently measure all the necessary aerosol parameters (Mishchenko et al. [2007b]). For example, in cloud free regions the Moderate Resolution Imager (MODIS) is capable of retrieving the aerosol optical depth (which is a measure of the decrease in atmospheric transmission) and a parameter related to particle size on a global basis (Remer et al. [2008]). While this is extremely useful, climate models also require the aerosol complex refractive index, bimodal size distribution, chemical composition, and the capacity for cloud interaction, among other parameters (Ghan and Schwartz [2007]). Much of the difficulty in determining all of these parameters is due to the limited information content available in orbital measurements. Because of this, retrievals of aerosol optical properties often require assumptions about the nature of those aerosols, and this explains some of the inconsistency that has been found in different satellite data sets (Mishchenko et al. [2009]).

Recently, several instruments have been constructed that provide a greater information content by utilizing polarization and multiple view angle observations, in addition to the multispectral capabilities of previous instruments. One such instrument is the Aerosol Polarimetry Sensor (APS) on the upcoming NASA Glory mission [Mishchenko et al., 2007a]. APS has nine spectral channels, with the shortest center wavelength at 410nm and longest at 2250nm. APS scans along the ground track, and observes a scene at about 250 viewing angles (between 60° forward and the limb aft of nadir). Furthermore, APS will observe the first three elements of the Stokes polarization vector, meaning it is sensitive to total and linearly polarized radiance. Prior to the launch of Glory, the Research Scanning Polarimeter (RSP) has been used to validate the aerosol and cloud retrieval potential of APS. The RSP is an airborne prototype of APS, and has very similar characteristics. Data collected during field campaigns by the RSP have been used to verify the ability of RSP and APS to retrieve aerosol optical properties over the ocean (Chowdhary et al. [2001], Chowdhary et al. [2002], Chowdhary et al. [2005a]) and over land (Elias et al. [2004], Waquet et al.

[2009a]) in the absence of clouds. These methods will be used to retrieve aerosol properties operationally with the APS when it is in orbit.

Aerosol property retrieval in cloud free regions is performed by current instruments on a global basis. The measurements made by the APS will dramatically increase the accuracy and quantity of retrieved parameters in the absence of clouds. This thesis is an exploration of the potential of RSP and APS observations to retrieve aerosol optical properties in other, more complex, scenes. The research is presented as a collection of peer-reviewed, or soon to be submitted, publications. Each publication describes the potential for additional types of information that can be extracted from RSP and APS. Chapter 3 describes an investigation of the retrieval capability of RSP and APS when the aerosols are very optically thick, absorbing, and vertically distributed in an inhomogeneous manner. This includes the use of lidar data to constrain the retrieval process, and involves observations of boreal forest fire smoke. Chapter 4 evaluates the potential for APS and RSP aerosol retrievals in the presence of clouds, specifically when aerosols are lofted over clouds. Aerosols above clouds are a highly uncertain component of the evaluation of the total radiative effect of aerosols, since aerosol forcing is dependent on the brightness of the underlying surface (Chung et al. [2005]), and few instruments are capable of observing them (Chand et al. [2009]). This chapter presents a method for simultaneous retrieval of aerosol and cloud optical properties with scanning polarimeters such as RSP and APS, and includes a sensitivity study and accuracy assessment for the method. Finally, RSP and APS can also be used to observe other geophysical parameters, such as surface reflectance. While the global coverage of an along track scanning instrument such as APS is limited, the high angular resolution of APS can be used to precisely determine the surface Bidirectional Reflectance Distribution Function (BRDF). Combined with accurate aerosol property retrieval, this can be used to validate global maps of surface reflectance. Chapter 5 is an example of this, where RSP observations were used to successfully validate MODIS retrievals at a site in central Oklahoma. This work also demonstrates that multi-view observations provide a good estimate of the surface albedo variation as a function of sun angle.

The remainder of this introduction presents the issue of aerosols in the global climate in more detail, including aerosol sources and types (section 1.1.1), and the ways they interact with climate (section 1.1.2). The present state of aerosol climate modeling is described (section 1.1.3), as is the history of global aerosol observation from space (section 1.2.1). The advantages of aerosol observation utilizing polarization are discussed next, followed by a full description of the RSP and APS instruments (sections 1.2.2 and 1.2.3).

The field of remote sensing pulls together several disparate sub-disciplines of physics, applied mathematics, engineering and environmental science. The research publications that constitute chapters 3 through 5 are intended for a specific journal audience and do not provide an adequate background and justification. Therefore, I have created an extensive background chapter (2) in order to address this inadequacy and provide a broader discussion of the current research state. Some of what is presented in the background may be redundant with portions of the research publications, but I felt it was best to leave those chapters intact as published. The background chapter includes an optical description of aerosols and the Stokes parameter formalism we use to describe polarized radiance (section 2.1). It then describes the methods I used to model atmospheric radiative transfer in both a single and multiple scattering context. I then describe how surface total and polarized reflectance is modeled. Finally, I describe the optimal estimation methods that are used to retrieve aerosol optical properties given observational data and a radiative transfer model. This includes a brief description of the Levenberg-Marquardt nonlinear optimization algorithm (LMA), the software that was created to implement this algorithm for RSP data, and the various tools I use to characterize the error and assess the information content in the system (section 2.6).

1.1 Aerosols and Climate

1.1.1 Types of Aerosols

Aerosols have both natural and anthropogenic sources, and a variety of processes control their creation, evolution and eventual removal from the atmosphere. Often, multiple types of aerosols are present at a location in the atmosphere at one time, each type with its own source, size distribution, optical properties, and potential for interaction with other aerosols, gases or clouds. As a result of such complexity, there is a rich literature describing the various aerosol types and their characteristics. Attempts have been made to identify and catalog major classes of aerosol types to define a climatology as far back as 1979 (Shettle and Fenn [1979]). More recent efforts, such as the Optical Properties of Aerosols and Clouds (OPAC) model generally identify about ten aerosol types (Hess et al. [1998]). These models are of simplified versions of geophysical reality, reflecting the limitations of observational capability and the quality and range of the data and literature that were used to construct them.

For our purposes, two distinctions should be made when describing aerosols. Since we are ultimately interested in anthropogenic modifications of climate, it is important to determine if the aerosols exist because of human activities. In some cases, such as fossil fuel combustion, the anthropogenic nature of aerosols is obvious, in others less so. For example, wind blown desert dust would generally be considered natural, but if humans have modified the surface hydrology by overgrazing livestock or diverting water runoff it becomes less clear. The second important distinction has to do with the aerosol size. Aerosols created by a mechanical processes, such as the aforementioned dust, tend to have diameters greater than 1 μm and are typically present in small quantities. These large particles are called the 'coarse' size mode. Aerosols created by chemical processes, such as combustion, have smaller diameters (between 100nm and 1 μm), and are typically present with much larger number concentrations. This aerosol mode is usually described as the 'fine', or accumulation, size mode when discussing atmospheric radiative transfer. Both

fine and coarse modes are usually present in a scene simultaneously, so aerosol retrievals typically assume bimodal size distributions with independent optical properties for each mode. Because of their size difference, fine and coarse mode aerosols tend to have dramatically different radiative properties, where coarse mode aerosols scatter radiation in a similar manner at a variety of wavelengths, while fine mode aerosol scattering increases as the observation wavelength decreases into the blue and ultra-violet. The only recent occasion when this bimodal paradigm was not valid globally for an extended period was after the eruption of Mount Pinatubo, when sulfuric acid aerosols in the stratosphere grew to a third, intermediate, size mode between typical fine and coarse size modes (Russell et al. [1993], McCormick et al. [1995]).

Several aerosol sources are briefly described below. These descriptions are not meant to be comprehensive, but rather to introduce the diversity of aerosol types and the implications that such diversity has for observations and modeling. A starting point for a more complete review of aerosols and their effects can be found in section 2.4 of the IPCC 4th assessment report (IPCC [2007]), or in observational classifications such as Dubovik et al. [2002].

1.1.1.1 *Maritime aerosols*

Maritime aerosols are comprised of sea salt that has been removed from the ocean by breaking waves and bursting bubbles. These coarse mode aerosols are wind driven and thus natural as long as one excludes wind changes due to anthropogenic climate change. Since they are hygroscopic, maritime aerosols can act as cloud condensation nuclei. Maritime aerosol sources are dispersed and significant sources are often located in very remote locations (such as the Southern Ocean). For this reason it has been difficult to verify the quantity of maritime aerosols that are observed by satellites with ground measurements. Recent efforts (Smirnov et al. [2009]) are improving the situation. Other examples of these types of aerosols can be found in Husar et al. [1997], Smirnov et al. [2002], Smirnov et al. [2003], and Knobelspiesse et al. [2004].

1.1.1.2 *Mineral aerosols*

Mineral aerosols are dust that has been lifted from areas of exposed soil, such as the Sahara, Arabian, Taklamakan and Gobi Deserts buy wind gusts. Their optical properties vary with the dominant minerals at the source. In some cases, dust aerosol loading can be quite large, and dust can be transported over large distances, such as from the Saharan Desert to South America (Prospero et al. [1981], Koren et al. [2006]) or from East Asia far into the North Pacific and over the west coast of North America (Duce et al. [1980]). Since they are created mechanically, dust aerosols usually have a size distribution that is predominantly in the coarse size mode. From a remote sensing standpoint, mineral aerosols are difficult to observe correctly, since they are often non-spherical (Sugimoto and Lee [2006]), meaning that radiative transfer methods that assume spherical particles will be incorrect (Mishchenko et al. [1995]). Like maritime aerosols, the amount of dust aerosols in the atmosphere is wind driven, and is also affected by land cover. Mineral aerosols can be considered natural if one excludes anthropogenic changes due to wind and land cover. Depending on the mineral source, dust can also be significantly absorbing, and the spectral dependence of this absorption usually leads to stronger absorption at ultra-violet (UV) compared to visible wavelengths (Bergstrom et al. [2007], McConnell et al. [2010]). Examples of dust aerosol optical property retrievals can be found in Smirnov et al. [1998], Wang et al. [2003], and Waquet et al. [2005]. The difficulties of estimating dust aerosol absorption mean that there continues to be substantial uncertainties in the effects of these aerosols on the radiative energy balance.

1.1.1.3 *Biomass burning aerosols*

Biomass burning is a chemically complex process that produces carbon containing aerosols. The two main components of biomass burning aerosols are particulate organic material, usually referred to as Organic Carbon (OC), and soot, or Black Carbon (BC). While BC is usually present in smaller amounts, it is very absorbing and potentially the source of a significant positive RF (Jacobson [2001], Hansen and Nazarenko [2004]). However, ra-

tios of OC and BC, along with other aspects of fire emissions, are extremely variable and related to fire strength, fuel type and moisture content, local meteorological conditions, and other factors. Furthermore, fires emit a variety of gas and particle phase Volatile Organic Compounds (VOCs) which through photochemical reactions and diffusion repeatedly condense into particles and evaporate into the gaseous phase (Donahue et al. [2009]). Biomass burning aerosols therefore age as a function of sunlight availability, dispersion rates, temperature, and other conditions (Abel et al. [2003], Grieshop et al. [2009]). To further complicate matters, some OC preferentially absorbs at shorter wavelengths. This so called ”Brown Carbon” (BrC) is not well characterized in terms of inherent optical properties, and is therefore difficult to confidently include in radiative transfer models (Andreae and Gelencser [2006], Sun et al. [2007] and Lewis et al. [2008]). The relationship between biomass burning aerosols and human activity is mixed, as forest fires can usually be considered natural (unless fire suppression efforts, or lack thereof, are taken into account), while agricultural fires, such as those set prior to sugarcane harvest, are anthropogenic. Aerosols generated by biomass burning are typically part of the fine size mode, and are small enough to be considered spheres if they have had a chance to age slightly (and thus collapse from carbon chains to a more compact form (Martins et al. [1998], Liu et al. [2008])). Because of the complexity of biomass burning in the environment, and its widespread occurrence, there is a rich literature describing these aerosols. Important review papers include Koppmann et al. [2005], Reid et al. [2005a], and Reid et al. [2005b], while observational examples can be found in Reid and Hobbs [1998], Remer et al. [1998], Wandinger et al. [2002], Mayol-Bracero et al. [2002], O’Neill et al. [2002], Eck et al. [2003], Mühle et al. [2007], and Yokelson et al. [2007].

1.1.1.4 *Urban-industrial aerosols*

Anthropogenic aerosols, produced by transportation, electricity generation, industrial emissions and other sources are primarily chemically produced and therefore part of the fine size mode. Generally, these aerosols are secondary, meaning that their precursors are emitted

as gases that react in the atmosphere and condense to particulate form. Often OC, BC and VOC's are part of the urban-industrial mix when fossil fuels are burned, as are sulfate aerosols. The latter is created by gaseous emissions of sulfur dioxide, which photo-oxidizes to form aerosols. Nitrate aerosols are also formed by reactions in the atmosphere, where the main precursors are ammonia and nitric acid (Bauer et al. [2007]). The presence of emissions controls and the varied efficiency of industrial combustion has a large effect on the relative contributions of different aerosol components and sources. Therefore, the prediction and modeling of these aerosol sources based upon inventories alone is challenging. To further complicate matters, reactions that create aerosols from gaseous precursors can also involve biogenic precursors, and are therefore dependent on both anthropogenic and natural sources. Examples of urban aerosol properties are found in a number of publications, including Remer et al. [1997], Wandinger et al. [2002], Chu et al. [2003], Mallet et al. [2003], Aiken et al. [2009] and Crounse et al. [2009].

1.1.1.5 *Biogenic and dimethylsulphide aerosols*

Other than the aerosols listed above, there are several types of natural aerosols that are the result of emissions of various plant or algal gaseous aerosol precursors. Oceanic algae emit dimethylsulphide (DMS), which condenses in the atmosphere to form a sulfate aerosol. Aerosols created by this process may seed clouds, particularly in remote regions of the ocean, and therefore modify the amount of shortwave solar radiation reaching the surface, which is a potential climate feedback that was first recognized more than twenty years ago (Charlson et al. [1987]). In addition, land based plants emit VOC's, which contribute to the formation and growth of Secondary Organic Aerosols (SOA) (Andreae and Crutzen [1997], Helmig et al. [2006], and Hallquist et al. [2009]).

1.1.1.6 *Volcanic aerosols*

Volcanoes can be a source of ash and sulfur dioxide. The latter, as described above, creates sulfate or sulfuric acid aerosols, which grow into a larger size mode than the 'fine'

component due to a lack of aerosol removal mechanisms in the stratosphere. Compared to anthropogenic aerosols, volcanic aerosols have a limited regional impact (Mather et al. [2003], Grutter et al. [2008], de Foy et al. [2009]). However, the climate impact can be significant if the sulfur dioxide is injected high into the tropical stratosphere during a particularly strong volcanic eruption. These aerosols persist for years rather than weeks, due to the weakness of removal mechanisms and large scale circulation factors in the stratosphere (such as Brewer-Dobson circulation, which transfers tropically injected aerosols globally (Salby [1996])). A notable example was the eruption of Mt. Pinatubo in the Philippine island of Luzon in 1991. The quantity of sulfur dioxide that Pinatubo injected into the stratosphere was significant, and reduced the global mean temperature at the surface for several years (Hansen et al. [1992], Minnis et al. [1993], McCormick et al. [1995]).

1.1.2 Aerosol climate impacts

For a number of reasons, aerosols are a much more uncertain component of the global climate than greenhouse gases. As described above, they have a variety of sources and optical properties. Depending on size and local meteorology, most aerosols are suspended for days to weeks in the troposphere. This contrasts with greenhouse gases, which persist for decades or centuries, and therefore have a nearly uniform global distribution. The short lifetime of aerosols means that their impacts are highly regional, and tend to vary dramatically in both space and time. This variability is the main reason the global sampling provided by satellite observations is required. To further complicate matters, aerosols interact with climate in many ways. Figure 1.1, from chapter 2 of IPCC [2007], is a diagram of some of the most important aerosol climate effects. This section will briefly describe these effects, and what aerosol properties are required to understand the magnitude of those effects. A more detailed review of this topic can be found in Haywood and Boucher [2000], and in the IPCC [2007] fourth assessment report.

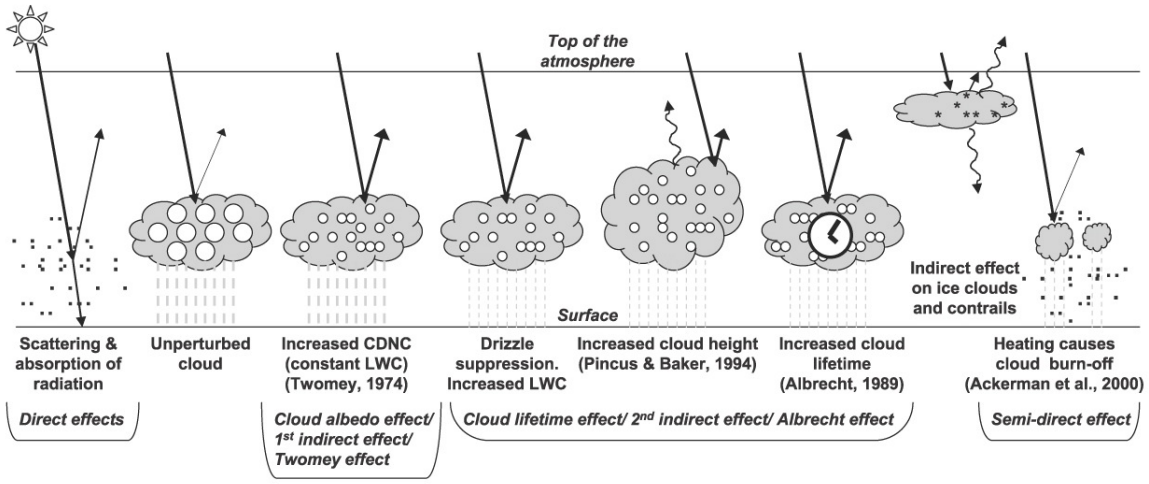

Figure 1.1: This figure, taken from chapter 2 of IPCC [2007], expresses the different ways aerosols can interact with climate, and is a modification of what was originally presented in Haywood and Boucher [2000]. Straight arrows indicate shortwave solar radiation, while wavy arrows are long wave radiation. Aerosol particles are the filled black dots, cloud water droplets are open circles, and black stars represent cloud ice. Dashed vertical grey lines are precipitation. Acronyms used in the description are cloud droplet number concentration (CDNC) and liquid water content (LWC).

1.1.2.1 *Direct effects*

Aerosols reflect and absorb shortwave solar radiation and prevent it from reaching the surface. Generally, this creates a negative radiative forcing, but it is dependent on aerosol optical properties. Important aerosol properties are the optical depth, τ, which is a measure of the quantity of extinction due to aerosols in the atmospheric column, the single scattering albedo, ϖ, which is the fraction of extinguished light that is scattered, and the scattering phase function, P, which describes the scattering directional dependence (these parameters will be described in more detail below). Since aerosols are easiest to observe in cloud free regions and this effect is rather simple, it is commonly simulated and understood to a much greater degree than other aerosol climate effects, although differences remain (Myhre [2009]).

Aerosol direct effects can create a positive radiative forcing if the aerosols are absorbing ($\varpi < 1$), but both the magnitude and sign of this forcing is also dependent on the reflectance of the surface beneath the aerosols (Haywood and Shine [1995]). The potential for positive radiative forcing from absorbing aerosols increases as the surface beneath the aerosol brightens. For this reason, the direct radiative effects of absorbing aerosols above clouds are particularly important. Unfortunately, the presence of clouds prevents aerosol property retrieval by most passive sensors. Retrieval of aerosols above clouds is a topic discussed later in this thesis (chapter 4), since the polarized observations of RSP and APS have the potential to make these observations.

1.1.2.2 *First indirect effect*

Aerosols modify cloud formation by becoming cloud condensation nuclei. This occurs because less energy is required for condensation to form on an existing surface than it is to spontaneously create a pure water droplet. Changes in the number of surfaces available for condensation can alter the optical properties of a cloud. An increase in the number of the available cloud condensation nuclei (CCN) acts to increase the total cloud droplet surface area for a given quantity of water, and thus the cloud optical thickness. This ef-

fect, also called the Twomey effect to honor the author of the original papers describing it (Twomey [1974], Twomey [1977]), acts to increase the cloud albedo and reflect more shortwave radiation. The result is a negative radiative forcing. Simulation of this effect requires an understanding of the number, size and solubility of potential CCN, along with the dynamical factors that control droplet formation, such as updraft strength and peak water vapor super-saturation. Like all aerosol indirect effects, the first indirect effect is highly nonlinear, and estimates of the radiative forcing magnitude associated with it vary depending on aerosol quantity, cloud type and model assumptions. Although there have been observational studies of the first aerosol indirect effect (Feingold et al. [2003]), most of the published work on aerosol indirect effects is based on models (Ackerman et al. [2000], Menon et al. [2002]).

1.1.2.3 *Second indirect effect*

Increasing droplet number and decreasing the cloud droplet size also modifies other cloud properties. Smaller particles are less likely to fall as precipitation, which in turn increases cloud lifetime (Albrecht [1989]), liquid water content (LWC), and cloud top height (Pincus and Baker [1994]). Each of these factors contribute to a negative radiative forcing, as longer lived clouds increase the mean global albedo, clouds with a higher LWC are more reflective, and physically thicker clouds absorb more emitted long wave radiation (Ramanathan et al. [2001], Lohmann and Feichter [2005]). Since these changes are dependent on the same modifications that create the first indirect effect, simulations require the same knowledge of aerosol and cloud properties.

1.1.2.4 *Indirect effects on ice clouds and contrails*

There are two main ways aerosols impact the formation and properties of cold (ice) phase clouds. Jet aircraft exhaust, which is warm and moist compared to surrounding cold and dry upper troposphere air, condenses to form ice phase contrails. The existence of these anthropogenically generated clouds does have a climate impact (Boucher [1999]), but the

role of aerosols on their generation and optical properties is still uncertain (Lohmann and Feichter [2005]). Anthropogenic aerosols such as soot can act as Ice Nuclei (IN) for the formation of cirrus clouds, increasing cloud optical thickness, lifetime and vertical distribution. Anthropogenic RF due to this effect is very dependent on the background availability of IN. Furthermore, the temperature at which these particles become IN depends on particle composition and size (Lohmann and Hoose [2009]). Observations of Mt. Pinatubo aerosols show a rather minimal impact on cirrus clouds (Lohmann et al. [2003]), although mechanisms exist for a strong influence in some scenarios (Lohmann and Feichter [2005]).

1.1.2.5 *Semi-direct effect*

Absorbing aerosols modify the atmospheric temperature profile, which can act to modify the presence of clouds. As an example, Ackerman et al. [2000] simulated trade cumulus clouds to show how they are cleared by the presence of absorbing aerosols such as would be encountered over the northern Indian Ocean during the northeast monsoon. This cloud clearing reduces the globally averaged albedo and would therefore be a positive RF. However, the impact of absorbing aerosols depends on their altitude and the local meteorological conditions. Koch and Del Genio [2010] found that absorbing aerosols within a cloud layer act to decrease the quantity of clouds, while aerosols underneath the cloud generally act to enhance convection and increase cloud cover. Absorbing aerosols above clouds increase the stability of the temperature profile, with varying effects for different cloud types. In global simulations investigating the semi-direct effect, the net RF was negative.

1.1.3 Aerosol climate modeling

A primary goal of aerosol remote sensing is to assist in the improved treatment of aerosols in global climate models through the imposition of robust constraints on aerosol loading, type and size. Models are essential if we are to identify and predict anthropogenic modifications to climate (Penner et al. [1994]). However, inclusion of aerosols in existing climate models is an evolving process, since most aerosol quantities and effects are prescribed from

offline simulations or parameterizations. Current climate models, in this context, are those that were used for the 4th assessment report of the IPCC (IPCC [2007]). These include the NASA Goddard Institute for Space Studies ModelE (Schmidt et al. [2006]), the National Center for Atmospheric Research CAM3 (Collins et al. [2006]), and the NOAA Geophysical Fluid Dynamics Laboratory CM2.1 (Ginoux et al. [2006]). Ghan and Schwartz [2007], in their review of current aerosol modeling capability, call these 4th generation models. 5th generation models are those that will be used for the 5th assessment report of the IPCC, and so on for subsequent generations.

In 4th generation climate models, only sulfate aerosol concentrations are created interactively in the model, whereas maritime, OC, BC and mineral aerosols are prescribed from offline simulations. Optical properties for each aerosol type are also prescribed. In 5th generation models aerosols will be generated by wind speed and soil moisture for maritime and mineral aerosols, and DMS aerosol precursors will depend on wind speed. Aerosol activation in 4th generation models is prescribed for each aerosol type, whereas in 5th generation models activation is parameterized in terms of updraft velocity and aerosol type. In both of these model generations, many aerosol evolution and removal processes are either neglected or highly simplified (Ghan and Schwartz [2007]). It is clear that climate models are only beginning to capture the geophysical complexity of aerosols.

Accurate observations of aerosols are required to properly quantify their direct and indirect effects. Mishchenko et al. [2004] describe the accuracy requirements that are the guidelines for the APS instrument, which is intended to gather data that will provide effective constraints on the components in aerosol models. As mentioned previously, modeling of aerosol direct effects will require global measurements of the aerosol optical thickness, τ, the single scattering albedo, ϖ and the scattering phase function, P for each aerosol mode. These, in turn, require observations of aerosol size, complex refractive index and shape. Quantification of the indirect effect requires information about both cloud and aerosol properties. Necessary cloud properties are the cloud albedo, droplet size, droplet number concentration and liquid water path, while number concentration, size and solubility

are required for aerosols.

1.2 Aerosol Observation

As mentioned previously, aerosols are currently included in climate models in a relatively simplistic manner, although this is changing rapidly (Bauer et al. [2010]). A major issue for the evaluation of aerosols in climate models is the limited accuracy and scope of global measurements of all the aerosol properties required for climate modeling. Generally speaking, the primary observed aerosol parameter is the optical depth. Optical depth has been observed from orbit for three decades by the Advanced Very High Resolution Radiometer (AVHRR) series of instruments (Ignatov and Stowe [2002], Mishchenko et al. [2007c]). However, even observations of this most basic parameter by the latest generation of instruments are sometimes inconsistent (Remer et al. [2006], Liu and Mishchenko [2008], Mishchenko et al. [2009]), especially over land surfaces. Furthermore, optical depth is only a measure of the total aerosol extinction, and does not differentiate between aerosol types and optical properties to the degree required by climate models (Mishchenko et al. [2007b]). Parameters that aid aerosol species differentiation, such as the Angström exponent (which expresses the spectral variation in optical thickness and is related to particle size), are even more inconsistent. The primary reason for the absence of better size and species products from current sensors is the need to estimate between ten and twenty aerosol parameters in each scene. Since current sensors usually have ten or fewer measurements for any given scene and these measurements are not independent, parameter estimation is indeterminate and requires a significant number of assumptions. These assumptions are not always transparent in the retrieval algorithm, or well justified by observation or models.

In this section I will provide a brief outline of the history of orbital observations of aerosol properties in order to provide insight into the design of next generation instruments such as the APS. Polarization is a primary component of the APS observational strategy, so

the basis of this approach will then be described. Finally, the details of the APS and RSP instruments will be described and compared.

1.2.1 Orbital instrument history

Aerosol measurements from orbit began in the late 1970's with the Advanced Very High Resolution Radiometer (AVHRR) and Total Ozone Mapping Spectrometer (TOMS) instruments, which use one or two nadir viewing channels to retrieve optical depth and Angström exponent. The AVHRR algorithms can only be applied over dark surfaces, such as the ocean (Husar et al. [1997], Mishchenko et al. [1999], Ignatov and Stowe [2002] and other references described in table 2.2 in IPCC [2007]). Since AVHRR, aerosol observing instruments have improved by increasing the quantity of information measured in each scene so that retrieval algorithms require fewer assumptions about aerosol properties. For example, newer single view angle instruments, such as the Sea-Viewing Wide Field-of-View Sensor (SeaWiFS, launched in 1997) and the Moderate Resolution Imaging Spectrometer (MODIS, two instruments launched in 1999 and 2002) utilize higher spatial resolution, better calibration and more spectral channels to retrieve more accurate optical depths and Angström exponents (Tanré et al. [1997], Remer et al. [2005], Wang et al. [2005] and other references described in table 2.2 in IPCC [2007]). Even more information is gathered with the multiple view angle Multi-angle Imaging Spectro-Radiometer (MISR, launched in 2000) which uses nine viewing angles and four spectral channels (Kahn et al. [2001], Kahn et al. [2005]). POLDER (Polarization and Directionality of the Earth's Reflectances) was the first instrument to utilize both multiple view angles and linear polarization. The first POLDER instrument was launched in 1996, but the spacecraft failed in 1997. Unfortunately, a second launch in 2003 also failed within a year. Nevertheless, POLDER was able to retrieve more detailed aerosol information than previous efforts, particularly over land (Deuzé et al. [2000], Deuzé et al. [2001]). A third, and to date successful, satellite called the Polarization and Anisotropy of Reflectance for Atmospheric Sciences coupled with Observations from a Lidar (PARASOL), was launched in 2004 (Fougnie et al. [2007]).

PARASOL carries a version of POLDER that is very similar to earlier instruments. Table 1.2.1 briefly lists the main characteristics of these instruments, along with the capabilities of RSP and APS.

Table 1.1: This table contains characteristics of the primary aerosol observing orbital instruments currently in orbit and the RSP and APS. For more details, see the references cited in section 1.2.1. Note that the ability to observe the I,Q, and U components of the Stokes polarization vector (see section 2.1) means that total and linearly polarized reflectances are detectable. POLDER does so with limited accuracy, while RSP and APS have a polarization accuracy of 0.2%.

Instrument	Visible Bands	Infrared Bands	View angles	Polarization
AVHRR	0.6-0.9μm	3.7μm	1	no
MODIS	0.47-0.86μm	1.24, 1.64, 2.12 μm	1	no
MISR	0.44-0.86μm	none	9	no
POLDER	0.44-0.86μm	none	14	I,Q,U
RSP	0.41-0.865μm	0.96, 1.59, 1.88, 2.25μm	150	I,Q,U
APS	0.41-0.865μm	0.91, 1.37, 1.59, 2.25μm	255	I,Q,U

UV observations have a very different aerosol sensitivity compared to measurements in the visible and NIR. Furthermore, surface reflectance is both low and stable in this spectral range. At these wavelengths, aerosol optical depth, vertical distribution and absorption significantly modify the Rayleigh (molecular) scattering contribution, and this modification is highly dependent upon the quantity of aerosol absorption. The low surface reflectance and strong sensitivity to aerosol absorption has been used to develop algorithms for TOMS and several other other similar instruments (Torres et al. [2007]). These algorithms have some accuracy limitations in terms of absorption and optical depth, but do provide for a tracking of the seasonality and variability of absorbing aerosols over the last three decades.

A more recent observing strategy has been to place several instruments in a similar orbit. This allows near-simultaneous observations of the same location, and provides potential for aerosol retrievals that are constrained by multiple sources of information (Anderson et al. [2005]). The primary orbit of this type is the so-called 'A-Train' low earth polar orbit. Four satellites are currently part of A-Train, and they carry several instru-

ments useful for studies of aerosols. This includes one of the MODIS instruments and the Ozone Monitoring Instrument (OMI), which has similar characteristics to TOMS (Torres et al. [2007]). PARASOL was a part of the A-Train orbit until the start of 2010, when it depleted the fuel it used to maintain its position within the A-Train and was moved to a safer orbit farther from other satellites. The A-Train also includes the Cloud-Aerosol Lidar and Infrared Pathfinder Satellite Observations (CALIPSO) satellite. CALIPSO carries the Cloud-Aerosol Lidar with Orthogonal Polarization (CALIOP), which is an active (Lidar) sensor. CALIOP is able to retrieve a different set of aerosol parameters than the instruments described previously, with a particular focus on vertical distribution of aerosols and clouds (Winker et al. [2004], Winker et al. [2007]). The A-Train is also the destination for the NASA Glory satellite and the APS it carries.

1.2.2 The advantages of polarization for aerosol remote sensing

Instruments that observe the polarized solar reflectance from orbit have several distinct advantages over instruments that only measure total reflectance. Polarized observations provide additional information that can be used to distinguish aerosol optical properties (Mishchenko et al. [2002]). Polarization also makes it easier to differentiate the effects of aerosols from other components of the radiative transfer system as observed at the top of the atmosphere (Cairns et al. [2009]). Compared to radiance only observations, polarized observations are more capable of distinguishing aerosols from reflecting surfaces underneath, such as the ocean, land or cloud layers. For this reason, polarized observations have the potential to retrieve aerosol properties more accurately than observations with radiance alone.

In the case of aerosol retrievals over the ocean, the observed polarized reflectance component at the sensor has only a small contribution from water leaving radiance when compared to total reflectance for blue and green wavelengths. Polarized observations can therefore be used to identify the aerosols above the water after a trivial correction is made for polarized water leaving radiance (Chowdhary et al. [2002]).

Aerosol retrievals over land must account for the contribution of the surface reflectance to the observation at the top of the atmosphere. For single view angle observations of total reflectance (such as with AVHRR or MODIS) this reflectance cannot be determined by instantaneous observations alone and must be assumed. This of course significantly degrades the capability of such retrievals and is the reason instruments such as MODIS do not attempt retrievals over bright land surfaces (such as deserts). This problem can be alleviated by the use of multi-temporal observations, which can separate the surface and atmospheric contributions to observed radiance to some degree (Hsu et al. [2006]). Instruments that observe with multiple view angles, such as MISR, are capable of simultaneously retrieving aerosol and surface properties over bright surfaces, albeit with larger uncertainties than over dark surfaces (Martonchik et al. [2002]). However, simulations show that these retrievals are underdetermined, and the uncertainty in the retrieved aerosol properties is too large for the requirements of climate models (Hasekamp and Landgraf [2007]). The same simulations show that multi-angle polarized observations do have enough information to accurately retrieve aerosol and surface properties. This is mainly because surface polarized reflectance, unlike total reflectance, tends to be spectrally grey. Thus multiple wavelength observations can distinguish between spectrally invariant surface effects and spectrally variable aerosols. This strategy has been used by POLDER (Leroy et al. [1997], Nadal and Breon [1999], Deuzé et al. [2001] and Herman et al. [1997]). RSP and APS take this method a step further. Observations from these instruments have channels in the near infrared (the longest at $2.25\mu m$), where aerosol scattering is minimal and measurements can be considered to provide direct observations of the surface reflectance properties. Since the polarized component of that surface is nearly spectrally invariant (the minimal polarized reflectance at solar backscattering angles direction does vary with wavelength), these observations can be used to constrain surface polarized reflectance at shorter wavelengths that are used to retrieve aerosol optical properties (Cairns et al. [1997b], Elias et al. [2004], Cairns [2003], Cairns et al. [2009], Waquet et al. [2009b], Waquet et al. [2009a], and Litvinov et al. [2010]).

Another important feature of observations of polarized reflectance is that they only represent interactions with the first few optical depths within a medium. For this reason, measurements of polarized reflectance above a cloud are insensitive to cloud optical depth for all but the thinnest of clouds (Breon and Goloub [1998]). This reduction of parameters affecting a scene means aerosols suspended above (warm phase) clouds can be retrieved, provided the polarized observations are of sufficient angular resolution and range to both observe the cloud bow (whose shape is determined by cloud droplet size) and the side scattering angles (determined largely by aerosols) (Goloub et al. [2000]). Attempts have been made to retrieve aerosol optical properties above clouds with POLDER (Waquet et al. [2009c]), but those efforts were limited by the coarse angular sampling of that instrument. RSP and APS, however, have a much higher angular resolution, and are capable of retrieving aerosol and cloud parameters simultaneously. A test of this technique for a scene with RSP data is the topic of chapter 4 in this thesis.

1.2.3 RSP and APS

The Aerosol Polarimetery Sensor (APS) on the NASA Glory mission is the next step in the technological progression of aerosol remote sensing instruments. Glory has a launch date in the spring of 2011. Like POLDER, APS has multiple view angles and the ability to measure the first three elements of the Stokes polarization vector. However, APS has many more view angles than the POLDER instrument, several channels in the near infrared, and a high (0.2%) degree of polarization accuracy.

The research in this thesis was performed using data from the airborne prototype of the APS, the Research Scanning Polarimeter. The RSP, which is mounted in a downward looking position in small aircraft, was deployed in a variety of field campaigns intended to test the measurement capability of instruments like the APS. Chapter 3 is based on data that were collected during the Arctic Research of the Composition of the Troposphere from Aircraft and Satellites (ARCTAS) field campaign. During ARCTAS, the RSP was mounted on the NASA B-200 aircraft, which was based in Yellowknife, Northwest Territories, Canada,

during June and July of 2008. Chapter 4 used data from the Megacity Initiative: Local and Global Research Observations (MILAGRO) field campaign, based in Veracruz, Mexico during the spring of 2006. Finally, chapter 5 uses data collected during the Aerosol Lidar Validation Experiment (ALIVE), based in Ponca City, Oklahoma, USA in September of 2005. The RSP was installed on the Sky Research Inc. J-31 aircraft during the latter two field campaigns.

A brief outline of the main characteristics of APS and the RSP follows. See Mishchenko et al. [2007a] for more details on the APS instrument.

- *Spectral bands*: The APS has nine narrow spectral window optical channels, with center wavelengths of 410, 443, 555, 670, 865, 910, 1370, 1620 and 2250nm. Center wavelengths for RSP are nearly the same, at 410, *470*, 555, 670, 865, *960*, *1590*, *1880* and 2250nm. Italicized values indicate RSP differences from APS.

- *Observation method*: Telescopes scan in the direction of instrument motion to view the atmosphere from a range of angles (about $+60°$ to $-60°$ from the nadir direction). Neither RSP nor APS are imaging instruments, as each scan is a single pixel wide. Wollaston prisms are used to split the incoming radiation in each telescope into orthogonal components. Since each component is observed simultaneously using identical optics, the polarized reflectances they represent are easily calibrated and very accurate.

- *Polarization*: Both instruments measure the first three components of the four element Stokes polarization vector (see section 2.1 for more details about the Stokes polarization vector). This means the total reflectance and the magnitude and direction of linearly polarized reflectance are observed. The fourth element of the Stokes vector, which is unobserved, represents circular polarization and is not expected to be significant for observations of reflected sunlight (Kawata [1978]).

- *Accuracy and calibration*: Both RSP and APS have a high (0.2%) absolute accuracy for the polarized reflectance, as the primary calibration for this measurement is the relative gain of the detectors observing orthogonal polarization and is performed with each scan. As mentioned above, this accuracy is possible because observations of the polarized components are simultaneous.

- *Angular resolution*: APS has a rotation rate of 40.7 revolutions per minute and an 8mrad instantaneous field of view (IFOV). About 250 un-vignetted observations are

performed for each scene. RSP has a rotation rate of 71.3 revolutions per minute and an 14mrad IFOV, and makes about 140 samples per scene.

- *Position*: The APS will be launched into the A-Train polar orbit. The A-Train orbit is ascending and has a nominal altitude of 705km above the surface, and APS will cross the equator at 13:34 local time. Since it is mounted on an aircraft, the RSP has a variety of potential observation altitudes and geometries. Cruising altitude for the B-200 is 8km above the ground, while the J-31 used many different flight plans and operated at a range of altitudes. Data collected during ALIVE for chapter 5 were as low as 200m above the ground.
- *Spatial resolution*: The APS instantaneous field of view (IFOV) is 5.6km at nadir and 8.0km at a view zenith angle of 45°. At the B-200 cruising altitude, the RSP has an IFOV of 112m at nadir and 158m at 45°. Low altitude (200m) flights during ALIVE had an IFOV of 2.8m at nadir and 4.0m at 45°.

Aerosol parameters are retrieved by matching an atmospheric model to measurements collected by the instrument. For a given scene there are hundreds of pieces of information, each representing different viewing angles, wavelengths, and Stokes vector components. While many of these observations are highly correlated, they contain a wealth of information that can be used to determine the dozen or so aerosol, cloud and surface specific parameters. The construction of the atmospheric model and its use with a nonlinear optimization technique to find these parameters is the topic of the next chapter.

Chapter 2

Background

Polarimetric remote sensing requires an understanding of atmospheric radiative transfer, instrumental observation techniques, and mathematical and computational concepts that link them. The goal of this section is to establish the terminology associated with these concepts and provide a brief background for material that is presented in subsequent chapters. Clearly, these topics are quite extensive and are covered in much more detail in the referenced literature, and material such as the review paper by Hansen and Travis [1974], optics and atmospheric radiation textbooks such as Born and Wolf [1980], Liou [2002], Mishchenko et al. [2002], and Mishchenko et al. [2006], and numerical methods texts such as Moré [1977], Moré et al. [1980], Rodgers [2000] and Markwardt [2009]. A thesis of similar scope and material was presented by Chowdhary [1999], who studied the use of polarization for remote sensing of atmosphere-ocean systems.

The structure of this chapter mimics the order in which the concepts are encountered in remote sensing. First, I will explain polarization and how electromagnetic (EM) radiation can be represented with the Stokes polarization vector, and how we formulate expressions of the vector that are convenient for our observational techniques. Next, single scattering by molecules and aerosols will be described by the concepts of Rayleigh scattering and Lorenz-Mie theory. Polarized surface reflectance will be covered next, followed by the methods that we use to compute observed radiances of a multiple layered atmosphere and surface system. Next, the nonlinear optimal estimation method, which connects instrument

observations to radiative transfer theory, will be addressed. Finally, the software we use to implement these methods, and the techniques we use to assess the success of our estimation will be covered.

2.1 Polarization

We can describe a plane wave scattered in the direction of the unit vector $\hat{\mathbf{z}} = \hat{\mathbf{r}} \times \hat{\mathbf{l}}$, by the pair of terms

$$\begin{aligned} E_l &= a_l e^{i(\omega t - kz - \varepsilon_l)} \\ E_r &= a_r e^{i(\omega t - kz - \varepsilon_r)} \end{aligned} \tag{2.1}$$

where a indicates the component EM amplitude and ε the phase. t is time, k is the wavenumber ($k = \frac{2\pi}{\lambda}$, where λ is wavelength), ω is the angular frequency ($\omega = \frac{2\pi}{T}$, where T is the period), and $i = \sqrt{-1}$. If we define the plane of scattering to include the vectors pointing in the illumination and scattering directions, E_l is the electric field paralleL and E_r is the electric field perpendiculaR to this plane.

Polarization of EM radiation is often described as a four element vector. One formulation is the Stokes polarization vector,

$$\begin{aligned} I &=< E_l E_l^* + E_r E_r^* > \\ Q &=< E_l E_l^* - E_r E_r^* > \\ U &=< E_l E_r^* + E_r E_l^* > \\ V &= -i < E_l E_r^* - E_r E_l^* > \end{aligned} \tag{2.2}$$

where the brackets indicate time averages and $*$ the complex conjugate. The Stokes vector element I is the intensity, which is the rate of energy flow across a unit area perpendicular to $\hat{\mathbf{z}}$ (with units of, for example, Wm^{-2}). The direction and magnitude of linearly polarized intensity are expressed with vector elements Q and U, while V is the circular polarization. This formulation of polarization is commonly used because it provides a convenient representation for numerical modeling of multiple scattering problems, and because it allows

for a straightforward expression of easily obtained observations. If we consider the intensity defined as a function of the retardance imposed on the perpendicular field with respect to the parallel field, ε by a perfect retarder, and that would be transmitted by a perfect polarizer oriented at an angle, $\Psi = \tan\frac{a_r}{a_l}$, with respect to the parallel field direction (ie $I = I(\Psi, \varepsilon)$), then it can be shown (Hansen and Travis [1974]) that

$$\begin{aligned} I &= I(0°, 0) + I(90°, 0) \\ Q &= I(0°, 0) - I(90°, 0) \\ U &= I(45°, 0) - I(135°, 0) \\ V &= I(45°, \tfrac{\pi}{2}) - I(135°, \tfrac{\pi}{2}) \end{aligned} \tag{2.3}$$

Time averaged versions of the first three elements of the Stokes vector are therefore easily obtainable with, for example, Wollaston prisms (as is the case for the RSP and APS) or linear polarizers (as is the case for POLDER). Circular polarization, which is quantified by V as the excess of right-handed polarization over left-handed polarization, is small ($< 0.2\%$ of the linear polarization) in remote sensing of atmospheric aerosols illuminated by sunlight (Kawata [1978], De Haan et al. [1987]) so it is neglected in the measurements made by the RSP and APS and from studies that are presented here.

We restrict ourselves to quasi-monochromatic, incoherent radiation, for which $I^2 \geq Q^2 + U^2 + V^2$, and the linearly polarized intensity, I_p is

$$I_p = \sqrt{Q^2 + U^2} \tag{2.4}$$

The relationship between Q and U can be described by the polarization angle, χ, which is the angle between the polarization direction and $\hat{\mathbf{l}}$:

$$\chi = \frac{1}{2}\tan^{-1}\frac{U}{Q} \tag{2.5}$$

Since more than one value of χ satisfies equation 2.5, the convention that is used (Hansen and Travis [1974]) is to select the value in the interval $0 \leq \chi < \pi$ for which $\cos 2\chi$ has the same sign as Q.

2.2 Observation units

From a remote sensing standpoint, it is often useful to express the polarization components of the Stokes vector in terms of reflectance. This takes the exo-atmospheric irradiance and solar geometry into account, so reflectances at different locations and times can be compared. Reflectance is calculated using the formulae

$$R_I = \frac{I\pi r_o^2}{F_o \cos\theta_s}$$

$$R_Q = \frac{Q\pi r_o^2}{F_o \cos\theta_s} \tag{2.6}$$

$$R_U = \frac{U\pi r_o^2}{F_o \cos\theta_s}$$

where F_o is the annual average exo-atmospheric irradiance (W/m^2), r_o is the solar distance in astronomical units (AU, thus compensating for solar distance deviation from average throughout the year), and θ_s is the solar zenith angle. As we shall see in the description of Rayleigh and Lorenz-Mie scattering, $R_U = 0$ for single scattering if the illumination Stokes vector is $\{1, 0, 0, 0\}$ (unpolarized) and $\hat{\mathbf{r}}$ and $\hat{\mathbf{l}}$ are defined with respect to the scattering plane defined by $\hat{\mathbf{z}}$ and the illumination unit vector. Thus R_I and R_Q are all that is required to describe the total and linearly polarized reflectance in a scene dominated by single scattering. In this situation, the polarization angle, χ, is either $0°$ or $90°$.

From a practical standpoint, this provides a means to assess the uncertainties of observation geometry, which is an important issue for airborne measurements from the RSP. If aircraft geometry is correct, the polarization angle will be $0°$ or $90°$ for observations where single scattering dominates (such as side scattering viewing angles at long wavelengths). If this is not the case, aircraft pitch, yaw or roll can be adjusted, within reasonable limits, until a valid polarization angle is found. This is the method that was used to correct aircraft geometry in chapter 4. An alternate technique is to minimize R_U in the plane of scattering, which was used in chapter 3. The former technique is a more recent development and

preferred over the latter, as it offers higher sensitivity.

An alternate formulation of scene polarization is to use the polarized reflectance. Polarized reflectance compresses the R_Q and R_U into a single value that is less sensitive to aircraft geometry because it is independent of the frame of reference used to define E_r and E_l.

$$R_p = \sqrt{R_Q^2 + R_U^2} \tag{2.7}$$

R_p has often been used as the measurement that is optimized during aerosol property retrieval, such as in Waquet et al. [2009a]. However, since it is always greater than or equal to zero, the polarized reflectance does not effectively define the polarization neutral points, which can be useful when comparing models to observations. For this reason, R_Q, defined with respect to the scattering plane, is the primary observational data used to retrieve aerosol optical properties with optimal estimation in this thesis. In some special cases, R_I is also used during retrieval, such as in chapter 3, but it plays a secondary role and has higher uncertainty.

2.3 Atmospheric single scattering

Quantification of atmospheric scattering requires a means to account for all the elements in the input and output Stokes vectors. In the far field, where the distance between the scattering particle and the observation location, R, is much larger than wavelength, this is done with the scattering matrix, $\mathbf{P}(\xi)$:

$$\mathbf{I}(\xi) = k_e \varpi \frac{dv}{4\pi R^2} \mathbf{P}(\xi) \mathbf{I}_o \tag{2.8}$$

where $\mathbf{I}_o$ is the incident Stokes vector, $\mathbf{I}$ is the scattered Stokes vector, and ξ is the scattering angle between them. dv is the volume containing the scattering elements, $\mathbf{I}_o$ and $\mathbf{I}$ are specified in terms of intensity [Wm^{-2}], and Stokes vectors are defined with respect to the

plane containing both $\mathbf{I}_o$ and $\mathbf{I}$ (the scattering plane). Equation 2.8 depends on three inherent optical properties of the scattering particles. The extinction coefficient, k_e, expresses the quantity of extinction in the volume and is related to the extinction cross section, σ_e,

$$k_e = \frac{\sigma_e}{dv} = \frac{1}{dv}\sum_i \sigma_{e,i} \tag{2.9}$$

where σ_e has units of $[m^2]$ and represents the cross section particles blocking intensity in a unit area. The summation is for all particles, i, in the volume dv. The fraction of extinction that is absorbed or scattered is expressed with the single scattering albedo, ϖ, which is the ratio of absorption to extinction in the volume, and is defined in various forms as

$$\varpi = \frac{\sigma_s}{\sigma_e} = \frac{\sigma_e - k_a}{\sigma_e} = \frac{k_s}{k_e} = \frac{k_e - k_a}{k_e} \tag{2.10}$$

where k_s and k_a are the scattering and absorption coefficients, while σ_s and σ_a are the scattering and absorption cross sections. For $\varpi = 1.0$, the volume is purely scattering, while it is purely absorbing for $\varpi = 0.0$.

For randomly oriented particles, k_s and ϖ are invariant with scattering angle. All that remains to define scattering in a unit volume is the phase matrix, $\mathbf{P}$. The phase matrix specifies the directionality of scattering, and is the transformation matrix from the incident Stokes vector, $\mathbf{I}_o$ to the scattered vector, $\mathbf{I}$. The I element of the phase matrix is normalized such that

$$\int_{4\pi} P_{1,1}(\xi)\frac{d\Omega}{4\pi} = 1 \tag{2.11}$$

where $d\Omega$ is the solid angle element. A useful parameter that expresses the angular dependence of scattering is the asymmetry parameter, g

$$g = \int_{4\pi} \cos\xi P_{1,1}(\xi)\frac{d\Omega}{4\pi} \tag{2.12}$$

where $g = 1$ means forward scattering is dominant, $g = -1$ means backscattering is dominant, and $g = 0$ means scattering is evenly distributed between the forward and backward

directions.

$\mathbf{P}(\xi)$ is a 4x4 element matrix. In certain conditions, it can be reduced to

$$\mathbf{P}(\xi) = \begin{bmatrix} a_1(\xi) & b_1(\xi) & 0 & 0 \\ b_1(\xi) & a_2(\xi) & 0 & 0 \\ 0 & 0 & a_3(\xi) & b_2(\xi) \\ 0 & 0 & -b_2(\xi) & a_4(\xi) \end{bmatrix} \tag{2.13}$$

with six individual elements, rather than the full sixteen. This reduction holds under one of the following conditions:

- a group of randomly oriented particles, each with a plane of symmetry (such as spheres or spheroids),
- a group of randomly oriented particles with an equal number of mirror particles, or
- a group particles so small compared to the wavelength of radiation that Rayleigh scattering can be used to determine the scattering matrix.

For our purposes, atmospheric scattering can be described by either Rayleigh or Lorenz-Mie theory, both of which meet the conditions described above. Rayleigh theory is for scattering by very small particles in an exact manner, while Lorenz-Mie theory can be used to describe scattering from larger, spherical, particles. Of course, aerosols are not always spherical (or small enough that they can be treated that way), so other methods have been developed to determine or approximate scattering from nonspherical particles. While the research in this thesis assumes spheres, further development will involve the use of nonspherical particles, whose scattering can be computed with the T-matrix method for spheroids (Mishchenko et al. [1996], Mishchenko and Travis [1998], Mishchenko et al. [2000]).

2.3.1 Rayleigh Scattering

EM radiation, when incident on very small particles, induces a dipole oscillation that in turn emits (or scatters) radiation. This form of scattering, called Rayleigh scattering after

the work of John Strutt, the Third Baron Rayleigh, is relevant if the size of the particle is far less than the wavelength of radiation. This relationship is conveniently expressed with the size parameter, x,

$$x = \frac{2\pi r}{\lambda} \tag{2.14}$$

where λ is the wavelength and r is some metric denoting size (such as radius for a sphere). Size parameters within the range $0.002 < x < 0.2$ indicate that Rayleigh scattering is the dominant process, which is the case for air molecules at visible and near infra-red (NIR) wavelengths (Petty [2006]).

The Rayleigh scattering coefficient, as described in Hansen and Travis [1974] and earlier sources, is

$$k_s = \frac{8\pi^3(m^2-1)^2}{3\lambda^4 n}\left[\frac{6+3\delta}{6-7\delta}\right] \tag{2.15}$$

where m is the refractive index, n is the number of molecules per unit volume, and δ accounts for the slightly anisotropic nature of molecular scattering (meaning that the molecules are not perfect dipoles and do not generate perfectly polarized light at a $90°$ scattering angle). For air, $\delta \sim 0.03$ and $m = 1.000277$ at visible wavelengths. If the refractive index is complex, absorption becomes the dominant component of extinction in Rayleigh scattering. This is the case in the NIR wavelength RSP and APS bands, where absorption by carbon dioxide becomes significant at $1.6\mu m$ and methane becomes significant at $2.2\mu m$. For other RSP bands, air is purely scattering ($\varpi = 1.0$). The Rayleigh scattering coefficient is inversely proportional to the fourth power of wavelength, which for observations by RSP and APS means that it is a much more important component of total scattering for the channels in the blue than it is for channels in the red or NIR.

The induced dipole oscillation is perpendicular to the EM wave propagation ($\hat{\mathbf{z}}$), so the scattered radiation is highly directional. The relationship is, however, a simple function of scattering angle and anisotropy, and the elements of the phase matrix in equation 2.13 are

$$
\begin{aligned}
a_1(\xi) &= \Delta_r \tfrac{3}{4}(1+\cos^2\xi) + (1-\Delta_r) \\
a_2(\xi) &= \Delta_r \tfrac{3}{4}(1+\cos^2\xi) \\
a_3(\xi) &= \Delta_r \tfrac{3}{2}\cos\xi \\
a_4(\xi) &= \Delta_r \Delta_r' \tfrac{3}{2}\cos\xi \\
b_1(\xi) &= -\Delta_r \tfrac{3}{4}\sin^2\xi
\end{aligned}
\tag{2.16}
$$

where all other components of the phase matrix are equal to zero. The parameters Δ_r and Δ_r' depend on the anisotropy of the molecular scattering.

$$
\begin{aligned}
\Delta_r &= \tfrac{1-\delta}{1+\delta/2} \\
\Delta_r' &= \tfrac{1-2\delta}{1-\delta}
\end{aligned}
\tag{2.17}
$$

At the wavelengths we encounter with the RSP and APS, the Rayleigh scattering optical depth is proportional to the molecular concentration integrated over the path length. This is possible because the scattering coefficient per unit mass is constant outside atmospheric absorption bands. For an atmosphere in hydrostatic equilibrium, the Rayleigh scattering optical depth between the top of the atmosphere and any level in the atmosphere can therefore be accurately predicted by the pressure. For this reason, molecular and aerosol scattering are easily differentiated in radiative transfer models, and aerosol optical properties are all that need to be optimized during a retrieval.

2.3.2 Lorenz-Mie scattering

For larger particles, whose size parameter is in the range of $0.2 < x < 2000$ (in our case aerosols and cloud droplets), Rayleigh scattering theory is no longer accurate. At the turn of the 20th century, Ludvig Lorenz and Gustav Mie independently developed a solution to Maxwell's equations in spherical polar coordinates. Derivation of the solution can be found in many sources, such as Bohren and Huffman [1983] and Mishchenko et al. [2002], and only the solution of this partial differential equation is briefly noted here. The salient point of Lorenz-Mie theory for our efforts is that the scattering from spheres can be predicted

given the number concentration of those spheres in a volume, along with their size and complex refractive index.

The Lorenz-Mie scattering phase matrix, specified as components of equation 2.13, is

$$\begin{aligned} a_1(\xi,x,m) &= a_2(\xi,x,m) = \tfrac{1}{2}(S_1S_1^* + S_2S_2^*) \\ a_3(\xi,x,m) &= a_4(\xi,x,m) = \tfrac{1}{2}(S_1S_2^* + S_2S_1^*) \\ b_1(\xi,x,m) &= \tfrac{1}{2}(S_1S_1^* - S_2S_2^*) \\ b_2(\xi,x,m) &= \tfrac{i}{2}(S_1S_2^* - S_2S_1^*) \end{aligned} \tag{2.18}$$

where S_1 and S_2 are the scattering functions, which are given by the Lorenz-Mie solution as complex infinite series that depend on scattering angle, size parameter and refractive index. As above, $*$ indicates the complex conjugate. The scattering functions are given by the summations

$$\begin{aligned} S_1(\xi,x,m) &= \sum_{j=1}^{\infty} \tfrac{2j+1}{j(j+1)}[a_j\pi_j(\cos\xi) + b_j\tau_j(\cos\xi)] \\ S_2(\xi,x,m) &= \sum_{j=1}^{\infty} \tfrac{2j+1}{j(j+1)}[b_j\pi_j(\cos\xi) + a_j\tau_j(\cos\xi)] \end{aligned} \tag{2.19}$$

where a_j and b_j are functions of size and refractive index, while π_j and τ_j are functions only of the scattering angle. π_j and τ_j are related to Legendre polynomials, and are

$$\begin{aligned} \tau_j(\cos\xi) &= \tfrac{d}{d\xi}P_j^1(\cos\xi) \\ \pi_j(\cos\xi) &= \tfrac{1}{\sin\xi}P_j^1(\cos\xi) \end{aligned} \tag{2.20}$$

where P_j^1 is the jth order Legendre polynomial. Computation of the generally complex scattering coefficients a_j and b_j is the most numerically intensive component of Lorenz-Mie scattering. These scattering coefficients depend on particle size and refractive index, and use spherical Bessel functions. More details about their computation can be found in De Rooij and Van der Stap [1984], Liou [2002] and Mishchenko et al. [2002].

Lorenz-Mie scattering coefficients can also be used to determine the particle scattering and extinction coefficients. Both coefficients are infinite series dependent on size and refractive index. The volume scattering coefficient is

$$k_s = \frac{n\lambda^2}{2\pi} \sum_{j=1}^{\infty} (2j+1)(a_j a_j^* + b_j b_j^*) \tag{2.21}$$

while the extinction coefficient is

$$k_e = \frac{n\lambda^2}{2\pi} \sum_{j=1}^{\infty} (2j+1)\Re(a_j + b_j) \tag{2.22}$$

where n is the particle number concentration in the volume and $\Re$ indicates the real component of a complex number. From equation 2.10, the single scattering albedo is then

$$\varpi = \frac{\sum_{j=1}^{\infty} (2j+1)(a_j a_j^* + b_j b_j^*)}{\sum_{j=1}^{\infty} (2j+1)\Re(a_j + b_j)} \tag{2.23}$$

In practice, determination of these quantities is limited by the number of series elements, j, that can be calculated given computational resources. The number of j terms should be slightly larger than the size parameter, x, (Petty [2006]). Computation of Lorenz-Mie scattering therefore becomes more expensive as the size parameter increases, and subject to roundoff error if many coefficients must be determined. For this reason, it becomes more reasonable to use alternate scattering computation methods, such as geometric optics, for size parameters greater than 2000. The largest sizes that we encounter in this work are at most an order of magnitude less than this, so the alternative scattering theories will not be described here.

For very small size parameters (less than 1), Lorenz-Mie scattering has characteristics that approach Rayleigh scattering (e.g., $g = 0$). There are equal amounts of scattering in the forward and backscattering directions, and minimal scattering in directions perpendicular to $\hat{\mathbf{z}}$. As size increases, scattering shifts to forward directions, and the asymmetry parameter, g, increases. As the size parameter becomes as large as cloud droplets, scattering side lobes develop, and are responsible for features such as cloud bows, coronas and glories. The cloud bow is much more strongly expressed in polarized than in total radiance, and is highly sensitive to the cloud droplet size distribution. As we will see in chapter 4, this can

be used to differentiate scattering due to clouds from aerosols, which are generally much smaller and do not create such strong scattering side lobes.

2.4 Surface reflectance

Both of the single scattering theories above are sufficient to describe EM interaction with the gases, aerosols and cloud droplets that we expect to observe with the RSP. The next step is to combine them in a way that adequately models the atmospheric vertical distribution and accounts for multiple scattering interactions. Since the lower boundary of the atmosphere, the surface, is reflecting, we must also find a way to model surface reflectance. There is a rich literature of both polarized and total surface reflectance observations, from which a variety of models have been created. Many of these models are *ad hoc*, and their results are not directly traced back to Maxwell's equations. However, they are suitable for our purposes, since the goal (at least for chapters 3 and 4) is not to retrieve surface properties from our observations, but to understand surface reflectance accurately enough to retrieve atmospheric properties above them. Indeed, in chapters 3 and 4, surface reflectance is either a very small or completely negligible contributor to observed reflectance. Chapter 5 does not involve aerosol property retrieval at all, but is a validation of surface reflectance observations from the MODIS instrument and an evaluation of how well the dependence on solar zenith angle of the surface albedo can be predicted from multi-angle observations. The MODIS surface reflectance is the result of fitting multiple observations to a surface reflectance model. While this model is also *ad hoc*, it has been shown to be robust (Schaaf et al. [2006]). To maintain consistency, we use the same model in our validation in chapter 5.

The bidirectional reflectance distribution function (BRDF) is the basic quantity that expresses surface reflectance as a function of wavelength and illumination and observation geometries. As described in chapter 5 and in Nicodemus et al. [1977], the BRDF is

$$BRDF(\theta_s, \theta_v, \phi_s, \phi_v, \lambda) = \frac{dL(\theta_s, \theta_v, \phi_s, \phi_v, \lambda)}{dE(\theta_s, \phi_s, \lambda)}[sr^{-1}] \tag{2.24}$$

where θ_s is the solar zenith angle, θ_v is the observation view zenith angle, ϕ_s is the solar azimuth angle, ϕ_v is the view azimuth angle, and λ is the observation wavelength, which we denote as Λ when referring to a spectral bandpass of finite width. The upwelling radiance, L (defined as the energy projected in a solid angle from a surface, with the units of $wm^{-2}sr^{-1}$, where sr is a solid angle) and downwelling irradiance, E can be associated with any of the elements of the Stokes polarization vector, as long as they do so for the same components. When the upwelling radiance is polarized, equation 2.24 defines the bidirectional polarized reflectance distribution function (BPRDF). The BRDF and BPRDF are quantities that are impossible to measure directly, since L and E are defined in infinitesimally narrow portions of the solid angle. It is also usually impractical to observe the scene in all combinations of solar and view geometry. In practice, the BRDF and BPRDF are estimated with observations of narrow, but finite portions of the solid angle, and typically matched to a model of surface reflectance.

In chapter 5, we use BRDF models that are also used for MODIS observations (Schaaf et al. [2002]). These models consist of three reflectance kernels, which have various geometric dependences. An observation is therefore parameterized by the selection of three scaling parameters corresponding to each kernel,

$$BRDF(\theta_s, \theta_v, \phi, \lambda) \simeq f_{iso}(\Lambda) + f_{vol}(\Lambda)K_{vol}(\theta_s, \theta_v, \phi) + f_{geo}(\Lambda)K_{geo}(\theta_s, \theta_v, \phi) \tag{2.25}$$

where K_{vol} and K_{geo} are the volumetric and geometric scattering kernels, respectively, and f_{iso}, f_{vol} and f_{geo}, are the isotropic, volumetric and geometric kernel scaling parameters. ϕ is the relative view-sun azimuth angle ($\phi = \phi_v - \phi_s$). A more detailed description of these kernels can be found in chapter 5.

As stated previously, polarized surface reflectance does not contribute significantly to the observed reflectance in the research presented in this thesis. However, an important

component of the RSP and APS instrument design is the ability to take advantage of specific polarized surface reflectance characteristics, which can be used to retrieve surface reflectance independently of aerosol properties. Since this is a cornerstone of the RSP and APS operational strategy for observations over land, characterization of surface polarized reflectance is briefly described here.

Most current polarized surface models assume that the source of polarization from the surface are specular reflections on the front facet alone. Polarization created deeper within a surface is dependent upon the random orientation of the reflecting surfaces within a material, and tends to cancel. The Fresnel polarized reflectance coefficient, which expresses the quantity of radiation reflected from the front facet of a surface, is therefore used as the basis for these models, along with modifications to account for macroscopic surface shape effects such as shadowing. The Fresnel polarized reflection coefficient depends on the solar and view geometry and the surface refractive index,

$$F_p(m, \theta_v, \phi_v, \theta_s, \phi_s) = \frac{1}{2}\left[\left(\frac{m\mu_R - \mu_I}{m\mu_R + \mu_I}\right)^2 - \left(\frac{m\mu_I - \mu_R}{m\mu_I + \mu_R}\right)^2\right] \tag{2.26}$$

where m is the surface refractive index, and μ_I and μ_r are defined to be

$$\begin{aligned} \mu_I &= \cos\tfrac{\pi-\xi}{2} \\ \mu_R &= \sqrt{1 - (\sin\tfrac{\pi-\xi}{2}/m)^2} \end{aligned} \tag{2.27}$$

and the scattering angle, ξ, is

$$\xi = \tfrac{1}{2}\cos^{-1}\left(\cos\theta_s\cos\theta_v + \sin\theta_s\sin\theta_v\cos(\phi_v - \phi_s)\right). \tag{2.28}$$

Some of the earliest observations of polarized surface reflectance were by Vanderbilt et al. [1985]. They found that polarized reflectance is, for the most part, spectrally invariant. Because of this and the angular dependence of the observed reflectance, they concluded that polarized reflectance is dominated by the specular component, and not Lorenz-Mie or Rayleigh type scattering. Based on these observations, they made one of the first empirical polarized reflectance models (Vanderbilt and Grant [1985]).

Surface reflectance models that are based upon the Fresnel reflectance coefficient have several important features. The Fresnel reflectance coefficient is zero at solar backscattering angles, and increases uniformly away from backscatter. The reflectance coefficient is mainly dependent on the real component of the refractive index, and has a very weak dependence upon the imaginary component of refractive index. The real component of the refractive index for many surfaces is nearly spectrally invariant. For example, the real refractive index for epicuticular wax, which coats the surfaces of nearly all types of vegetation, varies between 1.54 and 1.47 at visible and NIR wavelengths (Vanderbilt and Grant [1985]).

Several surface polarized reflectance models were created in preparation for the POLDER instrument, a predecessor to RSP and APS (Rondeaux and Herman [1991], Breon et al. [1995], Nadal and Breon [1999]). These models used the Fresnel reflectance coefficient, along with additional terms that account for the effects of macroscopic surface features, such as the orientation of surface facets for leaves, or the roughness of exposed soil. For our RSP retrievals, polarized surface reflectance is characterized with a the kernel approach similar to equation 2.25,

$$BPRDF(\theta_s, \theta_v, \phi, \lambda) \simeq f_{pol}(\Lambda) K_{pol}(m, \theta_s, \theta_v, \phi) \tag{2.29}$$

where f_{pol} is the polarized reflectance scaling parameter, and K_{pol} is a kernel based upon the Fresnel reflectance coefficient and geometric terms intended to account for macroscopic scale scattering effects (such as the canopy shape, leaf angle distribution, and so on). We use either the 'vegetation' or 'soil' polarized reflectance models from Breon et al. [1995],

$$\begin{aligned} K_{pol,v}(m, \theta_v, \theta_s, \phi) &= F_p(4(\cos\theta_v + \cos\theta_s))^{-1} \\ K_{pol,s}(m, \theta_v, \theta_s, \phi) &= F_p(4\cos\theta_v \cos\theta_s)^{-1} \end{aligned} \tag{2.30}$$

where $K_{pol,v}$ is the polarized reflectance kernel for vegetation, and $K_{pol,s}$ is the kernel for bare soil. In practice, RSP observations at 2250nm are used to determine the value of f_{pol}. At this wavelength, aerosol effects are negligible, so RSP observations have a "window"

to the surface with nearly no atmospheric influence. The polarized reflectance scaling parameter is chosen for the kernel in equation 2.30 that best matches the observations. The refractive index used in each kernel is 1.5, which is reasonable for most common surface types.

Once f_{pol} has been determined using observations at 2250nm, it is applied at shorter wavelengths (where aerosol effects on the observations are greater) to constrain surface polarized reflectance in the radiative transfer model. Since RSP (and APS) observe all channels simultaneously, this allows for the optimization to retrieve aerosol parameters without the need for assumptions about surface reflectance. This is a distinct advantage of this type of sensor over earlier aerosol remote sensing instruments, which either do not have polarization channels or do not have channels at long enough wavelengths to be used for surface characterization (Cairns et al. [2009]).

2.5 Multiple Scattering

To fully simulate the atmosphere in a manner that can be compared to observations, single scattering and surface reflectance models must be combined in a way that accounts for multiple scattering. This is done with a plane-parallel model, which is vertically inhomogeneous but composed of multiple homogeneous layers. At low altitudes, layers are composed of both Rayleigh and Lorenz-Mie scattering, while at higher altitudes there is no aerosol scattering and therefore no Lorenz-Mie scattering. Generally, high altitude scattering by thin cirrus should be included in the modeling when performing aerosol retrievals, but for an aircraft at 4-8 km the cirrus clouds are generally above the observer and cannot be observationally constrained. The analyses presented in this thesis therefore use identification of cirrus clouds by pilots, or other instrumentation to eliminate those observations for which there was cirrus cloud overhead. To account for multiple scattering within the atmosphere, the 'Doubling and Adding' approach is used [Lacis and Hansen, 1974]. The 'Doubling and Adding' approach uses analytically derived single scattering for an ex-

tremely optically thin atmospheric layer and 'doubles' this by computing all the multiple scattering between the two identical layers. The results are the optical properties for the combined layer. This is repeated until a desired optical thickness has been reached, and 'Added' to a similarly constructed layer with different original optical properties (de Haan et al. [1987]). Figure 2.1 is a schematic describing this technique.

Reflectance, diffuse transmission or direct transmission from a pair of layers is computed by a summation of all upwelling, diffuse downwelling or direct downwelling terms in figure 2.1. Combined layer reflectance, for example, is

$$\mathbf{R}_{ab} = \mathbf{R}_a + (\mathbf{X}_a\mathbf{R}_b\mathbf{X}_a + \mathbf{T}_a^*\mathbf{R}_b\mathbf{X}_a + \mathbf{X}_a\mathbf{R}_b\mathbf{T}_a + \mathbf{T}_a^*\mathbf{R}_b\mathbf{T}_a)(1 + \mathbf{R}_b\mathbf{R}_a^* + (\mathbf{R}_b\mathbf{R}_a^*)^2 + \cdots) \quad (2.31)$$

where each element is described in figure 2.1. Equation 2.31 contains a geometric series, and can be rewritten as

$$\mathbf{R}_{ab} = \mathbf{R}_a + \frac{(\mathbf{X}_a + \mathbf{T}_a^*)(\mathbf{R}_b\mathbf{X}_a + \mathbf{R}_b\mathbf{T}_a)}{(1 - \mathbf{R}_b\mathbf{R}_a^*)} \quad (2.32)$$

$\mathbf{X}_{ab}$ and $\mathbf{T}_{ab}$ are computed in a similar manner. The model above is only for a single ray of radiation, the full form of Doubling and Adding integrates over all input angles for for any term that involves diffuse transmission. More details about this approach can be found in de Haan et al. [1987] and Hansen and Travis [1974].

2.6 Optimal estimation

Aerosol parameters are retrieved by matching the radiative transfer model described above to the RSP or APS observations. The set of aerosol parameters in the model that has the best match to the observations are considered the retrieved parameters. Observation uncertainties are taken into account, so the model match is for a range of parameter values, which therefore have their own uncertainties. The magnitude of these uncertainties provides an assessment of optimization success and parameter sensitivity.

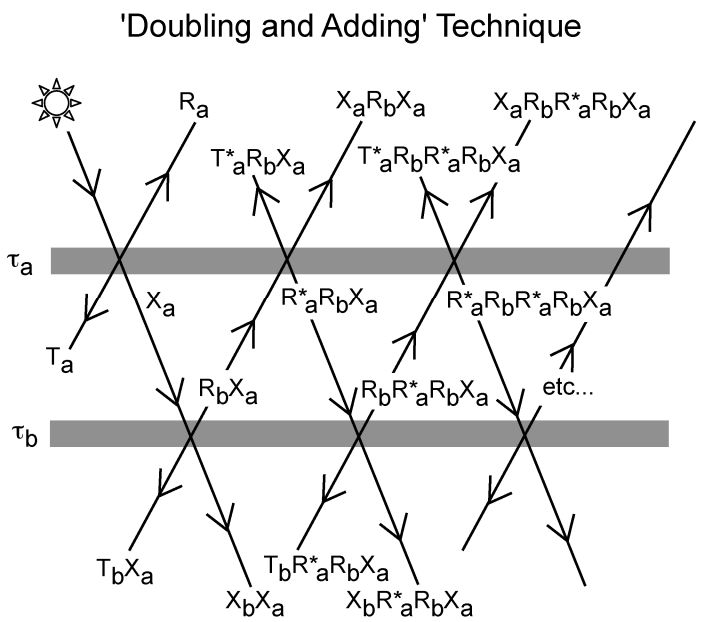

Figure 2.1: The Doubling and Adding technique is a summation of all possible multiple scattering interactions. This is similar to figure 3 in Lacis and Hansen [1974]. In this figure, layer a with an optical thickness of τ_a is added to layer b, which has an optical thickness of τ_b. Each layer is associated with a particular reflectance, R, diffuse transmission T, and direct transmission X, which for small optical thicknesses come from single scattering computations. Terms noted with a * indicate reflectance or diffuse transmission from beneath the layer. For inhomogenous layers (such as those after an 'addition'), these terms will be different than reflectance or transmission from above. The reflectance, diffuse transmission and direct transmission for the combined layers is the summation of all upwelling, diffuse downwelling, and direct downwelling terms above and below the layers respectively. For brevity, the interactions of the first diffuse scattered term, T_a are omitted in this figure.

Chapters 3 and 4 use software created by the author to perform the optimization. This software, called Doubling and Adding Optimization (DAO), couples GISS (Goddard Institute for Space Studies) radiative transfer software written by Brian Cairns, Andy Lacis and Larry Travis with a publicly available implementation of the Levenberg-Marquardt optimization algorithm written by Craig Markwardt (Markwardt [2009]). The GISS software combines Rayleigh and Lorenz-Mie single scattering computations with the Doubling and Adding technique to create simulated RSP observations, while the Levenberg-Marquardt algorithm adjusts the model parameters until an optimal solution is found. DAO is intended to be flexible, so that the retrieved parameter vector is easy to modify. This means that various parameters can be either prescribed (and are thus part of the overall model) or retrieved, which is useful if investigating alternative retrieval strategies. DAO can also be used to create synthetic scenes, which are used to asses the inherent parameter sensitivity in various conditions.

The radiative transfer model match to observations is found by minimizing a, generally nonlinear, cost function. This cost function expresses the difference between observations and model results, weighted by observational uncertainty. DAO uses a cost function, Φ, that is,

$$\Phi(\mathbf{x}) = \frac{1}{2}\|\mathbf{F}(\mathbf{x})\|^2 = \frac{1}{2}\left\|\frac{\mathbf{Y} - \mathbf{G}(\mathbf{x})}{\mathbf{C}_T}\right\|^2 \tag{2.33}$$

where **Y** is the measurement vector and **G(x)** is the modeled vector for aerosol parameters **x**. The use of $\|.\|$ indicates the Euclidean norm. $\mathbf{C}_T$ is the measurement error covariance matrix, which includes contributions from instrument calibration uncertainty, instrumental and shot noise, and errors from scene heterogeneity and aircraft geometry.

The Levenberg-Marquardt technique, which modifies the state vector, **x**, to minimize the cost function, Φ, is described in detail in section 3.2.3.1. For most cases, the observation vector, **Y**, consists of R_Q for up to six wavelength channels (three RSP channels are used for other purposes) and up to 152 view angles with each scan. This means that **Y** can be about 900 elements long, although the high degree of correlation between adjacent observations

means there are far less than that number of retrievable parameters. In some instances, such as in chapter 3, observations of R_I were be added to **Y**. This was possible because the effects of total surface reflectance, which is generally unknown, could be ignored because of the extremely optically thick aerosol layer in that scene. Furthermore, surface reflectance at 410 and 470nm is almost independent of the surface type, except for unusual surfaces such as salt flats (Kleipool et al. [2008]).

The state vector, **x**, contains model parameters that are tuned during optimization. These model parameters are required to either compute the single or multiple scattering within the radiative transfer model. The parameters included in the state vector can be easily modified in the DAO software, but generally include the following (for more information, see Hansen and Travis [1974] and Petty [2006]). Optical properties are typically defined for two size modes in each scene (see section 1.1.1). Cloud droplet size distribution can also become part of the state vector if clouds are identified in a scene.

- **Index of refraction,** m: Index of refraction differentiates aerosol materials, and is complex ($m = \Re(m) + i\Im(m)$). Refractive index is utilized in the single scattering component of the radiative transfer model. A non-zero imaginary component of the index of refraction indicates the presence of absorption. In the implementation of DAO used in this research, the real component of the refractive index is assumed to be spectrally invariant, while in chapter 4 two parameters are used to describe the spectral dependence of the imaginary component, which increases as wavelength decreases. Otherwise, the imaginary refractive index is also assumed to be spectrally invariant.

- **Effective radius,** r_e **and effective variance,** v_e: Although the scattering described in section 2.3 is defined with respect to a single size, in the atmosphere aerosols and cloud droplets exist with a variety of sizes. This size variability is usually well represented with a small number of parameters as a mathematical distribution. For example, DAO uses the log-normal size distribution for aerosols, and the gamma

distribution for cloud droplet size, which are supported by observations of both of those types of particles. Fortunately, is it relatively straightforward to account for these size distributions in the single scattering models of 2.3 (Hansen and Travis [1974]). Because of the variety of size distributions used in DAO, we chose uniform parameters to describe size that are not unique to a specific distribution. One choice could be the mean mode radius, but the effective radius, r_e is preferable in radiative transfer in that it accounts for radius in terms of its cross sectional area and thus attenuating effect. The effective variance, v_e is a second parameter that describes the variance about that mean, in terms of a normalized, unitless parameter:

$$\begin{aligned} r_e &= \frac{1}{G}\int_{r_1}^{r_2} r\pi r^2 n(r)dr \\ v_e &= \frac{1}{Gr_e^2}\int_{r_1}^{r_2}(r-r_e)^2\pi r^2 n(r)dr \end{aligned} \tag{2.34}$$

where the smallest particle radius is r_1, the largest is r_2, $n(r)$ is the number of particles with radius r, and G is the geometric cross sectional area of the particles in the volume. These parameters are easily transformed into the size distribution using the equation

$$n(r) = r^{(1-3v_e)/v_e} e^{-r/(r_e v_e)} \tag{2.35}$$

for the gamma distribution, and

$$\begin{aligned} n(r) &= \frac{1}{r\sigma_g(2\pi)^{1/2}} e^{\frac{-(\ln r - \ln r_g)^2}{2\sigma_g^2}} \\ r_g &= r_e/(1+v_e)^{5/2} \\ \sigma_g &= \ln(1+v_e) \end{aligned} \tag{2.36}$$

for the log-normal distribution.

- **Aerosol optical depth, $\tau_a(\lambda)$ or number concentration, n:** There is more than one way to estimate the total opacity of aerosols present in a volume. An earlier version

of DAO, used in chapter 3, used the number concentration of aerosols as an element of the retrieval vector. Later, DAO was modified so that the primary parameter associated with aerosol opacity was the optical depth at a reference wavelength,

$$\tau_a(\lambda, x_1, x_2) = \int_{x_1}^{x_2} n(x) k_e(\lambda) dx \tag{2.37}$$

where x represents the position on a line between arbitrary points x_1 and x_2 (such as the top and bottom of an aerosol layer). k_e is the extinction coefficient due to aerosols, which is calculated from equations 2.15 or 2.22 and is assumed constant throughout the layer. The reference wavelength in DAO is 555nm. Optical depth is related to direct beam transmission by the following relationship,

$$\mathbf{I}(\lambda, x_2) = \mathbf{I}(\lambda, x_1) e^{-\frac{\tau_a(\lambda, x_1, x_2)}{\mu}} \tag{2.38}$$

where $1/\mu = 1/\cos\theta$ expresses the path length through the atmosphere caused by a slant path at angle θ and x_1 and x_2 are depths in the atmosphere.

While they are technically similar measures of aerosol burden, there were several reasons for the shift from the use of n to τ_a as a retrieval parameter. Sun photometers, such as the AERONET network or the AATS airborne instrument, provide accurate observations of optical depth, while the column integrated number concentration is much more difficult to measure. Validation is therefore much easier if optical depth is a parameter that is part of the state vector, with directly retrieved uncertainties. Furthermore, optimization seems to be better behaved when optical depth, rather than number concentration, is a part of the state vector. While this is a subjective observation that needs to be further validated, it makes sense in that the observed radiances are directly dependent on the optical depth, which is the integral of the product of number concentration and extinction cross section, rather than number concentration alone.

- **Aerosol or cloud layer top and bottom heights,** h. The vertical placement of the aerosols or cloud droplets must also be specified within the radiative transfer model. For simplicity, we use layers of uniform aerosol or cloud properties that have an infinite horizontal extent (three dimensional effects are neglected).

Radiative transfer requires knowledge of all of the above parameters for each aerosol or cloud droplet size mode. Cloud droplet refractive index is of course known (we use the values from Segelstein [1981] weighted by RSP specral sensitivity convolved with the solar spectrum from Lean [2000]), and cloud optical depth is assumed to be large enough that variations have no impact on observed polarized reflectance (see chapter 4 for the justification for this). Otherwise, all parameters must be derived from external information, or assumption (thus formally becoming part of the radiative transfer model, **G**) or allowed to vary during optimization as part of the state vector, **x**.

2.7 Error characterization and information content analysis

An important component of optimal estimation is the ability to assess the sensitivity to various elements of the state vector, and determine the retrieval uncertainty. One of the primary goals of this research is an investigation of what parameters can be retrieved in a particular scene, and what strategies should be used for operational APS retrievals and the design of future instruments. This requires an accurate determination of several components of the optimization system. First, we need to understand the accuracy of our observation, which we express as the measurement error covariance matrix, $\mathbf{C}_T$. The error covariance matrix has the same length as the observation vector, **Y**, and expresses the individual error for each vector element. The covariance matrix is described thoroughly in section 3.2.3.1. We must also understand the inherent sensitivity of our forward model to perturbations in the state

vector. This is expressed with the Jacobian matrix,

$$\mathbf{J}_k = \left.\frac{\partial \mathbf{F}(\mathbf{x})}{\partial \mathbf{x}}\right|_{\mathbf{x}=\mathbf{x}_k} \tag{2.39}$$

where $\mathbf{x}_k$ is the state vector of the optimal estimate. As we shall see in section 3.2.3.1, the Jacobian must be computed for each iteration step of the Levenberg-Marquardt optimization algorithm, so the Jacobian from the final optimization step is the forward model sensitivity at the solution. The Jacobian must also be estimated numerically by perturbing the state vector by small quantities, which relies on the assumption that the forward model is linear over a small domain.

The Jacobian can then be used to project the observation error, expressed as the error covariance matrix, to parameter space. The retrieval error covariance matrix is

$$\mathbf{C}_x = (\mathbf{J}^T \mathbf{C}_T \mathbf{J})^{-1} \tag{2.40}$$

where the square root of the diagonal elements of $\mathbf{C}_x$ are the uncertainties of the associated parameter.

One technique that is helpful when designing an optimization strategy is to compute the Jacobian matrix for a simulated scene similar to what one expects to retrieve. If the observation error covariance matrix is known, then the associated parameter error covariance matrix can be computed. Simulated uncertainties for each parameter indicate if it is possible to retrieve that parameter within remote sensing requirements. This is the approach that was taken in chapter 4 for a scene with an aerosol suspended above a cloud.

Simulated retrieval uncertainty, however, does not indicate the correlation between different retrieval parameters. The correlation matrix is derived from the parameter error covariance matrix,

$$\rho_{i,j} = \frac{\mathbf{C}_{x,i,j}}{\sqrt{\mathbf{C}_{x,i,i}}\sqrt{\mathbf{C}_{x,j,j}}}. \tag{2.41}$$

Essentially, the correlation matrix element, $\rho_{i,j}$, is the error covariance normalized by parameter uncertainty. Strong positive correlation between elements indicates that their

retrieval is linked, so that the differences between those parameters are well constrained, while their sum is more poorly constrained than the diagonal elements of the covariance matrix would indicate.

Because of the effects of correlation and noise, the actual retrieval capability of an optimization system is more complex than the forward model sensitivity expressed by the Jacobian. One metric for quantifying this capability is to use the Shannon information content (H_s, see section 5.5 and Rodgers [2000]) defined in parameter space as

$$H_s = \frac{1}{2} \ln \left| \left(\mathbf{J}^T \mathbf{C}_T^{-1} \mathbf{J} + \mathbf{C}_a^{-1} \right) \mathbf{C}_a \right| \tag{2.42}$$

where $\mathbf{C}_a$ is the a priori error covariance matrix, which expresses the uncertainty in parameters prior to instrument observation and optimization. This is sometimes difficult to assess. In some cases, we use aerosol climatologies as the initial value during optimization, so the climatology uncertainty can be used to fill $\mathbf{C}_a$. However, some properties, such as aerosol optical depth, are not intrinsic to the aerosols themselves, and are highly variable. In any case, the information content can be seen as a type of signal-to-noise ratio. If the a priori error covariance matrix is kept constant, it can be a useful means to assess retrieval strategy. In chapter 4, for example, we tested if it is better to retrieve aerosol properties above a cloud when using a full RSP scan (which have high uncertainties in portions of the scan near the cloud bow) versus a restricted retrieval utilizing only more accurate side scattering angles. In this particular case, the full scan is a better approach, since simulated retrieval errors were better for all parameters. If it is not so obvious, the information content, expressed as a scalar, can be used to select the strategy that provides the greatest information increase.

Several assumptions must be made in the forward model so that optimization is tenable. For example, we assume that the atmosphere is made up of plane parallel aerosol and cloud layers, that the surface reflectance can be modeled with the Fresnel polarized reflectance coefficient, that aerosols and cloud droplets can be modeled with a log-normal and gamma size distributions, and so forth. It is often difficult to assess how accurate these assumptions are, but we can at least determine the impact that model errors have on re-

trieved parameters. To do so, we modify one of the assumptions in the forward model by our best estimate of its uncertainty, and recompute with the retrieved state vector, $\mathbf{x}$. The difference between this (which we will denote $\hat{F}(\mathbf{x})$) and the forward model results is the model error in measurement space. We can then use the Jacobian to project the error ($\mathbf{e}$) into state space.

$$\mathbf{e} = (\mathbf{J}\mathbf{J}^T)^{-1}\mathbf{J}[\hat{F}(\mathbf{x}) - F(\mathbf{x})] \tag{2.43}$$

We use this tactic in chapter 4, where this concept is described in more detail.

Combined retrievals of boreal forest fire aerosol properties with a Polarimeter and Lidar

to be submitted to the peer reviewed journal

Atmospheric Chemistry and Physics

full citation:

K. Knobelspiesse, B. Cairns, M. Ottaviani, R. Ferrare, J. Hair, C. Hostetler, M. Obland, R. Rogers, J. Redemann, Y. Shinozuka, A. Clarke, S. Freitag, S. Howell, V. Kapustin, and C. McNaughton. Combined retrievals of boreal forest fire aerosol properties with a Polarimeter and Lidar. *to be submitted to Atmos. Chem. Phys.*, 2010.

Chapter 3

Combined retrievals of boreal forest fire aerosol properties with a Polarimeter and Lidar

Absorbing aerosols play an important, but uncertain, role in the global climate. Much of this uncertainty is due to a lack of adequate aerosol measurements. The Aerosol Polarimetery Sensor (APS), which is on the NASA Glory satellite scheduled for launch in the spring of 2011, is designed to help resolve this issue by making accurate, multi-spectral, multi-angle polarized observations. Field observations with the Research Scanning Polarimeter (RSP, the APS airborne prototype), however, have established that simultaneous retrievals of aerosol absorption and vertical distribution over bright land surfaces are quite uncertain. We test a merger of RSP and High Spectral Resolution Lidar (HSRL) data with observations of boreal forest fire smoke, collected during the Arctic Research of the Composition of the Troposphere from Aircraft and Satellites (ARCTAS). During ARCTAS, the RSP and HSRL instruments were mounted on the same aircraft, and validation data were provided by instruments on an aircraft flying a coordinated flight pattern. We found that the lidar data did indeed improve aerosol retrievals using an optimal estimation method, although not primarily because of the contraints imposed on the aerosol vertical distribution. The more useful piece of information from the HSRL was the total column aerosol optical depth, which was used to select the initial value (optimization starting point) of the aerosol number concentration. When climatological values of number concentration were

used as an initial value we found that roughly half of the retrievals had unrealistic sizes and imaginary indices even though the retrieved spectral optical depths were in all cases in good agreement with independent measurements. The convergence to an unrealistic local minimum by the optimal estimator is related to the relatively low sensitivity to particles smaller than 0.1 μm at large optical thicknesses. Thus, optimization algorithms used for operational APS retrievals of the fine mode size distribution, when the total optical depth is large, will require initial values generated from table look-ups that exclude unrealistic size/complex index mixtures. External constraints from lidar on initial values used in the optimal estimation methods will also be valuable in reducing the likelihood of obtaining spurious retrievals.

3.1 Introduction

Polarimetric remote sensing is a valuable tool for the study of atmospheric particles. In the 1970's, Hansen and Hovenier used observations of (linear) polarization in sunlight reflected from Venus to conclude that the planet is shrouded by sulfuric acid clouds (Hansen and Hovenier [1974]). Today, the field has grown to include remote sensing of atmospheric aerosol particles surrounding our own planet. Aerosols are airborne particulate matter that are of interest because of the variety of ways they can affect the global climate, and because this interaction is not well understood. Unlike the greenhouse gases associated with climate change, aerosols typically survive in the atmosphere for only days or weeks, and are thus highly regional. They have both natural and anthropogenic sources and highly variable optical properties. For these reasons, the Intergovernmental Panel on Climate Change has identified aerosols as a major source of uncertainty in the radiative forcing of climate (IPCC [2007]). Much of this uncertainty is due to inadequacies in providing appropriate and comprehensive information for climate models (Mishchenko et al. [2004], Mishchenko et al. [2007b]).

The Aerosol Polarimetry Sensor (APS), onboard the upcoming NASA Glory orbital

mission, is an attempt to expand the quantity and quality of atmospheric aerosol descriptive parameters. APS will use polarimetric observations of reflected sunlight at about 240 viewing angles in nine channels at visible and near infra-red wavelengths (Mishchenko et al. [2007a]). Aerosol property retrievals will be determined by optimizing a radiative transfer simulation to match observed linear and polarized reflectance. In order to prepare for the launch of APS, the Research Scanning Polarimeter (RSP) was constructed (Cairns et al. [1997b]). The RSP is similar to the APS, but is deployed on an airborne, rather than orbital, observation platform. The RSP has been used in a number of field campaigns in the last decade to test the ability to accurately measure a variety of aerosol types (Cairns et al. [1997a], Chowdhary et al. [2001], Chowdhary et al. [2002], Cairns [2003], Elias et al. [2004], Chowdhary et al. [2005b], Chowdhary et al. [2005a], and Waquet et al. [2009a]).

In June and July of 2008, the RSP participated in the summer phase of the Arctic Research of the Composition of the Troposphere from Aircraft and Satellites (ARCTAS) field campaign (Jacob et al. [2010]). ARCTAS was the NASA contribution to the international Polar Study using Aircraft, Remote Sensing, Surface Measurements and Models, of Climate, Chemistry, Aerosols, and Transport (POLARCAT) program of observations for the International Polar Year. While stationed in Northern Canada, the RSP (and other instruments associated with ARCTAS) observed smoke aerosols from boreal forest fires. Biomass Burning (BB) aerosols tend to be both highly absorbing and unevenly distributed vertically in the atmosphere. The effects of aerosol absorption and vertical distribution were found to have similar impacts on the polarized reflectances observed over bright desert surfaces which increases the uncertainty in the retrieval of both aspects of the aerosol distribution (Waquet et al. [2009a]). Furthermore, retrievals of ocean optical properties may be affected by incorrect aerosol retrievals due to aerosol vertical distribution errors (Duforêt et al. [2007]). Fortunately, the Glory satellite will fly in the NASA/CNES 'A-Train' orbit, which includes a variety of earth observing instruments. One of these is the Cloud-Aerosol Lidar with Orthogonal Polarization (CALIOP) onboard the Cloud-Aerosol Lidar and Infrared Pathfinder Satellite Observation (CALIPSO) satellite (Winker et al. [2007], Winker

et al. [2004], and Winker et al. [2003]). CALIOP can determine the vertical layering of aerosols and reduce the ambiguity in APS BB aerosol retrievals due to aerosol vertical distribution uncertainty. During ARCTAS, the RSP flew onboard the NASA B-200 aircraft, which also carried the High Spectral Resolution Lidar (HSRL) (Hair et al. [2001], Hair et al. [2008], and Rogers et al. [2009]). In addition, the B-200 flew coordinated missions with an aircraft containing instrumentation whose data can validate RSP results. ARCTAS was therefore the ideal mission to evaluate combined polarimeter and lidar aerosol property retrievals, and that is the main goal of this paper.

In the next section, we will provide an overview of the RSP retrieval approach. We will also briefly describe the HSRL and in situ data collection and processing, and provide references to more detailed discussions. Next, we will present the results of our tests. RSP retrievals were performed with and without HSRL data, and were compared to in situ data to test their success. Finally, implications of these tests for future RSP/HSRL and APS/CALIPSO measurements will be discussed.

3.2 Method

3.2.1 RSP instrument specifics

The Research Scanning Polarimeter is an airborne prototype for the Aerosol Polarimetery Sensor. The main goals of both RSP and APS are to retrieve a complete suite of aerosol and cloud microphysical parameters from orbit (Mishchenko et al. [2004], Mishchenko et al. [2007b]). Both instruments have similar characteristics, but since the data we analyze in this paper were from RSP, that instrument alone will be discussed here. The RSP has nine optical channels with center wavelengths of 410, 470, 555, 670, 865, 960, 1590, 1880 and 2250nm, and is a passive, along track, scanning (not imaging), device. Each RSP scan begins about 60° forward of nadir in the direction of aircraft motion, and samples at 0.8° intervals to about 60° aft of nadir. The instantaneous field of view (IFOV) of the RSP is fourteen milliradians. For an average (during ARCTAS) aircraft height of 8680m above sea

level and ground elevation of 370m, this corresponds to ground pixel size of about 120m. For observation of elevated smoke plumes such as ours, the spatial resolution is about 65m.

The RSP/APS observes linearly polarized and total reflectance. This can be described by the first three terms of the Stokes polarization vector (Hansen and Travis [1974]), I, Q and U. I is the total radiance, while Q and U indicate the direction and magnitude of the linearly polarized radiance. The fourth term in the polarization vector, V, represents circular polarization, which is very small for atmospheric aerosols (Kawata [1978], for spherical particles), and is neglected in the analysis of RSP data. From a remote sensing standpoint, it is useful to express the polarization components of the Stokes vector in terms of reflectance. This takes the exo-atmospheric radiance into account, and is calculated as follows,

$$R_I = \frac{I\pi r_o^2}{F_o \cos\theta_s}$$

$$R_Q = \frac{Q\pi r_o^2}{F_o \cos\theta_s} \tag{3.1}$$

$$R_U = \frac{U\pi r_o^2}{F_o \cos\theta_s}$$

where F_o is the annual average solar exo-atmospheric irradiance (W/m^2) spectrally weighted for the particular RSP band, r_o is the solar distance in AU (thus compensating for solar distance deviation from average throughout the year), and θ_s is the solar zenith angle. The RSP instrument has a high accuracy (0.2%) of R_Q and R_U relative to R_I, as the same detectors are used to measure intensity and linear polarization, and because calibration of their relative gain is performed with each scan.

For each scene, the RSP makes observations of R_I, R_Q and R_U in nine wavelengths for 150 view angles. This provides upwards of four thousand measurements that are used to determine the aerosol optical properties that provide an optimal fit to the observations. In practice, far fewer measurements are used (for reasons described below), and there is also a strong correlation between observations at different view angles. However, this is sufficient information to retrieve the half dozen or so optically important parameters for

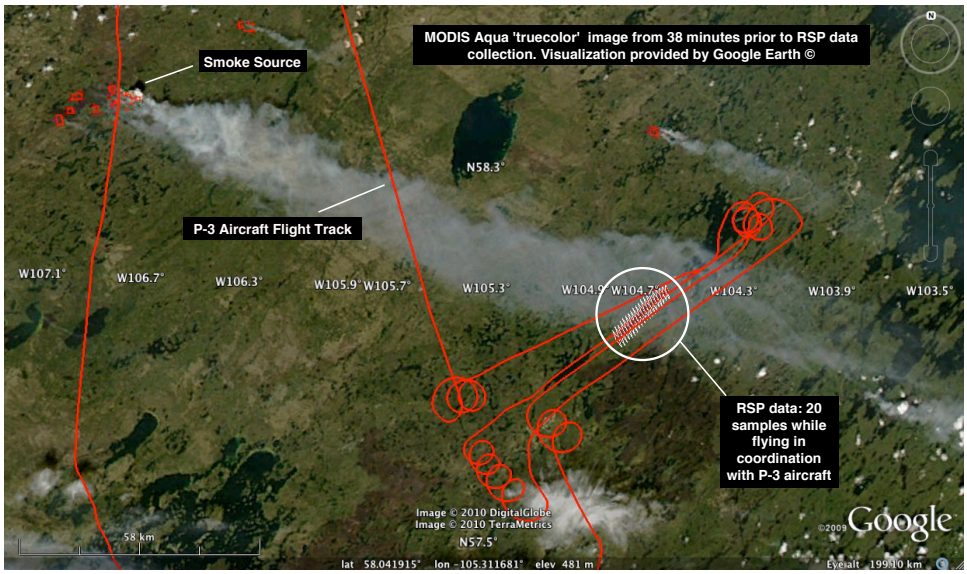

Figure 3.1: MODIS Aqua satellite fire imagery from 19:50 UTC. The RSP observations, indicated by the ordered white polygons at the right, were collected at 20:28 UTC on the B-200 aircraft. The flight track of the P-3 aircraft is shown in red. The portion of the P-3 flight under the indicated RSP observations was coordinated to occur at the same time. Google Earth was used to visualize these data.

each aerosol size mode. Furthermore, the broad spectral range of the RSP observations allows the surface to be constrained almost independently of the atmospheric state.

3.2.2 ARCTAS and data selection

The ARCTAS field campaign involved three aircraft in two, three week segments in 2008. The RSP was deployed during the summer (June - July) phase of the campaign (ARCTAS-B) on a Beechcraft King Air B-200 aircraft based at the NASA Langley Research Center in Hampton, Virginia. One of the primary goals of ARCTAS-B was to observe and characterize boreal forest fire smoke (Jacob et al. [2010]), so the B-200 was based in Yellowknife, Northwest Territories, Canada (62N, 114W) for this purpose. The B-200 flew coordinated flights with another ARCTAS aircraft during satellite overpass times. This aircraft, a Lockheed P-3 Orion from the NASA Wallops Flight Facility in Wallops, Virginia, carried a variety of instrumentation, including the Hawaii Group for Environmental Aerosol Re-

search (HiGEAR) aerosol in situ sampling instruments. Furthermore, the Ames Airborne Tracking Sunphotometer (AATS-14), a fourteen channel sun tracking sun photometer, was installed on the P-3. RSP data collected during these times is ideal for the validation of RSP and APS aerosol retrievals of vertically inhomogeneous, highly absorbing aerosols. We chose to study a small data subset from the smoke plume of a recent boreal forest fire. Surveys of other boreal forest fire aerosols can be found elsewhere, for example Eck et al. [2003], Koppmann et al. [2005], Reid et al. [2005b], Reid et al. [2005a] and Eck et al. [2009].

A scene on June 30th, 2008, was selected for analysis. On that day, the B-200 overflew a smoke plume downwind from its source in conditions that were otherwise nearly free of aerosols. The fire was in northern Sasketchewan, Canada (58.41°N, 106.81°W) and had been burning since the 29th of June. Natural Resources Canada, in its forest inventory of 2001 (CanFI2001), characterizes this region as a mixed soft and hardwood boreal forest. RSP observations were made about 130 km downwind from the source (see Fig. (3.1)). Back trajectory analysis (Fuelberg et al. [2010]) indicates that the smoke was 2 hours and 17 minutes old at this point, although it should be noted that this analysis did not account for local dynamics associated with the fire. We consider this scene to be ideal for a number of reasons, as described below.

1. The HSRL was operational at the time of RSP observation, indicating an optically thick plume detached from the surface.

2. The B-200 aircraft (containing the RSP and HSRL) was in a coordinated flight path with the P-3 aircraft (containing AATS and HiGEAR), which was under-flying the B-200 at a mean altitude of 627m above sea level.

3. A MODIS-Aqua image was collected about forty minutes prior to the scene. The ”truecolor” version of this scene provides the spatial context as observed in Fig. (3.1).

4. Aircraft orientation was close to the solar principal plane (the plane containing both

the solar illumination and observation vectors), providing a large range of scattering angles for use during optimization of RSP data.

5. The atmospheric state outside the plume was exceptionally free of aerosols. An RSP aerosol retrieval performed prior to contact with the plume yielded an aerosol optical thickness of 0.07 at 555nm, while AATS observations from the same location found an optical thickness of 0.04 at 520nm.

6. Back trajectory analysis (Fuelberg et al. [2010]), combined with the Canadian Wildland Fire Information System database (Canada [2009]) shows that the airmass in the days prior to the observation did not come into contact with any significant sources of biomass burning (or other) aerosols.

Aerosol retrieval optimization was performed individually for about twenty segments in each scene. Each segment is an average of five RSP scans. We used this approach (rather than performing a single optimization on an average of a larger number of scans) to test the consistency of the optimization approach, and to allow for the compensation, or quantification, of the effects of scene heterogeneity and changing aircraft geometry. In situ and sun photometer data on the P-3 indicate that aerosol optical thickness varies across the smoke plume, while intensive properties such as single scattering albedo remain mostly constant (see Figs. in Sect. (3.3)). We would therefore expect retrieved aerosol number concentration, n, (and thus optical thickness, τ), to vary across the plume, whereas intensive properties (size and composition) should vary less. For the time, location, solar geometry and other details associated with each segment, see Table 3.8.

3.2.3 Optimization Approach

We retrieved aerosol optical properties by matching the output from a radiative transfer model to polarized and unpolarized reflectances observed by the RSP. The Levenberg-Marquardt approach, which is a standard method for the solution of non-linear least squares

minimization problems, was used to find that match. With the exception of some methodological and software differences (outlined below), we used the approach described in detail in Waquet et al. [2009a]. Generally speaking, the radiative transfer model and software is identical, using Lorenz-Mie computations of single scattering properties and the Doubling and Adding approach to create multiple scattering in a layered atmosphere (Mishchenko and Travis [2008], Hansen and Travis [1974]). Optimization is performed differently than in Waquet et al. [2009a], with a slightly different cost function and measurement vector and using publicly available software to perform the Levenberg-Marquardt optimization. This software, implemented in the Interactive Data Language (IDL) as MPFIT (Markwardt [2009]), is a translation of the original FORTRAN language MINPACK-1 (Moré [1977]) solver, and is well documented. Since there are often subtle differences between different implementations of the Levenberg-Marquardt approach, we describe our methodology in more detail below.

3.2.3.1 Optimal Estimation

Optimal estimation is performed by the minimization of a, generally nonlinear, cost function. The cost function incorporates information about the uncertainty in the measurements so that the estimate that minimizes the cost function is optimal in the sense that it provides the best possible fit to the measurements given their uncertainties. In our case, this cost function, Φ, is the sum of squares of differences between the observational data and model calculation vectors weighted by their total uncertainty,

$$\Phi(\mathbf{x}) = \frac{1}{2}\|\mathbf{F}(\mathbf{x})\|^2 = \frac{1}{2}\left\|\frac{\mathbf{Y} - \mathbf{G}(\mathbf{x})}{\mathbf{C}_T}\right\|^2 \tag{3.2}$$

where **Y** is the measurement vector and **G(x)** is the modeled vector for aerosol parameters **x**. We use $\|.\|$ to indicate the use of the Euclidean norm. $\mathbf{C}_T$ is the measurement error covariance matrix, which can be broken down into component errors as

$$\mathbf{C}_T = \mathbf{C}_\varepsilon + \mathbf{C}_{cal} + \mathbf{C}_{pol} + \mathbf{C}_{ag} + \mathbf{C}_y + \mathbf{C}_p \tag{3.3}$$

Following the example of Waquet et al. [2009a], the instrumental noise, $\mathbf{C}_\varepsilon$ is shot noise limited, $\mathbf{C}_{cal}$ is the absolute radiometric calibration uncertainty of 3%, and $\mathbf{C}_{pol}$ accounts for the uncertainty in the relative polarimetric accuracy, which increases with the degree of linear polarization.

$$C_{\varepsilon,i} = 10^{-7} \cos\theta_s R_I(i)$$

$$C_{cal,i} = (0.03 R_Q(i))^2 \tag{3.4}$$

$$C_{pol,i} = (0.001[R_I(i) + |R_Q(i)|])^2$$

where the index, i, indicates that all the uncertainties are spectral band and view angle dependent and it is assumed that the measurement error covariance matrix is diagonal.

Waquet et al. [2009a] uses a fourth term, $\mathbf{C}_F$, which accounts for errors modeling the surface reflectance. The contribution of this term to the total error is very small, and since the smoke plume we observe is quite optically thick, for this case we can (and do) neglect $\mathbf{C}_F$. For the data we analyze here, we found two additional sources of uncertainty that must be included in the error budget for the observations. The variability encountered when averaging several scans of an inhomogeneous plume requires a new term, $\mathbf{C}_{ag}$, which represents the sampling uncertainty for that observation. We have also added two terms to account for uncertainties in the aircraft geometry. $\mathbf{C}_y$ is the uncertainty in the observed polarized reflectance caused by uncertainties in the aircraft heading angle (yaw), which expresses itself as an incorrect view azimuth angle. We estimated the magnitude of this uncertainty by shifting the observed data for a heading error of $0.5°$, and taking the difference between the observed and shifted observation. For R_Q, we add to $\mathbf{C}_y$ the error from an incorrect rotation into the scattering plane. $\mathbf{C}_p$ is the uncertainty in the observed polarized reflectance caused by aircraft pitch angle, which expresses itself as an incorrect view zenith angle. Uncertainty is computed in a manner similar to $\mathbf{C}_y$, and we again used a value of $0.5°$. Typically, the largest contributer to measurement uncertainty is aircraft pitch, closely followed by sampling uncertainty due to scene heterogeneity. Absolute cali-

bration uncertainties are usually a much smaller contributer to the observation errors than the uncertainties in aircraft geometry and scene variability.

The above covariance matrix definition applies to components of the measurement vector associated with the polarized reflectance. The covariance for the total reflectance is slightly different. Polarimetric accuracy does not affect the uncertainty in the total reflectance, instrumental noise remains the same, and the radiometric calibration uncertainty is now 3% of the total reflectance.

$$C_{cal}(i) = [0.03R_I(i)]^2 \tag{3.5}$$

The assumption of uncorrelated measurement errors is commonly used (Lebsock et al. [2007], Hasekamp [2010]) and is certainly valid for the instrument noise, and to a lesser extent for polarimetric accuracy. For radiometric accuracy and aircraft attitude, there will be correlation between measurement uncertainties at different view angles. For the data analyzed here, however, scene heterogeneity and random variations in aircraft attitude dominate the error budget and justify the assumption of uncorrelated measurements errors. Future work will incorporate error correlation for aerosol retrievals over the ocean, where surface heterogeneity does not reduce the effect of correlations between measurement errors for different view angles.

Starting from selected initial values for the aerosol parameters, $\mathbf{x}_o$ (see Sect. (3.2.3.3)), the Levenberg-Marquardt algorithm provides an iterative search for the parameter vector, $\mathbf{p}$, that minimizes the cost function $\Phi(\mathbf{x}_o+\mathbf{p})$ and thus gives the optimal solution $\mathbf{x} = \mathbf{x}_o+\mathbf{p}$. The iteration proceeds by constraining the minimization of the cost function at any step to lie within a trust region, Δ_k, around the current iteration step. A linearization about the current state vector, $\mathbf{x}_k$, is used to determine the size of the next step. At any given step, we are therefore attempting to solve

$$\min\{\|\mathbf{F}(\mathbf{x}_k) + \mathbf{J}_k\mathbf{p}_k\| : \|\mathbf{D}_k\mathbf{p}_k\| \leq \Delta_k\} \tag{3.6}$$

where k is an index indicating how many steps have been made, and $\mathbf{J}_k$ is the Jacobian

matrix, which expresses the forward model sensitivity to parameter change.

$$\mathbf{J}_k = \left.\frac{\partial \mathbf{F}(\mathbf{x})}{\partial \mathbf{x}}\right|_{\mathbf{x}=\mathbf{x}_k} \tag{3.7}$$

$\mathbf{D}_k$ is a diagonal, but not an identity matrix. This was introduced by Marquardt to allow for a large step in a direction with low curvature and a small step in a direction with high curvature. Heuristically, this serves to reduce the effects of a narrow valley with a relatively flat floor and is calculated as part of the iteration with the formula

$$\begin{aligned} \mathbf{D}_k &= \mathrm{diag}(d_1^{(k)}, \cdots, d_n^{(k)}) \\ d_i^{(k)} &= \max\left[d_i^{(k-1)}, \left\| \left.\frac{\partial \mathbf{F}(\mathbf{x})}{\partial x_i}\right|_{\mathbf{x}=\mathbf{x}_k} \right\|\right] \end{aligned} \tag{3.8}$$

The Levenberg-Marquardt method is based on the theorem that if $\mathbf{p}^*$ is a solution to equation 3.6, then $\mathbf{p}^* = \mathbf{p}(\Upsilon)$ for some $\Upsilon \geq 0$ where

$$\mathbf{p}(\Upsilon) = -(\mathbf{J}_k^T\mathbf{J}_k + \Upsilon\mathbf{D}_k^T\mathbf{D}_k)^{-1}\mathbf{J}_k^T\mathbf{F}(\mathbf{x}_k) \tag{3.9}$$

The constrained minimization is then implemented by the following algorithm, from Moré [1977]

1. Given $\Delta_k > 0$, find $\Upsilon_k \geq 0$ such that if

$$(\mathbf{J}_k^T\mathbf{J}_k + \Upsilon_k\mathbf{D}_k^T\mathbf{D}_k)\mathbf{p}_k = -\mathbf{J}_k^T\mathbf{F}(\mathbf{x}_k) \tag{3.10}$$

   then either $\Upsilon_k = 0$ and $\|\mathbf{D}_k\mathbf{p}_k\| \leq \Delta_k$, or $\Upsilon_k > 0$ and $(1-\sigma)\Delta_k < \|\mathbf{D}_k\mathbf{p}_k\| < (1+\sigma)\Delta_k$. σ is the relative error within which the iterative estimate of Υ_k is required to meet $\|\mathbf{D}_k\mathbf{p}_k\| = \Delta_k$.

2. If $\|\mathbf{F}(\mathbf{x}_k + \mathbf{p}_k)\| < \|\mathbf{F}(\mathbf{x}_k)\|$ then set $\mathbf{x}_{k+1} = \mathbf{x}_k + \mathbf{p}_k$. Otherwise, shrink the trust region ($\Delta_{k+1} = \frac{1}{2}\Delta_k$) and return to step 1, without modifying $\mathbf{x}$ and $\mathbf{J}$.

3. Choose Δ_{k+1}. The ratio of the actual reduction of the cost function to the predicted reduction is the criterion for adjusting Δ, viz.,

$$\rho_k = \frac{\|\mathbf{F}(\mathbf{x}_k)\|^2 - \|\mathbf{F}(\mathbf{x}_k + \mathbf{p}_k)\|^2}{\|\mathbf{F}(\mathbf{x}_k)\|^2 - \|\mathbf{F}(\mathbf{x}_k) + \mathbf{J}_k\mathbf{p}_k\|^2} \tag{3.11}$$

   The value of ρ_k is used to determine Δ_{k+1} as follows

   - if $\rho_k \leq 1/4$, then set $\Delta_{k+1} < \Delta_k$ using the method in Fletcher [1971].
   - if $\frac{1}{4} \leq \rho_k \leq \frac{3}{4}$ and $\Upsilon_k = 0$, set $\Delta_{k+1} = 2\|\mathbf{D}_k\mathbf{p}_k\|$
   - if $\frac{1}{4} \leq \rho_k \leq \frac{3}{4}$ and $\Upsilon_k > 0$, set $\Delta_{k+1} = \Delta_k$
   - if $\rho_k \geq 3/4$, then set $\Delta_{k+1} = 2\|\mathbf{D}_k\mathbf{p}_k\|$.

   To summarize, if the predicted and actual reductions in cost functions are similar then the trust region is increased, whereas if they are widely disparate the trust region is decreased based on a prescription by Fletcher [1971].

4. Update $\mathbf{D}_{k+1}$ using equation 3.8.

This iteration continues until either the step size is less than the expected uncertainty in state (aerosol parameter) space, or the reduction in the cost function is small. Once the iteration is complete, the retrieval error covariance matrix, $\mathbf{C}_x$, can be obtained from the Jacobians computed in the final step using the equation

$$\mathbf{C}_x = (\mathbf{J}^T\mathbf{C}_T\mathbf{J})^{-1} \tag{3.12}$$

Uncertainty associated with retrieved parameters is the square root of the diagonal elements of $\mathbf{C}_x$. The error covariance matrix can also be used to compute retrieval uncertainty of a parameter that is not directly retrieved during optimization (such as the aerosol optical thickness, see table 3.2), provided the dependent variables of the required parameter are part of the retrieval vector $\mathbf{x}$. This is done by computing the sensitivity of the indirectly retrieved parameter in the forward model to changes in each of the retrieved parameters.

Following the method of Hasekamp and Landgraf [2007], the uncertainty in the indirectly retrieved parameter (denoted with the subscript A) is

$$\sigma_A^2 = \sum_{i=1}^{N} \sum_{j=1}^{N} \mathbf{C}_{x,i,j} \frac{\partial G_a(\mathbf{x})}{\partial x_i} \frac{\partial G_a(\mathbf{x})}{\partial x_j} \tag{3.13}$$

where i and j are subscripts identifying elements of the retrieved parameter vector (which has a length of N). $G_a(\mathbf{x})$ is the forward model value for the indirectly retrieved parameter, A, evaluated at the optimal estimate, $\mathbf{x}$ (note that this is a scalar value not in the same space as $\mathbf{G}(\mathbf{x})$). We compute the forward model sensitivity for an indirectly retrieved parameter ($\frac{\partial G_a(\mathbf{x})}{\partial x}$) numerically, with a post-processing step after optimization is finished.

We chose this form of the Levenberg-Marquardt method for several reasons, which we briefly describe here. For more details about this method and its convergence properties, see Moré [1977], or the documentation of the MINPACK FORTRAN subroutines on which our technique is based (www.netlib.org/minpack/ and Moré et al. [1980]). The Levenberg-Marquardt technique is robust, and is efficient in its use of forward model calculations. Our vertically inhomogeneous vector radiative transfer model is computationally intensive, so it is not feasible to make multiple forward calculations to determine an optimal parameter Υ_k. The algorithm given above uses an iterative estimate of Υ_k, but the iteration is one that finds a step within a trust region that does not require additional forward model or Jacobian calculations (Hebden [1973]). For a trust region criterion of 10% ($\Delta = 0.1$), Υ is typically found within two iterations (Moré [1977]). The trust region grows whenever the predicted and actual cost function reductions are similar, so the transition between the steepest descent and Newton-Gauss components of the Levenberg-Marquardt technique is heuristically reasonable, as whenever the next step is within the trust region an efficient Newton-Gauss step is used.

3.2.3.2 The measurement vector

The measurement vector, $\mathbf{Y}$, contains observations of the Q component of polarized reflectance (R_Q) at six wavelength bands, and total reflectance (R_I) for one band. In each

band, observations were taken from a scan between 20° forward in the aircraft and 40° aft. Since the RSP has an angular resolution of 14 milliradians, this corresponds to 75 individual measurements in each scan, for a total of 450 observations of R_Q and 75 observation of R_I. The polarization frame of reference was rotated into the scattering plane (the plane containing both the solar and observation vectors) so that R_Q measurements alone are sufficient to represent the linear polarization (R_U is negligible for single scattering in the scattering plane). For the purposes of optimization using data near solar backscatter, the choice of R_Q is preferable to the polarized reflectance ($R_p = \sqrt{R_Q^2 + R_U^2}$) that was used in Waquet et al. [2009a]. R_Q is a signed measure and makes more effective use of observed neutral points than R_p.

The six wavelength bands used for R_Q were centered at 410, 470, 555, 670, 865 and 1590nm. Three RSP bands were not used. Bands centered at 960 and 1880nm are designed to allow the estimation of column water vapor and the identification and characterization of cirrus clouds, respectively. The 2250nm band is used to characterize the total and polarized surface reflectance for the radiative transfer model (see Sect. (3.2.3.3)). Our particular scene contains optically thick smoke aerosols, so we also used one short wavelength R_I band (410nm) in the optimization. Observations at this band have almost no contribution from surface reflectance, since surface reflectance is minimal in the blue (Guanter et al. [2008]) and the large aerosol load obscures what is reflected. Nevertheless, we used the methodology of Kaufman et al. [1997] to characterize R_I at 410nm based on observations at 2250nm, but should be insensitive to the uncertainty in this approach.

The measurement vectors were averages of five consecutive scans (a 'segment' as described above). Each scan is composed of data that have been reorganized so that all views point to a specific location, at a specific altitude, in the atmosphere. This is essential to reduce heterogeneity in the aerosol properties and loading within each segment. We performed this data reorganization so that the segment contains the various observation view angles of a 3800m altitude.

3.2.3.3 The radiative transfer model

The radiative transfer model, $\mathbf{G}(\mathbf{x})$, is actually two nested models. The inner model computes single scattering properties of bi-modal log-normal size distributions of aerosols using a Mie code for spheres (Hansen and Travis [1974]). The elements of the retrieval vector required by the single scattering model are the complex refractive index, m, effective radius, r_e, and effective variance, v_e, for each size mode. The smaller size mode, which we denote hereafter with a f subscript, represents 'fine' aerosols that are typically the product of chemical processes, while the larger, 'coarse' mode, denoted hereafter with a c subscript, represents larger aerosols that are the result of a mechanical process. We expect the fine mode to dominate in our scene, since smoke aerosols are chemically generated. We also expect that Mie models of spheres are adequate expressions of our aerosols. Indeed, the HSRL depolarization observations are very low, indicating spherical particle dominance (see Sect. 3.2.4.1). Furthermore, it is believed that smoke aerosols that have aged for an hour or more generally collapse into compact shapes that are well described, optically, by spheres (Martins et al. [1998], Reid and Hobbs [1998], Abel et al. [2003], Liu et al. [2008]). The doubling and adding (DA) technique is then used to compute the upwelling, downwelling and reflected polarized radiance fields generated by multiple scattering in an inhomogeneous atmosphere (Hansen and Travis [1974], De Haan et al. [1987]). The additional retrieval vector elements required for DA calculation are the vertical distribution of aerosol number concentration for each mode (n_f and n_c). The result is assembled into a vector representing the geometry and wavelengths required to fill $\mathbf{G}(\mathbf{x})$, and used in the optimization.

The radiative transfer model also requires that the ground reflectance is specified. For polarized reflectance, we can utilize established assumptions about surface polarized reflectance. Polarized reflectance of natural surfaces (such as the epicuticular wax coating the surfaces of leaves or the mineral facets of exposed rock) will be dominated by interactions at the surface, as bulk scattering within the material tends to be weakly polarized. Fresnel reflectance off surface facets is thus an appropriate basis for modeling the po-

larized surface reflectance (Vanderbilt et al. [1985], Grant [1987], Vanderbilt and Grant [1991], Breon et al. [1995], Nadal and Breon [1999], Cairns [2003], Elias et al. [2004] and Waquet et al. [2009a]). Since Fresnel polarized reflectance depends mainly on geometry and the real component of the refractive index, it exhibits little spectral variance. This is because most surface materials have a minimal real refractive index spectral variance (the imaginary component of the refractive index does vary spectrally and gives total surface reflectances color). We can therefore use the longest wavelength channel (2250nm), where aerosol effects are smallest, to characterize the surface reflectance at all wavelengths. This is used as the lower boundary condition in the DA radiative transfer model. In practice, the Fresnel polarized reflectance model is scaled to an appropriate value to match observed reflectances for each scene in order to account for surface roughness or variability in the real refractive index. We use a single scaling coefficient for all geometries, which differs from Waquet et al. [2009a], who used a value that varied with geometry. This simplification is feasible for our analysis because of the relatively weak contribution of the polarized surface reflectance due to optically thick aerosols, and allows the use a data closer to the solar backscattering angle.

For unpolarized ground reflectance, observations at 2250nm were fit to the ”RossThick-LiSparse” kernel based, bidirectional reflectance distribution function (BRDF) model. Fitting to the BRDF model mimicked the NASA Moderate-Resolution Imaging Spectroradiometer (MODIS) surface reflectance retrieval methodology (Lucht et al. [2000b]) and was performed previously with the RSP instrument in central Oklahoma in the United States (Knobelspiesse et al. [2008]). The results were multiplied by 0.25 and used as the reflectance at 410 nm. This is similar to the approximation of Kaufman et al. [1997] for MODIS retrievals of aerosol properties over land. While it has been found that the 0.25 scaling is not appropriate for all surfaces and viewing angles (Gatebe et al. [2001] and Remer et al. [2001]), the variation is small enough to be rendered irrelevant by the optically thick aerosol layer obscuring the surface. For example, the retrieved aerosol optical thickness at 410nm is 1.03 for the sample optimization in Fig. (3.2). This corresponds to a mere

36% transmittance at nadir, not including the effect of molecular scattering. Reflectances at 2250nm were typically low, averaging about 5%. According to Kaufman et al. [1997], the 410nm reflectance would be one quarter of this, 1.25%. This surface reflectance transmitted through the aerosol layer at nadir would only be about 0.5 in reflectance units, while the total unpolarized reflectance is typically between 15% and 20%. Errors associated with the approximation of 410nm reflectance would thus be suppressed in a similar manner. For this reason, one short wavelength band was included in the optimization vector $\mathbf{G}(\mathbf{x})$. Longer wavelength bands were not used because of the risk of sensitivity to inaccurate surface reflectance characterization, both due to higher surface reflectance values in the red and near-infrared, and lower surface-obscuring aerosol transmission.

Table 3.1 lists the model parameters, their units, and the a priori optimization values ($\mathbf{x}_o$). A priori values were selected using the boreal forest fire smoke properties in Dubovik et al. [2002], which were derived from systematic observations of sunphotometers in the Aerosol Robotic Network (AERONET). Parameters listed in italics in Table 3.1 are retrieved during optimization, while the others are fixed.

It has been suggested that the imaginary refractive index of some types of biomass burning smoke have a spectral dependence, specifically an increase in absorption (imaginary refractive index) in the blue and ultra-violet (Andreae and Gelencser [2006], Russell et al. [2010], Bergstrom et al. [2010]). Unfortunately, direct observations of smoke complex refractive indices are very limited. Absorption in smoke aerosols is typically associated with Black Carbon (BC) which is spectrally flat. Organic Carbon (OC), which covers a wide range of species with varying chemical concentrations, is the source of absorption at short wavelengths (Kirchstetter et al. [2004]). The relative contribution of BC and OC varies considerably depending on the fire type and smoke age. BC is usually more associated with hot, flaming fires, while OC is greater in cooler, smoldering fires. Since our smoke plume was created by young fires with many hotspots, we expect that BC will dominate. Initially we did include a retrieval parameter that allowed the refractive index to increase linearly (as wavelength decreases) for wavelengths less than 532nm. However, most of our

retrievals converged to a solution with no imaginary refractive index spectral dependence. Segments that did converge with a spectral dependence typically had a large residual error. We therefore conclude that either an imaginary refractive index spectral dependence does not exist for this smoke, or we are not sensitive to it. We therefore used a spectrally flat imaginary refractive index in our retrievals.

To facilitate comparison of our results with data collected by other instruments, we computed a variety of other aerosol properties using the retrieved aerosol properties. These derived parameters are listed in Table 3.2, along with information about the method used to derive them if they are not byproducts of the forward model. Retrieved parameter uncertainty was determined from equation 3.12 as described above, and derived parameter uncertainty was calculated numerically as in equation 3.13.

3.2.3.4 Atmospheric layer heights

As discussed in Waquet et al. [2009a], absorbing aerosol properties are difficult to retrieve without information about their vertical distribution. This paper is therefore intended to test how to best model absorbing aerosol vertical distribution. To do so, we performed optimizations with and without data supplied by the HSRL, and compare the results.

Retrievals performed without HSRL data modeled aerosols in a single, uniform layer attached to the ground. The top of the layer was allowed to vary as an optimization parameter. As listed in table 3.1, the initial altitude was 5000m, while initial values for aerosol number concentrations were selected to replicate the mean optical depth for biomass burning aerosols as given by Dubovik et al. [2002].

Unlike traditional backscatter lidars, the HSRL has the ability to discriminate between aerosol and molecular backscatter in the 532nm channel. This provides an independent estimation of aerosol extinction and backscatter coefficients, and means that the observed aerosol optical depth is directly estimated with no microphysical assumptions required. A more detailed description of this instrument can be found in Sect. 3.2.4.1. To find aerosol layer top and bottom heights, we took the derivative of the aerosol volume backscatter co-

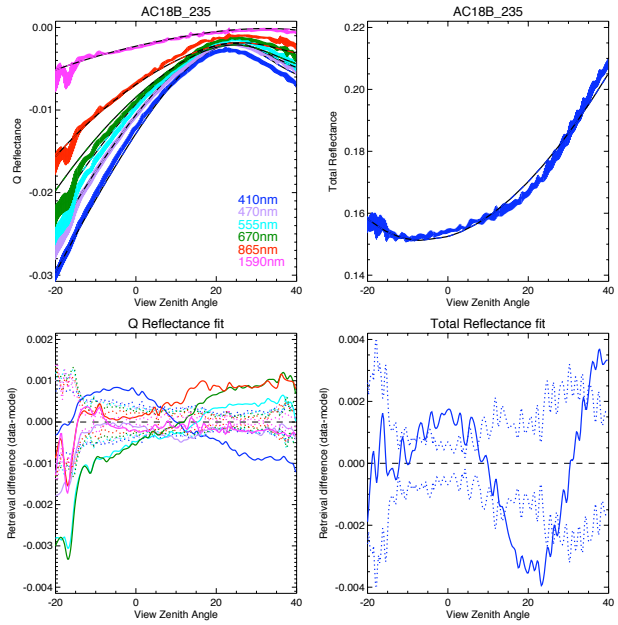

Figure 3.2: Sample results from an optimization using HSRL data. In the top panels, measured reflectances, and their associated errors, are plotted with solid lines with respect to the view zenith angle. Model results are plotted with dashed lines. Negative view zenith angles indicate aircraft forward scan directions, while positive values represent aft observations. R_Q is plotted on the left, while R_I is on the right. The bottom panels display the measurement minus model residuals. Dotted lines in these panels indicate the total error associated with that observation. 410mn results are in blue, 470nm in purple, 555nm in cyan, 670nm in green, 865nm in red and 1590nm in magenta.

efficient, b, after it had been weighted by the two pass atmospheric transmission (using the extinction coefficient, k_e) from the specified altitude, h, to the aircraft altitude, h_a (equation 3.14). Arbitrary thresholds were set for the result, $\gamma(h)$, where absolute values above the threshold indicate an aerosol layer top or bottom.

$$\gamma(h) = \frac{d}{dh}\left(b(h)e^{-2\int_h^{h_a} k_e(h')dh'}\right) \tag{3.14}$$

Aerosol layer heights were fixed within the optimization, and aerosols were distributed evenly with respect to pressure throughout each layer. The results of this layer identification can be seen in the first panel of Fig. 3.3. Red dashed lines indicate the tops and bottoms of the pair of layers identified using equation 3.14. An additional piece of information

from the HSRL is the total column aerosol optical depth at 532nm. This was used to select a priori n_c and n_f, which were distributed according to the aerosol optical depth in each layer. The relationship between n and aerosol optical depth was determined by the extinction cross-section calculated by the forward model for initial values of refractive index and size. Ratios of aerosol optical depth for both modes between different layers was maintained throughout the optimization.

3.2.4 Validation data

Results of the optimization with and without HSRL data were compared to a variety of contemporaneous measurements by other instruments. The first comparison we made was between optimization results and HSRL observations of aerosol optical thickness, τ, and the backscatter to extinction ratio, S, at 532nm. The former comparison is somewhat compromised by the fact that it was used to set the initial aerosol number concentration. However, since the initial values for size and complex refractive index are different than the retrieved values, the optical depth of a specified aerosol number concentration must also change. All of these values are unconstrained, so agreement between RSP and HSRL optical depth is by no means guaranteed by the choice of the initial value. In addition to comparisons with the HSRL, the B-200 flew in coordination with the NASA P-3 aircraft, which carried two instruments of interest to us. The AATS-14 instrument provided the column aerosol optical thickness (above the aircraft) in fourteen narrow wavelength channels. The aerosol Ångström exponent, α, was also calculated using these data. The HiGEAR suite of in situ sampling instruments provided the aerosol absorption (k_a) and scattering (k_s) coefficients, from which the single scattering albedo, ϖ is derived. HiGEAR instrument suite also measured aerosol size information, which we present as the effective radius, r_e and effective variance, v_e. Details about the collection of these data and the motivation for their use to validate RSP aerosol property retrievals are described below.

3.2.4.1 HSRL

The HSRL, as described above and in more detail in Hair et al. [2001, 2008] and Rogers et al. [2009] is a dual band (532 and 1064nm) lidar that was deployed along with the RSP on the B-200 aircraft. The HSRL uses an iodine cell with a narrow spectral absorption feature centered on the laser line at 532nm to absorb radiation scattered by aerosols (close to the laser line) and transmit light scattered by molecules (Doppler shifted away from the laser line). Another channel is used to measure the light scattered by aerosols and molecules at 532nm, similar to the usual elastic backscatter lidar measurement. This capability means that the HSRL can distinguish molecular from aerosol backscatter without the microphysical assumptions that are required for regular lidars. At 1064nm, the typical lidar approach is used, although the 532nm measurements can be used to constrain the derivation of backscatter profiles (Hair et al. [2008]). The HSRL also observes the depolarization ratio, d, which is the ratio of the perpendicular (cross-polarized) to parallel polarized aerosol backscatter coefficient. This parameter provides a measure of the sphericity of the aerosols since is a unitless ratio. In the case of single scattering it is zero for spheres. During this scene, the HSRL observed particulate depolarization of about 0.05, with is small enough that the aerosols can be treated as spheres (as they are in our radiative transfer model). The spherical assumption is reasonable for slightly aged smoke particles, which start as filaments and collapse into more compact shapes in the first few hours after creation (Abel et al. [2003], Reid and Hobbs [1998], Liu et al. [2008]).

3.2.4.2 AATS-14

The Ames Airborne Tracking Sunphotometer (AATS-14) is a fourteen channel (354nm to 2139nm) autonomous sun tracking sun photometer. It is mounted externally on the top of an aircraft, and provides above aircraft aerosol optical thickness automatically by continuously tracking the direct solar beam. This is successful provided the solar disk is not obscured by clouds or interference from the aircraft body and that the aircraft angular motion does not exceed 8° per second. Calibration is extremely stable, typically maintained within 1% over

the course of about a year. The AATS-14 has been deployed on a variety of aircraft during field campaigns since 1996 (for example, Russell et al. [1999], Schmid et al. [2003, 2006], Redemann et al. [2005] and Livingston et al. [2009]). During ARCTAS, the AATS-14 was mounted on the P-3 aircraft, which flew under the B-200 at a low altitude (Shinozuka et al. [2010]). AATS-14 should provide an excellent measure of the spectral dependence of aerosol optical depth. As we will see below (with the in situ instrument data), there are smoke related aerosols at the P-3 altitude, even if the total quantity of aerosols between the P-3 and the ground is much less than the quantity above. Thus, the column aerosol optical thickness that we observe with the RSP is at least as large as the values measured by the AATS-14, and should be slightly higher.

For validation purposes, we want to compare aerosol optical thickness at the same wavelength. The RSP optimization software can produce an optical thickness at any wavelength (with an extra radiative transfer model run with the final parameters at the specified wavelength), while the HSRL only provides an independent measure of column aerosol optical thickness at 532mn. This is not an AATS channel (the closest is 525nm), so AATS aerosol optical thickness at 532nm was determined by fitting an exponential function to the spectral data. Uncertainty values were interpolated in the same manner.

3.2.4.3 HiGEAR

HiGEAR is a suite of instrumentation deployed by the University of Hawaii on the P-3. HiGEAR provided validation data in the form of absorbing and scattering coefficients (from which the Ångström exponent and single scattering albedo can be derived) and the aerosol particle size distribution. Some examples of results from previous field campaigns can be found in Clarke et al. [2007] and McNaughton et al. [2009]. Shinozuka et al. [2010] integrated the in situ measurements over the vertical profiles flown during ARCTAS, and demonstrated that the resulting layer aerosol optical depth agrees with AATS-14 measurements within 3% or 0.02.

The aerosol size distribution was determined by two instruments. The Long Differential

Mobility Analyzer (LDMA) counts particles in the 0.01 to 0.5μm diameter range (Clarke et al. [1998]). The LDMA maintains the aerosols at ambient temperature and pressure, at dry (less than 30%) humidities. Particles in the 0.5 to 10μm range were measured by a TSI model 3321 aerodynamic particle sizer (APS) (McNaughton et al. [2007]). Like the LDMA, the APS operates at ambient temperature and pressure at dry humidities. Effective radius and variance were calculated by fitting a log-normal distribution to the data and deriving the effective radius and variance values from the fit parameters (see Eq. (2.60) and the next page of discussion in Hansen and Travis [1974]). The log-normal distribution is

$$n(r) = \frac{1}{r\sigma_g(2\pi)^{1/2}} e^{\frac{-(\ln r - \ln rg)^2}{2\sigma_g^2}} \tag{3.15}$$

where r is the aerosol radius and $n(r)$ is the number density of aerosols at radius r. r_g and σ_g are the fit parameters, and are used to derive the effective radius, r_e, and variance, v_e, with

$$r_e = r_g(1 + v_e)^{5/2} \tag{3.16}$$

$$v_e = e^{\sigma_g^2} - 1 \tag{3.17}$$

This fitting was performed to avoid the noise sensitivity associated with direct computation of effective radius and variance (Eq. (2.53) and (2.54) in Hansen and Travis [1974]), which are functions of the second, third and fourth moments of the size distribution, and therefore more prone to noise. Measurement uncertainty is the uncertainty associated with the fitting; observations with large uncertainty in either effective radius or variance indicate that the aerosol size distribution is not well represented by a log-normal distribution. Furthermore, fitting was performed with a bimodal size distribution (the total number concentration was the summation of two terms like that in equation 3.15). However, since the fine mode dominated the coarse mode to such a degree that the latter was difficult to even detect, subsequent comparisons of RSP and HiGEAR size distributions apply to the fine mode only.

Scattering and absorption coefficients are necessary to compute the Ångström exponent and single scattering albedo. Scattering coefficients were measured at 450, 550 and 700nm by a TSI model 3563 nephelometer. Data were corrected for ambient temperature and pressure and relative humidities within the instrument were low, no more than 30%. The Particle Soot Absorption Photometers (PSAP) measured the absorption coefficient at 470, 530 and 660nm. Measurements were corrected according to the methodology of Virkkula et al. [2005], and represent values at ambient temperature and pressure. The Single Scattering Albedo is calculated by combining both measurements with the ratio $\varpi = \sigma_s/(\sigma_s+\sigma_a)$. This was done after interpolating the scattering and absorbing coefficients to 532nm. The nephelometer has a higher measurement frequency than the PSAP, so temporal averaging of the scattering coefficient was also required.

3.3 Results

The primary goal of this paper was to test how observations from lidars such as the HSRL can be used to improve the analysis of RSP observations of optically thick smoke. We therefore performed a number of optimizations that incorporated HSRL data, then repeated them without that data and compared the results. This approach was taken so that the variability of retrieval results across the scene can be used to investigate the success of the method, and so the results can be compared in a statistical sense. The HSRL data that were incorporated into the RSP analysis included both an initial estimate of aerosol number concentration (derived from the HSRL optical depth at 532nm and the initial guess of aerosol size and refractive index) and the aerosol vertical distribution defined as layers.

Table 3.8 in the appendix lists the time and location of the individual data segments. Of note is the large difference (between 20° and 30°) between the aircraft heading and the actual ground track. This large 'crab' angle is due to the high winds experienced by the B-200 because of the proximity to the polar jet that day. Since the RSP was therefore unable to scan in the plane of forward motion, the spatial extent of a data segment, when projected at

the aerosol altitude, was larger in the cross track than the along track direction. This can be seen in Fig. 3.1, where the white polygons indicate the spatial extent of each data segment. For this reason, geometry data from the aircraft Inertial Monitoring Unit (IMU) was crucial. Unfortunately, we also found that there was occasionally some uncertainty associated with the IMU heading angle. A small correction to the heading angle was applied in order to ensure that the linear polarization angle remains parallel or perpendicular to the plane of scattering. This is what we expect for Fresnel (single interaction) polarized surface reflectance, so we use 2250nm observations at scattering angles away from backscatter for this purpose, as those observations have the largest surface contribution to total reflectance.

Tables 3.3 and 3.4 contain the mean and median values for retrieved and derived parameters, respectively, for retrievals with and without HSRL data. Table 3.5 contains comparable results from the validation data. Both mean and median values are presented, as differences between them indicate the possibility that values are not normally distributed. This is the case for several of the parameters for retrievals without HSRL data, such as the effective variance ($v_{e,f}$), fine mode number concentration (n_f), and scattering and extinction cross-sections (σ_s and σ_e). Since equivalent parameters measured by in situ instrumentation do not indicate a non-normal distribution, this is the first indication that the retrievals performed without the HSRL may not be successful.

Fig. 3.3 shows latitude indexed comparisons between RSP, HSRL, AATS and HiGEAR data, essentially the results as the aircraft flew through or above the smoke plume. Latitude was used as the reference because of the slight temporal difference between the B-200 and P-3 aircraft. The aircraft were traveling generally to the south, which in these plots is from left to right. HSRL data are the source of the imagery in each plot. The top panel is the aerosol backscatter coefficient at 532nm (km^{-1} sr^{-1}), which clearly shows elevated layers of aerosols at 3 to 4 km. While most of the backscatter in the profile occurs at the elevated level, the presence of backscatter below that layer indicates that aerosols are distributed down to the surface. The dashed white line overlay in this plot is the top of the aerosol layer as retrieved from RSP data when HSRL data are not utilized. Clearly, this

value is inconsistent, and rarely matches HSRL observations. Red line overlays indicate the layers derived from HSRL data using equation 3.14, while the orange dashed line near the bottom of the panel indicates the P-3 altitude (and thus the altitude of AATS and HiGEAR observations).

Our validation rests on several assumptions about the vertical distribution of aerosols that we acknowledge are somewhat contradictory. While these contradictions may physically exist, we believe that their radiative impacts are small enough so that they may be neglected. These assumptions are:

1. the P-3 aircraft was flying in aerosols with the same properties as observed from above by the RSP on the B-200, so that HiGEAR observations provide a valid test of RSP retrieval results,

2. the P-3 is flying under a sufficiently large portion of the column aerosol burden that AATS optical thickness can be compared to RSP retrieved results, and

3. aerosols in the direct solar beam measured by the upward looking AATS on the P-3 are the same as those observed by the downward viewing RSP on the B-200.

The HSRL data provide some indication as to the validity of these assumptions. For example, the HSRL extinction to backscatter ratio at 532nm is nearly uniform (about 50 sr) within the plume, indicating that the aerosol optical properties, at least as they are expressed in that ratio, are vertically consistent. Furthermore, the total optical depth from HSRL and AATS are also quite similar, which means that the AATS is observing a significant portion of the total aerosol column. At the solar zenith angle for our scene, the horizontal distance at the top of the aerosol layer between a zenith view from the P-3 and where the direct solar beam illuminating the P-3 enters the layer is on the order of two kilometers. Since the spatial resolution of a single scan at aerosol layer height is 65m (see Sect. 3.2.1), and given that aircraft crab angles enlarge the spatial resolution in the cross track direction (see earlier in this section and the white sample polygons in Fig. 3.1), we can expect that AATS observations are physically close to RSP and HSRL observations.

Another assumption we make is that spheres are an appropriate geometric model for scattering by aerosols. We are confident that this is the case, since the HSRL observes depolarization ratios less than 0.04 (at 532nm) throughout the column, indicating that the aerosols can be treated optically as spheres (Hair et al. [2008]).

Comparisons between RSP, AATS, HSRL and HiGEAR data are shown in the rest of the panels in Fig. 3.3. In each panel, RSP optimizations without HSRL data are in black, while optimizations using HSRL data are in red, and are staggered slightly with respect to latitude to aid visualization. AATS data are presented in blue, HSRL data in cyan, and HiGEAR data in green.

While this will be covered in more detail in Sect. 3.4, it is clear in Fig. 3.3 that the RSP retrievals without HSRL data are converging to two, significantly different, types of solutions. The first solution, which is similar to what is retrieved from RSP when HSRL data are used, involves low absorption and narrow size distribution aerosols, with real refractive index values less than 1.55. This agrees with results from the HiGEAR data for single scattering albedo and fine mode effective variance, and to a lesser degree effective radius. A second solution, retrieved only when the RSP is not using HSRL data, are aerosols that are very absorbing, very small, with large effective variances and real refractive indices. Since the results of this second type of solution do not agree with HiGEAR, we assume that the optimization has found a false minimum in the cost function representing aerosols that may not be physically realistic but are optically a reasonable match to the RSP observations. Presumably, this false minima is not found when the optimization uses HSRL data because those optimizations are started with a physically realistic fine mode number concentration. However, despite their size and refractive index differences, the aerosol optical thicknesses of both states are quite similar and match HSRL and AATS observations of spectral optical depth extremely well. Optical depth retrievals do therefore appear to be robust against the uncertainties caused by multiple minima in the measurement cost function.

The bottom panel of Fig. 3.3 contains two measures of optimization success. Solid lines are the Shannon information content, H_s, in parameter space as defined in Rodgers

[2000] as

$$H_s = \frac{1}{2} \ln \left| \left(\mathbf{J}^T \mathbf{C}_T^{-1} \mathbf{J} + \mathbf{C}_a^{-1} \right) \mathbf{C}_a \right| \tag{3.18}$$

The information content represents the decrease in uncertainty following optimization, or equivalently the reduction in entropy. It is directly related to the volume of uncertainty for a given confidence level before and after the measurement process. Uncertainty prior to optimization is expressed by the a priori error covariance matrix, $\mathbf{C}_a$, while the uncertainty following optimization is the error covariance matrix, $\mathbf{C}_T$ projected into state space using the Jacobian matrix. The solid lines in the bottom panel of Fig. 3.3 are this information content, which is slightly larger for retrievals using HSRL data during optimization compared to retrievals without HSRL data. Alternatively, optimization success can be expressed in observation space by the final value of the cost function as defined in equation 3.2 and plotted as dashed lines in Fig. 3.3. Like the information content, the final cost function value is slightly worse for optimizations performed without HSRL data, but does not indicate a convergence failure.

Fig. 3.4 presents the mean spectral aerosol optical thickness from the AATS instrument compared to both types of RSP optimization results. All three are nearly identical, with the exception of the of the very longest wavelengths, where optical thickness values are extremely low. This further illustrates how the spectral optical thickness is not affected by the divergent states retrieved with and without HSRL data.

3.4 Discussion

The primary goal of this paper is an investigation of the utility of lidar data in constraining and improving aerosol property retrievals with the RSP. First, we want to determine if the retrieved aerosol properties, when using HSRL data, are at least representative of boreal forest fire smoke. This appears to be the case. Comparisons with the ground sun photometer derived climatologies in Dubovik et al. [2002] show that our results are consistent

with the boreal forest biomass burning class. Of course, this was also the source of the initial optimization values, so this comparison is only meaningful in the sense that it shows the results did not stray far from their original values. Unfortunately, there are few observations, other than AERONET, of boreal forest fire smoke that simultaneously retrieve refractive index, size and concentration. One additional source is the three wavelength lidar observations of Müller et al. [2005], who studied boreal forest fire smoke transported long distances from Canada to Germany. Complex refractive index and single scattering albedo both are consistent with our results. However, Müller et al. [2005] finds significantly larger aerosols, with an effective radius of $0.36 \pm 0.05\mu m$ for the entire size distribution, compared to our $0.14 \pm 0.02\mu m$ for the fine mode and $0.22\mu m$ for the entire size distribution for retrievals that use HSRL data as a constraint. One explanation for this difference is the growth associated with smoke aerosol aging (Reid et al. [1998], Müller et al. [2007]), as our aerosols are much younger than those transported across the Atlantic to Europe. While few measurements of refractive index exist that are more accurate than the uncertainties in our retrievals, there are many measurements of single scattering albedo, which is closely related to the imaginary refractive index. Our value of 0.96 (at 532nm) is somewhat high compared to tables in the review by Reid et al. [2005a], indicating a low level of absorption for smoke aerosols. Boreal forest fires are known to produce less absorbing aerosols, and indeed the 'likely optical properties' for 'Temperate/Boreal Forest Aged' aerosols in Reid et al. [2005a] agree within uncertainties, with a value of 0.915 ± 0.05.

RSP results are compared to in situ observations of the smoke plume in Table 3.5, and Figs. 3.3, 3.4, 3.5, and 3.6. Optical thickness retrievals, both with and without HSRL data, compare well with HSRL column and AATS observations. Furthermore, the optical thickness spectral dependence is also well retrieved, as can be seen in Fig. 3.4. There is some difference at the longest wavelengths, but the magnitude of the optical depth at those wavelengths is so small that the estimates agree within measurement uncertainty. The only surprising aspect of the aerosol optical depth comparisons is the large RSP retrieval uncertainties (this will be discussed more below). 'Successful' RSP retrievals (we will use this

term to describe retrievals that used HSRL data and the retrievals without HSRL data that found nearly identical parameters) of single scattering albedo are slightly higher than, but within the uncertainty range of, HiGEAR observations. 'Unsuccessful' RSP retrievals of single scattering albedo (those performed without the aid of HSRL data that are substantially lower than 'successful' RSP retrievals or HiGEAR in situ observations) are drastically lower and generally have larger uncertainties. Comparisons to HiGEAR observations for size distribution appear reasonable for 'successful' RSP retrievals, with slightly larger effective radii and comparable effective variance values. 'Unsuccessful' RSP retrievals have smaller effective radii, and much larger effective variance values than HiGEAR observations. Agreement for effective radius and variance were within uncertainties for both 'successful' and 'unsuccessful' retrievals, although it should be noted that HiGEAR uncertainty values are rather large. This is most likely related to the deviation of the actual size distribution from the log normal function to which we are fitting. In fig. 3.6 we show the size distribution for a 'successful' and 'unsuccessful' RSP retrieval (Scan 170 in Table 3.8) compared to the closest HiGEAR observation. While this will be discussed in more detail below, it is notable that all three distributions are very similar in the 0.1-0.6 μm range. 'Unsuccessful' retrievals have an excess of small particles and the 'successful' retrievals have a deficit of small particles compared to the HiGEAR size distribution. Finally, we should note that we do not have in situ observations of the real refractive index for comparison. As mentioned above, 'successful' retrievals have refractive indexes that are similar to published boreal forest fire smoke values, although methods used to determine those published values have large uncertainty. 'Unsuccessful' retrievals have much larger values that could possibly be associated with smoke particles containing significant amounts of Black Carbon (which would be consistent with the larger absorption of these retrievals). Our hypothesis that this is not physically the case is based upon the larger (complex) refractive index uncertainty of these retrievals and their physically unrealistic size distribution and single scattering albedo when compared to HiGEAR observations.

The use of lidar data from the HSRL did improve RSP retrievals, but not in the way

we anticipated. We had expected that an appropriate vertical distribution of aerosols would create retrievals that match in situ observations better and reduce their uncertainties. While retrievals utilizing HSRL data are reasonable, about half of the retrievals performed without HSRL data converged to nearly the same solution with equivalent uncertainties (what we call 'successful' retrievals above). However, the other half of retrievals without HSRL data converged to an alternate solution that, while physically possible, is less consistent with in situ observations and has higher retrieval uncertainties (what we deem to be 'unsuccessful' retrievals). This appears to happen not because of an inappropriate vertical distribution (otherwise the 'successful' retrievals performed without HSRL data would not be so similar to those with HSRL data), but because of the initial values used to initiate the Levenberg-Marquardt iteration. Generally, the selection of inital parameter values is straightforward if there are clues to the type of aerosols present in the scene. In our case, the aerosols are obviously boreal forest fire smoke, so we used the climatology for this type from Dubovik et al. [2002]. Dubovik et al. [2002] do provide mean values of aerosol optical thickness (from which number concentration can be derived if the extinction cross-section is known), but the range of reported values is so large that the aerosol number concentration is unconstrained by climatology. This is because it is not an inherent quality of the aerosol type itself. Furthermore, aerosol optical thickness is log-normally, rather than normally, distributed (O'Neill et al. [2000], Knobelspiesse et al. [2004]), which means there is the possibility of very large concentrations that are far from the arithmetic mean. The selection of the initial value for the number concentration is therefore quite difficult. As we see here, an incorrect selection can converge to a physically feasible local minimum in the cost function that is noticeably different from the minima that agrees with in situ observations. The HSRL data, then, were important because it was used to choose the initial number concentration, and the result was convergence to a much more consistent retrieval with lower uncertainties.

We next want to address why the specific set of parameters retrieved in 'unsuccessful' cases matched RSP observations so well. As we can see from the dashed lines in the bottom

panel of Fig. 3.3, there is no obvious difference between the squared error for 'successful' and 'unsuccessful' retrievals. Both cases are capable of matching RSP observations well, so in this case fit quality does not distinguish between 'successful' and 'unsuccessful' retrievals. To illustrate, Fig. 3.5 shows the match of model results to RSP observations for segment 170 (see table 3.8). Retrieval results without HSRL data were 'unsuccessful' in this segment, but their simulated total and polarized reflectances (dashed lines) are not dramatically different than those for a 'successful' retrieval using HSRL data (dash-dot lines; RSP data are solid lines). It appears that both 'successful' and 'unsuccessful' retrievals are similar in the observation space, $\mathbf{Y}$. Fig. 3.6 presents an interesting clue as to why this may be the case. In this plot, the retrieved size distributions for segment 170 are shown, along with the closest HiGEAR observation. There are considerable differences between the retrieved and observed size distributions for very small and coarse mode aerosols, but a striking similarity for radii between 0.1 and 0.6 μm. It appears that this size range is the optically relevant portion of the size distribution, and that the optimization technique faithfully matched those sizes, albeit in two very different ways. Another possibility is that multiple scattering effects (recall that this is a scene with a large optical thickness and thus significant multiple scattering) could mask differences between the two aerosol states. Fig. 3.7 presents the single scattering total (left) and polarized (right) phase functions at 532nm for the same segment with (solid) and without (dashed) HSRL data. The full phase function is plotted in the top row, while a zoom of the scattering angles we observe is in the bottom row. Clearly, there is a difference in single scattering properties between the two states, and this appears to be masked by multiple scattering (as we can see in Fig. 3.3). The lower single scattering albedo for the 'unsuccessful' case must be compensating for the larger phase function magnitude when multiple scattering is considered, since the angular dependence over the range of observation angles is similar for both 'successful' and 'unsuccessful' phase functions. Indeed, the high absorption retrieved in the 'unsuccessful' cases can be seen as a symptom of an incorrect size distribution, as that absorption is needed to account for the larger amount of scattering by the smaller size distribution at the

observed scattering angles.

Differences between 'successful' and 'unsuccessful' retrievals imply that there is a trade-off between the number of small particles (less than $0.1\mu m$ and complex refractive index that is weakly constrained by the observations. Both cases represent minima that are within the range of plausible aerosol properties, so success is highly dependent on initial value. This situation appears similar to results from an analysis of simulated ground based estimates of polarized sky observations (Cairns et al. [1997a]). Simulated retrievals were performed for haze and bimodal aerosol size distributions. Haze effective radius was correctly retrieved, but there was a substantial overestimate of small particles. The retrieved real refractive index for this case was about 0.1 larger than it should be, and the effective radius was quite different. These errors are similar to our 'unsuccessful' case, especially since both the simulation and the retrieval size distributions were similar in the 0.1-1.0 μm range (see Fig. 5b in Cairns et al. [1997a]). Furthermore, differences between the single scattering phase functions were masked by multiple scattering when modeling an optical depth of 0.5.

This illustrates a weakness in the ability to retrieve the number of aerosols whose size is large enough to activate as a cloud condensation nuclei (CCN) at higher supersaturations (roughly 0.03 to 0.07 μm). The number of aerosols in this size range is important if we are to understand aerosol indirect effects on clouds, since Dusek et al. [2006] found that cloud nucleation is more determined by the aerosol size distribution than its chemical composition. However, aerosol plumes with number concentrations and opacity as thick as we have observed may also have difficulty nucleating in an updraft because of the strong competition for water vapor between particles. Sensitivity to CCN sized aerosols is a topic of ongoing interest that needs to be addressed for polarimetric remote sensing at lower aerosol optical depths, where concentrations of smaller particles may be important for the creation of cloud droplets.

The large uncertainty in the retrieved aerosol optical thickness must also be discussed. Aerosol optical depth uncertainty for both 'successful' and 'unsuccessful' retrievals is typ-

ically about 50%, which in an absolute sense has an average value 0.39 at 532nm for retrievals that use HSRL data. To find the source of this error we break down the components of the summation in equation 3.13, which are displayed in table 3.6. Uncertainties in effective radius are by far the largest source of optical thickness uncertainty, although uncertainties from effective variance, real refractive index and the correlation between effective radius and variance are also large contributors. It appears that the problems associated with a proper retrieval of the size distribution cascade down to the uncertainty analysis for optical depth. Even so, optical depth retrievals match in situ observations very well, and do not exhibit a sampling variability that is consistent with the large uncertainty in optical depth indicated by the analysis. The standard deviation of the set of HSRL assisted retrievals of optical thickness at 532nm is 0.05, which is far smaller than the mean assessed uncertainty, 0.39. This indicates that the assessment of optical thickness uncertainty is too high.

It is possible that our observation error covariance matrix, $\mathbf{C}_T$, is too large. A breakdown of the relative magnitude of the components of equation 3.3 shows that the error due to aircraft pitch angle, $\mathbf{C}_p$, is the largest contributer to the total error covariance matrix. This is based upon a rather arbitrary selection of 0.5° as the error in pitch angle. As described in Sect. 3.3, the Inertial Monitoring Unit (IMU) onboard the B-200 was not very accurate (and has since been replaced), so we needed to correct the heading and pitch angles. We did so by confirming that various features in observed data were aligned properly, including the polarization azimuth. We then chose the uncertainty in pitch and heading angle (0.5° each) to represent our best guess for our accuracy during that alignment. It is possible that we chose too large of an error for the pitch angle. Reducing the pitch angle error to 0.1° significantly reduces the assessed error. If this is done for our sample segment (170), the norm of the error covariance matrix is reduced by 32% and the optical thickness error is reduced from 46.6% to 35.1%. Pitch angle error reduction affects nearly all parameters, but the greatest impact is for optical thickness, as is displayed in table 3.7. In that table, we also show the uncertainties computed without any geometry related errors (as will presumably be the case for orbital sensors such as APS). Uncertainties are further reduced,

although optical thickness still has a relatively large 28.2% error. Another large contributer to $\mathbf{C}_T$ was $\mathbf{C}_{ag}$, which we included to account for the variability of the set of scans we averaged for each segment. $\mathbf{C}_{ag}$ is not as large as $\mathbf{C}_p$, but its reduction could also bring the optical depth uncertainty down to a level that is more consistent with what one would expect based on sampling uncertainty. In other scenarios, averaging over a greater number of scans would reduce $\mathbf{C}_{ag}$, but because of the large spatial variability we encountered in this plume we did not take this additional step.

3.5 Conclusion

In this paper, we have retrieved aerosol parameters of smoke from recent boreal forest fires. This is a particularly difficult type of aerosol to retrieve because it is both absorbing and unevenly distributed vertically, which is information that is difficult to retrieve simultaneously. We tested the utility of lidar data when calculating optimal estimates of aerosol properties using our airborne polarimeter. To do so, we did about twenty retrievals on data collected when our instrument, the RSP, was overflying a fresh smoke plume. We performed these retrievals with the RSP data alone, and then repeated them using information gathered by a lidar instrument called the HSRL. This information included observations of the altitude of the elevated aerosol layer and the aerosol column optical depth. The latter was used to compute the initial value for number concentration during optimization, while the aerosol layer altitude was held fixed with the structure determined by the lidar.

We retrieved aerosols that are characteristic of boreal forest fire smoke when our optimizations were constrained by HSRL data. These aerosols compared well to a variety of in situ observations measured concurrently within the smoke plume. Retrievals performed without HSRL data were successful (in terms of matching the HSRL constrained retrievals) only about half of the time. While 'successful' retrievals without HSRL data were nearly identical to retrievals performed with the aid of HSRL data, 'unsuccessful' retrievals found aerosols that were small (but with very wide size distributions and an excess of small par-

ticles) with unusually large real and imaginary modes of the complex refractive index (the latter indicating significant absorption). These 'unsuccessful' retrievals occur because the initial number concentration value is too far from the actual solution and the optimization became trapped in a local minimum. HSRL estimates of aerosol optical depth (and thus number concentration) were therefore an important factor in retrieval success, and resulted in more consistent and stable results for the set of analyzed scenes.

This work presents a strong argument that operational remote sensing of high loads of small particles with instruments such as the Aerosol Polarimetry Sensor will require either an independent estimate of number concentration, or the help of a table lookup to provide an initial value. Otherwise, incorrect values may be retrieved for refractive index and size, although it is important to note that mean retrieval single scattering albedos with and without HSRL data are within an acceptable uncertainty range of in situ observations. In all cases the spectral optical depth retrievals were consistent with AATS-14 measurements. Despite the substantially different microphysical retrievals, this retrieved property is robust. Aerosol vertical distribution does not appear as important as it was for the smoke aerosols analyzed by Waquet et al. [2009a], but this may be due to the large vertical extent and weak absorption of this boreal forest fire smoke.

We have also demonstrated the importance of an accurate understanding of aircraft geometry for retrievals such as this. Our error estimate of 0.5° for the view zenith angle was the largest contributor to our error covariance matrix and is responsible for the very large estimate of uncertainty for aerosol optical thickness (although it contributed to the uncertainty of all retrieved parameters).

The RSP and HSRL instruments remain on the B-200 aircraft in anticipation of the NASA Glory satellite launch. Validation field campaigns including in situ measurement instrumentation will have the capability to repeat the comparison methods presented here, and hopefully establish the utility of future APS observations for a variety of aerosol types.

3.6 Appendix

The retrieval segment location, time, and solar and instrument geometry is presented in table 3.8.

Table 3.1: Retrieved aerosol parameters and the initial values used in optimization. Parameters listed in italics are optimized during the retrieval, while all others are kept constant. †: Refractive Index values have no spectral dependence. ‡: For optimizations that utilize data from the HSRL, the a priori number concentration is determined by the HSRL observations. §: For optimizations that utilize data from the HSRL, the aerosol layer height is fixed by HSRL observations and not changed during optimization.

Parameter	**Symbol**	**Unit**	**a priori**
Fine mode parameters			
Real refractive index †	$\Re(m_f)$	n/a	1.52
Imaginary refractive index †	$\Im(m_f)$	n/a	0.0094
Effective radius	$r_{e,f}$	μm	0.15
Effective variance	$v_{e,f}$	n/a	0.20
Number concentration‡	n_f	# μm^{-2}	5.5
Coarse mode parameters			
Real refractive index †	$\Re(m_c)$	n/a	1.52
Imaginary refractive index †	$\Im(m_c)$	n/a	0.0094
Effective radius	$r_{e,c}$	μm	3.21
Effective variance	$v_{e,c}$	n/a	0.23
Number concentration‡	n_c	# μm^{-2}	0.0001
Other parameters			
Aerosol height§	h	m	5000

Table 3.2: Derived aerosol parameters. λ is wavelength.

Parameter	**Symbol**	**Unit**	**Calculation**
Scattering cross-section	$\sigma_s(\lambda)$	μm^2	model byproduct
Absorption cross-section	$\sigma_a(\lambda)$	μm^2	model byproduct
Extinction cross-section	$\sigma_e(\lambda)$	μm^2	$\sigma_e(\lambda) = \sigma_a(\lambda) + \sigma_s(\lambda)$
Asymmetry parameter	$g(\lambda)$	n/a	model byproduct
Aerosol optical thickness	$\tau(\lambda)$	n/a	$\tau(\lambda) = n\sigma_e(\lambda)$
Ångström exponent	α	n/a	Slope of $ln(\lambda)$ vs. $ln(\sigma_e(\lambda))$
Single scattering albedo	$\varpi(\lambda)$	n/a	$\varpi(\lambda) = \sigma_s(\lambda)/\sigma_e(\lambda)$
Phase function at backscatter	$P_{11}(\lambda, \Theta = 180°)$	n/a	model byproduct
Backscatter extinction ratio	$S(\lambda)$	sr	$4\pi/\left[\varpi(\lambda)P_{11}(\lambda, \Theta = 180°)\right]$

Table 3.3: Directly retrieved aerosol parameters. The mean and median are calculated for the set of optimizations. Uncertainties (denoted $\pm$) are the median value returned by the optimization routine. Ratios are the standard deviation of the set of optimization results divided by the median optimization uncertainty.

Parameter	**without HSRL**		**with HSRL**	
	median	*mean*	*median*	*mean*
$\Re(m_f)$	1.57	1.55 ± 0.075	1.44	1.45 ± 0.054
$\Im(m_f)$	0.015	0.016 ± 0.0064	0.005	0.005 ± 0.0036
$r_{e,f}$	0.10	0.11 ± 0.012	0.14	0.14 ± 0.018
$v_{e,f}$	0.38	0.32 ± 0.049	0.23	0.24 ± 0.048
n_f	82.25	61.74 ± 0.182	14.27	17.04 ± 0.111
n_c	0.0001	0.0001 ± 0.0020	0.0009	0.0008 ± 0.0020
h	5475	5457 ± 0.004		

Table 3.4: Derived aerosol parameters. The mean and median are calculated for the set of optimizations. Uncertainties (denoted $\pm$) are the median value returned by the optimization routine. Optical thickness (τ), scattering, absorption and extinction cross-sections (σ_s, σ_a and σ_e), and single scattering albedo (ϖ), are all expressed at 532nm.

Parameter	**without HSRL**		**with HSRL**	
	median	*mean*	*median*	*mean*
σ_s	0.008	0.019 ± 0.0044	0.033	0.032 ± 0.0196
σ_a	0.0010	0.0010 ± 0.00052	0.0011	0.0010 ± 0.00093
σ_e	0.009	0.020 ± 0.0048	0.034	0.033 ± 0.0200
τ	0.666	0.671 ± 0.3038	0.695	0.693 ± 0.3903
α	2.35	2.43 ± 0.204	2.53	2.52 ± 0.258
ϖ	0.915	0.917 ± 0.0318	0.960	0.960 ± 0.0210

Table 3.5: Retrieved aerosol results for validation data. The mean and median are calculated for the set of optimizations. Uncertainties (denoted $\pm$) are the median value returned by the optimization routine. Optical thickness (τ), single scattering albedo (ϖ) and the backscatter to extinction ratio (S) are expressed at 532nm.

Parameter	median	mean
AATS τ	0.617	0.614 $\pm$ 0.0051
HSRL τ	0.650	0.658 $\pm$ 0.0200
RSP without HSRLτ	0.666	0.671 $\pm$ 0.3038
RSP with HSRLτ	0.695	0.693 $\pm$ 0.3903
HiGEAR ϖ	0.941	0.940 $\pm$ 0.0007
RSP without HSRL ϖ	0.915	0.917 $\pm$ 0.0318
RSP with HSRL ϖ	0.960	0.960 $\pm$ 0.0210
HiGEAR $r_{e,f}$	0.112	0.112 $\pm$ 0.0022
RSP without HSRL $r_{e,f}$	0.100	0.113 $\pm$ 0.0118
RSP with HSRL $r_{e,f}$	0.142	0.140 $\pm$ 0.0180
HiGEAR $v_{e,f}$	0.252	0.252 $\pm$ 0.0011
RSP without HSRL $v_{e,f}$	0.380	0.325 $\pm$ 0.0492
RSP with HSRL $v_{e,f}$	0.230	0.238 $\pm$ 0.0476
HSRL S	49.4	49.5 $\pm$ 4.5
RSP without HSRL S	54.9	57.2 $\pm$ 8.6
RSP with HSRL S	66.0	65.7 $\pm$ 12.1

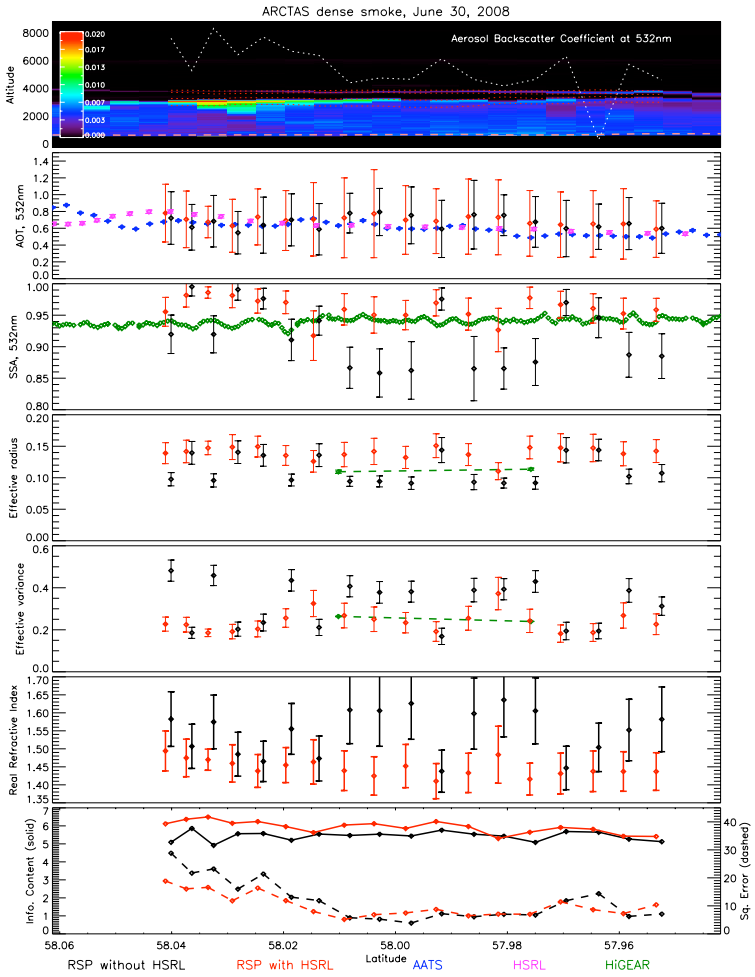

Figure 3.3: RSP, HSRL, AATS and HiGEAR data are plotted with respect to latitude (aircraft were flying to the South). The top panel shows the HSRL aerosol backscatter coefficient at 532nm. The dashed white line is the retrieved aerosol layer height for RSP observations that did not include HSRL data. Dashed red lines indicate the HSRL determined aerosol layer heights used for RSP retrievals that used HSRL data. The orange dashed line indicates the altitude of the P-3 aircraft, which carried the AATS and HiGEAR instruments. The second panel is the total aerosol optical thickness at 532nm for RSP retrievals without HSRL data (black), RSP retrievals with HSRL data (red), AATS (blue) and HSRL (magenta). That color scheme is maintained for the rest of the panels, with green indicating HiGEAR data in the third, fourth and fifth panels (Single Scattering Albedo, Effective Radius and Effective Variance, respectively). The sixth panel, with real refractive index, contains RSP data alone, indicating the validation difficulty of this parameter. Finally, the bottom panel is the information content (solid lines) and squared retrieval error (dashed lines) for the two RSP optimization methods.

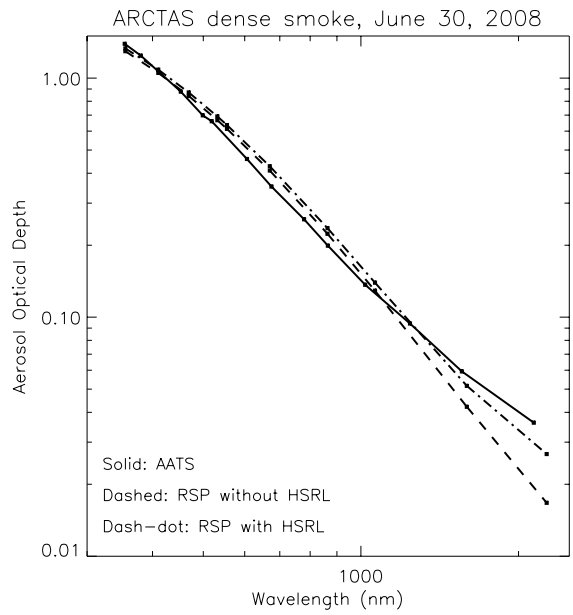

Figure 3.4: Here we compare spectrally dependent aerosol optical thicknesses for AATS (solid) and RSP retrievals with and without HSRL data (dash-dot and dashed, respectively). Values represent the average over the time and space shown in Fig. 3.3

Table 3.6: Error components for fine mode optical thickness at 532nm for the segment 170 retrieval with HSRL data and solar zenith angle error assessed at 0.5°. These are the elements within the summations in equation 3.13.

	n_f	$\Re(m_f)$	$\Im(m_f)$	$r_{e,f}$	$v_{e,f}$
n_f	0.0000	0.0000	0.0000	0.0000	0.0000
$\Re(m_f)$	0.0000	0.0143	-0.0002	-0.0379	-0.0100
$\Im(m_f)$	0.0000	-0.0002	0.0000	0.0007	-0.0001
$r_{e,f}$	0.0000	-0.0379	0.0007	0.1074	0.0272
$v_{e,f}$	0.0000	-0.0100	-0.0001	0.0272	0.0141

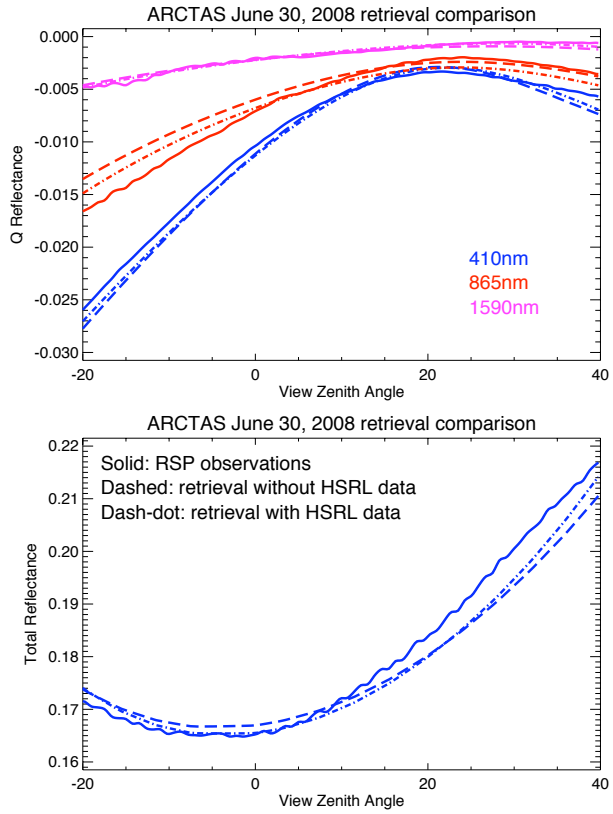

Figure 3.5: These plots show results from a successful optimization utilizing HSRL data (dash-dot) compared to an unsuccessful optimization performed without HSRL data (dashed). This segment is the third from the left in Fig. 3.3, and RSP observed reflectances are plotted with solid lines. For clarity, the 470, 555 and 670nm bands are omitted, although they show a similar situation: optimization retrieved reflectances are quite similar for both cases.

Table 3.7: Percent error for the segment 170 retrieval with HSRL data. The first row represents the original uncertainty assessment. The second is the uncertainty if the error covariance matrix is altered to represent a pitch angle uncertainty reduction from 0.5° to 0.1°. The last row represents the uncertainty if there is no contribution to the error covariance matrix from heading or pitch error.

	τ	ϖ	n_f	$\Re(m_f)$	$\Im(m_f)$	$r_{e,f}$	$v_{e,f}$	n_f
Original $\mathbf{C}_T$	46.6%	2.3%	10.8%	5.0%	0.4%	1.8%	3.0%	0.2%
$\sigma_\phi = 0.1°$	35.1%	1.7%	10.8%	3.6%	0.3%	1.3%	2.3%	0.2%
$\mathbf{C}_y = \mathbf{C}_p = 0$	28.2%	1.3%	10.8%	2.9%	0.2%	1.1%	1.8%	0.1%

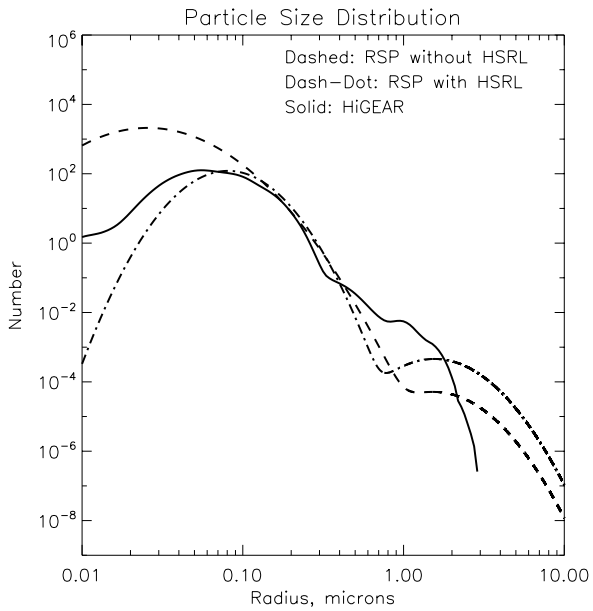

Figure 3.6: This plot presents the retrieved and observed size distributions for the segment in Fig. 3.5. RSP results for a failed optimization without HSRL have dashed lines, RSP results for a successful optimization using HSRL data are represented as dash-dots, and the closest HiGEAR size distribution has a solid line. Because of the differences in sampling area, the HiGEAR data were normalized to the successful RSP size distribution.

Table 3.8: Retrieval segment location, time, and solar and instrument geometry. Altitude is in meters above sea level. Optimizations without HSRL data for segments marked with a † were deemed 'unsuccessful'.

Starting Scan	index	UTC time	Latitude	Longitude	Heading	Track	Solar Azimuth	Solar Zenith	Altitude
160†	0	20:28:54	58.040	-104.606	259.7	240.0	213.2	38.3	8681
165	1	20:29:03	58.036	-104.618	256.3	237.0	213.2	38.3	8681
170†	2	20:29:11	58.032	-104.628	255.1	234.5	213.2	38.3	8680
175	3	20:29:20	58.028	-104.639	251.8	230.9	213.3	38.3	8680
180	4	20:29:28	58.024	-104.649	250.0	230.0	213.3	38.3	8681
185†	5	20:29:37	58.019	-104.660	248.2	226.7	213.4	38.3	8681
190	6	20:29:45	58.014	-104.669	246.5	225.0	213.4	38.3	8681
195†	7	20:29:53	58.008	-104.680	246.6	224.3	213.4	38.3	8682
200†	8	20:30:02	58.003	-104.689	246.5	222.3	213.5	38.3	8683
205†	9	20:30:10	57.997	-104.699	244.4	223.0	213.5	38.3	8683
210	10	20:30:19	57.992	-104.708	249.4	222.6	213.6	38.3	8684
215†	11	20:30:27	57.986	-104.718	244.1	222.3	213.6	38.3	8683
220†	12	20:30:35	57.981	-104.728	243.9	223.1	213.6	38.3	8685
225†	13	20:30:44	57.975	-104.738	240.4	223.4	213.7	38.3	8687
230	14	20:30:52	57.969	-104.747	242.1	223.3	213.7	38.3	8687
235	15	20:31:01	57.964	-104.757	242.7	222.1	213.8	38.3	8686
240†	16	20:31:09	57.958	-104.767	241.8	222.6	213.8	38.3	8686
245†	17	20:31:18	57.952	-104.777	240.9	222.5	213.8	38.3	8687

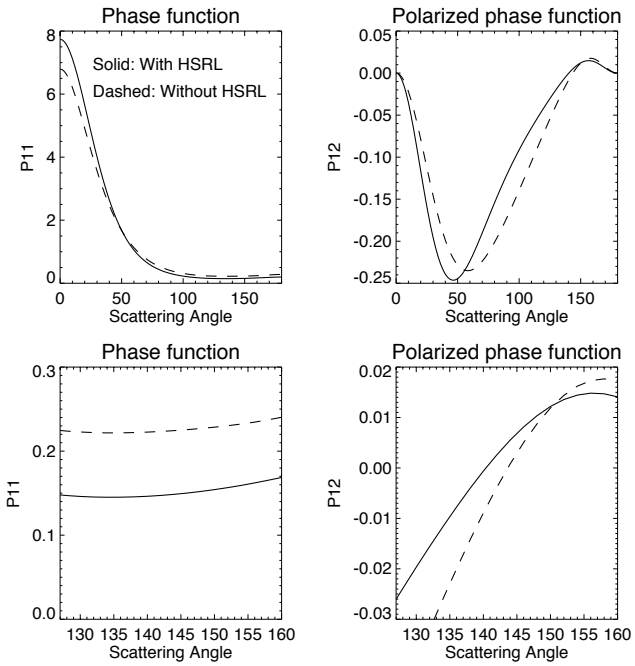

Figure 3.7: These plots show the phase functions at 532nm of the fine mode aerosols for the segment in Fig 3.5. Successful optimization results using HSRL data are shown with solid lines, while unsuccessful optimization results performed without HSRL data have dashed lines. Plots in the left column are the total (unpolarized) phase function, while plots in the right column are the polarized phase function. Figures in the top and bottom rows show the same quantities, although the bottom rows have been zoomed to a scattering angle range that was observed by the RSP in that segment.

Simultaneous retrieval of aerosol and cloud properties during the MILAGRO field campaign

to be submitted to the peer reviewed journal

Atmospheric Chemistry and Physics

full citation:

K. Knobelspiesse, B. Cairns, J. Redemann, R.W. Bergstrom, and A. Stohl. Simultaneous retrieval of aerosol and cloud properties during the MILAGRO field campaign. *to be submitted to Atmos. Chem. Phys.*, 2010.

Chapter 4

Simultaneous retrieval of aerosol and cloud properties during the MILAGRO field campaign

Estimation of Direct Climate Forcing (DCF) due to aerosols in cloudy areas has historically been a difficult task, mainly because of a lack of appropriate measurements. The Aerosol Polarimetry Sensor (APS), on the upcoming NASA Glory mission, has the potential to retrieve both cloud and aerosol properties because of its polarimetric, multiple view angle, and multi spectral observations. The APS airborne prototype is the Research Scanning Polarimeter (RSP), which has similar characteristics and can be used to demonstrate APS capabilities. In the spring of 2006, the RSP was deployed on an aircraft based in Veracruz, Mexico, as part of the Megacity Initiative: Local and Global Research Observations (MILAGRO) field campaign. On March 13th, the RSP over flew an aerosol layer lofted above a low altitude marine stratocumulus cloud close to shore in the Gulf of Mexico. We investigate the feasibility of retrieving aerosol properties over clouds using these data. Our approach is to first determine cloud droplet size distribution using the angular location of the cloud bow and other features in the polarized reflectance. The selected cloud was then used in a multiple scattering radiative transfer model optimization to determine the aerosol optical properties and fine tune the cloud size distribution. In this scene, we were able to retrieve aerosol optical depth, the fine mode aerosol size distribution and the cloud droplet size distribution to a degree of accuracy required for climate modeling. This required as-

sumptions about the aerosol vertical distribution and the optical properties of the coarse aerosol size mode. A sensitivity study was also performed to place this case study in the context of the potential for future systematic APS observations of this kind, which found that the aerosol complex refractive index can also be observed accurately if the aerosol optical depth is larger than roughly 0.8 at a wavelength of $0.555\mu m$.

4.1 Introduction

The radiative effects of atmospheric aerosols (suspended particles) are among the least certain components of global climate models [IPCC, 2007]. Even the most simple aerosol radiative effect, Direct Climate Forcing (DCF), is difficult to model, mainly due to the heterogeneity of aerosol sources, evolution, sinks, and radiative properties, and the difficulties of global observation (Mishchenko et al. [2009]). DCF is defined as the change in radiative forcing at the top of the atmosphere from the scattering and absorption of anthropogenic aerosols, and it neglects more complicated impacts due to aerosol induced changes in cloud properties or the atmospheric temperature vertical profile. Current modeling capability can be found in the results of the AeroCom model intercomparison effort. For example, Schulz et al. [2006] found a DCF range of +0.04 to -0.41 Wm^{-2}. A sensitivity analysis in this work found that DCF is strongly affected by aerosol forcing efficiency (the radiative forcing of a unit optical depth). Unfortunately, many factors that change aerosol forcing efficiency, such as particle size, absorption, and refractive index, are rarely observed to the level of accuracy required by climate models (Mishchenko et al. [2007b]). Furthermore, most aerosol remote sensing algorithms with passive instruments are successful only in cloudless conditions. Efforts to observe aerosols in the presence of clouds are still in their infancy, and are often intertwined with aerosol optical property assumptions.

The object of this study is the retrieval of aerosol properties when they are suspended above water phase boundary layer clouds. Aerosols above clouds (henceforth abbreviated as AAC) are a potentially important component of positive DCF, since absorbing AAC can

significantly reduce a high underlying cloud albedo and therefore alter forcing (Haywood et al. [1997]). However, reliable estimates of the global prevalence and anthropogenic component of this type of forcing are limited by a lack of appropriate observations, especially since DCF is strongly dependent on aerosol optical properties. Several approaches have been developed recently to observe AAC, but they are limited in their ability to distinguish aerosol types because of the significant assumptions required by their retrieval algorithms. Chand et al. [2008] used the active observations of the Cloud-Aerosol Lidar and Infrared Pathfinder Satellite Observations (CALIPSO) instrument to determine AAC optical depth at two wavelengths. The ratio of the optical depth spectral pair suggests the aerosol particle size. This method is therefore somewhat limited in its ability to determine DCF from AAC, although these type of data show promise in their potential for combined retrievals with passive remote sensing data. Another method uses passive spectrometer observations at ultra-violet wavelengths from instruments such as the Scanning Imaging Absorption Spectrometer for Atmospheric Chartography (SCIAMACHY). De Graaf et al. [2007] fit simulations of biomass burning (smoke) AAC to observations from the SCIAMACHY instrument to determine the aerosol total and absorbing optical thickness. An alternate technique, which we apply here, is to use multi-angle, multi-spectral, passive observations of polarized reflectance to simultaneously determine cloud and AAC optical properties. Waquet et al. [2009c] demonstrated this technique using data from the Moderate Resolution Imaging Spectroradiometer (MODIS) and the Polarization and Anisotropy of Reflectances for Atmospheric Sciences Coupled with Observations from a Lidar (PARASOL) instruments. Both instruments were a part of the so called 'A-train' polar orbit until recently (January, 2010), when the PARASOL instrument was moved to another orbit with the consumption of the fuel it needed to safely maintain its position. Waquet et al. [2009c] combined MODIS retrievals of cloud top height with PARASOL polarized observations at a variety of scattering angles to determine the aerosol optical thickness of biomass burning AAC in the South Atlantic Ocean. This required assumptions about the aerosol size and refractive index, since a single PARASOL band (at $0.865\mu m$) and a single scattering model

were used. PARASOL also has a somewhat coarse angular resolution, which means observations over a large area must be collected in order to observe the cloud bow (which is similar to a rainbow, but is due to scattering from cloud, and not rain, droplets) with enough angular sampling to accurately constrain cloud optical properties. Nevertheless, we believe this approach has potential for the Aerosol Polarimetery Sensor (APS), which will have greater angular resolution and more available spectral bands than PARASOL.

The Aerosol Polarimetery Sensor (APS) is a scanning polarimeter to be launched on the upcoming NASA Glory mission (Mishchenko et al. [2007a]). APS is intended to retrieve aerosol and cloud optical properties to a high degree of accuracy. It will do so by gathering a large amount of information in each scene: solar reflected linear polarization at about 250 viewing angles in nine channels at visible and near infra-red wavelengths. Cloud and aerosol properties will be retrieved by matching a doubling and adding radiative transfer model (Hansen and Travis [1974]) to observations. An airborne prototype of APS, the Research Scanning Polarimeter (RSP), was developed to test APS observational capabilities (Cairns et al. [1997b], Cairns [2003]). APS and RSP have very similar characteristics, where the latter has fewer view zenith angles (152) and slightly different center wavelengths for some bands. The RSP has flown on a variety of aircraft in many field campaigns. Field campaign data have been used to validate the ability of RSP/APS type instruments to observe aerosols over the ocean (Chowdhary et al. [2001], Chowdhary et al. [2002], Chowdhary et al. [2005a]), aerosols over land (Elias et al. [2004], Waquet et al. [2009a]), cloud optical properties (Chowdhary et al. [2005b]), surface reflectance properties (Knobelspiesse et al. [2008], Litvinov et al. [2010]), and of extremely optically thick plumes where the surface is obscured (Knobelspiesse et al. [2010]).

In the spring of 2006, the RSP participated in a large field campaign called Megacity Initiative: Local and Global Research Observations (MILAGRO). The goal of MILAGRO was to examine the behavior, transport, and evolution of emissions from the Mexico City Metropolitan Area (MCMA). More than 450 scientists from 150 institutions participated, involving instrumentation onboard seven aircraft, multiple ground sites, and the coordi-

nated use of atmospheric models and orbital observations (Molina et al. [2010]). NASA's participation in MILAGRO was called the Intercontinental Chemical Transport Experiment - B (INTEX-B), for which the RSP was deployed on the Sky Research, Inc., Jetstream-31 (J-31) aircraft. The J-31 was based in Veracruz, Mexico for three weeks in February and March, and performed a total of thirteen successful research flights. In addition to the RSP, several other instruments were part of the J-31 payload. This included the Ames Airborne Tracking Sunphotometer (AATS-14) (Redemann et al. [2009], Livingston et al. [2009]), the Solar Spectral Flux Radiometer (SSFR) (Bergstrom et al. [2010]), the Cloud Absorption Radiometer (CAR) (Gatebe et al. [2009]) and a Position and Orientation System (POS) and various meteorological sensors.

Aerosols encountered during MILAGRO were a complicated mix including urban/industrial particles from Mexico City (Doran et al. [2006], Lewandowski et al. [2010] Marley et al. [2009], Paredes-Miranda et al. [2009], Rogers et al. [2009] and others referenced in Molina et al. [2010]), smoke from local agricultural fires, and even volcanic sulfates (Grutter et al. [2008], de Foy et al. [2009]). In the first two weeks of March, 2006, transport from the MCMA was weak but generally to the east, allowing aerosols to mix and age before they were transported over the Gulf of Mexico. On the morning of March 13th, a layer of low altitude (probably marine stratocumulus) clouds formed over the Gulf coast of Mexico between the cities of Veracruz and Tamiahua (approximately 96.75°W and 20.25°N). The cloud slowly dissipated throughout the day, but was overflown by the J-31 aircraft, which later descended to the surface in a recently cloud free region. Observations by the SSFR and AATS-14 instruments on the J-31, along with aerosol transport model simulations, suggest that a layer of mixed aerosols were lofted above the cloud. This is therefore an ideal test scene for the ability of sensors such as RSP and APS to retrieve optical properties of AAC.

In the next section of this paper (4.2), we describe our methodology for the retrieval of AAC optical properties. Next (section 4.3), we perform a short sensitivity study to help us construct an appropriate optimization strategy for AAC scenes. We then examine the

retrieval results, and compare them with observations from other instruments on that day (section 4.4). We also investigate the optimization sensitivity to forward model assumptions. We then discuss the implications of our retrieval and sensitivity studies on the ability of RSP and APS to resolve AAC optical properties in the context of climate model requirements (section 4.5), followed by a brief conclusion.

4.2 Method

One benefit of multi-angle polarized measurements is that the various atmospheric components in a scene modify different angular portions of the observation. For our scene, where aerosols overlay a warm phase cloud, the cloud water droplet size distribution determines the angular location of the cloud bow (which typically exists at scattering angles somewhere around 142°) and the magnitude of secondary bows (Breon and Goloub [1998]). Aerosol properties such as optical depth, size distribution, and refractive index dominate the signal at side scattering angles less than 120° (Goloub et al. [2000]). Rayleigh scattering also contributes at these angles, which means multi-angle polarization observations can be used to determine cloud top heights in the absence of aerosols (Goloub et al. [1994]). When aerosols are present, retrieval of their optical properties requires external information about the cloud top height. Figure 4.1 illustrates the available information in a synthetic AAC scene. This is expressed by R_Q, which is defined below in equation 4.1. Note how the angular location of the cloud bow at high scattering angles changes with cloud droplet size distribution. Cloud top height has an impact at smaller scattering angles and the shorter wavelength, while AAC modify the magnitude of the cloud bow peak and alter the polarized reflectance at scattering angles less than $120°$ for all wavelengths.

In this paper, we test the capability of RSP to retrieve AAC optical properties. To do this, we start by identifying the cloud and aerosol vertical distribution using observations from other instruments on the J-31 aircraft. These are used to determine layer heights in a plane parallel radiative transfer model, which we iteratively modify to match to our obser-

vations using the Levenberg-Marquardt technique. The aerosol and cloud optical properties that create the best match are the 'retrieved' values. Initial optical properties must be close to the retrieved solution and therefore selected with care. We find cloud initial values by matching observations of the cloud bow angular location and width to single scattering simulations (scattering phase functions computed with Mie theory). Aerosol initial values were selected from the "Urban-industrial and mixed; Mexico City" class described in Dubovik et al. [2002]. This climatology was derived from a year of ground based measurements by the Aerosol Robotic Network (AERONET). The aerosol optical depth initial value comes from observations by the AATS-14 instrument during a spiral to the surface in a cloud free region near our scene.

The RSP observes the first three components of the Stokes polarization vector (I, Q and U), meaning it is sensitive to both linearly polarized and total radiance (Hansen and Travis [1974]). For remote sensing, it is often useful to express the polarization components of the Stokes vector in terms of reflectance. This takes the exo-atmospheric radiance into account, and is calculated:

$$R_I = \frac{I\pi r_o^2}{F_o \cos\theta_s}$$

$$R_Q = \frac{Q\pi r_o^2}{F_o \cos\theta_s} \tag{4.1}$$

$$R_U = \frac{U\pi r_o^2}{F_o \cos\theta_s}$$

where F_o is the annual average exo-atmospheric irradiance (W/m^2), r_o is the solar distance in AU (thus compensating for solar distance deviation from average throughout the year), and θ_s is the solar zenith angle. The RSP instrument has a high (0.2%) absolute accuracy for R_Q and R_U relative to R_I, as the same detectors are used to measure intensity and linear polarization, and because calibration of their relative gain is performed with each scan. R_U typically becomes very small when Q and U are defined with respect to the scattering plane (containing the solar illumination and observation vectors), so we subsequently use R_Q defined in this plane as a proxy for total linear polarization. R_U is only used to help

correct for errors in aircraft geometry.

Our radiative transfer model uses Mie theory to compute the polarized phase functions (single scattering) for various types of aerosols or cloud droplets, and Rayleigh scattering for gases (for a historical review of Mie theory, see Mishchenko and Travis [2008]). This means we require a measure of cloud droplet size distribution, aerosol size distribution (which is typically bimodal) and the complex aerosol refractive index ($m = \Re(m) + \Im(m)$), and that we assume the aerosols scatter like spheres. We express size distribution as an effective radius, r_e, and variance, v_e, where the former has units of microns and the latter is unitless (Hansen and Travis [1974]). The size distribution of aerosols is typically bimodal, so we use the subscripts f and c to refer to fine and coarse mode aerosols. The former is usually the product of a chemical reaction, such as sulfate photo-oxidation or the production of biomass burning aerosols, and the latter is due to physical processes such as the creation of sea salt or dust aerosols. Cloud size parameters are denoted with the subscript cl. We use the lognormal distribution for aerosols and the gamma distribution for cloud droplets (equations 2.60 and 2.56 in Hansen and Travis [1974]). The complex refractive index, m, is set independently for each mode. In this work we assume the real part of m is spectrally independent, while the imaginary component of the fine mode is specified with two parameters (see section 4.2.4).

Once the single scattering properties for an aerosol or cloud droplet have been determined, multiple scattering is computed for the full atmosphere to create the polarized reflectance at the observation altitude. We use the Doubling and Adding technique (Hansen and Travis [1974], De Haan et al. [1987]), which assumes plane parallel layers of clouds and aerosols. The altitude of these layers are determined during the J-31 atmospheric profile as described in section 4.2.2 and they are held constant in the optimization. The optical depth, τ, of each layer is also required. As noted above, initial aerosol optical depth values are derived from the AATS-14. Cloud optical depth is set arbitrarily large ($\tau_{cl}(0.555\mu m) = 10.0$) to saturate the signal, since polarized reflectance is only sensitive to the first few units of cloud optical depth. Because of this, the surface is obscured and we

Table 4.1: Retrieved aerosol parameters and the a priori values used in optimization. Parameters listed in italics are optimized during the retrieval, while all others are kept constant. †: Refractive Index values have no spectral dependence in the initial values, although the spectral dependence of the fine mode aerosol imaginary component is allowed to vary as described in Section 4.2.4.

Parameter	**Symbol**	**Initial value**
Fine mode aerosols		
Optical depth, 0.555μm	$\tau_f(0.555)$	0.12
Real refractive index †	$\Re(m_f)$	1.47
Imaginary ref. index, 0.555μm†	$\Im(m_f)$	0.014
Imaginary refractive index, p†	$\Im(m_{f,p})$	0.007
Imaginary refractive index, q†	$\Im(m_{f,q})$	0.007
Effective radius, [μm]	$r_{e,f}$	0.20
Effective variance	$v_{e,f}$	0.20
Coarse mode aerosols		
Optical depth, 0.555μm	$\tau_c(0.555)$	0.04
Real refractive index †	$\Re(m_c)$	1.47
Imaginary refractive index †	k_c	0.014
Effective radius [μm]	$r_{e,c}$	7.67
Effective variance	$v_{e,c}$	0.49
Cloud droplets		
Optical depth, 0.555μm	$\tau_{cl}(0.555)$	10.0
Effective radius [μm]	$r_{e,cl}$	6.25
Effective variance	$v_{e,cl}$	0.075

assume its reflectance is negligible.

A complete list of the model values is presented in table 4.1. Italicized parameters are allowed to vary during optimization and are thus retrieved, while other parameters are fixed and considered part of the radiative transfer model.

4.2.1 AAC scene

On March 13th, 2006, the J-31 aircraft, containing the RSP and a variety of other instruments, departed from the Veracruz airport. The airplane flew northwest along the Gulf of Mexico coast and above a marine stratocumulus cloud. The cloud was in the process of dis-

sipating, and it had a larger geographical extent earlier in the day (Bergstrom et al. [2010]). Following the cloud overflight, the J-31 descended to the surface in a recently cloud free region. Figure 4.2 is a map of this scene, the descending spiral, and the surrounding area. We used observations that were made in that profile to constrain cloud and aerosol layer heights in our scene, on the assumption that the atmospheric vertical profile had not changed dramatically in the 125km distance between the observation location and descending spiral. Figure 4.3 is the temperature profile and vertical change in aerosol optical depth from this spiral. The temperature profile was used to determine the cloud top height (480m) for our radiative transfer model, as shown in blue in figure 4.3. Change in aerosol optical depth (equivalent to the aerosol extinction coefficient), from the AATS-14 instrument, was used to constrain the AAC height (550m to 750m), shown in grey. Table 4.2 lists the geometry and other specifics associated with this scene and the downward spiral. A full description of this and other J-31 flights during MILAGRO can be found in Molina et al. [2010].

4.2.2 Aerosol sources

The AAC we encountered in our scene were a complicated mixture with a variety of sources. Wind conditions on the 13th of March were light and variable, preceded by southwesterly winds associated with a trough over the western portion of the USA. This portion of the MILAGRO field campaign was characterized by low humidity and few cirrus clouds, and there were probable interactions between MCMA emissions and biomass burning smoke (Fast et al. [2007]). Aerosols from a variety of sources were found during MILAGRO, including sulfates of both industrial and volcanic origin (de Foy et al. [2009], Grutter et al. [2008]), and organic carbon. Secondary organic carbon was more dominant than primary organic carbon, and was the result of both urban and (generally anthropogenic) biomass burning activities (Doran et al. [2006], Crounse et al. [2009], Yu et al. [2009], Paredes-Miranda et al. [2009]). The MCMA is in a high valley (2200m+ above sea level), so it is feasible for anthropogenic aerosols to be lofted above low level marine stratocumulus clouds on the coast.

Table 4.2: Geometry and other parameters associated with our AAC scene, and the subsequent downward spiral. Aerosol optical depths are from the AATS instrument

Parameter	**Value**
AAC scene	
Starting Time	16:05 UTC
J-31 altitude	5380m
Latitude	20.15° N
Longitude	96.68° W
Solar Zenith Angle	44°
Relative Azimuth Angle	20°
Number of averaged scans	22
Downward Spiral	
Starting Time	16:22 UTC
J-31 altitude	5360 to 51m
Latitude	21.06° N
Longitude	96.95° W
Cloud top	480m
Aerosol layer bottom	550m
Aerosol layer top	750m
$\tau(0.519\mu m)$ above 550m	0.165
$\tau(0.604\mu m)$ above 550m	0.130
$\tau(2.139\mu m)$ above 550m	0.040

This leads us to believe that the AAC aerosols in our scene are probably anthropogenic and that the fine size mode is the dominant contributor to scattering and absorption. To further investigate the aerosol sources, we used the FLEXPART Lagrangian particle dispersion model (Stohl et al. [2005]) to determine the sensitivity of our scene to emission in other regions. Figure 4.4 is the footprint emission sensitivity obtained from FLEXPART driven by European Centre for Medium Range Weather Forecasts (ECMWF) meteorological data. Values of high emission sensitivity can be found both over the MCMA and biomass burning areas in the vicinity of Veracruz. However, results are somewhat different when the meteorology is driven by an alternate model, the Global Forecast System (GFS) from the National Center for Environmental Prediction (NCEP). FLEXPART driven by GFS shows

an increased influence of Veracruz area smoke at the expense of MCMA pollution. This disparity is probably due to the weak and variable winds at that time, and indicates that the aerosols have had the opportunity to mix, accumulate, and age, with the exact distribution of contributing sources being somewhat more uncertain than for other cases.

4.2.3 Determination of initial cloud size distribution

Prior to performing our retrieval, we made an initial estimate of the cloud size distribution using a Look Up Table (LUT) of cloud droplet single scattering properties. Goloub, in his paper describing cloud property retrieval from the Polarization and Directionality of Earth Reflectances (POLDER) instrument (Goloub et al. [2000]), found that polarization of cloud reflectances is insensitive to multiple scattering. As cloud optical thickness becomes greater than 2, R_Q in the single scattering approximation becomes

$$R_Q(\theta_s, \theta_v, \xi) = \frac{1}{4(cos\theta_s + cos\theta_v)} Q(\xi, r_{e,cl}, v_{e,cl}) \tag{4.2}$$

where θ_s is the solar zenith angle, θ_v is the view zenith angle and Q is the Stokes vector component of the single scattering phase function. ξ is the scattering angle, defined with respect to the incident illumination vector, and $r_{e,cl}, v_{e,cl}$ are the cloud effective radius and variance.

At large viewing angles, where R_Q is dominated by the cloud signal (see figure 4.1), we can identify the cloud size distribution independently from cloud optical thickness or multiple scattering effects. R_Q is sensitive to cloud effective radius at scattering angles larger than 130°, and effective radius at angles larger than 145° (Waquet et al. [2009c]).

Our initial estimate of cloud size distribution is determined by matching R_Q to a LUT of $Q(\xi, r_{e,cl}, v_{e,cl})$ for a variety of size distributions. We used scattering angles between 135° and 162° (which was the largest scattering angle available in our scene). The LUT contained effective radii between 5 and 20 μm at 0.25 intervals, and effective variances between 0.01 and 0.25. Aerosol and molecular effects above the cloud are expressed in a manner that does not change rapidly with scattering angle (unlike the sharp cloud bow

features), so we used a Fourier domain high pass filter (Gonzalez and Woods [1992]) to remove this low frequency signal prior to matching R_Q to the LUT. To account for the possibility that absorbing AAC dampen the cloud signal, we allow both $r_{e,cl}$ and $v_{e,cl}$ to vary during optimization.

4.2.4 Optimization

Aerosol and cloud optical properties are retrieved by comparing a radiative transfer simulation of our scene to RSP observations, and tuning the model parameters until the best match is found. We use the Levenberg-Marquardt optimization technique as described in Moré [1977] and Markwardt [2009], and implemented for the RSP in Knobelspiesse et al. [2010]. This means the retrieved parameters are not real numbers but regions of state space that are associated with the scene considering observational uncertainty. Waquet et al. [2009a] also used a similar approach with RSP data for aerosol retrievals over land.

We used the software developed in Knobelspiesse et al. [2010] for this study with slight modifications. First, we increased the numerical accuracy of the radiative transfer model. While computationally more expensive, this is required to properly simulate cloud droplets, which have much stronger forward scattering and produce more dramatic features than aerosols (such as cloud bows). We also modified the software so that the aerosol optical depth of a layer is a directly retrieved parameter. Previously, the total quantity of aerosols in a layer was determined by the particle number concentration, and this was the parameter that was tuned during optimization. Validation, however, is usually performed by comparisons of optical depth, since this is a common observation made by instruments such as sun photometers. While optical depth can of course be computed using the number concentration (and aerosol extinction cross section, which depends on size and refractive index), we switched to directly optimizing this parameter so that error computation is simpler. We also noticed that the optimization itself appears to require fewer iterations and is better behaved, although this observation is limited to this AAC scene.

We also modified the software in Knobelspiesse et al. [2010] to allow the imaginary

component of the refractive index to have a spectral dependence. Rather than using the single value for each size mode, we now use a pair of parameters, $\Im(m_p)$ and $\Im(m_q)$:

$$\Im(m(\lambda)) = \Im(m_p) + \Im(m_q)(\lambda + 0.445)^{-10} \tag{4.3}$$

where λ is the wavelength in microns. This spectral dependence function is intended to allow for the increase in absorption at shorter wavelengths due to ”brown carbon” (BrC, absorbing organic carbon aerosols). This was observed by the SSFR instrument on the same flight as our AAC scene (Bergstrom et al. [2010]), which is our primary motivation for this change.

The choice of this form of specular dependence is unfortunately somewhat arbitrary, as direct observations of the imaginary refractive index of aerosols in their entirety are difficult and quite limited. Evidence of absorption in observations of the aerosol optical depth, on the other hand, are much more common. The absorption optical depth, τ_a, which is the optical depth due to absorption but not scattering, is generally characterized with the equation

$$\tau_a(\lambda) = \tau_{a,o}(\lambda/\lambda_o)^{-\alpha} \tag{4.4}$$

where λ_o is a reference wavelength and $\tau_{a,o}$ is the absorption aerosol optical depth at that wavelength. α is the Ångström Exponent, which should be equal to 1.0 for very small particles with spectrally invariant refractive indices (van de Hulst [1981] and Bond [2001]). Larger Ångström Exponent values have been found in some biomass burning (smoke) aerosol plumes, such as in Lewis et al. [2008], indicating an increase in the imaginary refractive index (and thus absorption) at shorter wavelengths. Authors such as Hoffer et al. [2006] and Dinar et al. [2008] have found imaginary refractive indices that increase with decreasing wavelength for Humic-Like Substances (HULIS), which are likely components of BrC, but direct observations of entire aerosol particles are limited. Others (Chen and Bond [2010], Kirchstetter et al. [2004] and references therein) have found increasing aerosol absorption coefficients with shorter wavelength. While this is evidence of an increase in

shortwave imaginary refractive index, the absorption coefficient is also dependent on particle size and real refractive index.

For small particles, the imaginary refractive index is proportional to wavelength and absorption coefficient ($\Im(m(\lambda)) \propto \lambda a$) (Sun et al. [2007]), which we use to connect our model for imaginary refractive index in equation 4.3 to observations. The $\Im(m_p)$ parameter indicates the quantity of spectrally independent absorption, while $\Im(m_q)$ expresses the quantity of spectrally dependent absorption. A large negative exponent has been selected so that variations in $\Im(m_p)$ and $\Im(m_q)$ have very different impacts, which allows their simultaneous retrieval during optimization, since they are more orthogonal. The exponent value of -10 was chosen from the upper limit to the absorption Ångström Exponent found by Chen and Bond [2010]. Spectral dependence is also shifted so that $k(0.555) = \Im(m_p) + \Im(m_q)$ and $\Im(m(\lambda))$ converges to $\Im(m_p)$ to as wavelength increases.

Our optimization methods provide the retrieval error for each model parameter (see section 4.3). Since it is not directly parameterized, the uncertainty in k must be derived from the uncertainties in $\Im(m_p)$ and $\Im(m_q)$. Assuming that correlation between $\Im(m_p)$ and $\Im(m_q)$ is minimal, σ_k is determined by the retrieval error for those parameters.

$$\sigma_k^2(\lambda) = \sigma_{k,p}^2 + \sigma_{k,q}^2(\lambda + 0.445)^{-20} \tag{4.5}$$

4.3 Simulated aerosol above cloud

To help us design an appropriate optimization strategy, we first assessed the information content available in an AAC scene. We did this by simulating a climatologically defined aerosol at a variety of optical depths suspended above a marine stratocumulus cloud. Other than optical depth, aerosol optical properties were chosen to match the ”Mexico City Urban/Industrial” class described in Dubovik et al. [2002] and used as the initial value during optimization.

For each simulation, we numerically estimated the Jacobian matrix, **J**, which expresses

the sensitivity of the forward model to change in each parameter,

$$J_{ij}(\mathbf{x}) = \frac{\partial F_i(\mathbf{x})}{\partial x_j} \tag{4.6}$$

where the partial derivative of forward model, $\mathbf{F}$, for the simulated set of parameters, $\mathbf{x}$, is computed for each observation (i) and each parameter (j). The partial derivative was estimated numerically by perturbing the jth element of $\mathbf{x}$ (which we denote as $\mathbf{x}'$) and recalculating the forward model, $\mathbf{F}$.

$$J_{ij}(\mathbf{x}) \approx \frac{F_i(\mathbf{x}') - F_i(\mathbf{x})}{x'_j - x_j} \tag{4.7}$$

While the Jacobian is a useful metric to identify the relative importance of different parameters in measurement space, we are interested in parameter sensitivity. This is expressed with the retrieval error covariance matrix.

$$\mathbf{C}_x = (\mathbf{J}^T \mathbf{C}_T \mathbf{J})^{-1} \tag{4.8}$$

This requires the measurement error covariance matrix, $\mathbf{C}_T$, which is specific to the RSP and accounts for measurement uncertainty due to errors in calibration, and observation geometry. It is computed as in equation 3 of Knobelspiesse et al. [2010]. The square root of the diagonal elements of $\mathbf{C}_x$ are the standard deviations of the errors for each parameter in $\mathbf{x}$, provided that $\mathbf{C}_T$ is accurate and the forward model is linear over the perturbation range used to numerically calculate $\mathbf{J}$ (Hasekamp and Landgraf [2007]).

We simulated a scene very similar to the initial values we selected for optimization, with the exception of optical depth. Aerosol and cloud optical properties that were used for the simulation are listed in table 4.1, while the cloud and aerosol vertical distribution is described in table 4.2. Unlike our RSP scene, however, we selected a view zenith angle of $45°$ and relative azimuth angle of $45°$. This geometry was chosen to generalize the results for the APS, which will typically make observations farther from the solar principal plane (where $\phi = 0°$) than the RSP did in this scene. Observations in the solar principal plane contain more information than those at other relative azimuth angles because a larger

range of scattering angles are measured. For this reason, we would expect lower errors for the RSP viewing geometry, although errors from brief simulations we performed at observational relative azimuth angles were nearly identical.

We performed two different sets of simulations. The first set simulated an optimization that used R_Q in seven RSP bands (centered at 0.410, 0.470, 0.555, 0.670, 0.865, 1.590 and 2.250μm) at half degree intervals in the view zenith angle range of $\pm 60^\circ$ from nadir. At this geometry, the scattering angle range is from 85° to 150° and includes both side scattering angles (where aerosol properties dominate the signal) and the cloud bow (where cloud properties dominate the signal). The second simulation also used R_Q at the wavelengths described above, but view angles restricted to 20° to 60° in the forward direction. The scattering angles that correspond with this are between 85° and 120°, excluding the cloud bow. This is similar to the scattering angle range used to retrieve AAC properties in Waquet et al. [2009c], who was limited in his ability to determine cloud properties (due to the coarser angular resolution of POLDER) and performed an optimization using only observations where aerosol properties dominate.

Simulated retrieval errors are shown in figure 4.5. Aerosol remote sensing accuracy requirements for climate models, as assessed by Mishchenko et al. [2004], are also presented. These requirements were not determined for AAC, but for retrievals of aerosols over land (without the presence of clouds) or clouds without aerosols above. We include them in figure 4.5 to compare the potential of AAC retrievals with the standard retrievals by the APS instrument for which these accuracy requirements were determined. For the full angular range simulation, these accuracy requirements are indeed met for aerosol optical depth, fine mode aerosol size, and cloud droplet size. Real refractive index and single scattering albedo requirements are not met, although errors decrease and nearly approach the requirements as aerosol optical depth increases. Errors for the simulation with fewer viewing angles are clearly higher. Aerosol optical depth accuracy requirements are no longer met, and errors for fine mode effective variance are too high at very low optical depths. Simulations also show sensitivity to cloud droplet size and effective variance within accuracy requirements

for aerosol optical depths less than one. This is surprising considering that this simulation did not use observations of the cloud bow, where cloud properties should be dominant. These results, however, do not indicate the degree of correlation between different parameters in the retrieval. For the simulation with a total optical depth of $\tau(0.555) = 0.12$, the cloud effective radius was strongly correlated with the fine mode optical depth and fine mode effective variance (see appendix 4.7). Cloud effective variance was strongly correlated with the optical depth of both fine and coarse aerosols. These strong correlations do not exist for the equivalent retrieval that used the full angular range of observations.

These simulations suggest several strategies for successful optimization. The most obvious is that optimizations should utilize observations both of the cloud bow and side scattering angles. Cloud size parameters should be retrieved during optimization, since their assessed errors are low and those parameters are not significantly correlated with others (with one exception, see appendix 4.7). Furthermore, fine and coarse mode aerosol optical depth and fine mode size parameters can all be retrieved accurately. The real refractive index and absorption, however, are not retrieved accurately. Furthermore, those parameters have a high degree of correlation between themselves and with other parameters (see appendix 4.7). An ideal situation would be to have an accurate external measure of the aerosol complex refractive index that can be specified during optimization. Obviously, such measurements typically do not exist, so we are forced to consider retrieving some of the complex refractive index parameters, even if their retrieval error is larger than requirements for typical aerosol values. We are most interested in AAC absorption, since absorption is an important factor in the overall radiative forcing of AAC. The imaginary component of refractive index, however, is highly correlated with the optical depth of coarse mode aerosols. For our optimization, we decided to fix the real refractive index at the climatological value for Mexico City aerosols as contained in Dubovik et al. [2002], while allowing both parameters describing the imaginary refractive index (see section 4.2.4) to vary. Since the latter are correlated with coarse mode optical depth, we fixed that parameter to the optical depth observed by the AATS sun photometer at long wavelengths (where the coarse mode should

contribute the most to overall extinction). Free parameters in our retrieval are therefore the aerosol fine mode optical depth, both parameters describing the imaginary component of fine mode refractive index, fine mode effective radius and variance, and cloud droplet effective radius and variance.

4.4 Results

4.4.1 Cloud properties

As described in section 4.2.3, initial values for cloud droplet size were determined by matching a look up table of cloud droplet single scattering properties to observations. Because RSP observations also contain the effects of Rayleigh scattering and aerosols above the cloud, the cloud parameters determined with this method were allowed to vary in the next step, optimization. Here, aerosol and Rayleigh scattering effects were minimized by removing the low angular frequency trend before comparing the observation to the look up table. The best match was found for a cloud whose droplets have an effective radius of $r_{e,cl} = 6.25\mu m$ and effective variance of $v_{e,cl} = 0.075$. Figure 4.6 shows this match (before low frequency trends are removed) for three wavelengths. While there are significant offsets between the RSP observation and cloud model, the angular location of the cloud bow in the data are well represented with the model.

4.4.2 Aerosol and cloud simultaneous retrieval

Optimization was performed using the data, methodology and initial values described above to retrieve seven aerosol and cloud parameters. Eleven iterations of the Levenberg-Marquardt method were required to converge to a solution. Figure 4.7 shows the radiative transfer model match to the observations, while table 4.3 is the aerosol and cloud parameters that were retrieved from the model. Comparisons between these results and observations made by other instruments are presented in figure 4.8.

The optimized radiative transfer model appears to match best at forward scattering angles, where aerosol properties dominate. This is somewhat understandable in that the measurement error (as expressed in the error covariance matrix, $\mathbf{C}_T$) is smallest for these viewing angles. Measurement error is largest for cloud bow view zenith angles (between $-20°$ and $0°$) because of uncertainties in aircraft geometry that have the largest impact on features that change rapidly with angle. Perhaps as a result, model results are worst here, and underestimate the polarization in the cloud bow in all channels. However, we also found that few combinations of aerosol or cloud parameters could create such strong polarization in the cloud bow, indicating that our cloud model may be too simplistic. Regardless, aerosol and cloud parameter values have errors that are similar to those of the simulation in section 4.3 for comparable optical depths. Aerosol optical depth and size parameters have low errors that meet the accuracy requirements of Mishchenko et al. [2004]. There are no accuracy requirements for the aerosol imaginary refractive index, but the related single scattering albedo has an uncertainty so large as to render that parameter nearly useless. This is not much of a surprise, however, since the predicted error in single scattering albedo in the sensitivity test is comparable. The sensitivity test also shows that this error will decrease with increasing aerosol optical thickness, so that optical thicknesses above $\tau(0.555) = 0.8$ have single scattering albedo errors nearly within accuracy requirements. In other words, absorption errors decrease for aerosol loads that will have the most significant radiative forcing impact.

The retrieved AAC properties show a somewhat thin (about half the climatological median optical thickness) layer of aerosols that have a fine mode effective radius very similar to the climatology of Dubovik et al. [2002]. This is reasonable, however, because the observed altitudes represent only a portion of the atmospheric column and do not include, for example, boundary layer aerosols. The width of the fine mode size distribution is quite small, which may be explained by the hypothesis in Bergstrom et al. [2010] that these aerosols have been cloud processed (although it should be noted that aerosol size distribution was not directly observed in that paper). The cloud droplet effective radius is close to,

Table 4.3: Retrieved aerosol and cloud parameters. †: These parameters are derived from other parameters, not directly retrieved. Errors in bold are larger than accuracy guidelines from Mishchenko et al. [2004] (note that guidelines were not provided in this publication for imaginary refractive index, and were not intended for AAC retrievals).

Symbol	**Unit**	**Retrieval**	**Error**	**Simulation Error**
$\tau_f(0.555)$	n/a	0.104	0.016	0.009
$\tau(0.555)^\dagger$	n/a	0.144	0.016	0.009
$\Im(m_{f,p})$	n/a	0.000	0.062	0.064
$\Im(m_{f,q})$	n/a	0.003	0.036	0.015
$\Im(m_f)(0.532)^\dagger$	n/a	0.004	0.077	0.063
$r_{e,f}$	μm	0.143	0.007	0.029
$v_{e,f}$	n/a	0.057	0.036	0.106
$r_{e,cl}$	μm	6.82	0.187	0.061
$v_{e,cl}$	n/a	0.028	0.009	0.012
$\varpi(0.532)^\dagger$	n/a	0.868	**0.450**	**0.306**

but slightly smaller than, the climatology for marine clouds in Miles et al. [2000]. Compared to the initial values, the cloud effective radius increased slightly, while the effective variance decreased. This is somewhat understandable in light of the method used to determine the cloud initial size parameters. Aerosols and Rayleigh scattering above a cloud would generally be expected to attenuate the strong polarized signal emanating from the cloud bow. This would act to decrease the polarization strength of the cloud bow, and dampen the secondary oscillations associated with narrow size distributions. Once incorporated into a full multiple scattering radiative transfer model, the effects of droplet size on the observations are more accurately calculated, providing a better estimate of the droplet size distribution.

One interesting result from this optimization is that it converged to a solution where the $\Im(m_{f,q})$ parameter is dominant, while $\Im(m_{f,p})$ became nearly zero. Initial values for both these parameters were an equal split of $\Im(m_f)$ from the Dubovik et al. [2002] Mexico City climatology. Errors for both $\Im(m_{f,p})$ and $\Im(m_{f,q})$ are large, but this indicates a likely spectral dependence in the imaginary refractive index. This was also found by Bergstrom

et al. [2010] in a nearby scene. We also tested optimizations that had spectrally flat initial conditions ($\Im(m_{f,p}) = 0.014$ and $\Im(m_{f,q}) = 0.0$), but they converged to what we found here, only with many more Levenberg-Marquardt iterations.

4.4.3 Comparison with other observations

Observations of the aerosol plume were also made by other instruments on the J-31 aircraft. The Ames Aerosol Tracking Sunphotometer (AATS) made observations of the spectral aerosol optical depth in a cloud free region about 125km northwest of our scene. Aerosol absorption was also observed in this area by the Solar Spectral Flux Radiometer (SSFR), and published in Bergstrom et al. [2010] (see figure 4.2). As described in section 4.2.2, atmospheric transport was weak prior to our observation, so we assume the aerosols at this location are similar to those in our AAC scene.

The aerosol optical thickness we retrieved agrees very well with AATS observations from an altitude of 480m (which was the cloud top height in our AAC scene). To some extent, this is by design, since the longest wavelength AATS optical thickness values were used to constrain the AAC coarse mode aerosol optical thickness during optimization. Even so, at wavelengths less than $0.8\mu m$, the majority of total aerosol optical thickness is determined by the fine mode, and AATS measurements at these wavelengths agree well within retrieval uncertainties.

The single scattering albedo that we retrieved has a very large uncertainty. However, comparisons with SSFR observations show some degree of similarity, at least for the shorter wavelengths of the spectrum. It is encouraging that agreement is better at these wavelengths since this is where the fine aerosol mode dominates extinction, and the imaginary refractive index of the fine mode was allowed to vary during optimization. Differences are greatest for the $0.7\mu m$ to $1.1\mu m$ wavelength range. The coarse aerosol mode contributes more to the total extinction at these wavelengths, but the imaginary refractive index for the coarse mode was held fixed during optimization. This may indicate that the coarse mode imaginary refractive index was not properly selected. Given the overall imaginary refractive index

Table 4.4: This table contains the parameter sensitivity to changes in the forward radiative transfer model. This sensitivity is expressed as a percentage of the retrieved parameter value ($100 \times \mathbf{e}/\mathbf{x}$). All of the parameter errors from model uncertainties are within the accuracy requirements of Mishchenko et al. [2004], and with one exception (the pitch angle uncertainty impact on the cloud effective radius, noted in bold), they are all less than the individual retrieval uncertainties.

	$\tau_f(0.555)$	$\Im(m_f)$	$r_{e,f}$	$v_{e,f}$	$r_{e,cl}$	$v_{e,cl}$
Aerosol layer top raised 30m	0.1%	4.5%	0.1%	0.9%	0.0%	0.0%
Cloud layer top raised 30m	0.8%	20.5%	0.4%	4.2%	0.0%	0.1%
Yaw angle changed by $0.5°$	0.6%	153.5%	0.3%	3.7%	0.8%	1.4%
Pitch angle changed by $0.5°$	1.0%	451.5%	1.6%	15.4%	**3.9%**	6.0%
$\Re(m_f)$ increased by 0.02	6.9%	57.8%	2.6%	12.1%	0.0%	0.2%
$\tau_c(0.555)$ increased by 0.02	4.0%	1481.6%	0.8%	16.3%	0.0%	3.3%
$\Re(m_c)$ increased by 0.02	0.1%	12.6%	0.0%	0.0%	0.0%	1.1%
k_c increased by 0.006	0.9%	9.1%	0.0%	1.6%	0.1%	1.7%
$r_{e,c}$ increased by 0.802	0.3%	33.2%	0.0%	1.1%	0.0%	0.6%
$v_{e,c}$ increased by 0.093	0.2%	44.3%	0.0%	1.0%	0.1%	0.6%

uncertainty, however, no firm conclusions can be made.

4.4.4 Model uncertainty

Forward model suitability is a major issue for optimizations such as this. Because of the finite information content available in our observations, we were required to make several assumptions about the nature of our scene. Many of these assumptions were based on external observations (such as the aerosol vertical distribution from AATS) or climatologies of aerosol properties (such as the coarse mode aerosol optical properties from Dubovik et al. [2002]). While it is difficult to quantitatively assess these assumptions without further information, we can determine if the uncertainty in the data that went into making them has an impact on the retrieved parameter values. To do so, we start by modifying one of the assumptions in the forward model by its uncertainty, and recomputing with the retrieved parameters. The difference between this (which we will denote $\hat{F}(\mathbf{x})$) and the forward

model results is the model error in measurement space. We can then use the Jacobian to project the error (**e**) into state space.

$$\mathbf{e} = (\mathbf{J}\mathbf{J}^T)^{-1}\mathbf{J}[\hat{F}(\mathbf{x}) - F(\mathbf{x})] \tag{4.9}$$

Table 4.4 contains values of **e** as a percentage of the retrieved parameter value for various model assumptions.

Model uncertainties come from a variety of sources. One class of model assumptions have to do with the physical description of the aerosol and cloud scene as plane parallel layers in a radiative transfer model. In this paper we test the validity of the vertical layering heights. Validity of the plane parallel model approach requires a comparison with a three dimensional radiative transfer model, which is beyond the scope of the current work and will be a topic of future research. Another class of assumptions has to do with the geometry of the scene. While presumably this will not be an issue for APS, the aircraft carrying the RSP is subject to rapid attitude changes, so the measurement geometry does have uncertainty. Finally, we also test the assumptions we make about the aerosol optical properties we were not able to retrieve, such as the fine mode real refractive index and the coarse mode size and refractive index.

Aerosol and cloud layer tops were perturbed by the vertical resolution of the CALIPSO lidar (Winker et al. [2006] and Winker et al. [2003]). CALIPSO is in the 'A-Train' orbit, which is also the destination of the APS instrument. Operational retrievals of AAC from the APS would likely use the cloud top height and aerosol vertical distribution from CALIPSO. Therefore, we used 30m perturbations, which are equivalent to the vertical resolution of CALIPSO for the lower troposphere. It is clear that **e** for most retrieved parameters is not strongly affected by this level of uncertainty in the vertical distribution, although cloud layer top is more important than the aerosol vertical distribution. The imaginary refractive index for the fine mode does have a somewhat large degree of error. However, this error is much smaller than the retrieval error itself, which was about twenty times larger than the imaginary refractive index parameter value, and other model uncertainties have a much

stronger effect on this parameter.

Proper knowledge of aircraft attitude is essential for accurate RSP retrieval. Aircraft attitude was provided by an Applanix POS-AV, which combines Global Positioning System technology with an inertial monitoring unit to determine position, velocity, pitch, roll and heading. There are of course limitations to the accuracy of such observations, and differences between the orientation of the POS-AV and the RSP instrument. To account for these errors, we modify our information about aircraft geometry using various features in the observed data. For example, R_U should be minimal when defined with respect to the scattering plane for single scattering, so slight modifications to the aircraft pitch and yaw are made until this is the case. To understand the effect of geometric error, we perturbed the aircraft pitch and yaw angles by $0.5°$. This choice was based on the sensitivity of our geometry correction techniques, but is probably an overestimate. The official POS-AV pitch accuracy is $0.03°$, while yaw accuracy is $0.1°$ (roll uncertainty is not accounted for in this work). Table 4.4 shows that uncertainty in aircraft yaw angle is not particularly important (although $\Im(m_f)$ uncertainty is large, as it is for many other model assumptions). Pitch angle uncertainty, however, has a significant impact on the ability to retrieve the fine mode aerosol effective variance, cloud droplet effective variance, and especially the cloud droplet effective radius. In fact, error in the cloud droplet effective radius is larger than the retrieved error for that parameter. Accurate retrievals of cloud droplet radius thus require accurate monitoring of instrument pitch angles.

As shown in section 4.3, the information available in RSP observations is not great enough to retrieve all optical properties for both aerosol modes. We therefore were required to assume some of these properties based on prior information. In this case, we used the fine mode real refractive index, and the coarse mode refractive index and size distribution from the Mexico City climatology of Dubovik et al. [2002]. We used the climatological uncertainty for each assumed parameter to test our retrieval sensitivity. As we can see in table 4.4, uncertainty in the assumed fine mode real refractive index value has a significant impact on the ability to retrieve fine mode optical depth, and a more moderate

impact on fine mode size distribution. Considering the impact on aerosol optical thickness, the retrieval success for that parameter (see figure 4.8) indicates that the assumed real refractive index value was also valid. Coarse mode optical thickness was determined by longest wavelength observations by the AATS sun photometer. The assumption is that coarse mode aerosols, because of their size, have very little optical thickness spectral variation. Fine mode aerosols, on the other hand, have a very pronounced spectral dependence, and a nearly negligible optical thickness at long wavelengths. Optical depth observations at long wavelengths can therefore be assumed to represent the coarse mode only, and that value should be constant for all wavelengths. It is difficult to assess the uncertainty associated with this assumption, but we select a value of 0.02, which is larger than the AATS uncertainty alone. Regardless, coarse mode aerosol uncertainty has a substantial effect on fine mode optical depth and effective variance, and a large effect on the fine mode imaginary refractive index. It appears that the selection of the coarse mode optical depth is important, so this must be done with care (or this parameter must be retrieved rather than assumed). Uncertainty in assumptions about the other coarse mode aerosol optical properties (complex refractive index and particle size distribution) have a minimal effect on retrieved parameter values, and can therefore be confidently assumed from climatologies.

4.5 Discussion

This research is a test of the capability of scanning polarimeters to retrieve the optical properties of aerosols lofted above clouds (AAC). The test was performed with observations from the Research Scanning Polarimeter (RSP), which is an airborne prototype of the Aerosol Polarimetry Sensor (APS), soon to be launched as part of the NASA Glory mission. The primary strategy for retrieving aerosol and cloud optical properties from RSP and APS is to match a multiple scattering radiative transfer model to observations by iteratively modifying model parameters until a match is found. The Levenberg-Marquardt method is used to perform this optimization. The software and tools that we used were developed

in Knobelspiesse et al. [2010], which couples a publicly available Levenberg-Marquardt software with a Doubling and Adding type radiative transfer model.

An AAC scene observed by the RSP during the Megacity Initiative: Local and Global Research Observations (MILAGRO) field campaign was the primary source of data for this work. A mixture of urban industrial and agricultural biomass burning aerosols from central Mexico were lofted above a marine stratocumulus cloud close to shore over the western portion of the Gulf of Mexico. Several other instruments, including the Ames Airborne Tracking Sunphotometer (AATS-14) and the Solar Spectral Flux Radiometer (SSFR) were onboard this aircraft, and collected data that were used to either guide the AAC optimization or validate the results.

This research had three main sections. First, we simulated the RSP/APS retrieval error for an AAC scene with climatologically defined aerosol properties (Dubovik et al. [2002]) at a variety of optical depths. We found that the aerosol optical depth, fine mode aerosol size distribution, and cloud droplet size distribution can all be retrieved for an AAC scene to the accuracy required for climate modeling in Mishchenko et al. [2004]. Aerosol refractive index simulated errors are much higher. The error in the real component of the refractive index decreases with increasing aerosol optical depth, and approach accuracy requirements as optical depth at $0.555\mu m$ exceeds 0.8. Aerosol single scattering albedo error (and the imaginary part of the refractive index from which it based) also decrease with increasing optical depth to values approaching accuracy requirements. Simulations also show that it is preferable to retrieve aerosol properties and cloud droplet size distributions simultaneously using all available angle observations, rather than to separate the two and retrieve cloud droplet properties from observations of the cloud bow and aerosol optical properties from observations at side scattering angles. We then performed an optimization for an example AAC scene. This optimization successfully converged to a solution, where a thin layer of aerosols overlay a marine stratocumulus cloud made up of relatively small sized droplets. Errors for this optical depth were quite similar to the predictions using simulated data. The retrieved aerosols appear similar to the climatology for Mexico City aerosols in Dubovik

et al. [2002], although with a narrow size distribution range possibly associated with particle humidification or cloud processing. We found evidence of an increase in absorption for the shortest wavelengths, which is a characteristic of Brown Carbon aerosols and was also observed by Bergstrom et al. [2010] for the same aerosols. However, the imaginary refractive index retrieval uncertainty (which determines aerosol absorption) is extremely large. While this was predicted with the scene simulations for aerosols with a thin optical depth, it limits any conclusions that can be drawn from these results. Nonetheless, optical depth and single scattering albedo results compare favorably with measurements by other instruments. Finally, we assessed the importance of uncertainty in various model components. We found that the aerosol and cloud layer height resolution as provided by the CALIPSO instrument will be sufficient for AAC retrievals by the APS when it on orbit. Accurate measurements of aircraft geometry, especially pitch, are important for retrievals with RSP data (but not for APS). Finally, while the coarse mode optical depth has a strong effect on retrieval uncertainty, assumptions about other coarse mode aerosol optical properties only have a small effect on the fine mode properties that are being retrieved.

This work suggests that the APS instrument will be capable of retrieving the total aerosol optical depth, fine mode size distribution, and cloud droplet size distribution for aerosols lofted above clouds. This is true provided that the scene can be simulated as plane layers within the APS pixel, and that the layer heights can be supplied by external observations (such as the CALIPSO lidar). Fine mode aerosol refractive index retrievals have a high error that decreases with increasing AAC optical depth. These errors approach modeling requirements as optical depths approach and exceed about 0.8 at a wavelength of $0.555\mu m$. Most AAC optical depths will probably not be that large, but it is encouraging that the retrievals will be most sensitive to events with the strongest potential to alter radiative forcing. For lower optical depths, we may need to fix refractive index values using a climatology or external measurements. The retrieved optical depth will be sensitive to the accuracy of that assumption. Considering this dependency, an alternate approach might be to fix the optical depth (since observations of optical depth are much more common than

those of refractive index), and allow refractive index parameters to vary. We did not attempt this technique in this work, but it may be a worthwhile approach in the future, if the RSP or APS are observing in coordination with lidars such as the High Spectral Resolution Lidar (HSRL), which retrieve both aerosol vertical distribution and aerosol optical depth (Hair et al. [2001], Hair et al. [2008], Rogers et al. [2009]).

4.6 Conclusions

The direct radiative effect of aerosols suspended above clouds (AAC) are a potentially important but rarely observed phenomenon. Scanning polarimeters, such as the Aerosol Polarimetry Sensor (APS) (due to be launched soon as part of the NASA Glory mission) and its airborne prototype, the Research Scanning Polarimeter (RSP), have the capability to retrieve AAC properties using nonlinear optimization methods that match a radiative transfer model to instrument observations. In this paper, we tested the capability of such a retrieval using RSP observations of a mixed urban and agricultural fire smoke aerosol above a marine stratocumulus cloud in the western portion of the Gulf of Mexico. Provided that the vertical structure of the cloud and aerosol are known, the aerosol optical depth, cloud droplet size distribution and aerosol fine size mode size distribution can be retrieved. Reasonable values were found for the complex refractive index of the fine aerosol size mode, but their associated uncertainty is too large to be used for climate models. We also performed a sensitivity study for a similar scene at a variety of AAC optical depths, and found that uncertainties decrease as optical depth increases. If the aerosol optical depth exceeds roughly 0.8 at a wavelength of $0.555\mu m$, refractive index uncertainties decrease to a degree that is almost sufficiently accurate for the needs of climate models. Once launched, the APS will be able to provide much more information about AAC than was previously available. However, the complex refractive index will be limited in its accuracy unless external data can be used as a constraint or the aerosol optical depth is unusually large.

Table 4.5: Correlation matrix for a simulated AAC scene with $\tau_f(0.555) = 0.1$ and an optimization utilizing angles within $60°$ of nadir. Elements with absolute values greater than 0.5, indicating strong correlation, are in bold.

	$\tau_f(0.555)$	$\Re(m_f)$	$\Im(m_{f,p})$	$\Im(m_{f,q})$	$r_{e,f}$	$v_{e,f}$	$\tau_c(0.555)$	$r_{e,cl}$	$v_{e,cl}$
$\tau_f(0.555)$	1.00								
$\Re(m_f)$	-0.36	1.00							
$\Im(m_{f,p})$	0.26	0.44	1.00						
$\Im(m_{f,q})$	-0.42	0.27	**-0.55**	1.00					
$r_{e,f}$	0.49	**-0.96**	-0.35	-0.30	1.00				
$v_{e,f}$	-0.10	**0.64**	0.00	0.32	**-0.68**	1.00			
$\tau_c(0.555)$	-0.40	-0.45	**-0.53**	0.30	0.33	-0.38	1.00		
$r_{e,cl}$	0.02	0.08	0.07	-0.01	-0.01	-0.01	-0.00	1.00	
$v_{e,cl}$	-0.17	-0.05	**-0.68**	0.30	0.03	0.24	0.01	0.09	1.00

4.7 Appendix: Correlation in simulations

The analysis in section 4.3 describes the parameter sensitivity of the retrieval, but does not express the correlations between the parameters. The off diagonal elements of $\mathbf{C}_x$ (equation 4.8) can be used for this purpose if they are normalized by the parameter error to create the correlation matrix

$$\rho_{ij} = \frac{\mathbf{C}_{x,ij}}{\sqrt{\mathbf{C}_{x,ii}}\sqrt{\mathbf{C}_{x,jj}}} \tag{4.10}$$

Tables 4.5 and 4.6 are the correlation matrices for the $\tau_f(0.555) = 0.1$ simulations in section 4.3.

Table 4.6: Correlation matrix for a simulated AAC scene with $\tau_f(0.555) = 0.1$ and an optimization utilizing angles $20°$ and $60°$ forward of nadir. Elements with absolute values greater than 0.5, indicating strong correlation, are in bold.

	$\tau_f(0.555)$	$\Re(m_f)$	$\Im(m_{f,p})$	$\Im(m_{f,q})$	$r_{e,f}$	$v_{e,f}$	$\tau_c(0.555)$	$r_{e,cl}$	$v_{e,cl}$
$\tau_f(0.555)$	1.00								
$\Re(m_f)$	0.44	1.00							
$\Im(m_{f,p})$	**0.63**	0.18	1.00						
$\Im(m_{f,q})$	-0.41	-0.24	**-0.73**	1.00					
$r_{e,f}$	0.10	**-0.82**	0.06	0.12	1.00				
$v_{e,f}$	0.38	**0.74**	-0.31	0.16	**-0.51**	1.00			
$\tau_c(0.555)$	**-0.90**	**-0.64**	**-0.61**	0.40	0.15	-0.42	1.00		
$r_{e,cl}$	**-0.70**	-0.28	-0.11	0.06	-0.12	**-0.55**	0.49	1.00	
$v_{e,cl}$	**0.71**	0.25	0.24	-0.10	0.19	0.39	**-0.62**	-0.45	1.00

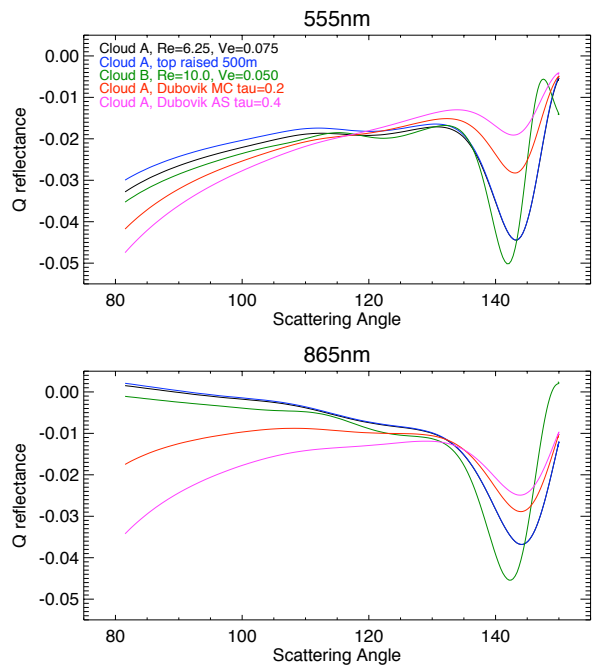

Figure 4.1: The sensitivity of multi-angle polarimetry to cloud and aerosol optical properties is demonstrated in this figure. Black lines are R_Q in the scattering plane for a simulated cloud (type A) with an optical thickness of 20.0 and a vertically uniform droplet size distribution of $r_e = 6.25\mu m$, $v_e = 0.75$ from the ground to 480m. The top panel is reflectance at $0.555\mu m$, while the bottom panel is reflectance at $0.865\mu m$. Blue lines are reflectance from the cloud when the top has been raised by 500m. Green lines are the reflectance of a cloud containing different droplet sizes, ($r_e = 10\mu m$, $v_e = 0.05$). Red and magenta lines indicate the reflectance of a cloud with aerosols above, the former for 'Mexico City' type urban aerosols with $\tau(0.555) = 0.2$ and the latter for 'African Savanna' biomass burning aerosols with an optical thickness of $\tau(0.555) = 0.4$ from Dubovik et al. [2002]. All scenes are simulated with a solar zenith angle of $\theta_s = 45°$ and a relative azimuth angle of $\phi = 45°$.

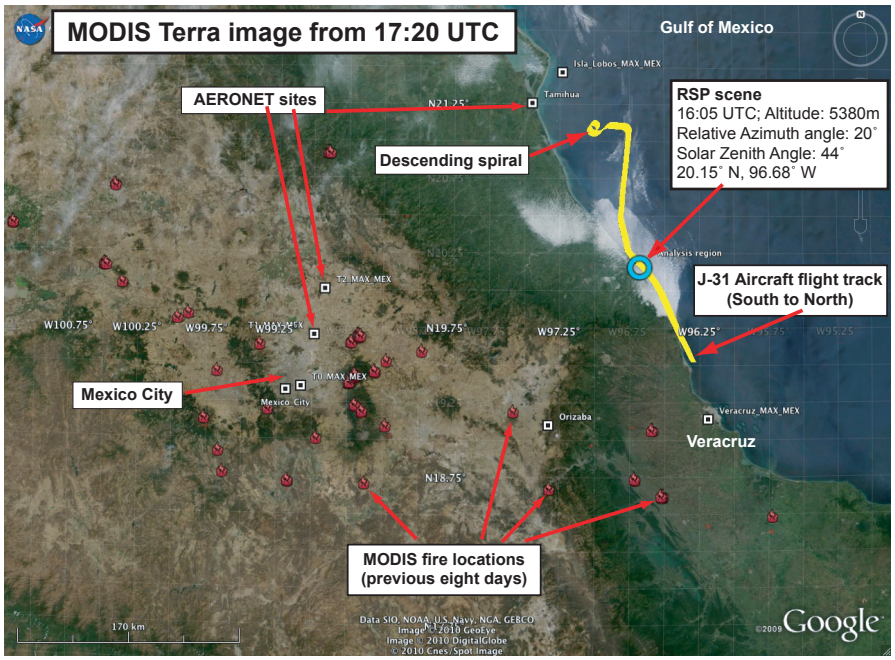

Figure 4.2: The spatial context of our AAC scene is presented in this figure. The blue circle indicates the location of RSP observations, above a marine stratocumulus cloud on the Gulf of Mexico coast. A portion of the J-31 flight track is shown in yellow. The J-31 performed a spiral to the surface about 125km northwest of the scene, and data collected during this descent provided information about cloud and aerosol vertical distribution. Aerosol sources include urban/industrial emissions in the Mexico City Metropolitan Area (MCMA) basin, a high valley to the west, and numerous (mostly agricultural) fires indicated by the red fire icons. Fire locations were identified by the MODIS active fire product and represent fires within the previous eight days. The MODIS Terra instrument captured the underlying image about an hour and fifteen minutes after our scene was observed.

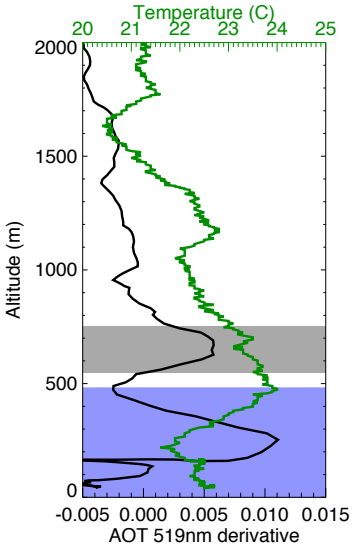

Figure 4.3: The aerosol optical depth and temperature during the downward spiral northwest of our scene are presented in this figure. Optical depth observations were made by the AATS-14 instrument, and the derivative with respect to height (equivalent to the extinction coefficient) of observations at 0.519μm is presented in black. Two layers of aerosols are present. The lowest, between about 150 and 350m, was most likely not observable in our scene. The upper layer, between 550 and 750m, was probably above the cloud and therefore the same AAC that we observed in our scene. The atmospheric temperature profile is shown in green. At 480m, there is a sharp change in the temperature profile. This probably marks the upper boundary of the marine stratocumulus cloud that existed at this location several hours before. Based on this information, we constructed our radiative transfer model so that the cloud top is at 480m, with an aerosol layer above between 550 and 750m. The initial aerosol optical thickness value of the upper layer was estimated to be 0.16 at 0.555μm from AATS-14 data.

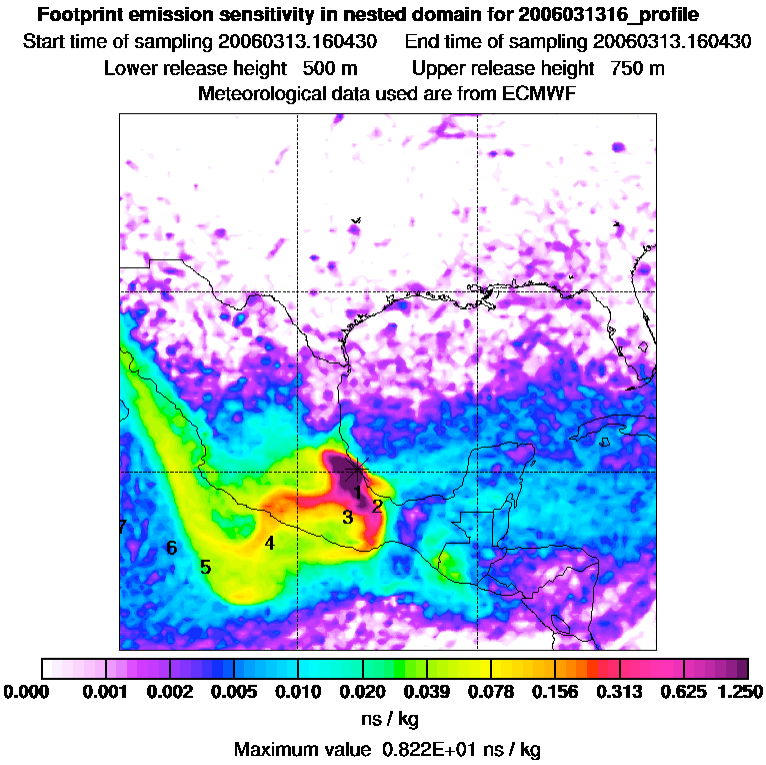

Figure 4.4: Emission sensitivity footprint for the 500-750m altitude range at our AAC scene obtained from FLEXPART driven by meteorological data from ECMWF.

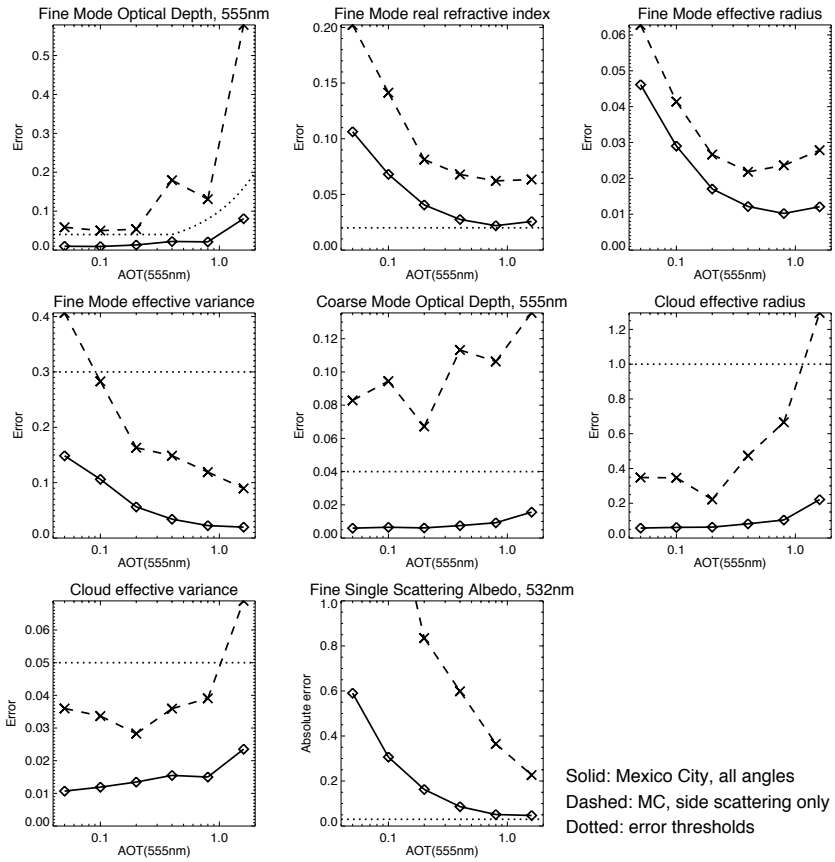

Figure 4.5: Simulated retrieval error for 'Mexico City' type aerosols (see Dubovik et al. [2002]) suspended above a marine stratocumulus cloud. The aerosols, which were placed in a uniform layer between 550 and 750m above sea level, were simulated at a variety of optical depths. The x-axis of each plot is the fine mode aerosol optical depth at 0.555μm. Coarse mode optical depth was maintained at 20% of the fine mode value for each simulation. The marine stratocumulus cloud had an effective radius of $r_{e,cl} = 6.25\mu m$ and effective variance of $v_{e,cl} = 0.075$, an optical depth of 10, and was uniformly distributed (with respect to pressure) from the ground to 480m. Solid lines are the simulated errors for an observation including all view zenith angles within $60°$ of nadir, which is similar to our scene and includes the cloud bow (and corresponds to a scattering angle range of $85°$ to $150°$). Dashed lines are the simulated errors for an optimization that only uses observations at angles between $20°$ and $60°$ in the forward direction, which excludes the cloud bow and is similar to the method of Waquet et al. [2009c], who had greater uncertainty when determining cloud parameters. These angles correspond to a scattering angle range of $85°$ to $120°$. Dotted lines are the accuracy thresholds described in Mishchenko et al. [2004] required to improve aerosol climate models. It is important to note that these values are intended for retrievals of aerosols in the absence of clouds or clouds in the absence of aerosols - not AAC. Also, the threshold for effective radius (top right) is $0.1\mu m$, greater than all the simulated errors in that plot. The single scattering albedo (bottom, center) accuracy threshold is 0.03, less than all simulated error values.

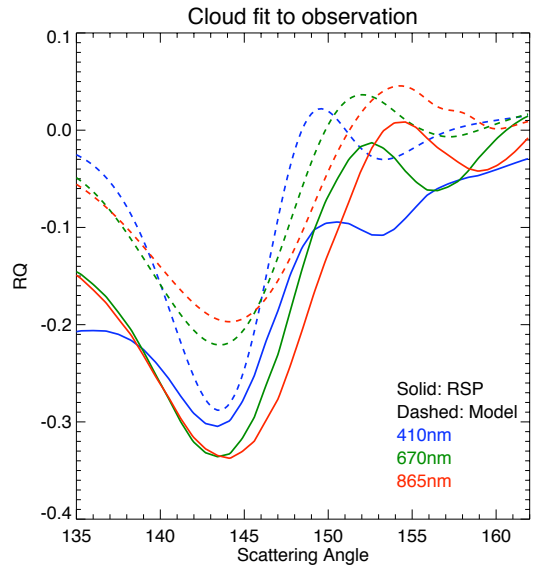

Figure 4.6: RSP observations (solid lines) were matched to a look up table of cloud optical properties (dashed lines) to determine initial cloud droplet size properties for the optimization. The cloud that matched best had droplets with an effective radius of $r_{e,cl} = 6.25\mu m$ and effective variance of $v_{e,cl} = 0.075$. Low frequency differences (bias) between cloud and RSP R_Q are due to the effects of aerosols and Rayleigh scattering on the observation.

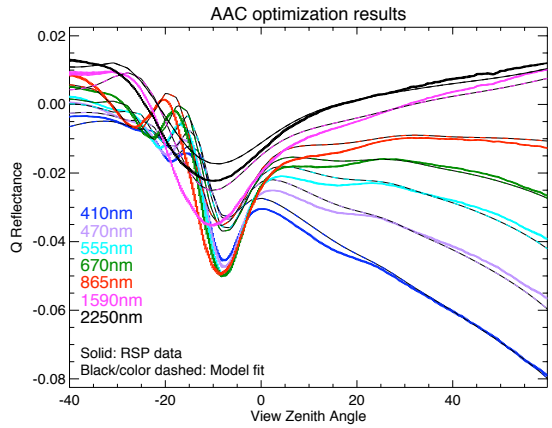

Figure 4.7: RSP observations (solid lines), and the model match (dashed color/black lines) to those observations.

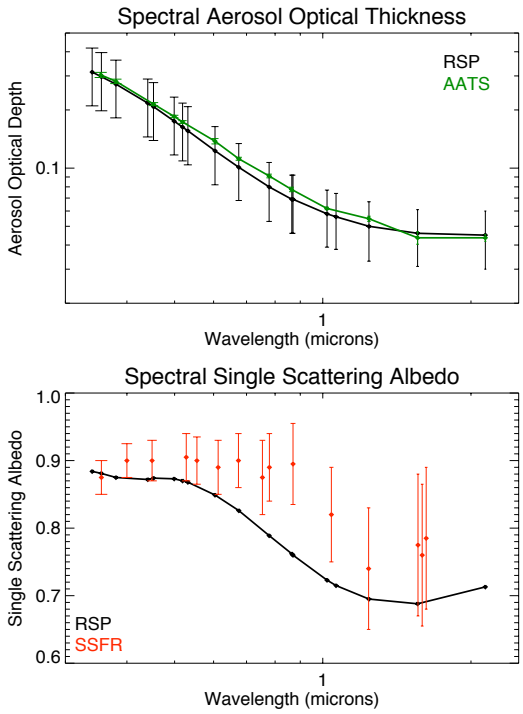

Figure 4.8: The topmost panel in this figure is the spectral dependence of retrieved total aerosol optical thickness (black line) and the AATS observation (green line) at an altitude of 480m during the downward spiral indicated in figure 4.2. The bottom panel is the spectral dependence of the total single scattering albedo. The black line is the RSP retrieved single scattering albedo, where the large error bars are omitted for clarity (they would fill the entire range of values in the plot). Red indicates SSFR observations as described in Bergstrom et al. [2010].

Surface BRDF estimation from an aircraft compared to modis and ground estimates at the southern great plains site

Peer reviewed article published in the

Journal of Geophysical Research

full citation:

K.Knobelspiesse, B.Cairns, C.Schaaf, B.Schmid, and M.Román. Surface BRDF estimation from an aircraft compared to MODIS and ground estimates at the Southern Great Plains site. *J. Geophys. Res.*, 113(D20105), October 2008.

Chapter 5

Surface BRDF estimation from an aircraft compared to MODIS and ground estimates at the Southern Great Plains site

5.1 Abstract

Surface albedo, which quantifies the amount of solar radiation reflected by the ground, is an important component of climate models. However, it can be highly heterogeneous, so obtaining adequate measurements are challenging. Global measurements require orbital observations, such as those provided by the Moderate Resolution Imaging Spectroradiometer (MODIS). Satellites estimate the surface bidirectional reflectance distribution function (BRDF), a surface inherent optical property, by correcting observed radiances for atmospheric effects and accumulating measurements at many viewing and solar geometries. The BRDF is then used to estimate albedo, an apparent optical property utilized by climate models. Satellite observations are often validated with ground radiometer measurements. However, spatial and temporal sampling differences mean that direct comparisons are subject to substantial uncertainties. We attempt to bridge the resolution gap using an airborne radiometer, the Research Scanning Polarimeter (RSP). RSP was flown at low altitude in the vicinity of the Department of Energy's Southern Great Plains Central Facility (SGP CF) in

Oklahoma during the Aerosol Lidar Validation Experiment (ALIVE) in September, 2005. The RSP's scanning radiometers estimate the BRDF in seconds, rather than days required by MODIS, and utilize the Ames Airborne Tracking Sunphotometer (AATS-14) for atmospheric correction. Our comparison indicates that surface albedo estimates from RSP and MODIS agree with Best Estimate Radiation Flux (BEFLUX) ground radiometer observations at the SGP CF. Since the RSP is an airborne prototype of the Aerosol Polarimetery Sensor (APS), due to be launched into orbit in 2009, these techniques could form the basis for routine BRDF validation.

5.2 Introduction

A proper understanding of surface albedo has been a priority of the remote sensing community since its origins. Besides providing information about the nature of the surface itself, remote-sensing retrievals of atmospheric properties must often account for the effects of the surface reflectance. Albedo is also an important determinant of where radiation is absorbed in climate models, yet it is spatially and temporally heterogeneous, and thus difficult to include realistically in those models. In addition, anthropogenic surface albedo changes can alter the global climate, but quantification of this process is dependent upon the data that are used by models [Myhre and Myhre, 2003]. Global albedo estimates from sensors on satellite platforms are now being compiled into climatologies appropriate for modeling (Lucht et al. [2000b], Schaaf et al. [2002], Luo et al. [2005]). It is important, then, to verify the validity and accuracy of these global albedo products, and to identify any features of these products that would improve the reality of global models without introducing unnecessary complexity.

Albedo is complex and highly variable. It is a function of the surface material and its topography, which is spatially and temporally heterogeneous, and the angle at which the surface is illuminated and observed. Low earth orbit satellite platforms with instruments such as the Moderate-Resolution Imaging Spectrometer (MODIS) and the Multi-angle Imaging

SpectroRadiometer (MISR), as well as instruments on geostationary satellites (Martonchik et al. [2002], Pinty et al. [2005]) are well suited to building climatologies for modeling purposes, as they have a spatial coverage and measurement repeat cycle that is impossible to achieve from ground or aircraft measurements. However, significant analysis is required to reduce the apparent optical properties (AOP's), as seen at a satellite, to inherent optical properties (IOP's) suitable for use in a climate model. Surface AOP's depend on the solar and viewing geometry and on the atmospheric state through extinction of the direct solar beam before and after it reaches the surface and scattering of radiation on its way to and from the surface. For example, the measurement that is closest to a direct estimate of albedo is the ratio of upwelling and downwelling fluxes, which is nonetheless an AOP since it depends on the atmospheric state. Since the atmospheric state varies within a climate model, the albedo must be described in an independent manner as an IOP of the surface, that is then used in a coupled calculation of the radiative transfer in the surface-atmosphere system. The bidirectional reflectance distribution function (BRDF) is an IOP that describes the reflectance of a surface when illuminated by an infinitesimally narrow beam of radiation and viewed through an equally infinitesimally narrow beam, and is a function of the geometry of those two beams. Because of this, the BRDF is a theoretical property that can only be estimated [Schaepman-Strub et al., 2006]. Although several approaches have been developed for the estimation of the BRDF over a wide angular range (Bruegge et al. [2000], Gatebe et al. [2003]) a more common BRDF estimation approach is to fit an atmospherically corrected and geometrically variable set of measurements to semi-empirical BRDF models (Engelsen et al. [1998], Lucht et al. [2000b]). The empirical BRDF model can then be used to derive quantities that are not readily observable, such as the variation of the albedo as a function of solar zenith angle that is the function of relevance to most current climate models.

BRDF estimation from orbit is subject to several hurdles. First, atmospheric effects must be removed, which is complicated by multiple surface-atmosphere interactions. Second, a sufficient angular range of measurements must be accumulated to provide a robust

estimate of the empirical BRDF model. In the case of fixed angle instruments such as MODIS, this accumulation requires several days, over which albedo characteristics may have changed. Multi-angle instruments such as MISR and the Research Scanning Polarimeter (RSP, described below) sample a much larger angular range nearly instantly, but this is at the expense of spatial coverage. Third, in order to be effective for global evaluation of albedo, the semi-empirical BRDF models must encompass a sufficient range of surface BRDF's that their marginal integrals, such as albedo, are not biased by the choice of model. Finally the data-model fitting method should be resistant to noise and methodological errors.

Because of the difficulties of BRDF estimation from orbit, a robust validation effort is required to have sufficient confidence to apply satellite derived climatologies to climate models. As we noted above, ground radiometers make a measurement that is more directly related to albedo than remote sensing measurements and they make that measurement as the solar zenith angle varies over the course of the day. Correctly modeling this energy input to the surface as a function of solar zenith angle is important for general circulation models. These measurements therefore provide the appropriate validation of the albedo derived from satellite, or aircraft measurements. However, care needs to be taken when comparing with the ground radiometers to properly account for the atmospheric state and the spectral sampling provided by the remote sensing measurements as compared to the total fluxes measured at the surface.

Recently, there have been several efforts to compare MODIS albedo products to ground radiometer data from the Department of Energy's (DOE) Southern Great Plains Central Facility (SGP CF) in North-Central Oklahoma, USA (Luo et al. [2003], Yang [2006], Schaaf et al. [2006]), and to other ground radiometers (Liang et al. [2002], Jin et al. [2003]). For example, Yang [2006], compared parameterizations of MODIS albedo (Liang et al. [2005], Wang et al. [2007]) to Best Estimate Radiation Flux (BEFLUX) radiometers (Shi and Long [2002]) and found some differences in the shape of the albedo as a function of solar zenith angle. Since the the BEFLUX radiometers provide the direct estimate of the energy input

to the surface that we are interested in for global applications it is important to understand whether these differences were due to inadequacies in the MODIS data itself, its parameterizations, or problems with the comparison method.

Albedo data measured from aircraft utilizing multi-angle and multi-spectral radiometers at the SGP CF offer the possibility to investigate and resolve this issue. The Aerosol Lidar Validation Experiment (ALIVE) took part in September of 2005 in the vicinity of the SGP CF in northern Oklahoma. During ALIVE, a Jetstream-31 (J-31) turboprop aircraft flew several low altitude transects about 200m above the SGP CF. The J-31 carried several instruments. The principal instrument used here is the Research Scanning Polarimeter (RSP), a scanning polarimeter that is intended for aerosol and cloud research and is a prototype for the Aerosol Polarimetery Sensor (APS). The APS is due to be launched as part of the NASA Glory mission in 2008 (Mishchenko et al. [2007a]). RSP was flown at low altitudes to collect data for the best possible estimate of the surface reflectance and BRDF. More details about the RSP are given in section 5.3.3.1. The Ames Airborne Tracking Sunphotometer (AATS-14) was also on the J-31. The AATS-14 is a fourteen spectral channel sun tracking sun-photometer [Schmid et al., 2006] that provides accurate measurements of aerosol optical depth above the aircraft. The AATS-14 measurements of aerosol above the aircraft in conjunction with measurements from AErosol RObotic NETwork (AERONET) [Holben et al., 1998] ground-based sun-photometers allows us to perform an extremely accurate atmospheric correction of the RSP measurements. The atmospherically corrected RSP surface measurements were fit to BRDF models from which albedos were derived and compared to MODIS and BEFLUX results. In addition, a land cover based approach, similar to that used in Liang et al. [2002], was used to evaluate the differences in spatial scale between MODIS, RSP and BEFLUX data.

The purpose of this paper is to evaluate the MODIS BRDF retrievals that use semi-empirical kernel models to derive albedos and surface albedo parameterizations. As part of this evaluation, we also investigate previous validation efforts at the SGP CF. RSP data provide a unique opportunity to bridge the spatial and temporal resolution differences be-

tween MODIS and ground radiometers in a well characterized atmospheric regime at the SGP CF.

5.3 Background

5.3.1 Albedo, BRDF, and other definitions

Instruments observe many forms of what we call reflectance, which can have a somewhat complicated and ambiguous terminology. We use nomenclature of Nicodemus et al. [1977], reviewed in Schaepman-Strub et al. [2006], which is briefly described here.

Reflectance, as it is most generally described, is the ratio of radiant exitance from a surface to the irradiance, E, incident upon that surface. Both radiant exitance and irradiance have units of $[Wm^{-2}]$, so reflectance, ρ, is unitless, and is constrained to the interval $[0, 1]$. The reflectance factor, R, is the ratio of the radiant exitance from a surface to the radiant exitance leaving a perfectly reflective, Lambertian (isotropic) surface under the same irradiance. Occasionally, such as the case of strong forward reflectance, the reflectance factor can exceed one. Both are functions of solar zenith angle, θ_s, view zenith angle, θ_v, solar azimuth angle, ϕ_s, view azimuth angle ϕ_v, and wavelength, λ. We define wavelength for the narrow band instruments of interest here (RSP and MODIS) as the solar spectrum weighted center, Λ, of the spectral band of a particular instrument.

The bidirectional reflectance distribution function ($BRDF$) describes the scattering of a parallel beam of incident light from one direction into another direction, defined as the ratio of the radiance observed through an infinitesimally small solid angle cone to the irradiance illuminating that surface within an infinitesimal solid angle.

$$BRDF(\theta_s, \theta_v, \phi_s, \phi_v, \lambda) = \frac{dL(\theta_s, \theta_v, \phi_s, \phi_v, \lambda)}{dE(\theta_s, \phi, \lambda)}[sr^{-1}] \tag{5.1}$$

The radiance, L, is the quantity of radiant flux per unit solid angle per unit wavelength and has units of $[Wm^{-2}sr^{-1}]$. The $BRDF$ is an inherent optical property (IOP) and thus

represents the intrinsic properties of the surface. Since it is defined with infinitesimal quantities it can not be directly measured. Its estimation, however, is important since apparent optical properties (AOP's) can be derived from the $BRDF$ in a consistent fashion appropriate for validation. Moreover, given the typical scale of angular $BRDF$ variations, it can be sampled and accurately estimated.

Schaepman-Strub et al. [2006] cites several AOP's that can be derived from the $BRDF$, but we use only two. The directional-hemispherical reflectance (DHR), called the 'black-sky' albedo in MODIS terminology, is the view geometry integrated, total radiant exitance when the surface is irradiated by a plane parallel beam. This is also known as the planetary albedo in the astronomical literature.

$$DHR(\theta_s, \phi_s, \lambda) = \int_0^{2\pi} \int_0^{\frac{\pi}{2}} BRDF(\theta_s, \theta_v, \phi_s, \phi_v, \lambda) cos(\theta_v) sin(\theta_v) d\theta_v d\phi_v \tag{5.2}$$

Many publications assume DHR is independent of the solar azimuth angle (ϕ_s) which is the case if the BRDF only depends on the difference between view and solar azimuth angles. If surface properties have no preferred direction this is a reasonable assumption. In our case in central Oklahoma, many of the surfaces are plowed fields or otherwise human influenced, so the DHR will not necessarily be invariant with respect to solar azimuth angle and the $BRDF$ will depend on both the view and solar azimuth angles independently. The magnitude of this azimuth angle dependence is unknown. To maintain consistency with previous literature and MODIS and BEFLUX products, we assume solar azimuth angle independence, but comment further on this issue in section 5.5.5.

Another albedo related quantity is the bihemispherical reflectance (BHR), which represents the solar and view geometry integration of the $BRDF$ (or the solar geometry integration of the DHR). When the solar downwelling is assumed isotropic, BHR is the 'white-sky' albedo in MODIS terminology. This is also known as the spherical albedo in the astronomical literature.

$$BHR(\lambda) = \int_0^{\frac{\pi}{2}} \int_0^{2\pi} \int_0^{\frac{\pi}{2}} \int_0^{2\pi} BRDF(\theta_s, \theta_v, \phi_s, \phi_v, \lambda) cos(\theta_v) sin(\theta_v) cos(\theta_s) sin(\theta_s) d\theta_v d\phi_v d\theta_s d\phi_s \tag{5.3}$$

A function that we will define is the normalized DHR ($nDHR$). Many climate models assume that the shape of the DHR is spectrally invariant, and thus take as inputs that shape and some scaling factor as a function of wavelength and surface type. The $nDHR$ is defined to be

$$nDHR(\theta_s) = \frac{DHR(\theta_s, \lambda)}{DHR(60^\circ, \lambda)} \tag{5.4}$$

The $nDHR$ will be used to compare different albedo related measurements and to provide a direct comparison with the previous work of Yang [2006].

5.3.2 Ross-Li BRDF kernel models

The BRDF is a theoretical parameter impossible to measure directly, even with the large number of view angles available with the RSP. BRDF estimation is aided with the use of surface reflectance models, where available measurements are fit with a combination of kernels, each representing the geometric reflectance behavior a particular surface type. In this work, we use the kernel models employed in MODIS BRDF products, as described in Lucht et al. [2000b], and hereafter referred to as the Ross-Li BRDF model. Previous work has identified these kernels as providing a robust and efficient framework for BRDF estimation (Schaaf et al. [2002]) on a global scale, even when only a limited geometric range of measurements are available. Our assessment of the use of these particular kernels here is therefore limited to how well they represent the dense angular sampling of the RSP measurements. An assessment of the BRDF model validity for use in the evaluation of the surface albedo in global climate models is provided by comparisons to BEFLUX data.

The Ross-Li BRDF model decomposes surface reflectance into three types of scattering, and combines them in the following form:

$$BRDF(\theta_s, \theta_v, \phi, \lambda) \simeq \rho(\theta_s, \theta_v, \phi, \Lambda) = f_{iso}(\Lambda) + f_{vol}(\Lambda)K_{vol}(\theta_s, \theta_v, \phi) + f_{geo}(\Lambda)K_{geo}(\theta_s, \theta_v, \phi) \tag{5.5}$$

where K_{vol} and K_{geo} are the volumetric and geometric scattering kernels, respectively, and f_{iso}, f_{vol} and f_{geo}, are the isotropic, volumetric and geometric kernel scaling parameters. ϕ is the relative view-sun azimuth angle ($\phi = \phi_v - \phi_s$). In practice, an optimization is used to find the best kernel scaling parameters (f) to a set of measured reflectances (ρ). The result is an estimation of the BRDF.

The first scaling parameter, f_{iso}, represents isotropic scattering, which has no dependence on incidence or view angle and thus does not have a geometrically dependent kernel. Volumetric scattering represents the scattering within a dense vegetation canopy, and is based on a radiative transfer approximation of single scattering due to small, uniformly distributed and non-absorbing leaves. The angular behavior of this kernel is to have a minimum near the backscatter direction and bright limbs. As described in Roujean et al. [1992] and Ross [1981], the volumetric kernel, normalized to zero for $\theta_v = \theta_s = 0$, is:

$$K_{vol} = \frac{(\pi/2 - \xi)cos\xi + sin\xi}{cos\theta_s + cos\theta_v} - \frac{\pi}{4} \tag{5.6}$$

where ξ is the scattering angle, defined to be $cos\xi = cos\theta_v cos\theta_s + sin\theta_v sin\theta_s cos\phi$.

Geometric scattering represents surfaces with larger gaps between objects, and thus accounts for self shadowing. The angular behavior of this kernel is therefore to have a maximum at backscattering where there are no shadows. K_{geo} is based on the work of Wanner et al. [1995] and Li and Strahler [1992], but is used in the reciprocal form given in (Lucht et al. [2000a]). This reciprocal form, in the special case that the ratio of the height of the tree at the center of the crown to the vertical crown radius (h/b in Luo et al. [2005]) is two and the ratio of the vertical crown radius to the horizontal crown radius is one (spherical, or compact crowns, b/r in Luo et al. [2005]) as is used in the MODIS data processing, is

$$
\begin{aligned}
K_{geo} &= O(\theta_s, \theta_v, \phi) - \sec\theta_s - \sec\theta_v + \frac{1}{2}(1 + cos\xi)\sec\theta_s \sec\theta_v \\
O &= \frac{1}{\pi}(t - \sin t \cos t)(\sec\theta_s + \sec\theta_v) \\
\cos t &= \frac{\sqrt{D^2 + (\tan\theta_s \tan\theta_v \sin\phi)^2}}{\sec\theta_s + \sec\theta_v} \\
D &= \sqrt{\tan^2\theta_s + \tan^2\theta_v - 2\tan\theta_s \tan\theta_v \cos\phi}
\end{aligned}
\tag{5.7}
$$

5.3.3 Instrument description

5.3.3.1 RSP

The Research Scanning Polarimeter is an airborne prototype for the Aerosol Polarimetery Sensor (APS), due to be launched in 2008 as part of the NASA Glory Project [Mishchenko et al., 2007a]. The main goals of RSP/APS are to retrieve a complete suite of aerosol and cloud microphysical parameters together with the vertical distribution and integrated number concentration of particles from orbit (Mishchenko et al. [2004], Mishchenko et al. [2007b]). The RSP has nine optical channels with center wavelengths of 410, 470, 555, 670, 865, 960, 1590, 1880 and 2250nm. This work utilizes all of these bands except for the 960 and 1880nm channels, which are used to estimate water vapor column amounts and detect thin cirrus clouds respectively. Details about the RSP/APS aerosol retrieval using polarimetry can be found in [Cairns, 2003] and [Chowdhary et al., 2002].

In addition to measuring the polarized reflectance beneath the RSP with each scan, the instrument also measures the total (unpolarized) reflectance. While this information is not currently utilized to retrieve aerosol parameters over land, it is useful to independently validate surface albedo values retrieved by MODIS or other orbital platforms. Each RSP scan begins about $60°$ forward of nadir in the direction of aircraft motion, and samples at $0.8°$ intervals to about $60°$ aft of nadir. Thus each scan contains about 150 instantaneous samples at a variety of sensor viewing geometries. A BRDF estimation is therefore possible with a larger set of surface anisotropic reflectances, as opposed to fixed viewing angle instruments, such as MODIS, which require an accumulation of observations over several days (16 in

case of the MODIS MCD43B product) before the BRDF can be estimated [Lucht et al., 2000b]. The instantaneous field of view (IFOV) of the RSP is fourteen milliradians, which corresponds to a 2.8m ground pixel size assuming an altitude of 200m above the ground. RSP measurements were made over a period of two weeks during the ALIVE campaign in September, 2005. Two flights, labeled JRF03 and JRF04 in ALIVE terminology, were on September 16th and were chosen for this analysis for the clear, cloudless conditions at that time, and the low altitude segments of those flights that were made in the vicinity of the SGP CF. More details about data selection for the RSP are in section 5.4.1.1.

The RSP performed two types of flights during ALIVE. The first type was to collect data at an altitude above the majority of the atmospheric aerosols, generally 4-5km above ground on September 16th, 2005. An indication of the required altitude was provided by the AATS-14, see section 5.3.3.2. The atmospheric state is determined from these measurements, which are then applied in the atmospheric correction of data from the second type of measurements, collected at as low an altitude as possible. These low altitude data (about 200m above the ground) were used for BRDF estimation. The low altitude was key to minimize the atmospheric effect between the RSP and the ground, maximize spatial resolution, and minimize the effect of aircraft motion on efforts to combine views from different scans into a multi-angle observation of a single surface location.

5.3.3.2 AATS-14, ancillary data, and the radiative transfer model

RSP surface reflectance retrievals utilized several types of ancillary data. These data were used in the atmospheric correction of the observed radiances to remove atmospheric effects. An important component of the RSP atmospheric correction was the Ames Airborne Tracking Sunphotometer (AATS-14), co-located on the J-31 with the RSP. The AATS-14 provides a continuous record of aerosol optical depth above the aircraft in fourteen channels from 354 to 2139nm [Schmid et al., 2006]. These data were used in three ways. First, AATS-14 measured the vertical extent and distribution of aerosols during aircraft ascent and descent. This identified the required altitude for 'high altitude' RSP measurements

where aerosol parameters are retrieved. Second, information about the aerosols, such as the nature of their vertical distribution and the presence of very large coarse mode aerosols helped constrain the RSP aerosol retrievals. Finally, AATS-14 measurements during 'low altitude' flights identified where in the aerosol layer the aircraft was located. This is particularly useful when AATS-14 data are compared to AERONET ground sun-photometers, which thus indicates the aerosol optical depth between the instrument and the ground.

Several other sources of data provide ancillary information necessary to remove the effect of various components of the atmosphere. Ozone absorption, which is greatest in the 470 and 555nm bands, is based on the daily $1^\circ \times 1^\circ$ values from the Total Ozone Mapping Spectrometer (TOMS) [McPeters and Center, 1998]. Absorption due to NO_2, greatest at the shortest wavelength channels, is estimated using Scanning Imaging Absorption Spectrometer for Atmospheric Chartography (SCIAMACHY) data [Bovensmann et al., 1999]. Water vapor content was measured by the Microwave Radiometer (MWR) located at the SGP CF [Morris, 2006].

5.3.3.3 MODIS

The MODerate resolution Imaging SpectroRadiometer (MODIS) is a multispectral remote sensing satellite in a polar orbit. There are actually two MODIS instruments, on the morning equator crossing NASA Terra (EOS-AM) and afternoon equator crossing NASA Aqua (EOS-PM) spacecraft. Terra was launched in 1999, and Aqua in 2002. Since ALIVE was in September of 2005, we used a combination of data from both instruments. MODIS produces a large number of atmospheric and surface products, but we have focused our attention on the surface albedo retrievals, referred to as product ID MCD43 in MODIS terminology. We used the 'collection five' processing version, which has a 500m ground resolution. MODIS measures surface reflectance at a single view zenith angle with each scan, so albedos are determined by fitting several days worth of data (containing a variety of view and solar zenith angles) to a set of BRDF models (described in section 5.3.2). The methodology for doing so is described in Lucht et al. [2000b] and Strahler et al. [1999],

and first operational results are presented in Schaaf et al. [2002].

A number of efforts have been made to validate MODIS albedo products. Often, this takes the form of a comparison of satellite MODIS results to measurements from ground based radiometers. However, care must be taken to ensure that this comparison accounts for the spatial and temporal resolution differences between remote sensing instruments and ground radiometers. MODIS (and RSP) measurements represent a combination of all reflectances within a pixel, which may include a variety of surface types, while ground radiometers measure albedo with a smaller spatial scale that is dependent on the height of the tower on which the upwelling flux measurement is made and the observed portion of the radiative spectrum. In addition, the multi-day data aggregation required with the MODIS dataset could be problematic if that aggregation period includes changes to surface properties. It is therefore difficult to determine if comparisons represent purely instrumental differences, or are also affected by resolution.

Prior to the launch of Terra, Lucht et al. [2000a] attempted to validate the BRDF kernel fitting method by comparing ground radiometer measurements to reflectances from other remote sensing platforms. Spatial resolution differences were controlled by doing this comparison in a region of low albedo variability (grass and scrubland in New Mexico, USA), and BHR results were close enough for accurate climate modeling. Liang et al. [2002] validated MODIS albedo by 'upscaling' ground radiometer measurements from an agricultural region in Maryland, USA. They report less than 5% absolute error. Jin et al. [2003] compared MODIS albedo to field measurements from the Surface Radiation Budget Network (SURFRAD) and found results that met an accuracy requirement of 0.02 for measurements between April and September. Winter measurements failed to meet requirements, most likely due to the influence of rapid albedo changes from snow. With the launch of Aqua, Salomon et al. [2006] updated MODIS albedo validation for the combined Terra/Aqua product using SURFRAD and radiometers at the SGP CF. He found that, while wintertime albedo remain uncertain as described in Jin et al. [2003], overall coverage improved while total data averages remained consistent with previous results.

Validation efforts described above are generally restricted to comparisons of BHR, whereas for climate modeling a DHR parameterization is also needed. Several attempts have been made to parameterize MODIS results for application in climate models. Liang et al. [2005] created a parameterization using DHR and BHR from MODIS, soil moisture from the North American and Global Land Data Assimilation System (LDAS), fractional vegetation cover, and leaf and stem area index. Wang et al. [2007] used a simplification of MODIS DHR and a measure of vegetation type to create another type of parameterization. Yang [2006] investigated the validity of these parameterizations of DHR by comparing them to BEFLUX radiometer values at the SGP CF. While both parameterizations agreed well with each other at this site, Yang [2006] found differences in comparison to ground radiometers. Parameterization values were much smaller than BEFLUX values at high solar zenith angles and larger than BEFLUX values at very small solar zenith angles. While the former is perhaps to be expected considering the lack of MODIS data at high solar zenith angles, the latter is unexpected and troubling. Our work was initiated as an attempt to further investigate and possibly resolve the differences found in Yang [2006] with regards to how well MODIS surface albedo data products can predict surface albedo.

5.3.3.4 BEFLUX

Ground radiometer data were supplied by the Best Estimate Flux (BEFLUX) value-added procedure (VAP), which is created from several radiometers at the Department of Energy's Atmospheric Radiation Measurement (ARM) Southern Great Plains Central Facility (SGP CF). BEFLUX radiometers measure diffuse and total hemispherical downwelling irradiance and total hemispherical upwelling irradiance in one minute intervals [Shi and Long, 2002]. These values were combined according to the methodology of Yang [2006] to compute a BHR and DHR representing the rural pasture at the SGP CF in North-central Oklahoma, USA. This was done in two steps. First, the BHR for the entire month of September, 2007 was determined by finding the average ratio of total upwelling to total downwelling irradiance from cloudy measurements. These cloudy measurements were identified by the

ratio of direct to total hemispherical downwelling irradiance. The BHR was then utilized to find the DHR on the day of the measurement.

5.4 Method

5.4.1 RSP data preparation

5.4.1.1 Data selection

The Aerosol LIdar Validation Experiment (ALIVE) was a field campaign performed in North-central Oklahoma in September of 2005. This is the location of the Southern Great Plains Central Facility (SGP CF) of the Atmospheric Radiation Measurement (ARM) Program (Department of Energy). While the primary goals of the ALIVE campaign were not to investigate RSP surface characterization, the proximity to the suite of ground based instruments at the SGP site, simultaneous measurements of the aerosol profile from AATS-14, and a series of low altitude flights, provide an ideal data-set with which to investigate the surface characterization.

Several short, low altitude flight segments were made in the vicinity of the SGP site, typically preceded or followed by a spiral maneuver used by the AATS-14 to determine an aerosol optical thickness altitude profile. Surface characteristics were typical for the rural mid-west of the United States in the fall. The ground was relatively flat, and covered by a patchwork of late-season crops, bare soil exposed by recent harvesting, and mixtures of trees and shrubs [Luo et al., 2003]. There are few buildings and the occasional paved road.

Data from two flights were used. Table 5.1 presents these flight times, along with geometry, aerosol and weather conditions. Aerosol optical thickness at 500nm from an AERONET Project [Holben et al., 1998] sun photometer at the SGP site is also included to provide an understanding of aerosol properties from that day.

In table 5.1, the tags in the first row (JRFx) identify the research flight. Start time for a data file within that flight is listed in UTC. Local time was five hours earlier. Scans

Table 5.1: Low altitude ALIVE flight segments used for surface characterization

	JRF3	**JRF4**
Date	09/16/2005	09/16/2005
Start time, UTC	16:32:25	22:09:32
Number of RSP scans	270	41
J-31 Altitude above sea level	510m	475m
Relative sensor-solar azimuth	$-45°$	$156°$
Solar zenith angle	$43°$	$62°$
AERONET $\tau_a(\lambda = 500nm)$	0.07	0.05
AATS-14 $\tau_a(\lambda = 499nm)$	0.06	0.05
sky conditions	clear	clear

were selected from a particular data file so that they included only low altitude, constant heading segments. Altitude is listed as meters above sea level. Ground height at the SGP site is about 315m, so flights had an above ground height between 160 and 195m. The (relative) azimuth is the instrument heading minus solar azimuth, in degrees. Aerosol optical thickness at 500nm (τ_a) was measured by the AERONET Project with a ground sun photometer at the SGP site. Values from the time of flight are provided for comparison. AATS-14 optical thickness was measured on the J-31. Thus differences between AATS-14 and AERONET represent the optical thickness between the aircraft and the ground, a value which is well within the AERONET and AATS-14 uncertainty. The last row contains a visual description of the cloud scenario from the instrument operator.

There were a total of twelve research flights as part of ALIVE, but only flights JRF3 and JRF4, listed above, were suitable for BRDF estimation. JRF3 and JRF4 were the only flights with low altitude segments when the sky was completely devoid of clouds. As we shall see later (see section 5.4.1.3), some effort was put into determining the diffuse downwelling irradiance while estimating the BRDF. This determination is only accurate, with our models, for clear skies. Including the effects of clouds under partially cloudy skies, even if implemented with a three dimensional radiative transfer code, would introduce large uncertainties, as there is limited informational to specify the vertical and horizontal cloud

distribution.

5.4.1.2 Classification and mixed pixel removal

Before the Ross-Li BRDF models were fit to the data, we separated it into similar classes, and performed our fitting on each class individually. This was done to limit the dependence on data coverage differences from flight to flight, and also to facilitate comparisons with other lower spatial resolution data sets. Prior to image classification, gaseous absorption effects were removed as described above, and a metric describing the amount of vegetation (a vegetation index) was calculated for each data point. Data were then split into 'soil' and 'vegetation' classes and extreme vegetation index values were removed. Boundary or mixed surfaces were also removed using an edge detection convolution kernel on the spatial image of vegetation index. In addition, analyses were performed on an 'all' class which contains the entire data-set except for data that were removed as part of the quality control process. For each of these classes the data were then fit with the Ross-Li BRDF model.

Simple thresholding of the Aerosol Resistant Vegetation Index (ARVI, see Appendix 5.8.2 for details on how it is computed) was used to split the data into a 'soil' and 'vegetation' class. ARVI values between -0.25 and 0.075 were classified as 'soil', while ARVI values between 0.375 and 0.775 were classified as 'vegetation'. Such narrow ARVI regions centered on the modes of each surface type were chosen to avoid mixed pixel data and focus on the properties of generic 'soil' and 'vegetation'. Figure 5.4.1.2 is a histogram of the ARVI for each flight. Peaks for both classes are pronounced, and vertical dashed lines show the regions used for each class. The histogram computed using different small segments of the view angle range (not pictured here) is similar to the one shown here indicating an absence of significant BRDF effects on this index. Each flight flew over slightly different areas in the region of the SGP CF, so there are some differences between the histograms of each flight. In particular, JRF03 has a third peak at about an ARVI of 0.25, possibly indicating post-harvest, sparsely vegetated, fields that were not observed during JRF04. Since that surface type is not present in JRF04 data, it was omitted in the study.

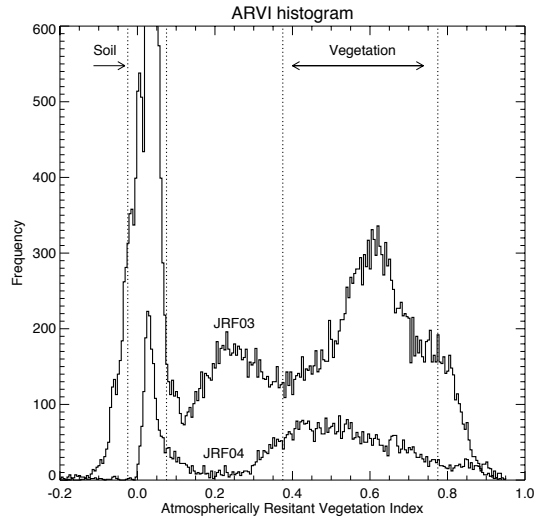

Figure 5.1: Histograms of the Atmospherically Resistant Vegetation Index (ARVI) for each flight. Vertical dotted lines represent the boundaries of the 'soil' and 'vegetation' class thresholds.

Furthermore, JRF04 contains less data than JRF03, as the length of flight time dedicated to the low altitude segment was less in JRF04. Few measurements passed the 'soil' class criteria. After additional screening, described below, only the 'vegetation' class remained from JRF04. Finally, a third, 'all' class was created for ARVI values between -0.25 and 0.775. For consistency, additional screening procedures described below were applied to this class as well.

To further restrict our data to generic land types, the ARVI spatial image is used to identify data that is in the middle of a patch of soil or vegetation. An edge detection algorithm was applied that uses a discrete convolution with a 3×3 spatial kernel. This kernel is applied as a multiplier to each pixel and its neighbors in the image, and the summed result of each multiplication forms the value of that pixel in the resulting image. This is a discrete version of the gradient and the technique (when this mask is added to the original image to enhance boundaries) is also called unsharp masking [Gonzalez and Woods, 1992]. The gradient image is used to remove boundary and mixed pixels. A threshold, $\eta = 0.1$, was

chosen such that pixels satisfying $|\nabla(ARVI)| > \eta$ are excluded. η was selected arbitrarily, but it is of the same magnitude as the ARVI range for the soil class, thus adjacent pixels containing as much variability as the narrowest class (or more) are removed. Figure 5.2 illustrates the classification and imagery from flight JRF3. Classification results (in part 5.2d) compare favorably with intuition from the imagery (part 5.2a), and take boundary and edge pixels (part 5.2c) into account. Note also the small quantity of data available for analysis. For safety reasons, the aircraft was flown at low altitude for only short segments near the SGP site.

Several geometric screening criteria were also applied. Data with view zenith angles greater than $65°$ were removed. This was done to avoid view angles at the extremes of measurement capability. Since the RSP is scanning in the direction of aircraft motion, data from turns were excluded because those scans may not represent a single ground location. Thus, data from aircraft headings $3°$ greater or less than an average heading were removed. The effects of both of these geometric screening criteria are evident in figure 5.2d, where data at the right of the image have been removed because their zenith angle was too large, and data at the top removed because this is were the aircraft began banking into its spiral ascent for the next segment of the flight.

Image data were rearranged so that each scan represents a set of view angles about a single ground location, rather than the actual order of measurements (which represent a set of view angles about an airborne location). While this has no effect on the actual data, classification results for each scan were checked for consistency. This final screening criteria (which is not displayed in figure 5.2) required that 50% of the data in a scan must have passed all previous screening criteria and were grouped into a single class. The result is a set of data that is of a consistent surface type over most of the view angle range and that has had any outlier measurements, which may represent noise, surface boundary or mixed pixel effects removed.

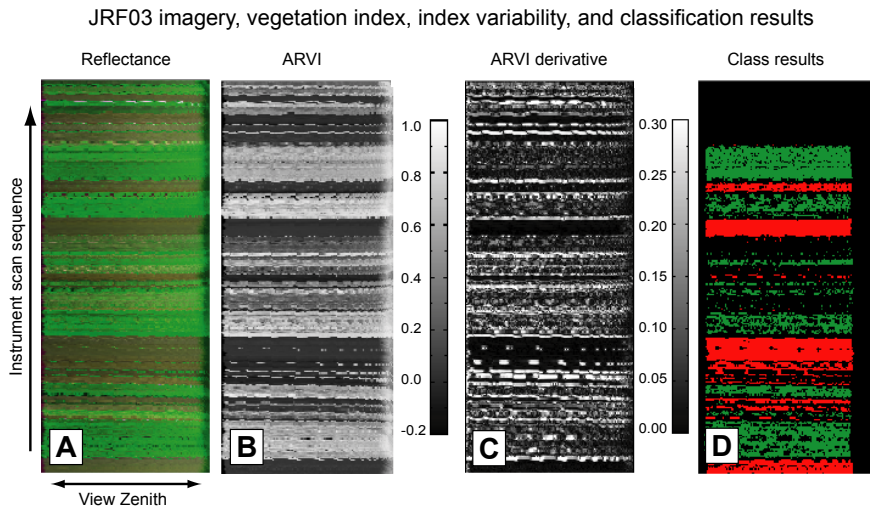

Figure 5.2: Data from flight JRF03 was used to show (from left to right), **a)** Ground reflectance, where the 670nm band is displayed in the red channel, the 865nm band in the green channel, and the 470nm band in the blue channel, **b)** Atmospherically Resistant Vegetation Index (ARVI), with the color bar at the right, **c)** gradient of ARVI, used to remove boundary and edge pixels with its color bar at the right, and **d)** classification results, where red indicates 'soil' type, green indicates 'vegetation', and black are unclassified areas.

5.4.1.3 Determination of ground reflectance and the diffuse effect

Measurement of ground reflectance from an aircraft requires adequate compensation for atmospheric effects. During ALIVE, a high quality characterization of the atmospheric scattering was provided by the combination of polarized RSP measurements (above the aerosol layer) with the vertical profile of aerosol optical thicknesses from the AATS-14. This cannot be used to determine the ground reflectance directly because of the multiple scattering that occurs between the atmosphere and the surface. The atmospheric correction is therefore performed using an iterative process, where initial estimates of surface reflectance are adjusted until the surface-atmosphere scattering model reproduces the reflectance measured by the RSP.

The atmospheric-surface model uses the doubling and adding method (Lacis and Hansen [1974], Hansen and Travis [1974]), and produces a reflectance to compare to RSP data, given aerosol and other atmospheric properties together with solar and instrument geometry and kernel values for the Ross-Li BRDF reflectance model. The observed reflectance can be separated into an atmospheric and a surface component:

$$\rho^o(\theta_s, \theta_v, \phi, \lambda) = \rho^a(\theta_s, \theta_v, \phi, \lambda) + S(\theta_s, \theta_v, \phi, \lambda) \tag{5.8}$$

where ρ^o is the reflectance at the altitude of the observations, ρ^a is the reflectance due to atmospheric scattering of radiance into the instrument field of view without interacting with the surface (path radiance) and S includes all surface interaction terms. In what follows we are primarily interested in S and the correction for diffuse and multiple interaction terms, since we have an accurate and comprehensive characterization of the atmosphere from high altitude RSP measurements that allows us to calculate ρ^a. We will differentiate between measurements and model calculations by using a caret for those quantities that are direct observations. The surface interaction term, S, can be calculated using the expression

$$S(\theta_s, \theta_v, \phi, \lambda) =$$
$$\left[t^{\uparrow}(\theta_v, \lambda) + T^{\uparrow}(\lambda)*\right] \rho^g(\theta_s, \theta_v, \phi, \lambda) \left[t^{\downarrow}(\theta_s, \lambda) + *T^{\downarrow}(\lambda)\right] +$$
$$\left[t^{\uparrow}(\theta_v, \lambda) + T^{\uparrow}(\lambda)*\right] \Sigma(\theta_s, \theta_v, \phi, \lambda) * \rho^g(\theta_s, \theta_v, \phi, \lambda) \left[t^{\downarrow}(\theta_s, \lambda) + *T^{\downarrow}(\lambda)\right] \tag{5.9}$$

where ρ^g is the surface reflectance, t is the direct solar transmittance, and T is the diffuse transmittance, with the arrows indicating whether they apply to transmission from the sun to the ground ($\downarrow$) or from the ground to the observational altitude ($\uparrow$). The star symbol, $*$, indicates that integrations over zenith and azimuth are performed for diffuse interactions. As is usually the case for scattering problems with no preferred azimuthal plane, that integration is actually implemented using a Fourier decomposition and re-summation (Hovenier [1971], Hansen and Travis [1974], and de Haan et al. [1987]). The function Σ is used in the calculation of multiple surface atmosphere interaction terms and is given by the formula

$$\Sigma(\theta_s, \theta_v, \phi, \lambda) = \sum_{i=1}^{\infty} \left(\rho^g(\theta_s, \theta_v, \phi, \lambda) * \rho^{a\star}(\theta_s, \theta_v, \phi, \lambda)\right)^i \tag{5.10}$$

where $\rho^{a\star}$ is the reflectance of the atmosphere illuminated from below. The implementation of this summation is described in (Hovenier [1971], Hansen and Travis [1974], and de Haan et al. [1987]).

In equation 5.8, ρ^o is measured by the RSP and calculated with the doubling-adding model, while ρ^a, t, T and Σ are determined from the model based on the atmospheric state that is prescribed by AATS-14, AERONET and high altitude RSP data. The model includes the effects of both Rayleigh (molecular) and aerosol scattering. In order to find an estimate of ρ^g that has the effects of diffuse transmission and multiple surface-atmosphere scattering removed, we use the following iteration

$$\rho^g_{p+1}(\theta_s,\theta_v,\phi,\lambda) = \left[\frac{\hat{S}(\theta_s,\theta_v,\phi,\lambda)}{S_p(\theta_s,\theta_v,\phi,\lambda)}\right]\rho^{g,k}_p(\theta_s,\theta_v,\phi,\lambda) = \gamma_p(\theta_s,\theta_v,\phi,\lambda)\rho^{g,k}_p(\theta_s,\theta_v,\phi,\lambda) \tag{5.11}$$

where p is the iteration index, $\rho^{g,k}$ is the kernel fit to the latest estimate of surface reflectance and $\hat{S}$ is the observation corrected for path radiance. We have implicitly defined the function γ_p, which is the ratio of measurement to model S, to adjust the surface reflectance until the model calculated reflectance matches the observations. This iteration is similar to that introduced by Chahine [1968] for atmospheric sounding. The kernel fit to the reflectance uses a least mean square estimate of the kernel coefficients, so the vector of kernel coefficients, **f**, is given by the expression

$$\mathbf{f}_{p+1} = \left(\left[\mathbf{K}(\theta_v)^T\mathbf{K}(\theta_v)\right]^{-1}\mathbf{K}(\theta_v)^T\right)\rho^g_{p+1}(\theta_v) \tag{5.12}$$

and the kernel estimate for the surface reflectance at the observed viewing geometry is

$$\rho^{g,k}_{p+1}(\theta_v) = \mathbf{K}(\theta_v)\mathbf{f}_{p+1} \tag{5.13}$$

with **K** being the 3xN reflectance kernel matrix formed from the isotropic, volumetric and geometric kernels (cf. equation 5.5) and N is the number of view angles for the given viewing geometry. **K** and **f** depend on the same set of wavelength (λ) and other geometric parameters (θ_s, ϕ), so those subscripts are omitted from the above equations. The iteration is initialized with the value

$$\rho^g_1(\theta_s,\theta_v,\phi,\lambda) = \frac{\hat{S}(\theta_s,\theta_v,\phi,\lambda)}{t^{\uparrow}(\theta_v)t^{\downarrow}(\theta_s)} \tag{5.14}$$

In an atmosphere with no scattering this initial value gives the atmospherically corrected surface reflectance, and no further iterations are therefore necessary. Otherwise, equations 5.11 through 5.13 are iterated until γ is close to unity. If there is scattering in the atmosphere, we can determine that $\gamma < 1$ from equation 5.9 for the first step in the iteration.

This is a necessary condition for the convergence of this iteration [Twomey, 1977]. Convergence also requires that the matrix associated with the estimate of the kernel parameters is diagonally dominant (Dubovik and King [2000], Appendix C). Since we are interested in the convergence of the estimation of the weights associated with the kernels we define matrix **M**

$$M_{jk} = \left(\frac{\partial ln \left[\rho^{g,k}(\theta_{v,l}) \right]}{\partial ln \left[f_j \right]} \right)^{-1} \frac{\partial ln \left[S(\theta_{v,l}) \right]}{\partial ln \left[f_k \right]} \tag{5.15}$$

where we use the convention that there is a summation over repeated subscripts. The average degree of diagonal dominance of that matrix, dd, is

$$dd = \sum_i \frac{\sum_{i \neq j} |M_{ij}|}{M_{ii}} \tag{5.16}$$

As expected (see figure 5.3), dd is largest at shortest wavelengths, where the effects of scattering are largest, and smallest at the longer wavelengths, where the effects of scattering are negligible.

The final iteration products are the kernel values of the Ross-Li surface reflectance model. The iteration was repeated between 5-9 times for each band until the change in kernel values for each iteration was smaller than 10^{-5}.

5.4.1.4 Spectral to broadband albedo computation

DHR and BHR, as calculated in the previous section, represent surface properties in a set of narrow instrument bands. Data from these narrow bands must be spectrally interpolated if they are to be compared to broadband ground radiometer data such as that from BEFLUX. In MODIS products, this is done according to the methodology of Liang [2001] and validated in Liang et al. [2003]. Liang [2001] used libraries of surface reflectance spectra and model simulations to create a set of coefficients that are applied to scene albedo values to approximate a broadband DHR or BHR. These coefficients are applied uniformly across the entire MODIS dataset. Our RSP-ALIVE dataset comprises a single day with

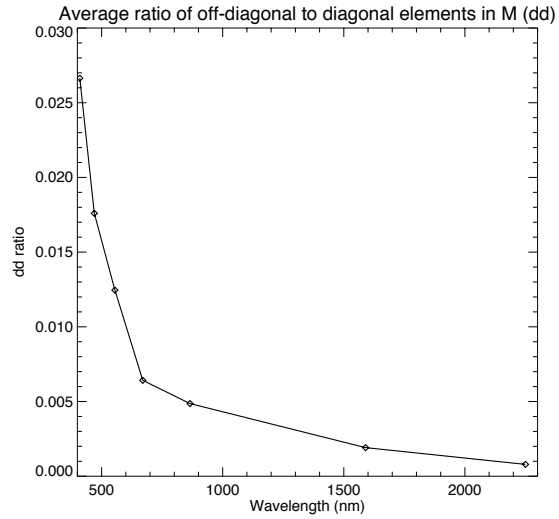

Figure 5.3: Average (for each wavelength band) ratio of off-diagonal to diagonal elements of matrix **M** (see equation 5.15). This ratio, dd, is described in equation 5.16.

a well known atmospheric scenario. In this sense, we are fortunate in that we can utilize knowledge about the atmosphere in our broadband albedo computation, and we do so as follows.

Conversion of $DHR(\Lambda, \theta_s)$ to the broadband version $DHR_{bb}(\theta_s)$ involves the spectral integration of the DHR weighted by the downwelling solar irradiance. Irradiances are computed using a hyperspectral version of the doubling and adding model applied in section 5.4.1.3 (Cairns et al. [2003]). Spectral DHR's are created using linear interpolations of Ross-Li kernel weights, f, determined in section 5.4.1.3. This is then normalized by the total downwelling solar irradiance appropriate for a particular day at all wavelengths

$$DHR_{bb}(\theta_s) = \frac{\int_{\lambda_{min}}^{\lambda_{max}} E_o(\lambda)t(\lambda)DHR(\lambda, \theta_s)d\lambda}{\int_{\lambda_{min}}^{\lambda_{max}} E_o(\lambda)t(\lambda)d\lambda} \tag{5.17}$$

where $E_o(\lambda)$ is the exo-atmospheric irradiance and $t(\lambda)$ is the direct solar transmittance. Spectrally dependent $DHR(\lambda)$ is created by linear interpolation of kernel weights and

application of the DHR parameterization described in Lucht et al. [2000b].

$$
\begin{aligned}
DHR(\lambda, \theta_s) = & \\
& f_{iso}(\lambda) + f_{vol}(\lambda) g_{0,vol}(\lambda) + f_{geo}(\lambda) g_{0,geo}(\lambda) + \\
& \theta^2 \left[f_{vol}(\lambda) g_{1,vol}(\lambda) + f_{geo}(\lambda) g_{1,geo}(\lambda) \right] + \\
& \theta^3 \left[f_{vol}(\lambda) g_{2,vol}(\lambda) + f_{geo}(\lambda) g_{2,geo}(\lambda) \right]
\end{aligned}
\tag{5.18}
$$

g parameters from Lucht et al. [2000b] are in table 5.2. BHR_{bb} is computed in a similar fashion, where spectrally interpolated kernel weights are applied to Lucht et al. [2000b]'s BHR parameterization. This parameterization is then integrated in a weighted manner.

$$
BHR_{bb} = \frac{\displaystyle\int_{\lambda_{min}}^{\lambda_{max}} E_o(\lambda) t(\lambda) BHR(\lambda) d\lambda}{\displaystyle\int_{\lambda_{min}}^{\lambda_{max}} E_o(\lambda) t(\lambda) d\lambda} \tag{5.19}
$$

$$
BHR(\lambda) = f_{iso}(\lambda) w_{iso} + f_{vol}(\lambda) w_{vol}(\lambda) + f_{geo}(\lambda) w_{geo}(\lambda) \tag{5.20}
$$

For consistency, broadband BHR_{bb} and DHR_{bb} are computed using the same method for both RSP and MODIS, and are thus integrated over the same spectral range (400nm to 2500nm). It should be noted that this is not the same spectral range as the standard MODIS broadband albedo products, but it matches the range of BEFLUX radiometers. We also analyzed the radiative effect of albedo beyond this spectral range using the hyperspectral doubling and adding model from Cairns et al. [2003] and estimates of surface albedo by extrapolating the RSP 'vegetation' and 'soil' data from within the measured spectral range. We found that the relative error in estimation of DHR (of the entire radiative system) using our restricted spectral range was 3.0% for 'vegetation' and 0.7% for the darker 'soil' data. The absolute bias for a surface with an albedo of 0.2 is 0.0058 and 0.0014 for 'vegetation' and 'soil', respectively. This estimation accounted for Rayleigh (molecular) scattering alone. Aerosols and absorbing gases would have the effect of further reducing the out of band radiance, and thus decreasing the above errors.

Table 5.2: Lucht et al. [2000b] DHR parameters

	Isotropic	Volumetric	Geometric
g_0	1.0	-0.007574	-1.284909
g_1	0	-0.070987	-0.166314
g_2	0	0.307588	0.041840
w	1.0	0.189184	-1.377622

5.4.2 MODIS data preparation

The newly reprocessed (Collection V005) MODIS BRDF/Albedo product is now being produced from Aqua and Terra data every eight days at an increased 500-meter spatial resolution. The spectral product provides semi-empirical, kernel-driven anisotropy models which are retrieved from all clear-sky, high quality, atmospherically-corrected surface reflectances available over a 16-day period. This is done by fitting multiple observations to the Ross-Li BRDF kernel models, as described in section 5.3.2 and in Lucht et al. [2000b]. The resulting BRDF parameters (f_{iso} , f_{vol} and f_{geo}) are then used to compute integrated albedos for MODIS spectral bands 1-6 (centered at 0.648, 0.858, 0.470, 0.555, 1.240, and 1.640um respectively). Collection V005 MODIS / Terra+Aqua BRDF / Albedo products are Validated Stage 1, meaning that accuracy is estimated using a small number of independent measurements obtained from selected locations at particular times

MODIS data utilized in this study was taken from a $0.4^\circ \times 0.4^\circ$ box surrounding the SGP CF. This geographic area was selected to encompass both the SGP CF and RSP overflight locations. Direct pixel to pixel comparisons were not performed due to the vast differences in spatial (and temporal) resolution between the terrestrial BEFLUX, airborne RSP and orbital MODIS (Liang et al. [2002]). Figure 5.4 shows the spatial context of the three datasets. An attempt was made to identify 'vegetation' and 'soil' classes as was done in section 5.4.1.2 for the RSP data. However, since band spectral sensitivities and the spatial scale of MODIS and RSP are different, this is impossible to reproduce exactly. The NDVI was calculated (equation 5.24) for each pixel, where the MODIS $BHR(859nm)$ was used in

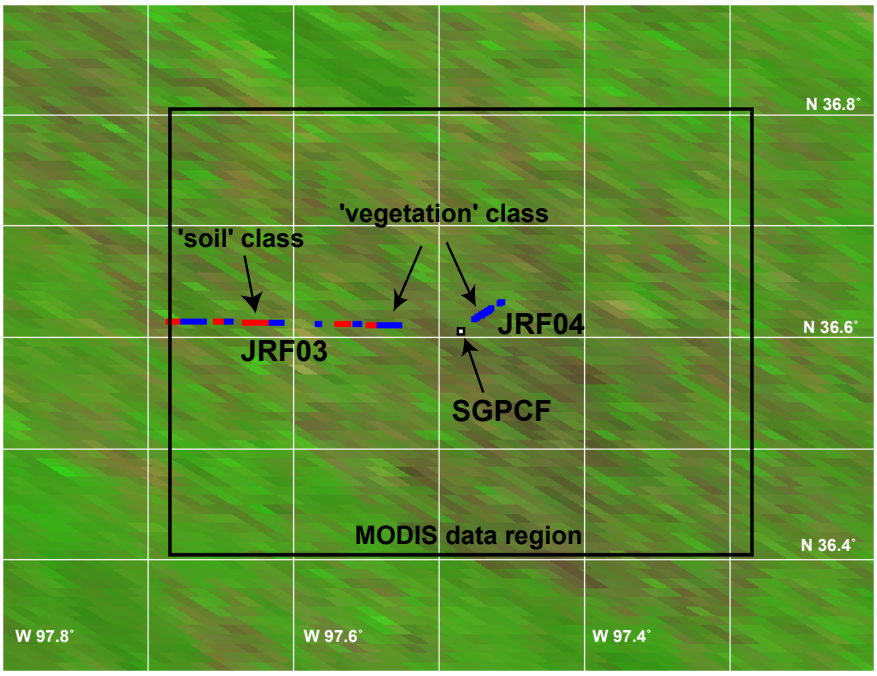

Figure 5.4: MODIS nadir reflectances from September 16th, 2005, overlaid with RSP data and SGP CF locations. MODIS data are a composite of reflectance from band 1 (645nm) in the red channel, band 2 (859nm) in the green channel, and band 3 (469nm) in the red channel. Data were scaled to give an intuitive impression of vegetation or bare soil dominance in each pixel. The black box identifies the region of MODIS data utilized in this study. RSP flight data locations are indicated in blue ('vegetation' class) or red ('soil' class) for both JRF03 (left) and JRF04 (right). The SGP CF is indicated with the black and white square.

place of L_{NIR} and $BHR(645nm)$ was used in place of L_{red}. The distribution of the result has a mean NDVI of about 0.5, with a normally distributed, half maximum width of about 0.4. In an attempt to identify pixels that were 'pure' with respect to ground surface type, those with NDVI values less than 0.3 were classified as 'soil' pixels, while those with NDVI values greater than 0.7 were identified as 'vegetation' pixels. Since these class types are not defined the same way as RSP classes and are of a different spatial scale, they cannot be definitively compared. However, this classification is representative of the spectral diversity present in the MODIS data.

5.4.3 BEFLUX data preparation

BEFLUX ground radiometer data were prepared in the same manner as Yang [2006]. Irradiances measured by the BEFLUX radiometers are a combination of DHR_{bb} and BHR_{bb}, which must be separated prior to comparisons with MODIS or RSP data. This is done by measuring the albedo when the surface is illuminated diffusely (when it is cloudy), so the measured albedo is BHR_{bb} alone. The BHR_{bb} is then removed from the observations for cloud free days to compute the DHR_{bb}.

The BEFLUX BHR_{bb} was calculated using data from the month of September, 2005. This length of time was chosen because it is long enough to have cloudy days for computation of BHR_{bb}, yet short enough that changes in surface properties can be ignored. Prior to BHR_{bb} calculation, data were screened to remove poor quality irradiances (as identified by Quality Control values), albedos greater than 0.4, and measurements made when the upwelling radiometers observed irradiances less than 10 W/m^2 (which is the instrument uncertainty). Measurements where the solar zenith angle was greater than $80°$ were removed as an additional screening that was not part of Yang [2006]. Cloudy days were identified where the ratio of downwelling diffuse irradiance to total hemispheric downwelling irradiance was greater than 0.99. For September, 2005, 1901 measurements fit this criteria, which is just over 10% of the total number of measurements passing the initial screening criteria. The average BHR_{bb} from BEFLUX is 0.185, with a standard deviation of 0.012. BHR_{bb} was invariant for the month of September, 2005, as a linear fit with respect to time increases by only 0.002 during the month. As an aside, this helps confirm that the sixteen day period over which MODIS gathered measurements to form its BRDF estimate was free of temporal variability that could add to the error in these measurements, at least in the area immediately surrounding the BEFLUX radiometers. It should also be noted that the effective BHR observed by the BEFLUX radiometers under cloudy skies is not necessarily the same as that for clear skies. This is due to the different effective regions of influence that contribute to the measurements from multiple scattering between the surface and the atmosphere or cloud. Thus, although the spatial domain that contributes to the

DHR estimated from BEFLUX is primarily determined by the height and location of the mount from which the downward looking measurements are made, the corrections used in equation 5.21 have a much more poorly defined spatial domain.

DHR_{bb} is found by removing the effect of BHR_{bb} from the ratio of upwelling to downwelling irradiances in cloud-free conditions. Specifically, this uses the expression

$$DHR_{bb}(\theta_s) = \frac{U_{all}(\theta_s) - BHR_{bb}D_{diff}(\theta_s)}{D_{dir}(\theta_s)} \tag{5.21}$$

where $U_{all}(\theta_s)$ is the total hemispherical upwelling irradiance measured by the radiometer, $D_{dir}(\theta_s)$ is the direct downwelling irradiance, and $D_{diff}(\theta_s)$ is the diffuse downwelling irradiance. We performed this calculation for data from September 16th, 2005. Total Sky Imager (TSI) derived products [Long et al., 2001] indicate that there were small (less than 10%) amounts of cloud cover during the morning and for part of the late afternoon. Data whose opaque cloud sky percentage was greater than 1% or whose thin cloud sky percentage was greater then 5% were removed. Unlike Yang [2006], we did not fit a polynomial to the computed DHR_{bb}, as we have a much smaller set of data and do not want to introduce fitting artifacts. The results were instead compared directly to MODIS, RSP and the parameterized MODIS data.

5.4.4 Albedo parameterizations

The final component of this multiple instrument comparison is a parameterization of MODIS albedos suitable for use in climate models. Wang et al. [2007] proposed a parameterization based only upon the MODIS reflectance factor at $\theta_s = 60°$ and two vegetation type dependent parameters. This parameterization was also tested in Yang [2006]. The Wang et al. [2007] parameterization is motivated by the polynomial fit to the Ross-Li BRDF kernels presented in equation 46 of Lucht et al. [2000b], and has the following form (equation 7 in Wang et al. [2007])

$$DHR(\theta_s, \Lambda) = DHR(60^\circ, \Lambda)\,(1 + B_1(\Lambda)\,[g_1(\theta_s) - g_1(60^\circ)] + B_2(\Lambda)\,[g_2(\theta_s) - g_2(60^\circ)]) \tag{5.22}$$

Here, g_1 and g_2 are the Ross-Li BRDF kernel polynomial fit coefficients from table 1 in Lucht et al. [2000b], B_1 and B_2 are the ratios $f_{vol}/DHR(60^\circ, \Lambda)$ and $f_{geo}/DHR(60^\circ, \Lambda)$, respectively. Wang et al. [2007] used global MODIS measurements to determine median $DHR(60^\circ, \Lambda)$ and B values for about a dozen surface vegetation types. He did so using spectrally broad, visible (VIS) and Near-InfraRed (NIR) spectral bands. We compared to the 'Grassland' and 'Cropland' vegetation types, as they are most consistent with the observed surface at the SGP CF. Table 5.3 lists parameter values for those vegetation types, along with the kernel values they imply.

Table 5.3: Wang et al. [2007] albedo parameters

Vegetation type:	Type 10: Grassland	Type 12: Cropland
$DHR(60^\circ, \Lambda_{VIS})$:	0.099	0.066
$DHR(60^\circ, \Lambda_{NIR})$:	0.295	0.286
B_1 :	0.57	0.62
B_2 :	0.12	0.13
$f_{geo}(\Lambda_{VIS})$:	0.056	0.041
$f_{vol}(\Lambda_{VIS})$:	0.012	0.009
$f_{geo}(\Lambda_{NIR})$:	0.168	0.177
$f_{vol}(\Lambda_{NIR})$:	0.035	0.037

5.5 Results

5.5.1 RSP model fitting results

The first, and most direct way of comparing $BRDF$ estimation results from RSP and MODIS is to examine the approximated $BRDF$ retrievals. As described in equation 5.1, $BRDF$ is a function of spectra (λ), solar and viewing zenith angles (θ_s and θ_v), and the rel-

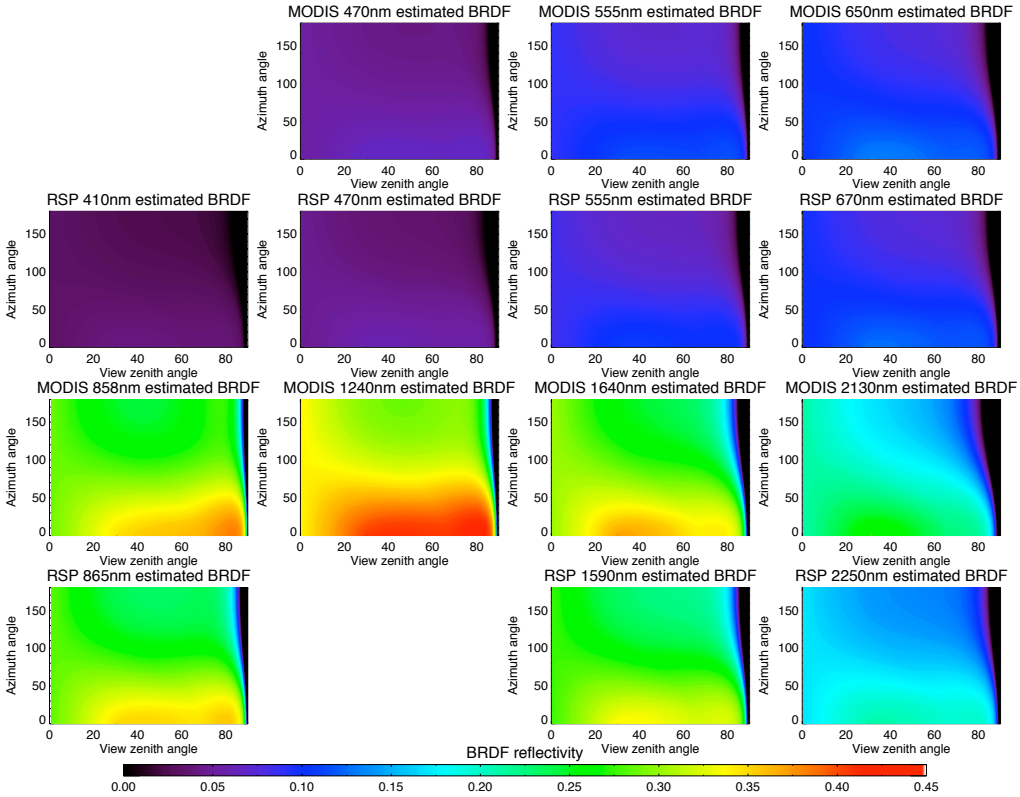

Figure 5.5: BRDF approximation results for MODIS (first and third rows) and RSP (second and fourth rows) during ALIVE. These results are for the 'all' surface type class with a solar zenith angle of $30°$.

ative azimuth angle ($\phi = \phi_v - \phi_s$, an assumption made in most literature). Because of the high dimensionality, we present a 'slice' of the $BRDF$ estimated for the 'all' surface class for RSP and MODIS in figure 5.5. Generally speaking, the magnitude and $BRDF$ angular dependence for RSP and MODIS are similar. Largest differences are for the longest wavelength values, where the band locations for RSP and MODIS have the greatest dissimilarities. Better agreement in the visible bands could also be due to their use in the classification routines described previously, as divergent longer wavelength reflectances are not used to identify a class.

5.5.2 BHR (white-sky albedo)

Figure 5.6 is a plot of the spectral and broadband BHR values for RSP and MODIS 'all', 'soil' and 'vegetation' classes. Spectral dependence is very similar to the magnitude of isotropic kernel values in figure 5.5. BHR peaks are evident in the 'vegetation' class in the green and NIR bands, while 'soil' class BHR values are greatest at longer wavelengths. For 'vegetation' and 'soil' classes, RSP and MODIS BHR agree best in the visible wavelength bands that were used to classify the data, and generally agree within a BHR of 0.05 at other wavelengths. Broadband BHR comparisons show similar levels of agreement, with the difference between RSP and MODIS for the 'all' class of 0.023. The RSP 'all' BHR_{bb} is the closest match to the BEFLUX BHR, with a BHR_{bb} 0.0001 greater than that derived from BEFLUX. Interestingly, the best match of spectral BHR between RSP and MODIS are with the 'all' classes, with similar spectral bands having differences less than 0.025. Although the 'vegetation' and 'soil' classes were derived with the intent of creating comparable RSP and MODIS albedos, the best agreement is for the average behavior of the two data sets. This is presumably because spatial averaging reduces the effects of the different spatial resolutions of the two sensors. Table 5.4 contains the tabulated BHR values displayed in figure 5.6.

5.5.3 DHR (black-sky albedo)

Figure 5.7 is a plot of the DHR for each spectral band and the broadband DHR_{bb}. RSP vegetation and soil classes are plotted along with vegetation and soil from MODIS. As expected, DHR_{bb} roughly represents the mean magnitude and shape of the spectral DHR from which it is created. This is particularly true for longer wavelengths, which were more heavily weighted in the spectral to broadband conversion due to a combination of higher exo-atmospheric irradiance, atmospheric transmittance, and surface reflectance. The shape and spectral variation of the DHR is similar for RSP and MODIS, as we would expect based on the similarity of the kernel values and the spectral BHR values presented in

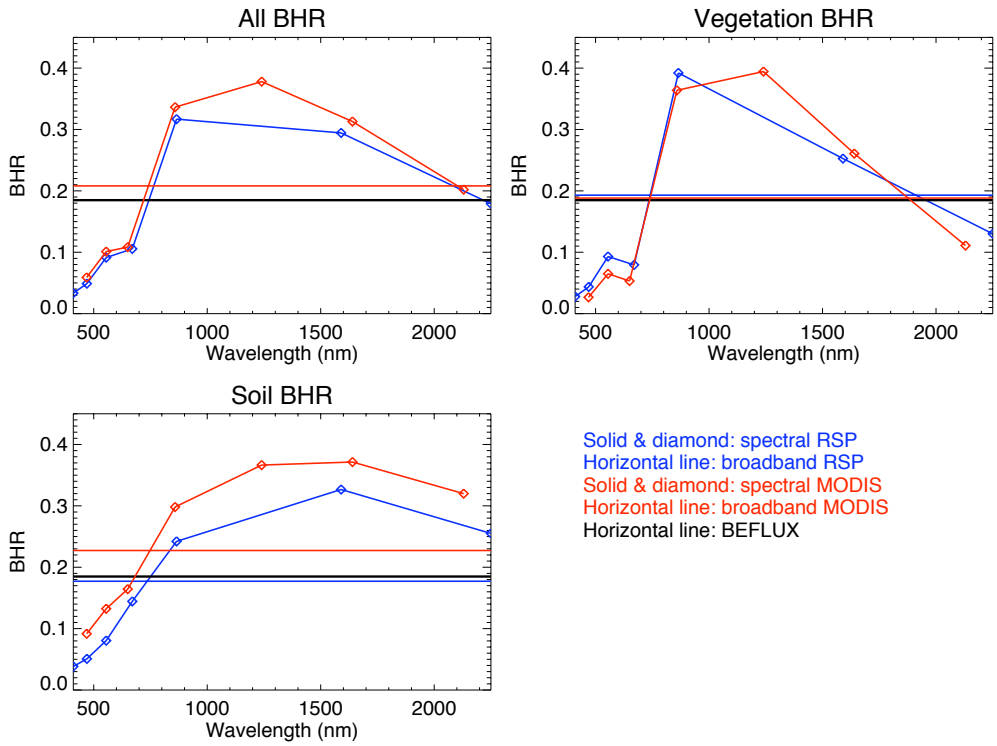

Figure 5.6: RSP (blue lines with diamonds) and MODIS (red lines with diamonds) $BHR(\Lambda)$. 'All' results are on the top left, 'vegetation' class results on the top right, and 'soil' class results on the bottom left. Straight horizontal lines represent the broadband BHR_{bb}, where again RSP is indicated in blue and MODIS in red. The thick black line is the BEFLUX BHR_{bb}.

Table 5.4: BHR from RSP, MODIS and the Wang et al. [2007] parameterizations. RSP 'all', 'vegetation' and 'soil' classes are indicated RSP-A, RSP-V and RSP-S, respectively. Likewise, MODIS 'all', 'vegetation' and 'soil' classes are indicated MOD-A, MOD-V and MOD-S. Wang et al. [2007] 'grassland' and 'cropland' visible and NIR BHR values are indicated by Wang-G and Wang-C. The final row is the difference between the column BHR_{bb} and the BEFLUX derived $BHR_{bb} = 0.185$.

	RSP-A	RSP-V	RSP-S	MOD-A	MOD-V	MOD-S	Wang-G	Wang-C
410nm	0.033	0.028	0.038					
470nm	0.049	0.044	0.051	0.059	0.027	0.092		
555nm	0.091	0.093	0.081	0.101	0.065	0.132		
650nm				0.108	0.053	0.164		
670nm	0.106	0.079	0.144					
858nm				0.336	0.364	0.298		
865nm	0.317	0.392	0.242					
1240nm				0.378	0.394	0.366		
1590nm	0.294	0.253	0.327					
1640nm				0.313	0.261	0.371		
2130nm				0.202	0.111	0.320		
2250nm	0.179	0.130	0.255					
Visible				0.086	0.045	0.126	0.095	0.068
NIR				0.317	0.319	0.314	0.282	0.271
BB	0.185	0.193	0.177	0.208	0.188	0.227		
Diff	0.000	0.008	-0.008	0.023	0.003	0.042		

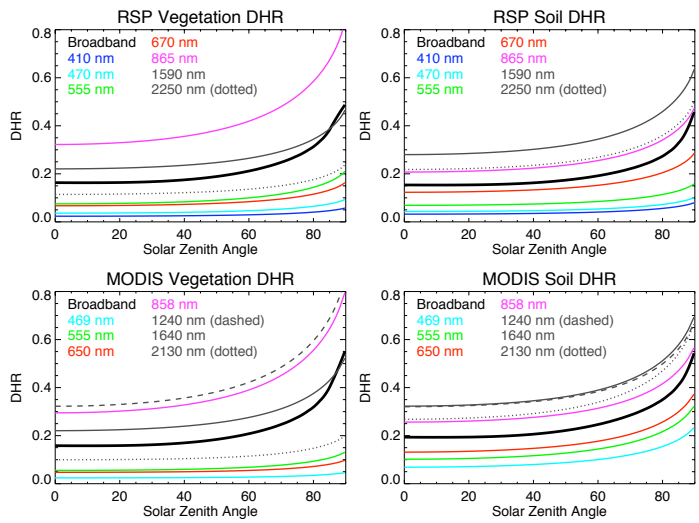

Figure 5.7: RSP (top panels) and MODIS (bottom panels) $DHR(\Lambda, \theta_s)$ values. 'Vegetation' results are on the left, 'soil' class results on the right. $DHR_{bb}(\theta_s)$ is indicated in black.

figures 5.5 and 5.6.

It is important to note that estimation of the BRDF using the kernel approach may be unphysical for angles other than those used to estimate the BRDF. Although the DHR calculated directly from the integrals of the BRDF kernels (as given by Lucht et al. [2000b]) remains physical (positive) for the kernel values analyzed here, the underlying BRDF may actually have negative values for high view or solar zenith angles. Great care should therefore be exercised in the use of these kernel estimated BRDF's at such high (greater than $75°$) angles.

Model inputs require, among other things, the shape of DHR with respect to solar zenith angle. Yang [2006] expresses this shape by normalizing DHR by its value at $\theta_s = 60°$. Figure 5.8 shows those normalized DHR ($nDHR$) values for both broadband and spectral values from the 'vegetation' and 'soil' classes of RSP and MODIS. Here, the broadband $nDHR$ is most similar to the longer wavelength visible or NIR $nDHR$. This illustrates the significance of those bands in forming broadband DHR.

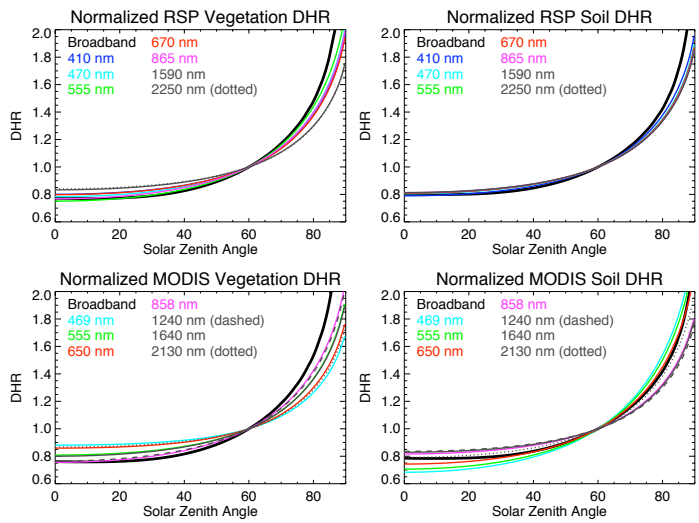

Figure 5.8: RSP (top panels) and MODIS (bottom panels) $DHR(\Lambda, \theta_s)$ normalized to $DHR(\Lambda, 60°)$. 'Vegetation' results are on the left, 'soil' class results on the right.

5.5.4 Remote sensing, ground radiometer and parameterization comparison

Perhaps the most important results of this work, figure 5.9, is a comparison of DHR estimates from all RSP and MODIS classes to those derived from BEFLUX ground radiometers and parameterizations from two surface classes of Wang et al. [2007]. BEFLUX data represent individual measurements on September 16, 2005, where any potentially cloud contaminated values are removed. Despite the thorough cloud screening, measurements at the same solar zenith angle (between $33°$ and $55°$) are different for the morning and afternoon. This variability expresses the magnitude of potential systematic uncertainties, such as differences due to solar azimuth angle or multiple ground-atmosphere interactions occurring in different areas adjacent to the radiometers.

While it is impossible to be sure which type of surface class is best to compare with BEFLUX derived DHR (as discussed in section 5.4.3), it is reasonable to assume that it should be similar to one of the classes or a mixture of the two, as the small area of

pasture where the BEFLUX radiometers are located is sampled in both RSP and MODIS data-sets. Indeed, this *is* the case for absolute DHR from both RSP and MODIS. The best matches are the RSP and MODIS 'vegetation' classes, although other RSP classes are close as well. Of course, this comparison is limited to solar zenith angles greater than about $33°$ and less than about $80°$, as this is the range of DHR solar zenith angles derived from BEFLUX. However, a lack of a comparison beyond this angular range should not be a significant problem when evaluating kernel based estimates of DHR and BHR. As mentioned previously, very high solar zenith angles are neither routinely measured nor energetically important for climate modeling, while the data used to estimate the Ross-Li kernel values included nadir view angles. Reciprocity of the kernel BRDF's should therefore ensure acceptable behavior of the DHR values at small solar zenith angles. The agreement between RSP predicted and BEFLUX broadband BHR and DHR is excellent (0.0001 and on average 0.0058 for BHR and DHR, respectively, in the RSP 'all' class) over the angular range from $30°$ to $80°$. This indicates the capability of well corrected, multi-angle, narrowband results to predict the radiative balance at the surface. Although we have found larger discrepancies with MODIS results, broadband DHR agreement is still better than 0.0042 for even the most poorly matched surface type ('soil').

5.5.5 Azimuth angle independence

RSP estimates of the BRDF are aided by the large number and range of view zenith angles of measurement available at one time. However, the results presented here represent two flights (for the 'vegetation' and 'all' classes) or one flight (for the 'soil' class) and therefore measurements have a limited range of relative solar - view azimuth angles. Thus, while BRDF estimation is based on a well sampled meridional plane the number of such planes is very limited. While it is impossible to fully investigate the consequences of this azimuth angle measurement limitation without more data, some indication of the potential variability or uncertainty in BRDF estimates caused by this limitation can be determined by comparing results from the two flights. Figure 5.10 is a comparison of BRDF estima-

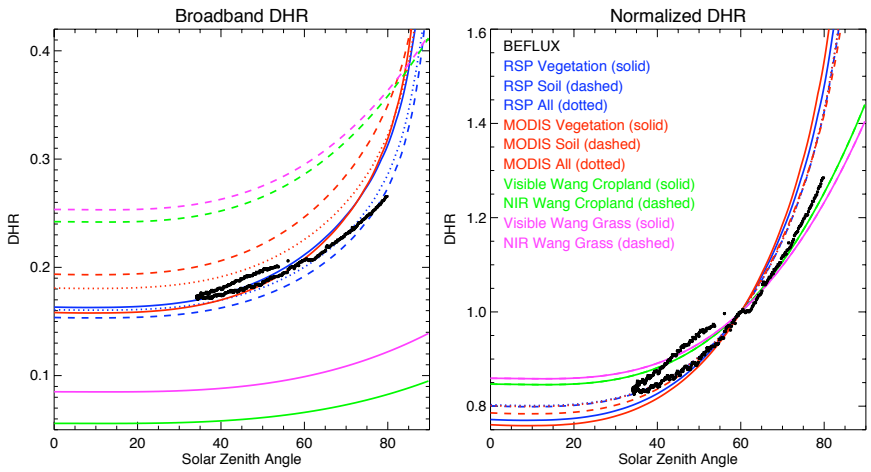

Figure 5.9: Comparison of broadband (left) and normalized broadband (right) DHR for BEFLUX ground radiometer data (black), RSP data (blue), MODIS data (red) and the parameterization from Wang et al. [2007] for 'cropland' (green) and 'grassland' (magenta). For RSP and MODIS, different surface types are indicated by solid lines ('vegetation'), dashed lines ('soil') and dotted lines ('all'). Parameterizations for visible wavelengths are indicated with solid lines, and dashed lines for the NIR.

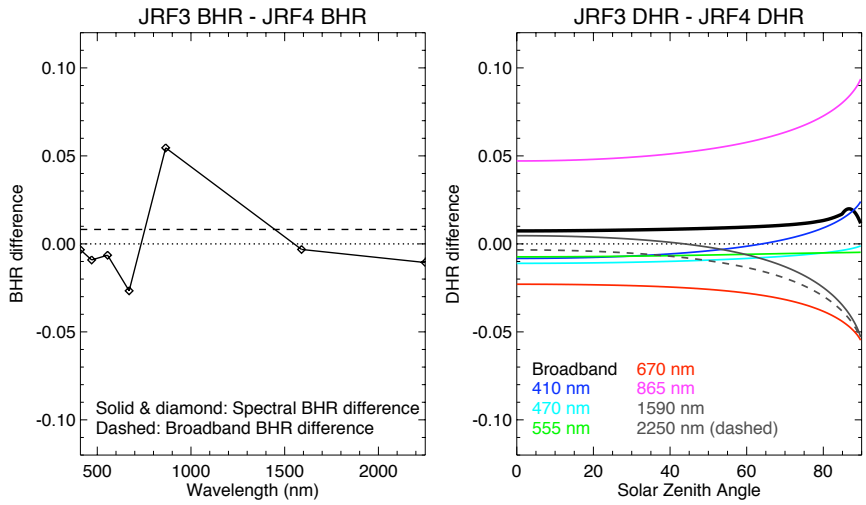

Figure 5.10: Differences in BHR and DHR estimated from data restricted to one flight, and thus one relative solar-view azimuth angle. The plot on the left is the difference between spectral $BHR(\Lambda)$ and broadband BHR_{bb} for JRF3 and JRF4 for the 'vegetation' class. The right side is the same for $DHR(\Lambda, \theta_s)$ and $DHR_{bb}(\theta_s)$.

tion results for JRF3 (relative solar - view azimuth, $\phi = 315°$ for forward scans) and JRF4 (relative solar - view azimuth, $\phi = 156°$ for forward scans) for the 'vegetation' class.

Comparisons of spectral BHR reveal inter-flight differences equal to or less than 0.07 for angles less than $80°$. The maximum difference is in the 865nm band, which for vegetation is by far the brightest channel (see figure 5.6). Broadband BHR differences are less than 0.01, less than most of the spectral BHR differences. It appears that computation of the broadband BHR removes some of the difference between the flights, which may be related to differences in the observed vegetation. Spectral DHR shows a similar pattern as BHR. Maximum differences are about 0.06 at $60°$ for the 865nm band, and increase with solar zenith angle. At solar zenith angles less than $80°$, the flight to flight DHR_{bb} difference is about 0.01.

5.6 Discussion

The foremost purpose of this paper is to evaluate MODIS BRDF estimates. This is done by comparing MODIS derived BHR and DHR (white and black sky albedos, in MODIS terminology) to the same values derived from an airborne sensor (RSP) and a group of ground radiometers (BEFLUX) during September in north-central Oklahoma. This is a region whose ground cover mainly included grassland and late season or recently harvested cropland. This location is important because of the presence of the SGP CF, where a host of atmospheric and radiometric instruments provide a continuous set of validation data. MODIS overestimates BHR_{bb} with respect to BEFLUX by between 0.003 and 0.042 (depending on the surface class, see table 5.4). The average MODIS DHR deviation (over all angles less than $80°$) from BEFLUX is 0.018, -0.002 and 0.035 for the 'all', 'vegetation' and 'soil' classes, respectively. Considering that BEFLUX derived DHR has differences up to 0.01 between measurements with the same solar zenith angle but at different times of day (morning and evening), we regard the MODIS DHR estimates as successful.

An important component of any validation work is to identify which differences are due to the data processing necessary to perform the validation, and which represent actual instrumental differences. In this case, we recognize several processing steps that may add to or mask actual instrumental differences. Both RSP and MODIS were fit to Ross-Li BRDF models, and thus are only capable of measuring the types of BRDF that are included in those models. Another potential source of error is the need to create broadband BHR and DHR from spectral RSP and MODIS values, in order to compare to naturally broadband BEFLUX derived values. This involves interpolating between spectral bands prior to integration to broadband values, and this interpolation could miss spectral variation in the BHR or DHR that is included in the broadband values derived from BEFLUX. Finally, spatial and temporal resolution differences between satellites and point sensors on the ground are a well known source of error. We have attempted to account for these problems by separating the data into comparable classes roughly representing vegetated crops or grassland and bare (recently harvested) soil. MODIS and RSP classes are consistent with

one another (see figures 5.6, 5.7, 5.8 and 5.9), and closest with the 'all' classes containing the entire dataset prior to classification. As figure 5.4 shows, RSP and MODIS data-sets have a somewhat different spatial extent. So, while the classification techniques for RSP and MODIS may not be compatible, other aspects of RSP and MODIS data processing (such as spectral to broadband conversion and model fitting) produce remarkably similar results. MODIS BHR_{bb} shows a bias with respect to RSP of 0.023, -0.005 and 0.050 for the 'all', 'vegetation' and 'soil' classes, respectively. Average (with respect to solar zenith angles less than $80°$) biases for DHR_{bb} between MODIS and RSP are 0.036, 0.006 and 0.076 for the 'all', 'vegetation' and 'soil' classes, respectively. $nDHR_{bb}$ has an average bias typically an order of magnitude less than absolute DHR_{bb}, indicating that differences between the instruments are primarily due to differences in the absolute magnitude of their estimates. MODIS-RSP comparisons of individual spectral bands show the same small bias for both DHR and $nDHR$.

This research began as an effort to investigate some of the differences between BEFLUX radiometers and MODIS parameterizations identified by Yang [2006]. We implemented the novel DHR BEFLUX computation technique described in that paper, but did so for the much more limited time range of the ALIVE campaign. Yang [2006] compared $nDHR$ to parameterizations described by Wang et al. [2007] and Liang et al. [2005], and found the BEFLUX derived values to be larger than both parameterizations at solar zenith angles greater than $80°$, and more troubling, smaller than parameterizations at angles less than $35°$. Yang's comparison utilized a third order polynomial fit because its similarity to an approximation given in Schaaf et al. [2002]. However, unlike the standard third-order polynomial that Yang used, the polynomial in Schaaf et al. [2002] is restricted to have a zero coefficient on the first-order term. Figure 5.11 presents the difference between these two fitting routines, where we fit both types of polynomials to our BEFLUX data. Schaaf's polynomial fit clearly matches RSP and MODIS DHR and $nDHR$, while the Yang polynomial diverges in a similar manner to that presented in Yang [2006]. Thus, the biases that were identified in Yang [2006] are both beyond the solar zenith angle range of the reference

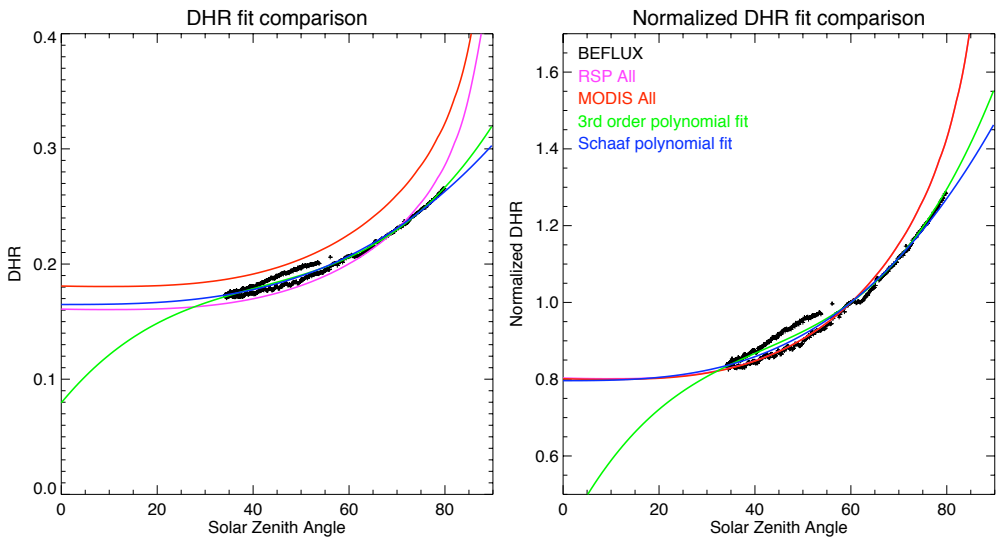

Figure 5.11: BEFLUX derived DHR (left) and $nDHR$ (right) and the corresponding polynomial fits to our subset of BEFLUX data, as described by Yang [2006] (green) and Schaaf et al. [2002] (blue). Original BEFLUX derived DHR are in black. For comparison, the 'all' classes of RSP (magenta) and MODIS (red) are also included.

dataset and most likely due to the choice of the data fit, rather than the data itself.

The albedo parameterization presented in Wang et al. [2007] is also included in the comparison in figure 5.9. Wang's parameterization, described in section 5.4.4, is an attempt to reduce the number of parameters describing MODIS albedo from three for each band to two each for broad visible and NIR bands (which are specified for various surface types). Although these broad visible and NIR channels cannot be compared directly to broadband BEFLUX DHR, the Wang et al. [2007] $nDHR$ is spectrally invariant, and thus can be compared to BEFLUX derived $nDHR$. Figure 5.9 shows that both of the selected surfaces (grass and cropland) produce $nDHR$ with slightly shallower slopes than BEFLUX derived $nDHR$. Thus, Wang's parameterizations show slightly smaller variation in DHR as a function of solar zenith angle compared to BEFLUX. Average (for solar zenith angle less than $80°$) biases for $nDHR$ are between 0.022 and 0.028, depending on the land surface type selected for the parameterization.

5.7 Conclusion

Generally speaking, this validation shows that there is good agreement between MODIS, RSP and BEFLUX ground radiometer derived albedos, at least for the conditions of the ALIVE experiment at the SGP CF. MODIS, which is capable of producing global BRDF estimates, produces DHR and BHR ('black-sky' and 'white-sky', albedos, respectively) that agree with aircraft measurements from RSP. RSP has a higher spatial and temporal resolution than MODIS, and its data are atmospherically corrected with more sophisticated algorithms, yet differences between the two are minimal. It is important to note that RSP used the same Ross-Li BRDF models employed by MODIS, so some potential instrumental differences may be masked by this similarity. However, model fitting results are robust and physically realistic. RSP and MODIS also agree well with DHR and BHR derived from the BEFLUX ground radiometers, whose methodology is quite different than the BRDF model fitting routines employed by the remote sensing instruments. A potential source

of non-instrumental comparison error are the methods used to convert spectral DHR and BHR to broadband values. In our case we were required to interpolate spectral albedos and model the ground-atmosphere interaction. Previously identified differences between BEFLUX ground radiometers and MODIS were shown to be for DHR in solar zenith angles beyond the range of available comparison angles and were most likely due to the choice of the type of polynomial fit to the data, rather than instrumental effects in the data itself.

This validation effort is hindered by the small quantity of data available for comparison. Cloud free, low altitude RSP measurements were limited to a single day (September 16, 2005) during the ALIVE campaign. RSP serves as an airborne prototype to the Aerosol Polarimetery Sensor (APS), due to be launched as part of the NASA Glory mission in 2008. APS is not an imaging instrument and will not be able to create global BRDF estimates as like MODIS. However, the rapid angular scanning and accurate atmospheric correction of APS means that it is an ideal platform for validation of BRDF estimates from MODIS and other instruments. Pending a successful launch, Glory will join the NASA 'A-train' orbit, and APS will begin gathering a validation dataset much, much larger than what was available for the work in this paper. The methods used here could become part of routine BRDF remote sensing validation effort.

5.8 Appendix

5.8.1 Correction for gas absorption

Prior to assessing ground reflectance, water vapor, ozone and NO_2 absorption effects were removed from the direct solar beam. Water vapor was measured at SGP CF with a MWR, while ozone and NO_2 measurements were provided by the TOMS and SCIAMACHY orbital instruments, respectively. Absorption coefficients were computed using the spectral sensitivity of each RSP band, and applied to RSP measurements as follows:

$$I_c = I\left(e^{-M\left(K_{O_3}x_{O_3}+K_{NO_2}x_{NO_2}\right)-\alpha[wM]^{\beta})}\right)^{-1} \tag{5.23}$$

where I and I_c are the original and corrected radiances, respectively. K_{O_3} is the ozone absorption coefficient, x_{O_3} is the ozone quantity in centimeters per atmosphere, K_{NO_2} is the NO_2 absorption coefficient, x_{NO_2} is the quantity of NO_2 in parts per billion, w is the column water vapor, in centimeters, and parameters α and β define the optical depth due to water vapor. α, β, K_{oz} and K_{NO_2} are given in table 5.5. M is the airmass, which defines the length of the atmospheric path from the sun to the Earth surface and is well approximated for the solar zenith angles encountered here by $M = cos(\theta_s)^{-1}$. The use of the correction procedure defined by equation 5.23 is justified for ozone and nitrogen dioxide by the fact that they absorb light primarily in the stratosphere, above most atmospheric scattering. It is acceptable for water vapor because this only affects RSP bands at 1590 and 2250nm, for which single scattering is a valid approximation of the effects of aerosols and molecules. Gas quantities for the day of our experiment were: 0.285 Dobson Units of Ozone, 0.74 ppb of NO_2, and precipitable water vapor between 1.237 and 1.498cm, depending on the time of day.

Table 5.5: Gas absorption parameters

Band	Wavelength	K_{O_3}	K_{NO_2}	α	β
1	410	0.000278	0.012860	0.00000	1.000000
2	469	0.010035	0.008135	0.00000	1.000000
3	555	0.096960	0.001827	0.00026	0.990068
4	670	0.044982	0.000144	0.00053	0.958742
5	864	0.002060	0.000000	0.00061	0.953774
7	1589	0.000000	0.000000	0.00251	0.645347
9	2264	0.000000	0.000000	0.01141	0.739948

5.8.2 Vegetation Indicies

The canonical method for assessing surface vegetation content is the Normalized Difference Vegetation Index (NDVI):

$$NDVI = \frac{L_{NIR} - L_{red}}{L_{NIR} + L_{red}} \tag{5.24}$$

where L is the radiance detected by a red or near-infra red (NIR) sensor. Vegetation has a low reflectance at red wavelengths, and much higher reflectance in the NIR, while soils and other non-vegetated surfaces have much smaller spectral contrast between the red and NIR. NDVI has been used for years to assess vegetation health and cover from space, although it is important to note that it is simply an index not an actual physical parameter. However, there is the possibility that the spectral dependence of the aerosol optical properties modifies L_{NIR} and L_{red} in a manner that affects NDVI [Kaufman and Tanre, 1992]. We therefore used Kaufman and Tanré's Atmospherically Resistant Vegetation Index (ARVI) which is less sensitive to the effects of atmospheric aerosols [Kaufman and Tanre, 1992]. ARVI uses a channel at a blue wavelength in order to correct for atmospheric effects. It is defined in terms of normalized reflectances as:

$$\begin{aligned} ARVI &= \frac{\rho_{NIR} - \rho_{rb}}{\rho_{NIR} + \rho_{rb}} \\ \rho_{rb} &= \rho_{red} - \gamma(\rho_{blue} - \rho_{red}) \end{aligned} \tag{5.25}$$

where γ is a parameter that depends on the aerosol type. We used a value of $\gamma = 0.9$ as suggested by Kaufman and Tanré for continental aerosols. RSP channels 2 (470nm), 4 (670nm) and 5 (865nm) were used for ρ_{blue}, ρ_{red}, and ρ_{NIR}, respectively.

Chapter 6

Conclusion

Accurate global climate simulations are essential if we are to understand, predict and adapt to climate change. Despite recent advances, historical simulations of the climate record by models and predictions of future change still have considerable uncertainty, much of it associated with the radiative forcing imposed by atmospheric aerosols. Aerosols, which are suspended particulate matter, interact with the global climate directly by scattering and absorbing radiation, or indirectly by altering the optical properties and lifetime of clouds. Unlike greenhouse gases, they are short lived and have a variety of chemical and physical compositions, sources and sinks. Climate model uncertainties are primarily associated with aerosol radiative forcing and cloud feedbacks. A substantial amount of the uncertainty associated with the aerosol radiative forcing is caused by a lack of consistent and accurate observations, which require satellite remote sensing to provide global coverage. The current suite of satellite observations are unable to capture all the necessary aerosol descriptive parameters, but scanning instruments that utilize polarimetry at both visible and NIR wavelengths offer the possibility to do so. This thesis is an investigation of the potential for aerosol optical property retrieval with the Aerosol Polarimetry Sensor (APS) on the upcoming NASA Glory mission, and its airborne prototype, the Research Scanning Polarimeter (RSP). These instruments represent a substantial advance over previous Earth observing polarization measurements because of their wide spectral range, high polarimetric accuracy, and high angular resolution.

While the APS has yet to be launched, its retrieval capabilities for aerosol optical properties in typical cloudless scenes over land and ocean have been investigated using RSP data in various publications, including Chowdhary [1999], Chowdhary et al. [2001], Chowdhary et al. [2002], Cairns [2003], Chowdhary et al. [2005a], Cairns et al. [2009] and Waquet et al. [2009a]. This thesis is a continuation of that work, where the utility of scanning polarimeter observations is investigated for more complex scenes, such as observations of extremely optically thick, absorbing, and vertically stratified biomass burning aerosols (chapter 3) and aerosols suspended above marine stratocumulus clouds (chapter 4). This used the Doubling and Adding Optimization (DAO) optimization algorithm, which was created to extract aerosol and cloud information from RSP scenes. DAO is very flexible, and retrieves both aerosol parameters and their uncertainty. It is therefore an ideal tool for investigating the remote sensing capability of scanning polarimeters. A procedure to determine the best optimization strategy for various types of scenes has been established in this thesis. This procedure, and the software that was created as part of it, will be used for future scanning polarimeter research. An additional component of this thesis was an investigation of the surface reflectance validation capability of scanning polarimeters for instruments such as the Moderate Resolution Imaging Spectroradiometer (MODIS), which has coarser angular resolution but better spatial coverage. While DAO was not used directly as part of this work, it did involve the use of the same radiative transfer model with a simpler iteration scheme to fit RSP observations.

This thesis is a collection of three papers intended for peer-reviewed publication. The main conclusions of each paper are described below.

Chapter 3, which is ready to submit to the journal *Atmospheric Chemistry and Physics*, was both a test of aerosol optical property retrieval for extremely optically thick plumes, and of the utility of merger with data from active Lidar instruments. Optimization was performed for a series of RSP observations using Lidar data, then repeated without Lidar data (which included aerosol layer heights and optical thicknesses). We found that all scenes with Lidar data compared well to in situ observations, while about half of the scenes with-

out Lidar data did not converge to a solution that matched the in situ observations. This anomalous convergence was not due to the lack of information about aerosol layer heights, but because the Lidar provided an accurate initial estimate of aerosol optical depth. Correct initial optical depth values ensured that the optimization did not find a false minimum, but converged to an aerosol type similar to what was observed by in situ measurements of the scene. Correctly and incorrectly retrieved aerosol types differed in size and quantity of absorption, highlighting the difficulty of observations of optically thick and absorbing plumes such as these, and the value of appropriate initial values provided by external sources such as a lidar. Furthermore, aircraft geometry, specifically pitch angle, was identified as a significant potential source of retrieval error in this paper.

Chapter 4 tested the ability of RSP and APS to retrieve optical properties of scenes where aerosols are lofted above clouds (AAC). This was tested both with simulations and with observations of a scene with mixed urban/smoke aerosols lofted above a marine stratocumulus cloud. Provided the cloud top height is known, aerosol and cloud droplet size distribution are retrievable, along with aerosol optical depth. Uncertainties in these values were within climate model accuracy requirements. Reasonable aerosol refractive indices were found, but their assessed uncertainties were very large. Sensitivity studies show that retrieval uncertainties for all parameters except cloud droplet size distribution decrease as aerosol optical depth increases, but that complex refractive index uncertainty meets accuracy requirements only for very large optical depths. Despite these limitations, this technique will extend satellite observations to a category of aerosols, AAC, that previously were unobservable by passive instruments. This chapter will be submitted soon to *Atmospheric Chemistry and Physics*.

Chapter 5 is a validation of the ability of the MODIS instrument to systematically retrieve surface reflectance using data from the RSP. Surface reflectance, represented by the bidirectional reflectance distribution function (BRDF), can be robustly estimated by the RSP because of that instrument's high spatial and angular resolution, view angle range, and accurate atmospheric correction. MODIS makes systematic global observations, but has

much lower spatial resolution, limited angular sampling and much simpler atmospheric correction algorithms. The RSP observations can therefore be used to validate the MODIS estimates of surface BRDF, and the APS, when it is launched, can regularly validate MODIS surface reflectance within its narrow swath, since it will be launched into the 'A-train' orbit, which contains one of the two MODIS instruments. Additionally, the dependence of the surface albedo on solar illumination angle is of particular interest for climate models, which was also evaluated in this chapter using simultaneous surface observations. This chapter was published in the *Journal of Geophysical Research* in 2008 (Knobelspiesse et al. [2008]).

6.1 Future work

Much of the motivation for this thesis is the upcoming launch of the APS instrument and the anticipated future use of similar polarimeters. The Doubling and Adding Optimization (DAO) algorithm, which has the capability to determine atmospheric optical properties and quantify their uncertainties, is an ideal tool to investigate retrieval methods. Based on the analyses described in chapters 3 and 4, I have developed a procedure to systematically investigate retrieval capability using DAO and the radiative transfer model that forms its core. This utilizes both simulated and observed data, along with in situ measurements, if available. This procedure is appropriate for future investigations of scanning polarimeter capability, and is briefly described below.

1. **Simulation** Investigation begins by first simulating the anticipated observation. Select a reasonable aerosol (and if applicable, cloud or surface) scene, and create simulated observations for a variety of optical depths using the radiative transfer model that is part of DAO. As in section 4.3, compute the Jacobian sensitivity matrix for each of these simulations. Given the observation error covariance matrix, compute the retrieval error covariance matrix (equation 4.8). This step expresses the parameter sensitivity for the given scene, and can be used to determine the value of improved

measurement accuracy and pointing knowledge. Further information can be found in the Shannon information content (equation 3.18) which is a scalar value indicating the information gained during measurement and optimization. This is useful to compare various retrieval strategies, especially if the simulated retrieval error covariance matrices are not obviously distinct. Finally, the error correlation matrix, which is related to the retrieval error covariance matrix (equation 4.10), can be used to determine relationships between retrieved parameters. All of this information is used to determine a retrieval strategy, where tradeoffs between observations and their uncertainties are used to determine which parameters to retrieve and which to assume based on climatologies or external information.

2. **Optimization** Test the optimization strategy determined above using data collected during a real scene. If possible, use a scene where several observations have been made under similar conditions. The variability in retrieved parameters can be compared to uncertainty estimates (as in section 5.5) to help identify if the latter are realistic. Retrieval uncertainties, correlation and information content can be compared to the simulated values, which will indicate whether the information used to determine the optimization strategy was coherent with reality. If necessary, the simulation or optimization steps can be repeated in light of these comparisons. Chapters 3 and 4 both present scene optimizations.

3. **Validation** If in situ data are available, comparisons can be made between these observations and optimization results. Examples of this are in sections 3.3 and 4.4.3

4. **Forward model testing** The optimization Jacobian matrix can be used to investigate the impact of errors in model assumptions by perturbing individual assumptions in the forward model, recomputing, and comparing the results to the optimized model results. The Jacobian is used to project this difference into parameter space. This establishes the importance of various model assumptions, and identifies which must be chosen with the most care. For an example of this, see section 4.4.4

5. **Determine systematic retrieval strategy** The above steps are used to identify a systematic retrieval strategy for instruments such as APS. The retrieval strategy should be universal, and not specifically require the use of DAO, which is not optimized for speed. The design of future instruments can also rely on the sensitivities, strengths, and weaknesses revealed above.

The steps outlined above provide a plan for future investigations. For example, these steps will be followed in my proposed postdoctoral research, which is an investigation of the feasibility of simultaneous retrieval of aerosol and cloud properties for pixels contains both cloud covered and cloud free regions. While the difficulty of retrievals such as this is obviously higher than for pixels containing clouds alone, or an entirely cloud free scene, the simulation and testing strategy outlined above can illustrate what information can be gleaned from this type of scene.

This research could be extended and continued in many ways, which are briefly described here. Some of this research involves increasing the capability of DAO, while others involve assessment of new scene types and data analysis. Most of these items will take considerable effort to implement, and are presented merely to show the potential direction of this research in the next few years.

- **Create scene Look up Tables** Climatologies of aerosol properties and ancillary information about the scene were used in this research to identify the initial parameter values used during optimization. Since this requires human intervention, this is not feasible for systematic aerosol retrievals. A more automated and objective method uses a Look up Table (LUT), composed of simulations of a wide variety of aerosol optical properties and optical depths. Rather than selecting initial optimization values by hand, the parameters of the LUT scene most similar to observations are used as initial optimization values. Creating the LUT requires considerable computing resources, which is one of the reasons it was not done for this research. If Jacobian matrices are also computed with each LUT scene, the synthetic uncertainty can be determined and more accurate interpolation between LUT entries can be performed.

- **Error correlation** The error correlation matrix that was used in chapters 3 and 4 assumed that there is no correlation between observations. While this is an assumption that has also been made for simplicity in other publications (such as Lebsock et al. [2007] and Waquet et al. [2009a]), the reality of observations with high angular resolution is that they have a large degree of correlation. For various computational reasons (the MPFIT Levenberg-Marquardt implementation in DAO does not easily allow for correlated errors), this was not done for this research, but it is a subject worthy of investigation, particularly for homogeneous, clear sky scenes where the angle to angle relative accuracy of the observations can be used to improve the accuracy of microphysical retrievals.

- **Improve the radiative transfer model** The radiative transfer model that forms the core of DAO is, like any model, highly simplified. There are various ways to improve the model and add to its range of capabilities. One of the most useful improvements would be include a database of calculations of single scattering by nonspherical particles. Methods exist to do this (Mishchenko and Travis [1998], Mishchenko [2000], Dubovik et al. [2006]), and this would be a matter of integrating preexisting software into DAO.

- **Surface polarized reflectance** Chapter 5 involved the use of highly accurate surface reflectances to validate MODIS observations. Polarized surface reflectance was also collected with this data, but has yet to be analyzed and presented. These data are ideal to identify the validity of RSP and APS assumptions about the spectral dependence of surface polarized reflectance, and can be used to identify the potential for error that should be added to the error correlation matrix.

- **Add ocean optics model to DAO** An accurate and well validated model has been created to simulate in water radiative transfer for use with RSP and APS data (Chowdhary [1999], Chowdhary et al. [2001], Chowdhary et al. [2002], Chowdhary et al. [2005a], Chowdhary et al. [2005b], and Chowdhary et al. [2006]). However, this

model is not currently used as part of an optimization technique. Coupling it with the DAO radiative transfer model would be a powerful extension of capability over water bodies.

- **Allow for optimization of surface parameters** The current implementation of the DAO radiative transfer model first computes surface reflectance, which is then used by the doubling and adding component of the model to simulate observations. Surface reflectance is only computed during the first radiative transfer step, which means that surface reflectance parameters cannot be optimized. Adding this capability would allow us to investigate simultaneous retrieval of aerosol properties and surface total reflectance. As we can see in chapter 5, most of the spectral variability inherent in surface reflectance is expressed in an isotropic manner, while the angular shape of the BRDF is nearly spectrally invariant. This feature could be used to add total reflectance observations to the measurement vector and possibly increase the information content available in a scene. In fact, this feature of surface reflectance is used in the aerosol retrieval algorithms of multi-angle instruments that are not sensitive to polarization, such as the Advanced Along-Track Scanning Radiometer (A)ATSR, (Curier et al. [2009], Grey and North [2009]) and Multi-angle Imaging SpectroRadiometer, MISR (Hu et al. [1999], Martonchik et al. [2002]).

- **Analytic Jacobians** The results of a doubling and adding radiative transfer model calculation include all the internal fields required to calculate perturbations of the radiation field with respect to any parameter, analogous to the adjoint method. The advantage of the doubling and adding method for calculating Jacobians for multi-angle data is that only one forward model calculation is required, rather than an additional calculation for every pseudo-source (viewing geometry) which is required for other adjoint methods (Hasekamp and Landgraf [2007]). This means that the use of analytical Jacobians can reduce the time for each iteration in a Levenberg-Marquardt search by an order of magnitude (for 10 parameters) and I will implement

this approach to the calculation of Jacobian in a future implementation of the DAO software.

There is a wealth of data that have been gathered by scanning polarimeters, which we are still learning to analyze. In fact, since the most recent field campaign used in this thesis (ARCTAS, which was in the summer of 2008), there have been RSP field campaigns in the central valley of California, central Oklahoma, the Birmingham metropolitan area in Alabama, over the Gulf of Mexico, and in Bermuda. With the launch of APS, the field of polarimetery will be enriched by copious volumes of data, so the future holds much promise for further developments.

Chapter 7

Symbols and Acronyms

Symbol	Description, with units if applicable
a	EM wave amplitude
a_1	Phase matrix element $P_{1,1}$
a_2	Phase matrix element $P_{2,2}$
a_3	Phase matrix element $P_{3,3}$
a_4	Phase matrix element $P_{4,4}$
a_j	Lorenz-Mie scattering coefficient of the jth order
b	Aerosol backscatter coefficient [$km^{-1}sr^{-1}$]
b_1	Phase matrix element $P_{1,2}$ and $P_{2,1}$
b_2	Phase matrix element $P_{3,4}$ and $-P_{4,3}$
b_j	Lorenz-Mie scattering coefficient of the jth order
BHR	Bihemispherical reflectance
BHR_{bb}	Broadband bihemispherical reflectance
$BPRDF$	Bidirectional polarized reflectance distribution function
$BRDF$	Bidirectional reflectance distribution function
$\mathbf{C}_a$	A priori error covariance matrix
$\mathbf{C}_{ag}$	Data aggregation error covariance matrix
$\mathbf{C}_{cal}$	Radiometric calibration error covariance matrix
$\mathbf{C}_p$	Aircraft pitch error covariance matrix
$\mathbf{C}_{pol}$	Polarization error covariance matrix
$\mathbf{C}_T$	Measurement error covariance matrix
$\mathbf{C}_x$	Retrieval error covariance matrix
$\mathbf{C}_y$	Aircraft yaw error covariance matrix
$\mathbf{C}_\varepsilon$	Measurement error covariance matrix
$\mathbf{D}$	Levenberg-Marquardt scaling matrix
DHR	Directional-hemispherical reflectance
DHR_{bb}	Broadband directional-hemispherical reflectance
$\mathbf{e}$	Model error vector

E	Irradiance [Wm^{-2}]
E_l	Electric field parallel to the direction of wave propagation [$Wm^{-2}sr^{-1}$]
E_r	Electric field perpendicular to the direction of wave propagation [$Wm^{-2}sr^{-1}$]
f_{iso}	Isotropic scattering scaling parameter
f_{geo}	Geometric scattering kernel scaling parameter
f_{pol}	Polarized reflectance kernel scaling parameter
f_{vol}	Volumetric scattering kernel scaling parameter
$\mathbf{f}$	Vector of kernel scaling parameters
$\mathbf{F}$	Forward model weighted deviation from observation vector
F_o	Exo-atmospheric irradiance [Wm^{-2}]
F_p	Fresnel polarized reflectance coefficient
g	Asymmetry parameter
G	Geometric cross sectional area of a particle [m^2]
$\mathbf{G}$	Radiative transfer forward model
G_a	Forward model that returns indirect parameters
h	Altitude [m]
H_s	Shannon information content
I	First element of Stokes polarization vector [$Wm^{-2}sr^{-1}$]
I_p	Linearly polarized radiance [$Wm^{-2}sr^{-1}$]
$\mathbf{I}$	Stokes polarization vector ($\mathbf{I} = \{I, Q, U, V\}$) [$Wm^{-2}sr^{-1}$]
$\mathbf{I}_o$	Incident Stokes polarization vector, typically ($\mathbf{I} = \{1, 0, 0, 0\}$) [$Wm^{-2}sr^{-1}$]
$\mathbf{J}$	Jacobian matrix
k	Wavenumber [μm^{-1}]
k_a	Absorption coefficient [m^{-1}]
k_e	Extinction coefficient [m^{-1}]
k_s	Scattering coefficient [m^{-1}]
K_{geo}	Geometric scattering kernel
K_{NO_2}	Nitrogen Dioxide absorption coefficient
K_{O_3}	Ozone absorption coefficient
$K_{pol,v}$	'Vegetation' polarized reflectance kernel
$K_{pol,s}$	'Soil' polarized reflectance kernel
K_{vol}	Volumetric scattering kernel
$\mathbf{K}$	the 3xN kernel matrix formed from the isotropic, volumetric and geometric kernels, where N is the number of observations
$\hat{\mathbf{l}}$	Unit vector parallel to the direction of EM radiation propagation
L	Radiance [$Wm^{-2}sr^{-1}$]
m	Complex refractive index, $m = \Re(m) + \Im(m)$
M	Airmass
$\mathbf{M}$	Multiple scattering convergence matrix

n	Aerosol volume number concentration [μm^{-2}]
$NDVI$	Normalized Difference Vegetation Index
$nDHR$	Normalized directional-hemispherical reflectance
$\mathbf{p}$	Parameter vector that, when added to $\mathbf{x}_o$, minimizes Φ
P	Scattering phase function
P_j^1	Legendre polynomial of the jth order
Q	Second element of Stokes polarization vector [$Wm^{-2}sr^{-1}$]
r	radius [μm]
r_e	Effective radius [μm]
r_g	Log-normal aerosol size distribution radius parameter [μm]
r_o	Solar distance [AU]
$\hat{\mathbf{r}}$	Unit vector perpendicular to the direction of EM radiation propagation
R_I	I reflectance
R_Q	Q reflectance
R_U	U reflectance
R_p	Polarized reflectance
S	Backscatter to extinction ratio [sr]
S_1	Lorenz-Mie scattering function
S_2	Lorenz-Mie scattering function
t	Time [s]
$t^{\downarrow}$	Direct solar transmittance from the sun to the ground
$t^{\uparrow}$	Direct solar transmittance from the ground to the observation
T	Period [s]
$T^{\downarrow}$	Diffuse solar transmittance from the sun to the ground
$T^{\uparrow}$	Diffuse solar transmittance from the ground to the observation
U	Third element of Stokes polarization vector [$Wm^{-2}sr^{-1}$]
v_e	Effective variance
V	Fourth element of Stokes polarization vector [$Wm^{-2}sr^{-1}$]
w	Column water vapor [cm]
x	Size parameter
x_{O_3}	Ozone quantity [cm]
x_{NO_2}	Nitrogen Dioxide quantity [ppb]
$\mathbf{x}$	Radiative transfer model parameter vector
$\mathbf{x}_o$	Radiative transfer model initial parameter vector
$\mathbf{Y}$	Measurement vector
$\hat{\mathbf{z}}$	Unit vector in the direction of EM radiation propagation
α	Ångström exponent
δ	Rayleigh scattering anisotropy parameter
Δ	Levenberg-Marquardt trust region
Δ_r	Rayleigh scattering anisotropy parameter
Δ_r'	Rayleigh scattering anisotropy parameter

θ_s	Solar zenith angle
θ_v	View zenith angle
λ	Wavelength [μm]
Λ	Narrow spectral band center wavelength
μ	$\cos(\theta)$
ε	EM wave phase
ξ	Scattering angle from the incident illumination vector
π_j	Lorenz-Mie scattering angle dependent coefficient
ϖ	Single scattering albedo
ρ	Correlation matrix element
ρ^o	Observed reflectance at aircraft altitude
ρ^a	Reflectance to to atmospheric scattering
ρ^g	Surface reflectance
σ_A	Indirectly retrieved parameter standard deviation
σ_a	Extinction cross-section [μm^2]
σ_e	Extinction cross-section [μm^2]
σ_g	Log-normal aerosol size distribution width parameter
σ_s	Scattering cross-section [μm^2]
Σ	Function used to calculate multiple surface atmosphere interactions
τ	Optical depth
τ_j	Lorenz-Mie scattering angle dependent coefficient
Υ	Levenberg-Marquardt parameter
ϕ	Relative azimuth angle (view azimuth - solar azimuth)
ϕ_s	Solar azimuth angle
ϕ_v	View azimuth angle
Φ	Optimization cost function
χ	Polarization angle
ω	Angular frequency [s^{-1}]

Acronym	Description
AAC	Aerosols Above Clouds
AATS	Ames Airborne Tracking Sunphotometer
(A)ATSR	Advanced Along-Track Scanning Radiometer
AERONET	Aerosol Robotic Network
ALIVE	Aerosol Lidar Validation Experiment
AOP	Apparent Optical Property
APS	Aerosol Polarimetry Sensor
APS	Aerodynamic Particle Sizer
ARCTAS	Arctic Research of the Composition of the Troposphere from Aircraft and Satelites
ARVI	Aerosol Resistant Vegetation Index
AU	Astronomical Unit
AVHRR	Advanced Very High Resolution Radiometer
BB	Biomass Burning
BC	Black Carbon
BEFLUX	Best Estimate Radiation Flux
BHR	Bihemispherical Reflectance
BrC	Brown Carbon
BRDF	Bidirectional Reflectance Distribution Function
CALIPSO	Cloud-Aerosol Lidar and Infrared Pathfinder Satellite Observations
CALIOP	Cloud-Aerosol Lidar with Orthogonal Polarization
CAR	Cloud Absorption Radiometer
CCN	Cloud Condensation Nuclei
CDNC	Cloud Droplet Number Concentration
DAO	Doubling and Adding Optimization (software)
DCF	Direct Climate Forcing
DHR	Directional-Hemispherical Reflectance
ECMWF	European Centre for Medium Range Weather Forecasts
EM	Electromagnetic
GFS	Global Forecast System
GISS	Goddard Institute for Space Studies
HiGEAR	Hawaii Group for Environmental Aerosol Research
HSRL	High Spectral Resolution Lidar
HULIS	Humic-Like Substances
IDL	Interactive Data Language
IFOV	Instantaneous Field of View
IMU	Inertial Monitoring Unit
IN	Ice Nuclei
INTEX	Intercontinental Chemical Transport Experiment
IOP	Inherent Optical Property
IPCC	Intergovernmental Panel on Climate Change

LLGHG	Long Lived GreenHouse Gases
LDMA	Long Differential Mobility Analyzer
LUT	Look Up Table
LWC	Liquid Water Content
MCMA	Mexico City Metropolitan Area
MILAGRO	Megacity Initiative: Local and Global Research Observations
MISR	Multi-angle Imaging Spectro-Radiometer
MODIS	Moderate Resolution Imaging Spectroradiometer
MWR	Microwave Radiometer
NCEP	National Center for Environmental Prediction
nDHR	Normalized Directional-Hemispherical Reflectance
NIR	Near infra-red
NDVI	Normalized Difference Vegetation Index
OC	Organic Carbon
OMI	Ozone Monitoring Instrument
OPAC	Optical Properties of Aerosols and Clouds
PARASOL	Polarization and Anisotropy of Reflectance for Atmospheric Sciences coupled with Observations from a Lidar
POLARCAT	Polar Study using Aircraft, Remote Sensing, Surface Measurements and Models of Climate, Chemistry Aerosols and Transport
POLDER	Polarization and Directionality of the Earth's Reflectances
POS	Position and Orientation System
RF	Radiative Forcing
RSP	Research Scanning Polarimeter
SCIAMACHY	SCanning Imaging Absorption spectroMeter for Atmospheric CartograpHY
SGP-CF	Southern Great Plains Central Facility
SOA	Secondary Organic Aerosol
SSFR	Solar Spectral Flux Radiometer
SURFRAD	Surface Radiation Budget Network
TOMS	Total Ozone Mapping Spectrometer
UV	Ultra-violet
VOC	Volatile Organic Compounds

Bibliography

S.J. Abel, J.M. Haywood, E.J. Highwood, J. Li, and P.R. Buseck. Evolution of biomass burning aerosol properties from an agricultural fire in southern Africa. *Geophys. Res. Lett.*, 30(15):1783, 2003.

A.S. Ackerman, O.B. Toon, D.E. Stevens, A.J. Heymsfield, V. Ramanathan, and EJ Welton. Reduction of tropical cloudiness by soot. *Science*, 288(5468):1042, 2000.

AC Aiken, DR Worsnop, A. Trimborn, M. Northway, EA Stone, JJ Schauer, RM Volkamer, E. Fortner, and B. Foy. Mexico City aerosol analysis during MILAGRO using high resolution aerosol mass spectrometry at the urban supersite (T0)- Part 1: Fine particle composition and organic source apportionment. *Atmos. Chem. Phys*, 9(17):6633–6653, 2009.

B.A. Albrecht. Aerosols, Cloud Microphysics, and Fractional Cloudiness. *Science*, 245 (4923):1227, 1989.

T.L. Anderson, R.J. Charlson, N. Bellouin, O. Boucher, M. Chin, S.A. Christopher, J. Haywood, Y.J. Kaufman, S. Kinne, J.A. Ogren, L. A. Remer, T. Takemure, D. Tanré, O. Torres, C.R. Trepte, B.A. Wielicki, D.M. Winker, and H. Yu. An "A-Train" strategy for quantifying direct climate forcing by anthropogenic aerosols. *Bull. Amer. Meteor. Soc.*, 86:1795–1809, 2005.

M.O. Andreae and P.J. Crutzen. Atmospheric Aerosols: Biogeochemical Sources and Role in Atmospheric Chemistry. *Science*, 276(5315):1052–1058, 1997.

MO Andreae and A. Gelencser. Black carbon or brown carbon? The nature of light-absorbing carbonaceous aerosols. *Atmos. Chem. Phys*, 6(10):3131–3148, 2006.

S. E. Bauer, D. Koch, N. Unger, S. M. Metzger, D. T. Shindell, and D. G. Streets. Nitrate aerosols today and in 2030: a global simulation including aerosols and tropospheric ozone. *Atmos. Chem. Phys.*, 7(19):5043–5059, 2007. doi: 10.5194/acp-7-5043-2007.

SE Bauer, S. Menon, D. Koch, TC Bond, and K. Tsigaridis. A global modeling study on carbonaceous aerosol microphysical characteristics and radiative forcing. *Atmospheric Chemistry and Physics Discussions*, 10:4543–4592, 2010.

R. W. Bergstrom, P. Pilewskie, P. B. Russell, J. Redemann, T. C. Bond, P. K. Quinn, and B. Sierau. Spectral absorption properties of atmospheric aerosols. *Atmos. Chem. Phys. Discuss.*, 7:10669–10686, 2007.

R. W. Bergstrom, K. S. Schmidt, O. Coddington, P. Pilewskie, H. Guan, J. M. Livingston, J. Redemann, and P. B. Russell. Aerosol spectral absorption in the mexico city area: results from airborne measurements during milagro/intex b. *Atmos. Chem. Phys.*, 10: 6333–6343, 2010.

C.F. Bohren and D.R. Huffman. *Absorption and Scattering of Light by Small Particles*. Wiley-VCH Verlag GmbH and Co. KGaA, 1983.

T.C. Bond. Spectral dependence of visible light absorption by carbonaceous particles emitted from coal combustion. *Geophys. Res. Lett.*, 28(21):4075–4078, 2001.

M. Born and E. Wolf. *Principles of Optics: Electromagnetic Theory of Propagation, Interference and Diffraction of Light*. Pergamon Press, 1980.

O. Boucher. Air traffic may increase cirrus cloudiness. *Nature*, 397(6714):30–31, 1999.

H. Bovensmann, JP Burrows, M. Buchwitz, J. Frerick, S. Noël, VV Rozanov, KV Chance, and APH Goede. SCIAMACHY: Mission Objectives and Measurement Modes. *J. Atmos. Sci.*, 56(2):127–150, 1999.

F.M. Breon and P. Goloub. Cloud droplet effective radius from spaceborne polarization measurements. *Geophys. Res. Lett.*, 25(11):1879–1882, 1998.

F.M. Breon, D. Tanre, P. Lecomte, and M. Herman. Polarized reflectance of bare soils and vegetation: measurementsand models. *IEEE Trans. Geosci. Remote Sens.*, 33(2): 487–499, 1995.

C.J. Bruegge, M.C. Helmlinger, J.E. Conel, B.J. Gaitley, and W.A. Abdou. PARABOLA III- A sphere-scanning radiometer for field determination of surface anisotropic reflectance functions. *Remote Sensing Reviews*, 19(1):75–94, 2000.

B. Cairns. Polarimetric remote sensing of aerosols. *IEEE Trans. Geosci. Remote Sens.*, pages 518–520, 2003.

B. Cairns, B.E. Carlson, A.A. Lacis, and E.E. Russell. Analysis of ground-based polarimetric sky radiance measurements. *Proc. SPIE*, 3121:382–393, 1997a.

B. Cairns, L.D. Travis, and E.E. Russell. An analysis of polarization: ground based upward looking and aircraft/satellite based downward looking measurements. In *Satellite Remote Sensing of Clouds and the Atmosphere II*. SPIE, September 1997b.

B. Cairns, B.E. Carlson, R. Ying, A.A. Lacis, and V. Oinas. Atmospheric correction and its application to an analysis of Hyperion data. *IEEE Trans. Geosci. Remote Sens.*, 41(6): 1232–1245, 2003.

B. Cairns, F. Waquet, K. Knobelspiesse, J. Chowdhary, and J.L. Deuzé. *Satellite Aerosol Remote Sensing over Land*, chapter Polarimetric remote sensing of aerosols over land surfaces, pages 295–325. Springer-Praxis Books in Environmental Sciences, 2009.

Canada. Forest fire conditions for june 20 to june 30, 2008, August 2009. URL `https://nofc1.cfsnet.nfis.org/mapserver/cwfis/index.phtml`.

M.T. Chahine. Determination of the temperature profile in an atmosphere from its outgoing radiance. *J. Opt. Soc. Am*, 58:1634–1637, 1968.

D. Chand, TL Anderson, R. Wood, RJ Charlson, Y. Hu, Z. Liu, and M. Vaughan. Quantifying above-cloud aerosol using spaceborne lidar for improved understanding of cloudy-sky direct climate forcing. *J. Geophys. Res*, 113, 2008.

D. Chand, R. Wood, TL Anderson, SK Satheesh, and RJ Charlson. Satellite-derived direct radiative effect of aerosols dependent on cloud cover. *Nature Geoscience*, 2009.

R.J. Charlson, J.E. Lovelock, M.O. Andreae, S.G. Warren, et al. Oceanic phytoplankton, atmospheric sulphur, cloud albedo and climate. *Nature*, 326(6114):655–661, 1987.

Y. Chen and T.C. Bond. Light absorption by organic carbon from wood combustion. *Atmos. Chem. Phys*, 10:1773–1787, 2010.

J. Chowdhary. *Multiple scattering of polarized light in atmosphere-ocean systems: application to sensitivity analyses of aerosol polarimetry*. PhD thesis, Columbia University, 1999.

J. Chowdhary, B. Cairns, M. Mishchenko, and L. Travis. Retrieval of aerosol properties over the ocean using multispectral and multiangle photopolarimetric measurements from the research scanning polarimeter. *Geophys. Res. Lett.*, 28(2):243–246, 2001.

J. Chowdhary, B. Cairns, and L. Travis. Case studies of aerosol retrievals over the ocean from multiangle, multispectral photopolarimetric remote sensing data. *J. Atmos. Sci.*, 59 (3):383–397, 2002.

J. Chowdhary, B. Cairns, M.I. Mishchenko, P.V. Hobbs, G.F. Cota, J. Redemann, K. Rutledge, B.N. Holben, and E. Russell. Retrieval of aerosol scattering and absorption properties from photopolarimetric observations over the ocean during the clams experiment. *J. Atmos. Sci.*, 62:1093–1117, 2005a.

J. Chowdhary, B. Cairns, M.I. Mishchenko, and L.D. Travis. Using multi-angle multi-spectral photo-polarimetry of the NASA Glory mission to constrain optical properties of aerosols and clouds: results from four field experiments. *Proceedings of SPIE*, 5978: 59780G, 2005b.

J. Chowdhary, B. Cairns, and L.D. Travis. Contribution of water-leaving radiances to multiangle, multispectral polarimetric observations over the open ocean: bio-optical model results for case 1 waters. *Appl. Opt.*, 45(22):5542–5567, 2006.

DA Chu, YJ Kaufman, G. Zibordi, JD Chern, J. Mao, C. Li, and BN Holben. Global monitoring of air pollution over land from the earth observing system-terra moderate resolution imaging spectroradiometer (modis). *J. Geophys. Res.*, 108(D21), 2003.

C.E. Chung, V. Ramanathan, D. Kim, and I.A. Podgorny. Global anthropogenic aerosol direct forcing derived from satellite and ground-based observations. *J. Geophys. Res*, 110, 2005.

A. Clarke, C. McNaughton, V. Kapustin, Y. Shinozuka, S. Howell, J. Dibb, J. Zhou, B. Anderson, V. Brekhovskikh, H. Turner, et al. Biomass burning and pollution aerosol over North America: Organic components and their influence on spectral optical properties and humidification response. *J. Geophys. Res*, 112, 2007.

AD Clarke, JL Varner, F. Eisele, RL Mauldin, D. Tanner, and M. Litchy. Particle production in the remote marine atmosphere: Cloud outflow and subsidence during ACE 1. *J. Geophys. Res.-Atmospheres*, 103(D13), 1998.

W.D. Collins, P.J. Rasch, B.A. Boville, J.J. Hack, J.R. McCaa, D.L. Williamson, B.P. Briegleb, C.M. Bitz, S.J. Lin, and M. Zhang. The formulation and atmospheric simulation of the Community Atmosphere Model version 3 (CAM3). *Journal of Climate*, 19:2144–2161, 2006.

J. D. Crounse, P. F. DeCarlo, D. R. Blake, L. K. Emmons, T. L. Campos, E. C. Apel, A. D. Clarke, A. J. Weinheimer, D. C. McCabe, R. J. Yokelson, J. L. Jimenez, and P. O. Wennberg. Biomass burning and urban air pollution over the central mexican plateau. *Atmos. Chem. Phys.*, 9(14):4929–4944, 2009. doi: 10.5194/acp-9-4929-2009.

L. Curier, G. de Leeuw, P. Kolmonen, A-M. Sundstrom, L. Sogacheva, and Y Bennouna. *Satellite Aerosol Remote Sensing over Land*, chapter Aerosol retrieval over land using the (A)ATSR dual-view algorithm. Springer-Praxis Books in Environmental Sciences, 2009.

B. de Foy, N. A. Krotkov, N. Bei, S. C. Herndon, L. G. Huey, A.-P. Martínez, L. G. Ruiz-Suárez, E. C. Wood, M. Zavala, and L. T. Molina. Hit from both sides: tracking industrial and volcanic plumes in mexico city with surface measurements and omi so_2 retrievals during the milagro field campaign. *Atmos. Chem. Phys.*, 9(24):9599–9617, 2009. doi: 10.5194/acp-9-9599-2009.

M. De Graaf, P. Stammes, and EAA Aben. Analysis of reflectance spectra of UV-absorbing aerosol scenes measured by SCIAMACHY. *J. Geophys. Res*, 112:D02206, 2007.

JF De Haan, PB Bosma, and JW Hovenier. The adding method for multiple scattering calculations of polarized light. *Astron. Astrophys.*, 183:371–391, 1987.

JF de Haan, PB Bosma, and JW Hovenier. The adding method for multiple scattering calculations of polarized light. *Astron. Astrophys.*, 183(2):371–391, 1987.

WA De Rooij and C. Van der Stap. Expansion of Mie scattering matrices in generalized spherical functions. *Astronomy and Astrophysics*, 131:237–248, 1984. ISSN 0004-6361.

J.L. Deuzé, P. Goloub, M. Herman, A. Marchand, G. Perry, S. Susana, and D. Tanré. Estimate of the aerosol properties over the ocean with polder. *J. Geophys. Res.*, 105(D12): 15329–15346, 2000.

J.L. Deuzé, F.M. Bréon, C. Devaux, P. Goloub, M. Herman, B. Lafrance, F. Maignan, A. Marchand, F. Nadal, G. Perry, and D. Tanré. Remote sensing of aerosols over land surfaces from polder-adeos-1 polarized measurements. *J. Geophys. Res.*, 106(D5):4913, 2001.

E. Dinar, A.A. Riziq, C. Spindler, C. Erlick, G. Kiss, and Y. Rudich. The complex refractive index of atmospheric and model humic-like substances (HULIS) retrieved by a cavity ring down aerosol spectrometer (CRD-AS). *Faraday Discussions*, 137:279–295, 2008.

N.M. Donahue, A.L. Robinson, and S.N. Pandis. Atmospheric organic particulate matter: From smoke to secondary organic aerosol. *Atmos. Environ.*, 43(1):94 – 106, 2009. ISSN 1352-2310. doi: DOI:10.1016/j.atmosenv.2008.09.055. Atmos. Environ. - Fifty Years of Endeavour.

J. C. Doran, W. P. Arnott, J. C. Barnard, R. Cary, R. Coulter, J. D. Fast, E. I. Kassianov, L. Kleinman, N. S. Laulainen, T. Martin, G. Paredes-Miranda, M. S. Pekour, W. J. Shaw, D. F. Smith, S. R. Springston, and X.-Y. Yu. The t1-t2 study: evolution of aerosol properties downwind of mexico city. *Atmos. Chem. Phys. Discuss.*, 6(6):12967–12999, 2006. doi: 10.5194/acpd-6-12967-2006.

O. Dubovik and M.D. King. A flexible inversion algorithm for retrieval of aerosol optical properties from sun and sky radiance measurements. *J. Geophys. Res*, 105:20 673–20 696, 2000.

O. Dubovik, B. Holben, T.F. Eck, A. Smirnov, Y.J. Kaufman, M.D. King, D. Tanré, and I. Slutsker. Variability of absorption and optical properties of key aerosol types observed in worldwide locations. *J. Atmos. Sci.*, 59(3):590–608, 2002.

O. Dubovik, A. Sinyuk, T. Lapyonok, B.N. Holben, M. Mishchenko, P. Yang, T.F. Eck, H. Volten, O. Muñoz, B. Veihelmann, et al. Application of spheroid models to account for aerosol particle nonsphericity in remote sensing of desert dust. *J. Geophys. Res*, 111, 2006.

RA Duce, CK Unni, BJ Ray, JM Prospero, and JT Merrill. Long-range atmospheric transport of soil dust from Asia to the tropical North Pacific: Temporal variability. *Science*, 209(4464):1522, 1980.

L. Duforêt, R. Frouin, and P. Dubuisson. Importance and estimation of aerosol vertical structure in satellite ocean-color remote sensing. *Appl. Opt.*, 46(7):1107–1119, 2007.

U. Dusek, GP Frank, L. Hildebrandt, J. Curtius, J. Schneider, S. Walter, D. Chand, F. Drewnick, S. Hings, D. Jung, et al. Size matters more than chemistry for cloud-nucleating ability of aerosol particles. *Science*, 312(5778):1375, 2006.

T.F. Eck, B.N. Holben, J.S. Reid, N.T. O'Neill, J.S. Schafer, O. Dubovik, A. Smirnov, M.A. Yamasoe, and P. Artaxo. High aerosol optical depth biomass burning events: A comparison of optical properties for different source regions. *Geophys. Res. Lett*, 30(20): 2035, 2003.

T.F. Eck, B.N. Holben, J.S. Reid, A. Sinyuk, E.J. Hyer, N.T. O'Neill, G.E. Shaw, J.R.V. Castle, F.S. Chapin, O. Dubovik, A. Smirnov, E. Vermote, J.S. Schafer, D. Giles, I. Slutsker, M. Sorokine, and W.W. Newcomb. Optical properties of boreal region biomass burning aerosols in central Alaska and seasonal variation of aerosol optical depth at an Arctic coastal site. *J. Geophys. Res*, 114, 2009.

T.G. Elias, B. Cairns, and J. Chowdhary. Surface optical properties measured by the airborne research scanning polarimeter during the CLAMS experiment. *Remote Sensing of Clouds and the Atmosphere VIII. Edited by Schaefer, Klaus; Comeron, Adolfo; Carleer, Michel R.; Picard, Richard H. Proceedings of the SPIE,*, 5235:595–606, 2004.

O. Engelsen, B. Pinty, MM Verstraete, and JV Martonchik. Parametric surface bidirectional reflectance factor models foratmospheric radiative transfer modeling. *Geoscience and Remote Sensing Symposium Proceedings, 1998. IGARSS'98. 1998 IEEE International*, 2, 1998.

J. D. Fast, B. de Foy, F. Acevedo Rosas, E. Caetano, G. Carmichael, L. Emmons, D. McKenna, M. Mena, W. Skamarock, X. Tie, R. L. Coulter, J. C. Barnard, C. Wiedinmyer, and S. Madronich. A meteorological overview of the milagro field campaigns. *Atmos. Chem. Phys.*, 7(9):2233–2257, 2007. doi: 10.5194/acp-7-2233-2007.

G. Feingold, W.L. Eberhard, D.E. Veron, and M. Previdi. First measurements of the Twomey indirect effect using ground-based remote sensors. *Geophys. Res. Lett*, 30(6): 1287, 2003.

R. Fletcher. A modified marquardt subroutine for non-linear least squares. Technical report, United Kingdom Atomic Energy Authority, Theoretical Physics Division, Atomic Energy Research Establishment, Harwell, Berkshire, UK, 1971.

B. Fougnie, G. Bracco, B. Lafrance, C. Ruffel, O. Hagolle, and C. Tinel. PARASOL in-flight calibration and performance. *Appl. Opt.*, 46(22):5435–5451, 2007.

HE Fuelberg, DL Harrigan, and W. Sessions. A meteorological overview of the ARCTAS 2008 mission. *Atmos. Chem. Phys*, 10:817–842, 2010.

C.K. Gatebe, M.D. King, S.C. Tsay, Q. Ji, G.T. Arnold, and J.Y. Li. Sensitivity of off-nadir zenith angles to correlation between visible and near-infrared reflectance for use in remote sensing of aerosol over land. *IEEE Trans. Geosci. Remote Sens.*, 39(4):805–819, 2001.

C.K. Gatebe, M.D. King, S. Platnick, G.T. Arnold, E.F. Vermote, and B. Schmid. Airborne spectral measurements of surface–atmosphere anisotropy for several surfaces and ecosystems over southern Africa. *J. Geophys. Res.*, 108(D13):8489, 2003.

CK Gatebe, O. Dubovik, MD King, and A. Sinyuk. Simultaneous retrieval of aerosol and surface optical properties from combined airborne-and ground-based direct and diffuse radiometric measurements. *Atmospheric Chemistry & Physics Discussions*, 9:26491–26538, 2009.

S.J. Ghan and S.E. Schwartz. Aerosol properties and processes. *Bull. Amer. Meteor. Soc*, 88:1059–1083, 2007.

P. Ginoux, L.W. Horowitz, V. Ramaswamy, I.V. Geogdzhayev, B.N. Holben, G. Stenchikov, and X. Tie. Evaluation of aerosol distribution and optical depth in the Geophysical Fluid Dynamics Laboratory coupled model CM2. 1 for present climate. *J. Geophys. Res.*, 111 (D22):D22210, 2006.

P. Goloub, JL Deuzé, M. Herman, and Y. Fouquart. Analysis of the POLDER polarization measurements performed overcloud covers. *IEEE Trans. Geosci. Remote Sens.*, 32(1): 78–88, 1994.

P. Goloub, M. Herman, H. Chepfer, J. Riedi, G. Brogniez, P. Couvert, and G. Sèze. Cloud thermodynamical phase classification from the POLDER spaceborne instrument. *J. Geophys. Res.*, 105:14, 2000.

R.C. Gonzalez and R.E. Woods. *Digital Image Processing*. Addison Wesley Publishing Company, New York, NY, 1992.

L. Grant. Diffuse and specular characteristics of leaf reflectance. *Remote Sens. Environ.*, 22:309–322, 1987.

W.M.F. Grey and P.R.J. North. *Satellite Aerosol Remote Sensing over Land*, chapter Aerosol optical depth from dual-view (A)ATSR satellite observations. Springer-Praxis Books in Environmental Sciences, 2009.

A. P. Grieshop, J. M. Logue, N. M. Donahue, and A. L. Robinson. Laboratory investigation of photochemical oxidation of organic aerosol from wood fires 1: measurement and simulation of organic aerosol evolution. *Atmos. Chem. Phys.*, 9(4):1263–1277, 2009. ISSN 1680-7316.

M. Grutter, R. Basaldud, C. Rivera, R. Harig, W. Junkerman, E. Caetano, and H. Delgado-Granados. So_2 emissions from popocatépetl volcano: emission rates and plume imaging using optical remote sensing techniques. *Atmos. Chem. Phys.*, 8(22):6655–6663, 2008. doi: 10.5194/acp-8-6655-2008.

L. Guanter, L. Gómez-Chova, and J. Moreno. Coupled retrieval of aerosol optical thickness, columnar water vapor and surface reflectance maps from ENVISAT/MERIS data over land. *Remote Sens. Environ.*, 2008.

John W. Hair, Loren M. Caldwell, David A. Krueger, and Chiao-Yao She. High-spectral-resolution lidar with iodine-vapor filters: Measurement of atmospheric-state and aerosol profiles. *Appl. Opt.*, 40(30):5280–5294, 2001.

Johnathan W. Hair, Chris A. Hostetler, Anthony L. Cook, David B. Harper, Richard A. Ferrare, Terry L. Mack, Wayne Welch, Luis Ramos Izquierdo, and Floyd E. Hovis. Airborne high spectral resolution lidar for profiling aerosol optical properties. *Appl. Opt.*, 47(36):6734–6752, 2008.

M. Hallquist, JC Wenger, U. Baltensperger, Y. Rudich, D. Simpson, M. Claeys, J. Dommen, NM Donahue, C. George, AH Goldstein, et al. The formation, properties and impact of secondary organic aerosol: current and emerging issues. *Atmospheric Chemistry and Physics*, 9(14):5155, 2009.

J. Hansen and L. Nazarenko. Soot climate forcing via snow and ice albedos. *Proceedings of the National Academy of Sciences*, 101(2):423–428, 2004.

J. Hansen, A. Lacis, R. Ruedy, and M. Sato. Potential climate impact of Mount Pinatubo eruption. *Geophys. Res. Lett.*, 19(2):215–218, 1992.

J. Hansen, R. Ruedy, M. Sato, and K. Lo. Global Warming Continues. *Science*, 295(5553): 275–275, 2002.

J. Hansen, L. Nazarenko, R. Ruedy, M. Sato, J. Willis, A. Del Genio, D. Koch, A. Lacis, K. Lo, S. Menon, et al. Earth's Energy Imbalance: Confirmation and Implications. *Science*, 308(5727):1431–1435, 2005.

J.E. Hansen and JW Hovenier. Interpretation of the Polarization of Venus. *J. Atmos. Sci.*, 31(4):1137–1160, 1974.

J.E. Hansen and L.D. Travis. Light scattering in planetary atmospheres. *Space Science Reviews*, 16:527–610., 1974.

J.E. Hansen, M. Sato, A. Lacis, R. Ruedy, I. Tegen, and E. Matthews. Climate forcings in the Industrial era. *Proceedings of the National Academy of Sciences*, 95(22):12753–12758, 1998.

OP Hasekamp. Capability of multi-viewing-angle photo-polarimetric measurements for the simultaneous retrieval of aerosol and cloud properties. *Atm. Meas. Tech. Disc.*, 3: 1229–1262, 2010.

O.P. Hasekamp and J. Landgraf. Retrieval of aerosol properties over land surfaces: capabilities of multiple-viewing-angle intensity and polarization measurements. *Appl. Opt.*, 46(16):3332–3344, 2007.

J. Haywood and O. Boucher. Estimates of the direct and indirect radiative forcing due to tropospheric aerosols: A review. *Rev. Geophys*, 38(4):513–543, 2000.

JM Haywood and KP Shine. The effect of anthropogenic sulfate and soot aerosol on the clear sky planetary radiation budget. *Geophys. Res. Lett.*, 22(5):603–606, 1995.

JM Haywood, DL Roberts, A. Slingo, JM Edwards, and KP Shine. General circulation model calculations of the direct radiative forcing by anthropogenic sulfate and fossil-fuel soot aerosol. *Journal of Climate*, 10:1562–1577, 1997.

MD Hebden. An Algorithm for Minimization Using Exact Second Derivatives. Technical Report TP515, Atomic Energy Research Establishment, Harwell, England, 1973.

D. Helmig, J. Ortega, A. Guenther, J.D. Herrick, and C. Geron. Sesquiterpene emissions from loblolly pine and their potential contribution to biogenic aerosol formation in the Southeastern US. *Atmos. Environ.*, 40(22):4150–4157, 2006.

M. Herman, J.L. Deuzé, C. Devaux, P. Goloub, F.M. Bréon, and D. Tanré. Remote sensing of aerosols over land surfaces including polarization measurements and application to polder measurements. *J. Geophys. Res.*, 102(D14):17,039–17,050, 1997.

M. Hess, P. Koepke, and I. Schult. Optical properties of aerosols and clouds: The software package OPAC. *Bull. Amer. Meteor. Soc.*, 79(5):831–844, 1998.

A. Hoffer, A. Gelencser, P. Guyon, G. Kiss, O. Schmid, GP Frank, P. Artaxo, and MO Andreae. Optical properties of humic-like substances(HULIS) in biomass-burning aerosols. *Atmos. Chem. Phys.*, 6(11):3563–3570, 2006.

B.N. Holben, Y.J. Kaufman, T.F. Eck, I. Slutsker, D. Tanre, J.P. Buis, A. Setzer, E. Vermote, and J. Reagan. Aeronet - a federated instrument network and data archive for aerosol characterization. *Remote Sens. Environ.*, 66:1–16, 1998.

J.W. Hovenier. Multiple Scattering of Polarized Light in Planetary Atmospheres. *Astron. Astrophys.*, 13:7, 1971.

N.C. Hsu, S. Tsay, M.D. King, and J.R. Herman. Deep blue retrievals of Asian aerosol properties during ACE-Asia. *IEEE Transactions on Geoscience and Remote Sensing*, 44 (11):3180–3195, 2006. ISSN 0196-2892.

B Hu, W. Lucht, and A.H. Strahler. The interrelationship of atmospheric correction of reflectances andsurface brdf retrieval: a sensitivity study. *IEEE Trans. Geosci. Remote Sens.*, 37(2):724–738, 1999.

R.B. Husar, J.M. Prospero, and L.L. Stowe. Characterization of tropospheric aerosols over the oceans with the noaa advanced very high resolution radiometer optical thickness operational product. *J. Geophys. Res.*, 102(D14):16889–16910, 1997.

A. Ignatov and L. Stowe. Aerosol Retrievals from Individual AVHRR Channels. Part I: Retrieval Algorithm and Transition from Dave to 6S Radiative Transfer Model. *J. Atmos. Sci.*, 59(3):313–334, 2002.

IPCC. *Climate Change 2007 - The Physical Science Basis : Contribution of the Working Group I to the Fourth Assessment Report of the IPCC*. Cambridge University Press, New York, NY, 2007.

D.J Jacob, J.H. Crawford, H. Maring, A.D. Clarke, J.E. Dibb, L.K. Emmons, R.A. Ferrare, C.A. Hostetler, P.B. Russell, H.B. Singh, A.M. Thompson, G.E. Shaw, E. McCauley, J.R. Pederson, and J.A. Fisher. The arctic research of the composition of the troposphere from aircraft and satellites (arctas) mission: design, execution, and first results. *Atmos. Chem. Phys.*, 10:5191–5212, 2010.

M.Z. Jacobson. Strong radiative heating due to the mixing state of black carbon in atmospheric aerosols. *Nature*, 409(6821):695–697, 2001.

Y. Jin, C.B. Schaaf, C.E. Woodcock, F. Gao, X. Li, A.H. Strahler, W. Lucht, and S. Liang. Consistency of modis surface bidirectional reflectance distribution function and albedo retrievals: 2. validation. *J. Geophys. Res*, 108(D5):4159, 2003.

R. Kahn, P. Banerjee, and D. McDonald. Sensitivity of multiangle imaging to natural mixtures of aerosols over ocean. *J. Geophys. Res.*, 106(D16):18,219–18,238, 2001.

R.A. Kahn, B.J. Gaitley, J.V. Martonchik, D.J. Diner, K.A. Crean, and B. Holben. Multiangle Imaging Spectroradiometer (MISR) global aerosol optical depth validation based on 2 years of coincident Aerosol Robotic Network (AERONET) observations. *J. Geophys. Res.*, 110:D10S04, 2005.

Y. J. Kaufman and D. Tanre. Atmospherically resistant vegetation index (arvi) for eos-modis. *IEEE Trans. Geosci. Remote Sens.*, 30:261–270, 1992.

YJ Kaufman, AE Wald, LA Remer, B.C. Gao, R.R. Li, and L. Flynn. The MODIS 2.1-μm channel-correlation with visible reflectancefor use in remote sensing of aerosol. *IEEE Trans. Geosci. Remote Sens.*, 35(5):1286–1298, 1997.

Y. Kawata. Circular polarization of sunlight reflected by planetary atmospheres. *Icarus*, 33:217–232, 1978.

T.W. Kirchstetter, T. Novakov, and P.V. Hobbs. Evidence that the spectral dependence of light absorption by aerosols is affected by organic carbon. *J. Geophys. Res.-Atmospheres*, 109(D21):D21208, 2004.

QL Kleipool, MR Dobber, JF de Haan, and PF Levelt. Earth surface reflectance climatology from 3 years of OMI data. *Journal of Geophysical Research*, 113(D18):D18308, 2008. ISSN 0148-0227.

K.D. Knobelspiesse, C. Pietras, G.S. Fargion, M. Wang, R. Frouin, M.A. Miller, A. Subramaniam, and W.M. Balch. Maritime aerosol optical thickness measured by handheld sun photometers. *Remote Sens. Environ.*, 93(1-2):87–106, 2004.

K.D. Knobelspiesse, B. Cairns, C.B. Schaaf, B. Schmid, and M.O. Román. Surface brdf estimation from an aircraft compared to modis and ground estimates at the southern great plains site. *J. Geophys. Res.*, 113(D20105), October 2008.

K.D. Knobelspiesse, B. Cairns, M. Ottaviani, R. Ferrare, J. Hair, C. Hostetler, M. Obland, R. Rogers, J. Redemann, Y. Shinozuka, V. Brekhovskikh, A. Clarke, S. Freitag, S. Howell, V. Kapusti, and C. McNaughton. Combined retrievals of boreal forest fire aerosol properties with a polarimeter and lidar. *to submit to Atm. Meas. Tech.*, 2010.

D. Koch and A. Del Genio. Black carbon absorption effects on cloud cover, review and synthesis. *Atmos. Chem. Phys.*, 10:7685–7696, 2010.

R. Koppmann, K. Von Czapiewski, and JS Reid. A review of biomass burning emissions, part I: gaseous emissions of carbon monoxide, methane, volatile organic compounds, and nitrogen containing compounds. *Atmos. Chem. Phys. Discuss.*, 5(5):10455–10516, 2005.

I. Koren, Y.J. Kaufman, R. Washington, M.C. Todd, Y. Rudich, J.V. Martins, and D. Rosenfeld. The bodele depression: a single spot in the sahara that provides most of the mineral dust to the amazon forest. *Environmental Research Letters*, 1:014005, 2006.

A. Lacis and J. Hansen. A parameterization for the absorption of solar radiation in the earth's atmosphere. *J. Atmos. Sci.*, 31(1):118–133, 1974.

J. Lean. Evolution of the Sun's spectral irradiance since the Maunder Minimum. *Geophys. Res. Lett.*, 27(16):2425–2428, 2000.

M.D. Lebsock, T.S. L'Ecuyer, and G.L. Stephens. Information content of near-infrared spaceborne multiangular polarization measurements for aerosol retrievals. *J. Geophys. Res.*, 112(D14), 2007.

M. Leroy, JL Deuzé, FM Bréon, O. Hautecoeur, M. Herman, JC Buriez, D. Tanré, S. Bouffies, P. Chazette, and JL Roujean. Retrieval of atmospheric properties and surface bidirectional reflectances over land from POLDER/ADEOS. *J. Geophys. Res*, 102 (17,023):17–037, 1997.

P. A. Lewandowski, W. E. Eichinger, H. Holder, J. Prueger, J. Wang, and L. I. Kleinman. Vertical distribution of aerosols in the vicinity of mexico city during milagro-2006 campaign. *Atmos. Chem. Phys.*, 10(3):1017–1030, 2010. doi: 10.5194/acp-10-1017-2010.

K. Lewis, W. P. Arnott, H. Moosmuller, and C. E. Wold. Strong spectral variation of biomass smoke light absorption and single scattering albedo observed with a novel dual-wavelength photoacoustic instrument. *J. Geophys. Res.*, 113(D16203), 2008.

X. Li and AH Strahler. Geometric-optical bidirectional reflectance modeling of thediscrete crown vegetation canopy: effect of crown shape and mutualshadowing. *IEEE Trans. Geosci. Remote Sens.*, 30(2):276–292, 1992.

S. Liang. Narrowband to broadband conversions of land surface albedo. I- Algorithms. *Remote Sens. Environ.*, 76(2):213–238, 2001.

S. Liang, H. Fang, M. Chen, C.J. Shuey, C. Walthall, C. Daughtry, J. Morisette, C. Schaaf, and A. Strahler. Validating MODIS land surface reflectance and albedo products- methods and preliminary results. *Remote Sens. Environ.*, 83(1):149–162, 2002.

S. Liang, C.J. Shuey, A.L. Russ, H. Fang, M. Chen, C.L. Walthall, C.S.T. Daughtry, and R. Hunt Jr. Narrowband to broadband conversions of land surface albedo. II- Validation. *Remote Sens. Environ.*, 84(1):25–41, 2003.

X.-Z. Liang, M. Xu, W. Gao, K. Kunkel, J. Slusser, Y. Dai, Q. Min, P. R. Houser, M. Rodell, C. B. Schaaf, and F. Gao. Development of land surface albedo parameterization based on moderate resolution imaging spectroradiometer (modis) data. *J. Geophys. Res. (Atmospheres)*, 110:11107, June 2005. doi: 10.1029/2004JD005579.

K.N. Liou. *An Introduction to Atmospheric Radiation*. Academic Press, New York, NY, second edition, 2002.

P. Litvinov, O. Hasekamp, B. Cairns, and M. Mishchenko. Reflection models for soil and vegetation surfaces from multiple-viewing angle photopolarimetric measurements. *J. Quant. Spectrosc. Radiat. Transfer*, 111:529–539, 2010.

L. Liu and M.I. Mishchenko. Toward unified satellite climatology of aerosol properties: Direct comparisons of advanced level 2 aerosol products. *J. Quant. Spectrosc. Radiat. Transfer*, 109(14):2376–2385, 2008.

L. Liu, M.I. Mishchenko, and W. Patrick Arnott. A study of radiative properties of fractal soot aggregates using the superposition T-matrix method. *J. Quant. Spectrosc. Radiat. Transfer*, 109(15):2656–2663, 2008.

JM Livingston, J. Redemann, PB Russell, O. Torres, B. Veihelmann, P. Veefkind, R. Braak, A. Smirnov, L. Remer, RW Bergstrom, et al. Comparison of aerosol optical depths from the Ozone Monitoring Instrument (OMI) on Aura with results from airborne sunphotometry, other space and ground measurements during MILAGRO/INTEX-B. *Atmos. Chem. Phys. Discuss.*, 9(2):9961–10013, 2009.

U. Lohmann and J. Feichter. Global indirect aerosol effects: a review. *Atmos. Chem. Phys*, 5(5):715–737, 2005.

U. Lohmann and C. Hoose. Sensitivity studies of different aerosol indirect effects in mixed-phase clouds. *Atmos. Chem. Phys*, 9:8917–8934, 2009.

U. Lohmann, B. Karcher, and C. Timmreck. Impact of the Mount Pinatubo eruption on cirrus clouds formed by homogeneous freezing in the ECHAM4 GCM. *J. Geophys. Res*, 108:4568, 2003.

CN Long, DW Slater, and T.P. Tooman. *Total Sky Imager Model 880 Status and Testing Results*. Pacific Northwest National Laboratory, Atmospheric Radiation Measurement Program, 2001.

W. Lucht, A.H. Hyman, A.H. Strahler, M.J. Barnsley, P. Hobson, and J.P. Muller. A comparison of satellite-derived spectral albedos to ground-based broadband albedo measurements modeled to satellite spatial scale for a semidesert landscape. *Remote Sens. Environ.*, 74(1):85–98, 2000a.

W. Lucht, C.B. Schaaf, and A.H. Strahler. An algorithm for the retrieval of albedo from space using semiempirical brdf models. *IEEE Trans. Geosci. Remote Sens.*, 38(2):977–998, 2000b.

Y. Luo, A.P. Trishchenko, R. Latifovic, and Z. Li. Surface bi-directional reflectance properties over the arm sgp area from satellite multi-platform observations. In D. Carrothers, editor, *Proceedings of the Thirteenth Atmospheric Radiation Measurement (ARM) Science Team Meeting,*, Richland, WA, 2003. Department of Energy.

Y. Luo, A. P. Trishchenko, R. Latifovic, and Z. Li. Surface bidirectional reflectance and albedo properties derived using a land cover based approach with moderate resolution imaging spectroradiometer observations. *J. Geophys. Res*, 110, 2005.

M. Mallet, JC Roger, S. Despiau, O. Dubovik, and JP Putaud. Microphysical and optical properties of aerosol particles in urban zone during ESCOMPTE. *Atmos. Res.*, 69(1-2): 73–97, 2003.

C.B. Markwardt. Non-linear Least Squares Fitting in IDL with MPFIT. *Arxiv preprint arXiv:0902.2850*, 2009.

N. A. Marley, J. S. Gaffney, T. Castro, A. Salcido, and J. Frederick. Measurements of aerosol absorption and scattering in the mexico city metropolitan area during the milagro field campaign: a comparison of results from the t0 and t1 sites. *Atmos. Chem. Phys.*, 9 (1):189–206, 2009. doi: 10.5194/acp-9-189-2009.

J.V. Martins, P.V. Hobbs, R.E. Weiss, and P. Artaxo. Sphericity and morphology of smoke particles from biomass burning in Brazil. *J. Geophys. Res.-Atmospheres*, 103(D24), 1998.

J.V. Martonchik, D.J. Diner, K.A. Crean, and M.A. Bull. Regional aerosol retrieval results from misr. *IEEE Trans. Geosci. Remote Sens.*, 40(7):1520–1532, 2002.

TA Mather, DM Pyle, and C. Oppenheimer. Tropospheric volcanic aerosol. *GEOPHYSICAL MONOGRAPH-AMERICAN GEOPHYSICAL UNION*, 139:189–212, 2003.

O.L. Mayol-Bracero, P. Guyon, B. Graham, G. Roberts, M.O. Andreae, S. Decesari, M.C. Facchini, S. Fuzzi, and P. Artaxo. Water-soluble organic compounds in biomass burning aerosols over amazonia, 2, apportionment of the chemical composition and importance of the polyacidic fraction. *J. Geophys. Res.*, 107(D20), 2002.

C. L. McConnell, P. Formenti, E. J. Highwood, and M. A. J. Harrison. Using aircraft measurements to determine the refractive index of saharan dust during the dodo experiments. *Atmos. Chem. Phys.*, 10(6):3081–3098, 2010. doi: 10.5194/acp-10-3081-2010.

M.P. McCormick, L.W. Thomason, and C.R. Trepte. Atmospheric effects of the Mt Pinatubo eruption. *Nature*, 373(6513):399–404, 1995.

C.S. McNaughton, A.D. Clarke, S.G. Howell, M. Pinkerton, B. Anderson, L. Thornhill, C. Hudgins, E. Winstead, J.E. Dibb, E. Scheuer, et al. Results from the DC-8 inlet characterization experiment (DICE): Airborne versus surface sampling of mineral dust and sea salt aerosols. *Aerosol Sci. Technol.*, 41(2):136–159, 2007.

CS McNaughton, AD Clarke, V. Kapustin, Y. Shinozuka, SG Howell, BE Anderson, E. Winstead, J. Dibb, E. Scheuer, RC Cohen, et al. Observations of heterogeneous reactions between Asian pollution and mineral dust over the Eastern North Pacific during INTEX-B. *Atmos. Chem. Phys. Discuss.*, 9(2):8469–8539, 2009.

R.D. McPeters and G.S.F. Center. *Earth Probe Total Ozone Mapping Spectrometer (TOMS) Data Product User's Guide*. Number NASA TP-1998-206895. National Aeronautics and Space Administration, Goddard Space Flight Center; National Technical Information Service, distributor, 1998.

S. Menon, J. Hansen, L. Nazarenko, and Y. Luo. Climate effects of black carbon aerosols in China and India. *Science*, 297(5590):2250, 2002.

N.L. Miles, J. Verlinde, and E.E. Clothiaux. Cloud droplet size distributions in low-level stratiform clouds. *J. Atmos. Sci.*, 57:295–311, 2000.

P. Minnis, EF Harrison, LL Stowe, GG Gibson, FM Denn, DR Doelling, and WL Smith Jr. Radiative climate forcing by the Mount Pinatubo eruption. *Science*, 259(5100):1411, 1993.

M.I. Mishchenko. Calculation of the amplitude matrix for a nonspherical particle in a fixed orientation. *Appl. Opt*, 39(6):1026–1031, 2000.

M.I. Mishchenko and L.D. Travis. Capabilities and limitations of a current FORTRAN implementation of the T-matrix method for randomly oriented, rotationally symmetric scatterers-Computational Methods. *J. Quant. Spectrosc. Radiat. Transfer*, 60(3):309–324, 1998.

M.I. Mishchenko and L.D. Travis. Gustav Mie and the evolving discipline of electromagnetic scattering by particles. *Bull. Amer. Meteor. Soc.*, 89(12):1853–1861, 2008.

MI Mishchenko, AA Lacis, BE Carlson, and LD Travis. Nonsphericity of dust-like tropospheric aerosols: Implications for aerosol remote sensing and climate modeling. *Geophys. Res. Lett.*, 22(9):1077–1080, 1995.

M.I. Mishchenko, L.D. Travis, and D.W. Mackowski. T-Matrix Computations of Light Scattering by Nonspherical Particles: a Review. *J. Quant. Spectrosc. Radiat. Transfer*, 55(5), 1996.

M.I. Mishchenko, I.V. Geogdzhayev, B. Cairns, W.B. Rossow, and A.A. Lacis. Aerosol retrievals over the ocean by use of channels 1 and 2 AVHRR data: Sensitivity analysis and preliminary results. *Appl. Opt*, 38(36):7325–7341, 1999.

M.I. Mishchenko, J.W. Hovenier, and L.D. Travis. *Light Scattering by Nonspherical Particles: Theory, Measurements, and Applications*. Academic Press, New York, NY, 2000.

M.I. Mishchenko, L.D. Travis, and A.A. Lacis. *Scattering, Absorption, and Emission of Light by Small Particles*. Cambridge University Press, 2002.

M.I. Mishchenko, B. Cairns, J.E. Hansen, L.D. Travis, R. Burg, Y.J. Kaufman, J. Vanderlei Martins, and E.P. Shettle. Monitoring of aerosol forcing of climate from space: analysis of measurement requirements. *J. Quant. Spectrosc. Radiat. Transfer*, 88(1-3): 149–161, 2004.

M.I. Mishchenko, L.D. Travis, and A.A. Lacis. *Multiple scattering of light by particles: radiative transfer and coherent backscattering*. Cambridge Univ Press, 2006.

M.I. Mishchenko, B. Cairns, G. Kopp, CF Schueler, BA Fafaul, JE Hansen, RJ Hooker, T. Itchkawich, HB Maring, and LD Travis. Accurate monitoring of terrestrial aerosols and total solar irradiance: introducing the Glory mission. *Bull. Amer. Meteorol. Soc*, 88, 2007a.

M.I. Mishchenko, I.V. Geogdzhayev, B. Cairns, B.E. Carlson, J. Chowdhary, A.A. Lacis, L. Liu, W.B. Rossow, and L.D. Travis. Past, present, and future of global aerosol climatologies derived from satellite observations: A perspective. *J. Quant. Spectrosc. Radiat. Transfer,*, 106:325–347, 2007b.

M.I. Mishchenko, I.V. Geogdzhayev, WB Rossow, B. Cairns, BE Carlson, AA Lacis, L. Liu, and LD Travis. Long-term satellite record reveals likely recent aerosol trend. *Science*, 315(5818):1543, 2007c.

M.I. Mishchenko, I.V. Geogdzhayev, L. Liu, A.A. Lacis, B. Cairns, and L.D. Travis. Toward unified satellite climatology of aerosol properties: What do fully compatible MODIS and MISR aerosol pixels tell us? *J. Quant. Spectrosc. Radiat. Transfer*, 2009.

LT Molina, S. Madronich, JS Gaffney, E. Apel, B. de Foy, J. Fast, R. Ferrare, S. Herndon, JL Jimenez, B. Lamb, et al. An overview of the MILAGRO 2006 campaign: Mexico City emissions and their transport and transformation. *Atmos. Chem. Phys. Discuss*, 10: 7819–7983, 2010.

J. Moré. The levenberg-marquardt algorithm: Implementation and theory. In G. A. Watson, editor, *Lecture Notes in Mathematics: Numerical Analysis*, volume 630, pages 105–116. Proceedings of the Biennial Conference Held at Dundee, Springer-Verlag: Berlin, 1977.

J. J. Moré, B. S. Garbow, and K. E. Hillstrom. *User Guide for MINPACK-1*. Argonne National Laboratory Report ANL-80-74, Argonne, Ill., 1980.

V.R. Morris. Microwave radiometer (mwr) handbook. Technical Report ARM TR-016, U.S. Department of Energy, 2006.

J. Mühle, T.J. Lueker, Y. Su, B.R. Miller, K.A. Prather, and R.F. Weiss. Trace gas and particulate emissions from the 2003 southern California wildfires. *J. Geophys. Res.*, 112 (D3), 2007.

D. Müller, I. Mattis, U. Wandinger, A. Ansmann, D. Althausen, and A. Stohl. Raman lidar observations of aged siberian and canadian forest fire smoke in the free troposphere over germany in 2003: Microphysical particle characterization. *J. Geophys. Res*, 110:17201, 2005.

D. Müller, I. Mattis, A. Ansmann, U. Wandinger, C. Ritter, and D. Kaiser. Multiwavelength raman lidar observations of particle growth during long-range transport of forest-fire smoke in the free troposphere. *Geophys. Res. Lett.*, 34(5):L05803, 2007.

G. Myhre. Consistency between satellite-derived and modeled estimates of the direct aerosol effect. *Science*, 325(5937):187, 2009.

G. Myhre and A. Myhre. Uncertainties in radiative forcing due to surface albedo changes caused by land-use changes. *Journal of Climate*, 16(10):1511–1524, 2003.

F. Nadal and F.-M. Breon. Parameterization of surface polarized reflectance derived from polder spaceborne measurements. *IEEE Trans. Geosci. Remote Sens.*, 37(3):1709, 1999.

F.E. Nicodemus, National Bureau of Standards, and United States. *Geometrical Considerations and Nomenclature for Reflectance*. US Dept. of Commerce, National Bureau of Standards: for sale by the Supt. of Docs., US Govt. Print. Off., 1977.

NT O'Neill, A. Ignatov, BN Holben, and TF Eck. The lognormal distribution as a reference for reporting aerosol optical depth statistics: Empirical tests using multi-year, multi-site AERONET sunphotometer data. *Geophys. Res. Lett*, 27(20):3333–3336, 2000.

N.T. O'Neill, T.F. Eck, B.N. Holben, A. Smirnov, A. Royer, and Z. Li. Optical properties of boreal forest fire smoke derived from sun photometry. *J. Geophys. Res.*, 107(D11), 2002.

G. Paredes-Miranda, W. P. Arnott, J. L. Jimenez, A. C. Aiken, J. S. Gaffney, and N. A. Marley. Primary and secondary contributions to aerosol light scattering and absorption in mexico city during the milagro 2006 campaign. *Atmos. Chem. Phys.*, 9(11):3721–3730, 2009. doi: 10.5194/acp-9-3721-2009.

J.E. Penner, R.J. Charlson, S.E. Schwartz, J.M. Hales, N.S. Laulainen, L. Travis, R. Leifer, T. Novakov, J. Ogren, and LF Radke. Quantifying and Minimizing Uncertainty of Climate Forcing by Anthropogenic Aerosols. *Bull. Amer. Meteor. Soc.*, 75:375–400, 1994.

G.W. Petty. *A First Course in Atmospheric Radiation*. Sundog Publishing, Madison, Wisconsin, second edition, 2006.

R. Pincus and M.B. Baker. Effect of precipitation on the albedo susceptibility of clouds in the marine boundary layer. *Nature*, 1994.

B. Pinty, A. Lattanzio, J.V. Martonchik, M.M. Verstraete, N. Gobron, M. Taberner, J.L. Widlowski, R.E. Dickinson, and Y. Govaerts. Coupling Diffuse Sky Radiation and Surface Albedo. *J. Atmos. Sci.*, 62(7):2580–2591, 2005.

J.M. Prospero, R.A. Glaccum, and R.T. Nees. Atmospheric transport of soil dust from Africa to South America. *Nature*, 289(5798):570–572, 1981.

V. Ramanathan, PJ Crutzen, JT Kiehl, and D. Rosenfeld. Aerosols, climate, and the hydrological cycle. *Science*, 294(5549):2119, 2001.

J. Redemann, B. Schmid, JA Eilers, R. Kahn, RC Levy, PB Russell, JM Livingston, PV Hobbs, WL Smith, and BN Holben. Suborbital measurements of spectral aerosol optical depth and its variability at subsatellite grid scales in support of CLAMS 2001. *J. Atmos. Sci.*, 62(4):993–1007, 2005.

J. Redemann, Q. Zhang, J. Livingston, P. Russell, Y. Shinozuka, A. Clarke, R. Johnson, and R. Levy. Testing aerosol properties in modis collection 4 and 5 using airborne sunphotometer observations in intex-b/milagro. *Atmos. Chem. Phys.*, 9(21):8159–8172, 2009. ISSN 1680-7316.

J.S. Reid and P.V. Hobbs. Physical and optical properties of young smoke from individual biomass fires in Brazil. *J. Geophys. Res.-Atmospheres*, 103(D24), 1998.

J.S. Reid, P.V. Hobbs, R.J. Ferek, D.R. Blake, J.V. Martins, M.R. Dunlap, and C. Liousse. Physical, chemical, and optical properties of regional hazes dominated by smoke in Brazil. *J. Geophys. Res.-Atmospheres*, 103(D24), 1998.

J.S. Reid, T.F. Eck, S.A. Christopher, R. Koppmann, and O. Dubovik. A review of biomass burning emissions part III: intensive optical properties of biomass burning particles. *Atmos. Chem. Phys. Discuss*, 5:827–849, 2005a.

J.S. Reid, R. Koppmann, T.F. Eck, and D.P. Eleuterio. A review of biomass burning emissions part II: intensive physical properties of biomass burning particles. *Atmos. Chem. Phys*, 5(3):799–825, 2005b.

L. A. Remer, Y.J. Kaufman, B.N. Holben, A.M. Thompson, and D. McNamara. Biomass burning aerosol size distribution and modeled optical properties. *J. Geophys. Res.*, 103 (D24):31879–31892, 1998.

L. A. Remer, R. G. Kleidman, R. C. Levy, Y.J. Kaufman, D. Tanré, S. Mattoo, J. V. Martins, C. Ichoku, I. Koren, H. Yu, and B.N. Holben. Global aerosol climatology from the modis satellite sensors. *J. Geophys. Res.*, 113(D14S07), 2008.

L.A. Remer, S. Gassò, D.A. Hegg, Y.J. Kaufman, and B.N. Holben. Urban/industrial aerosol: Ground-based Sun/sky radiometer and airborne in situ measurements. *J. Geophys. Res*, 102(16):849–16, 1997.

L.A. Remer, A.E. Wald, and Y.J. Kaufman. Angular and seasonal variation of spectral surface reflectanceratios: implications for the remote sensing of aerosol over land. *IEEE Trans. Geosci. Remote Sens.*, 39(2):275–283, 2001.

L.A. Remer, Y.J. Kaufman, D. Tanré, S. Mattoo, D.A. Chu, J.V. Martins, R.R. Li, C. Ichoku, R.C. Levy, R.G. Kleidman, T.F. Eck, E. Vermote, and B.N. Holben. The MODIS Aerosol Algorithm, Products, and Validation. *J. Atmos. Sci.*, 62(4):947–973, 2005.

L.A. Remer, Y.J. Kaufman, and R.G. Kleidman. Comparison of three years of terra and aqua modis aerosol optical thickness over the global oceans. *Geoscience and Remote Sensing Letters, IEEE*, 3(4):537– 540, 2006.

C.D. Rodgers. *Inverse Methods for Atmospheric Sounding: Theory and Practice*. World Scientific, 2000.

R.R. Rogers, J.W. Hair, C.A. Hostetler, R.A. Ferrare, M.D. Obland, A.L. Cook, D.B. Harper, S.P. Burton, Y. Shinozuka, C.S. McNaughton, A.D. Clarke, J. Redemann, P.B. Russell, J.M. Livingston, and L. I. Kleinman. NASA LaRC airborne high spectral resolution lidar aerosol measurements during MILAGRO: observations and validation. *Atmos. Chem. Phys. Discuss.*, 9(2):8817–8856, 2009.

G. Rondeaux and M. Herman. Polarization of light reflected by crop canopies. *Remote Sens. Environ.*, 38:63–75, 1991.

J. Ross. *The radiation regime and architecture of plant stands*. W. Junk, Norwell, MA, 1981.

J.L. Roujean, M. Leroy, and P.Y. Deschanps. A bidirectional reflectance model of the Earth's surface for the correction of remote sensing data. *J. Geophys. Res.*, 97(D18): 20455–20468, 1992.

PB Russell, JM Livingston, EG Dutton, RF Pueschel, JA Reagan, TE DeFoor, MA Box, D. Allen, P. Pilewskie, BM Herman, et al. Pinatubo and pre-Pinatubo optical-depth spectra: Mauna Loa measurements, comparisons, inferred particle size distributions, radiative effects, and relationship to lidar data. *Journal of Geophysical Research*, 98 (D12):22969, 1993. ISSN 0148-0227.

PB Russell, JM Livingston, P. Hignett, S. Kinne, J. Wong, A. Chien, R. Bergstrom, P. Durkee, and PV Hobbs. Aerosol-induced radiative flux changes off the United States mid-Atlantic coast: Comparison of values calculated from sunphotometer and in situ data with those measured by airborne pyranometer. *J. Geophys. Res.-Atmospheres*, 104(D2), 1999.

P.B. Russell, R.W. Bergstrom, Y. Shinozuka, A.D. Clarke, P.F. DeCarlo, J.L. Jimenez, J.M. Livingston, J. Redemann, O. Dubovik, and A. Strawa. Absorption Angstrom Exponent in AERONET and related data as an indicator of aerosol composition. *Atmos. Chem. Phys*, 10:1155–1169, 2010.

M.L. Salby. *Fundamentals of Atmospheric Physics*. Academic Press, 1996.

J.G. Salomon, C.B. Schaaf, A.H. Strahler, F. Gao, and Y. Jin. Validation of the MODIS Bidirectional Reflectance Distribution Function and Albedo Retrievals Using Combined Observations From the Aqua and Terra Platforms. *IEEE Trans. Geosci. Remote Sens.*, 44(6):1555–1565, 2006.

C. Schaaf, A. Strahler, M. Roman, J. Salomon, and J. Hodges. Assessment of albedo derived from the moderate-resolution imaging spectroradiometer at the southern great plains site. In *Proceedings of the Sixteenth ARM Science Team Meeting*, Alburquerque, NM, March 2006.

C.B. Schaaf, F. Gao, A.H. Strahler, W. Lucht, X. Li, T. Tsang, N.C. Strugnell, X. Zhang, Y. Jin, and J.P. Muller. First operational brdf, albedo nadir reflectance products from modis. *Remote Sens. Environ.*, 83(1):135–148, 2002.

G. Schaepman-Strub, M.E. Schaepman, T.H. Painter, S. Dangel, and J.V. Martonchik. Reflectance quantities in optical remote sensing: definitions and case studies. *Remote Sens. Environ.*, 103(1):27–42, 2006.

B. Schmid, J. Redemann, PB Russell, PV Hobbs, DL Hlavka, MJ McGill, BN Holben, EJ Welton, JR Campbell, O. Torres, et al. Coordinated airborne, spaceborne, and ground-based measurements of massive, thick aerosol layers during the dry season in Southern Africa. *J. Geophys. Res*, 108(D13):8496, 2003.

B. Schmid, R. Ferrare, C. Flynn, R. Elleman, D. Covert, A. Strawa, E. Welton, D. Turner, H. Jonsson, J. Redemann, J. Eilers, K. Ricci, A. G. Hallar, M. Clayton, J. Michalsky, A. Smirnov, B. Holben, and J. Barnard. How well do state-of-the-art techniques measuring the vertical profile of tropospheric aerosol extinction compare. *J. Geophys. Res*, 111, 2006.

G.A. Schmidt, R. Ruedy, J.E. Hansen, I. Aleinov, N. Bell, M. Bauer, S. Bauer, B. Cairns, V. Canuto, Y. Cheng, et al. Present-Day Atmospheric Simulations Using GISS ModelE: Comparison to In Situ, Satellite, and Reanalysis Data. *Journal of Climate*, 19(2):153–192, 2006.

M. Schulz, C. Textor, S. Kinne, Y. Balkanski, S. Bauer, T. Berntsen, T. Berglen, O. Boucher, F. Dentener, S. Guibert, et al. Radiative forcing by aerosols as derived from the AeroCom present-day and pre-industrial simulations. *Atmos. Chem. Phys.*, 6(12):5246, 2006.

D.J. Segelstein. *The complex refractive index of water*. PhD thesis, Department of Physics. University of Missouri-Kansas City, 1981.

E.P. Shettle and R.W. Fenn. Models for the aerosols of the lower atmosphere and the effects of humidity variations on their optical properties. Technical Report AFGL-TR-79-0214, Air Force Geophysics Laboratory, Hanscom Air Force Base, United States Air Force, 1979.

Y. Shi and CN Long. *Best Estimate Radiation Flux Value-added Procedure: Algorithm Operational Details and Explanations*. Number ARM TR-008. Pacific Northwest National Laboratory, 2002.

Y. Shinozuka, J. Redemann, JM Livingston, PB Russell, AD Clarke, SG Howell, S. Freitag, NT O'Neill, EA Reid, R. Johnson, et al. Airborne observation of aerosol optical depth during ARCTAS: vertical profiles, inter-comparison, fine-mode fraction and horizontal variability. *Atmos. Chem. Phys., submitted*, 2010.

A. Smirnov, I. Slutsker, BN Holben, EJ Welton, and P. Formenti. Optical properties of Saharan dust during ACE 2. *J. Geophys. Res.*, 103(D21):28079–28092, 1998.

A. Smirnov, B.N. Holben, Y.J. Kaufman, O. Dubovik, T.F. Eck, I. Slutsker, C. Pietras, and R.N. Halthore. Optical properties of atmospheric aerosol in maritime environments. *J. Atmos. Sci.*, 59:501–523, 2002.

A. Smirnov, B. N. Holben, O. Dubovik, R. Frouin, T. F. Eck, and I. Slutsker. Maritime component in aerosol optical models derived from aerosol robotic network data. *J. Geophys. Res*, 108(D1):4033, 2003.

A. Smirnov, B. N. Holben, I. Slutsker, D. M. Giles, C. R. McClain, T. F. Eck, S. M. Sakerin, A. Macke, P. Croot, G. Zibordi, P. K. Quinn, J. Sciare, S. Kinne, M. Harvey, T. J. Smyth, S. Piketh, T. Zielinski, A. Proshutinsky, J. I. Goes, N. B. Nelson, P. Larouche, V. F. Radionov, P. Goloub, K. Krishna Moorthy, R. Matarrese, E. J. Robertson, and F. Jourdin. Maritime aerosol network as a component of aerosol robotic network. *J. Geophys. Res.*, 114(D06204), 2009.

A. Stohl, C. Forster, A. Frank, P. Seibert, and G. Wotawa. Technical note: The Lagrangian particle dispersion model FLEXPART version 6.2. *Atmos. Chem. Phys. Discuss.*, 5(4): 4739–4799, 2005.

A.H. Strahler, W. Lucht, C.B. Schaaf, T. Tsang, F. Gao, X. Li, J.P. Muller, P. Lewis, and M.J. Barnsley. MODIS BRDF/Albedo Product: Algorithm Theoretical Basis Document Version 5.0. Technical report, National Aeronautics and Space Administration, 1999.

N. Sugimoto and C.H. Lee. Characteristics of dust aerosols inferred from lidar depolarization measurements at two wavelengths. *Appl. Opt.*, 45(28):7468–7474, 2006.

H. Sun, L. Biedermann, and T.C. Bond. Color of brown carbon: A model for ultraviolet and visible light absorption by organic carbon aerosol. *Geophys. Res. Lett.*, 34(17):L17813, 2007.

D. Tanré, YJ Kaufman, M. Herman, and S. Mattoo. Remote sensing of aerosol properties over oceans using the MODIS/EOS spectral radiances. *J. Geophys. Res.*, 102(D14): 16971–16988, 1997.

O. Torres, A. Tanskanen, B. Veihelmann, C. Ahn, R. Braak, P.K. Bhartia, P. Veefkind, and P. Levelt. Aerosols and surface UV products from Ozone Monitoring Instrument observations: An overview. *Journal of Geophysical Research*, 112(D24):D24S47, 2007. ISSN 0148-0227.

S. Twomey. The Influence of Pollution on the Shortwave Albedo of Clouds. *J. Atmos. Sci.*, 34(7):1149–1152, 1977.

S. Twomey. Pollution and the planetary albedo. *Atmos. Environ.*, 8(12):1251–1256, 1974.

H.C. van de Hulst. *Light scattering by small particles*. Dover Pubns, 1981.

V.C. Vanderbilt and L. Grant. Plant canopy specular reflectance model. *IEEE Trans. Geosci. Remote Sens.*, 23:722–730, 1985.

V.C. Vanderbilt and L. Grant. *Photon-vegetation interactions: applications in optical remote sensing and plant ecology*, chapter Polarization of Light by Vegetation, pages 194–228. Springer-Verlag, 1991.

V.C. Vanderbilt, L. Grant, L. L. Biehl, and B. F. Robinson. Specular, diffuse, and polarized light scattered by two wheat canopies. *Appl. Opt.*, 24:2408–2418, 1985.

A. Virkkula, N.C. Ahlquist, D.S. Covert, W.P. Arnott, P.J. Sheridan, P.K. Quinn, and D.J. Coffman. Modification, calibration and a field test of an instrument for measuring light absorption by particles. *Aerosol Sci. Technol.*, 39(1):68–83, 2005.

U. Wandinger, D. Muller, C. Bockmann, D. Althausen, V. Matthias, J. Bosenberg, V. Weiß, M. Fiebig, M. Wendisch, A. Stohl, et al. Optical and microphysical characterization of biomass-burning and industrial-pollution aerosols from multiwavelength lidar and aircraft measurements. *J. Geophys. Res*, 107(10.1029), 2002.

J. Wang, S.A. Christopher, J.S. Reid, H. Maring, D. Savoie, B.N. Holben, J.M. Livingston, P.B. Russell, and S.-K. Yang. Goes 8 retrieval of dust aerosol optical thickness over the atlantic ocean during pride. *J. Geophys. Res.*, 108(D19), 2003.

M. Wang, K. D. Knobelspiesse, and C. R. McClain. Study of the sea-viewing wide field-of-view sensor (seawifs) aerosol optical property data over ocean in combination with the ocean color products. *J. Geophys. Res*, 110(D10S06), 2005.

Z. Wang, X. Zeng, and M. Barlage. Moderate resolution imaging spectroradiometer bidirectional reflectance distribution function–based albedo parameterization for weather and climate models. *J. Geophys. Res.*, 112(D02103), 2007.

W. Wanner, X. Li, and A.H. Strahler. On the derivation of kernel-driven models of bidirectional reflectance. *J. Geophys. Res*, 100(D10):21077–21090, 1995.

F. Waquet, J.-F. Léon, P. Goloub, J. Pelon, D. Tanré, and J.-L. Deuzé. Maritime and dust aerosol retrieval from polarized and multispectral active and passive sensors. *J. Geophys. Res.*, 110(D10S10), 2005.

F. Waquet, B. Cairns, K. Knobelspiesse, J. Chowdhary, LD Travis, B. Schmid, and MI Mishchenko. Polarimetric remote sensing of aerosols over land. *J. Geophys. Res*, 114, 2009a.

F. Waquet, J.F. Léon, B. Cairns, P. Goloub, J.L. Deuzé, and F. Auriol. Analysis of the spectral and angular response of the vegetated surface polarization for the purpose of aerosol remote sensing over land. *Appl. Opt.*, 48(6):1228–1236, 2009b.

F. Waquet, J. Riedi, LC Labonnote, P. Goloub, B. Cairns, J.L. Deuzé, and D. Tanré. Aerosol Remote Sensing over Clouds Using A-Train Observations. *J. Atmos. Sci.*, 66(8):2468–2480, 2009c.

D.M. Winker, J. Pelon, and M.P. McCormick. The calipso mission: Spaceborne lidar for observation of aerosols and clouds. *Int. Society for Optical Engineering*, 4893:1–11, 2003.

D.M. Winker, W. Hunt, and C. Hostetler. Status and performance of the caliop lidar. *Int. Society for Optical Engineering*, 5575:8–15, 2004.

D.M. Winker, C.A. Hostetler, M.A. Vaughan, and A.H. Omar. Caliop algorithm theoretical basis document, part i. Technical Report PC-SCI-202 Part I, NASA Langley Research Center, 2006.

D.M. Winker, W.H. Hunt, M.J. McGill, et al. Initial performance assessment of CALIOP. *Geophys. Res. Lett*, 34:19, 2007.

F. Yang. Parameterizing the dependence of surface albedo on solar zenith angle using atmospheric radiation measurement observations. In *Proceedings of the Sixteenth ARM Science Team Meeting Proceedings*, Alburquerque, NM, March 2006.

R. J. Yokelson, S. P. Urbanski, E. L. Atlas, D. W. Toohey, E. C. Alvarado, J. D. Crounse, P. O. Wennberg, M. E. Fisher, C. E. Wold, T. L. Campos, K. Adachi, P. R. Buseck, and W. M. Hao. Emissions from forest fires near mexico city. *Atmos. Chem. Phys.*, 7(21): 5569–5584, 2007. doi: 10.5194/acp-7-5569-2007.

X.-Y. Yu, R. A. Cary, and N. S. Laulainen. Primary and secondary organic carbon downwind of mexico city. *Atmos. Chem. Phys.*, 9(18):6793–6814, 2009. doi: 10.5194/acp-9-6793-2009.